Optical Control of the Temporal Contrast in Chirped-Pulse-Amplification Lasers

Optische Steuerung des zeitlichen Kontrastes in Chirped-Pulse-Amplification Lasern
Zur Erlangung des Grades eines Doktors der Naturwissenschaften (Dr. rer. nat.)
Genehmigte Dissertation von Simon Röder
Tag der Einreichung: 16. Oktober 2023, Tag der Prüfung: 06. November 2023
Veröffentlichungsjahr auf TUprints: 2024

1. Gutachten: Prof. Dr. Vincent Bagnoud
2. Gutachten: Prof. Dr. Markus Roth
Darmstadt, Technische Universität Darmstadt

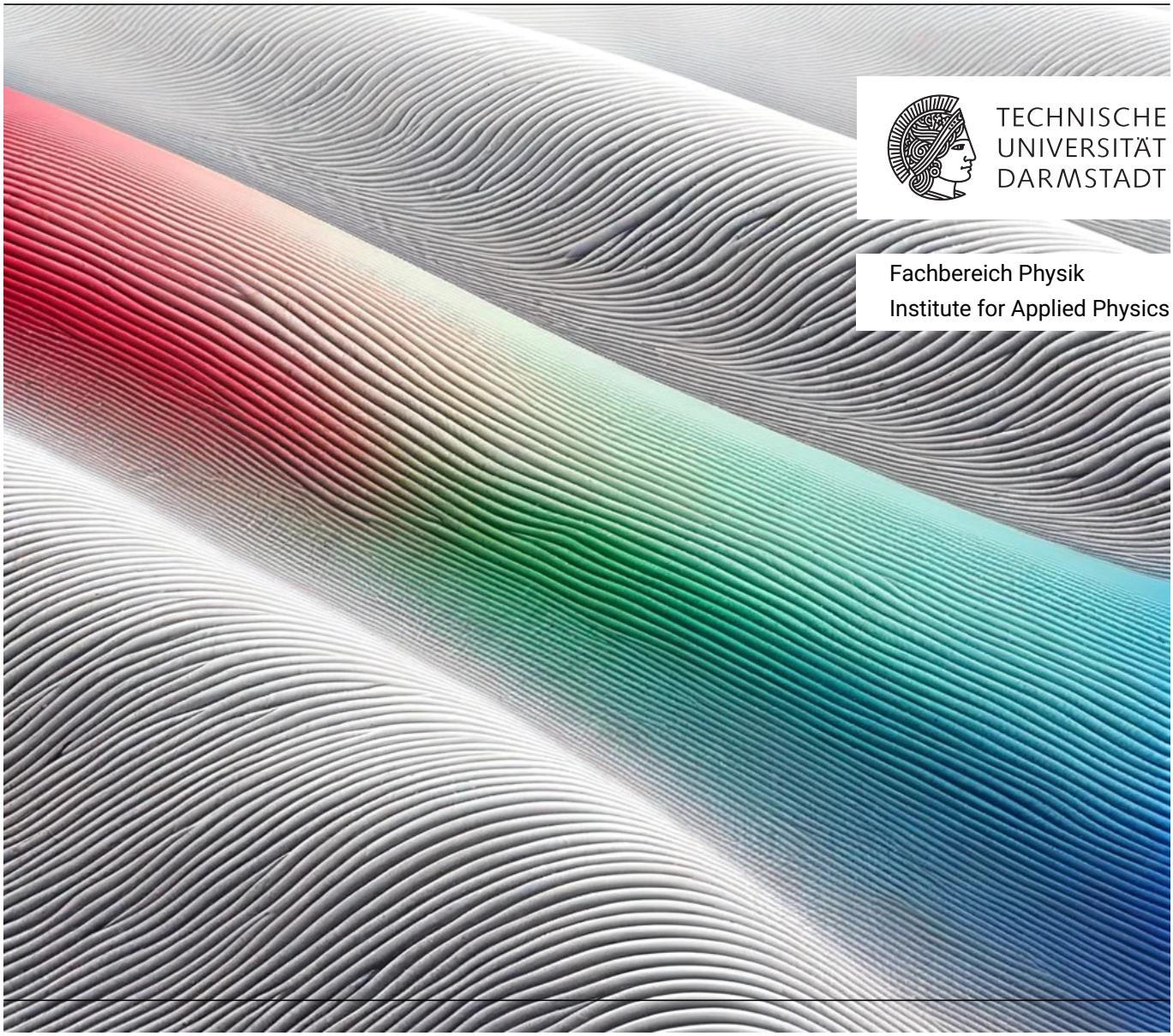

Optical Control of the Temporal Contrast in Chirped-Pulse-Amplification Lasers
Optische Steuerung des zeitlichen Kontrastes in Chirped-Pulse-Amplification Lasern

Genehmigte Dissertation von Simon Röder

Tag der Einreichung: 16. Oktober 2023
Tag der Prüfung: 06. November 2023
Veröffentlichungsjahr auf TUprints: 2024

Darmstadt, Technische Universität Darmstadt

The image on the cover was generated using DALL-E 3, a machine-learning model developed by OpenAI. The process involved inputting text prompts to guide the artificial intelligence in creating visual representations, after which the generated image was selected and utilized for this academic publication. The usage of AI-generated imagery is in compliance with OpenAI's guidelines, ensuring adherence to ethical standards and content policies. The author, Simon Röder, takes ultimate responsibility for the selection and utilization of this AI-generated image in this academic context.

Erklärungen laut Promotionsordnung

§ 8 Abs. 1 lit. c PromO

Ich versichere hiermit, dass die elektronische Version meiner Dissertation mit der schriftlichen Version übereinstimmt.

§ 8 Abs. 1 lit. d PromO

Ich versichere hiermit, dass zu einem vorherigen Zeitpunkt noch keine Promotion versucht wurde. In diesem Fall sind nähere Angaben über Zeitpunkt, Hochschule, Dissertationsthema und Ergebnis dieses Versuchs mitzuteilen.

§ 9 Abs. 1 PromO

Ich versichere hiermit, dass die vorliegende Dissertation selbstständig und nur unter Verwendung der angegebenen Quellen verfasst wurde.

§ 9 Abs. 2 PromO

Die Arbeit hat bisher noch nicht zu Prüfungszwecken gedient.

Darmstadt, 16. Oktober 2023

S. Röder

Kurzfassung

Diese Arbeit zielt auf die Entwicklung neuartiger, rein optischer Methoden zur Steuerung der Anstiegsflanke im zeitlichen Profil von ultra-intensiven Lasern ab. Das Ziel dabei ist es, Forschung mit kontrollierten Vorplasmabedingungen bei höchsten Intensitäten zu ermöglichen.
Der in dieser Arbeit verfolgte Ansatz hierfür besteht darin, eine Abhängigkeit zwischen der Strahlgröße im Pulsstrecker und der Form der Anstiegsflanke auszunutzen. Im Rahmen dieser Arbeit habe ich ein analytisches Model entwickelt, welches die Bildung einer Anstiegsflanke in einem Strecker eines chirped pulse amplification Lasersystems beschreibt. Zur Verifizierung dieses Modells im Rahmen einer experimentellen Kampagne habe ich einen entsprechenden Streckeraufbau entwickelt. Während dieser Kampagne habe ich die Abhängigkeit der Steigung der Anstiegsflanke von der Strahlgröße experimentell nachgewiesen.
Im Rahmen dessen habe ich weiterhin validiert, dass räumliche Begrenzungen im Strahlengang zum Strecker die Anstiegsflanke konditionieren, genauso wie Schäden auf den optischen Oberflächen in der Fourierebene im Strecker.
Im Anschluss an die experimentelle Validierung habe ich eine entfaltete Konfiguration des entwickelten Streckers auf die Bedingungen im Strahlengang eines *chirped-pulse-amplification* Systems angepasst. In diesem entfalteten Aufbau werden optische Elemente in der Fourierebene vermieden, was im Einklang mit dem analytischen Model den Anstiegsflankenkontrast verbessert. Der Aufbau nutzt zudem eine Strahlaufweitung, um den Kontrast durch die Abhängigkeit zwischen Strahlgröße und Anstiegsflanke weiter zu verbessern. Diese neuartige, rein optische Methode der Steuerung des zeitlichen Kontrastes wurde in dieser Arbeit zum ersten Mal demonstriert.
Durch die Implementierung des entwickelten Streckeraufbaus im Petawatt Hoch-Energie Laser für SchwerIoneneXperimente (PHELIX) war ich in der Lage, die Anstiegsflanke des Systems soweit zu reduzieren, dass sie unter ein Kontrastniveau von $5{,}7 \cdot 10^{-10}$ innerhalb von 30 ps vor dem Hauptpuls fällt, anstelle von zuvor ca. 100 ps.
Hydrodynamische Simulationen der Interaktion von dieser Anstiegsflanke mit einer 100 nm dicken Polystyrolfolie ergeben, dass die erreichte Anstiegsflankenverbesserung einer Verringerung der Skalenlänge des Vorplasmas um fast einen Faktor drei entspricht.

Ich habe die Resultate dieser Arbeit in der Zeitschrift „High Power Laser Science and Engineering“, veröffentlicht [1].

Abstract

This work aims to develop novel techniques for purely optical control of the rising edge in the temporal profile ultra-intense laser pulses. The purpose of this is to facilitate research with controlled preplasma conditions at highest intensities.
The approach pursued in this work for this purpose consists of exploiting the dependency between the beam size in the pulse stretcher and the shape of the rising edge. Over the course of this thesis, I have developed an analytical model that is capable of describing the formation of a rising edge in the stretcher of a chirped-pulse-amplification laser system. For the validation of this model in the frame of an experimental campaign, I have developed a corresponding stretcher setup. During this campaign, I experimentally validated the dependency of the slope of the rising edge on the beam size.
Furthermore, I have validated that spatial apertures in the beam path to the stretcher condition the rising edge, as well as damages on optical surfaces in the Fourier plane in the stretcher.
Subsequent to the experimental validation, I adapted the unfolded configuration of the developed stretcher to the requirements in the beam path of a chirped-pulse-amplification system. This unfolded setup omits optical elements in the Fourier plane, which, in agreement with the analytical model, causes an improvement of the rising edge. The setup further employs beam expansion for further improvement of the contrast due to the conditioning of the rising edge by the beam size. This novel, purely optical method for temporal-contrast manipulation was demonstrated in this work for the first time.
By implementing the developed stretcher design at the Petawatt Hoch-Energie Laser für SchwerIoneneXperimente (PHELIX), I was able to improve the rising edge to a degree where it decreases below a contrast level of $5.7 \cdot 10^{-10}$ within 30 ps prior to the main pulse, in comparison to previously around 100 ps.
Hydrodynamic simulations of the interaction of this rising edge with an 100 nm thick polystyrene foil yield that the achieved rising edge improvement corresponds to a reduction of the preplasma scale length by almost a factor of three.

I published the results of this work in the journal "High Power Laser Science and Engineering" [1].

Contents

List of Figures

List of Abbreviations

ASE Amplified Spontaneous Emission

COS Compressor Output Sensor

CPA Chirped-Pulse Amplification

DFG Difference-Frequency Generation

EICHEL Enhanced Intensity Cross-correlator for High Energy Lasers

FF Far-Field

FTL Fourier Transform Limit

FWHM Full Width Half Maximum

ICF Inertial Confinement Fusion

lb large beam

MA Main-Amplifier

MAS Main Amplifier Sensor

NF Near-Field

OPA Optical Parametric Amplification

OPCPA Optical Parametric Chirped-Pulse Amplification

PA Pre-Amplifier

PC Pockels Cell

PF Parametric Fluorescence

PHELIX Petawatt Hoch-Energie Laser für SchwerIoneneXperimente

PoP Proof-of-Principle

PSD Power Spectral Density

PTA Petawatt Target Area

PTAS Petawatt Target Area Sensor

PtV Peak-to-Valley

sb small beam

SFG Sum-Frequency Generation

SHG Second Harmonic Generation

SHS Shack-Hartmann-Sensor

SSAC Single-Shot AutoCorrelator

STC Spatio-Temporal Coupling

SVEA Slowly-Varying Envelope Approximation

uOPA ultrafast Optical Parametric Amplification

XPW Cross-Wave Polarization

1. Introduction

In the year 1960, Theodore H. Maiman built the first laser [2], marking the start of a research field that has quickly become the backbone of numerous applications. Shortly after its invention, the implementation of lasers as scientific instruments began. This made many experiments feasible, e.g. in spectroscopy, which otherwise could not have been performed [3, 4].

The increased field strength available with laser radiation over the past decades unlocked new regimes of physical effects to study. Reaching field strengths of 10^7 V/m-10^8 V/m, quickly enabled observing non-linear optical effects such as Second Harmonic Generation (SHG) [5]. Even greater field strengths first allowed observing excitation processes in the atomic structure and then the break-down of this structure into a ionized state, called plasma [6].

Whenever commercially available laser systems in the newly unlocked regimes became available, applications based on the effects found at these field strengths have emerged quickly. Within the currently unlocked regimes, today research groups around the world are implementing lasers for the generation of secondary particle sources, by focusing ultra-intense laser pulses onto different target materials. Depending on the configuration, this can be used to generate $\gamma-$ [7], electron- [8], ion- [9] or even neutron-beams [10]. In contrary to conventional particle accelerators, which are limited to field strengths of the order of GV/m [11], that correspond to accelerating e.g. electrons over a distance of 0.1 m to an energy of 100 MeV, lasers can achieve the same energies in an acceleration distance of a few microns, due to the extreme field strengths in the TV/m regime [12].

Currently, the newest generation of laser facilities approaches the next regime where the field-strength is strong enough to influence the structure of the nucleus. And in the future we expect to reach field-strengths high enough to influence elemental particles.

In general new applications come with increased requirements in performance, which motivate development in laser technology. The necessary degree of control does however increases with the field strength. This is the case since when using a laser for a specific effect, the laser field-strength transitions through all regimes below the field-strength where this effect occurs, triggering the corresponding break down of molecules, atoms and at some point possibly the nucleus. We must be able to control the interactions that occur on the transitioned regimes since this conditions the state of the matter during the interaction with the peak-field strength of the laser, where the specific effect is taking place, thereby influencing the outcome of this effect.

A prominent example for applications with highest demands on control is Inertial Confinement Fusion (ICF), where the laser is used to compress fuel until the fuel reached densities and temperatures that allow the ignition of a nuclear fusion process [13]. While a fusion reactor would positively contribute to solve the energy problem of mankind, it is putting very hard requirements in average power, pulse energy and temporal shape, beyond state-of-the-art [14, 15, 16].

An example that puts especially hard constrains on the temporal shape of the laser pulse is the generation of surface high-harmonics [17]. This effect relies on the formation of a plasma and the reflection of the laser at this plasma, akin to a perfect mirror. Due to the relativistic movement of this plasma surface in the laser field, short light bursts are emitted with durations in the atto-second scale.Since this effect is extremely reliant on the flatness of the plasma mirror, the temporal laser profile must be temporally clean enough to avoid pre-expansion of the plasma [18].

This application and many others rely on the interaction between the laser itself and the material, many requiring precisely knowledge and control of the parameters of the generated laser-plasma, like the generation of THz radiation [19] and radiation pressure acceleration [20].

With the current state of the art of laser technology many applications remain out of reach due to the limited control of the temporal profile over the many relevant orders of magnitude. Improving this control requires a sophisticated understanding of the origin of the limiting factors that degrade the temporal profile of the laser pulse. While considerable progress has been made in this field over the past decades, the reasons for the degradation of the temporal profile remain under discussion.

Developing new methods of producing ultra-intense, ultra-short laser pulses that are temporally clean enough for the newest generation of applications is the fundamental task of this thesis. The contribution to this topic provided with this manuscript is a novel analytical model, capable of predicting deterioration of the temporal profile, based on laser parameters. The implications of this model are that controlled shaping of the spatial profile at strategic points in the laser chain can be used to directly control the shape of the temporal profile over many orders of magnitude. By implementing these implications at the PHELIX laser facility I was able to improve the cleanness of their temporal profile.

The remaining part of this introduction gives an overview over the plasma-physical effects necessitating such improvements and lies out the current understanding of the origin of temporal profile degrading effects. The chapter concludes by revisiting the central thesis objective and a lineout of the contents of this work.

1.1. Basics of Laser-Matter Interactions for High-Intensity Lasers

In order to motivate why the control of the laser-plasma conditions is necessary for researching regimes at higher field strengths and for many predicted laser-plasma interaction applications, this sections starts by introducing the process of the laser-induced ionization itself before moving on to the formation of such a plasma during laser-matter experiments.

1.1.1. Laser-Induced Ionization Processes

There are several ways in which the electric field of a laser can ionize an atom. Either by photo ionization [21], where one photon is absorbed, which excites a bound electron to a free state or conductive state. However, this requires substantial energy per photon (typically in the UV to X-ray range [22]) and is not directly a result of high field strength. A similar process occurs in the presence of many photons of lower energy than required for direct ionization. This case is called multi-photon ionization [23] and its probability to occur increases the less photons are required and the more are available [24] - thus, for shorter wavelengths and higher field strengths.

For low energies per photon the dominating effect for ionization becomes something called barrier tunneling [25, 26]. The field that the electron experiences is the sum of the field of the atom and that of the laser. For large enough field strengths the probability to find the electron outside of the ion potential becomes non-negligible for short time windows during the oscillation of the laser field. During barrier tunneling the electron can tunnel through the distorted potential barrier of the atoms. This becomes more likely with increasing field strength of the laser, until the field strength of the laser becomes stronger than that of the ion. In this case,called barrier suppression [27], the electron can be directly ionized.

As soon as these first free electrons are present an avalanche process can lead to the complete ionization of the target. These free electrons are accelerated by the laser field and gather sufficient kinetic energy between collisions to cause further ionization processes. The avalanche process and subsequent increase of the free electron density n_e over time can be described by a differential equation [28]

$$\frac{dn_e(t)}{dt} = \nu(E)n_e(t) + \left(\frac{dn_e(t)}{dt}\right)_{\text{PI}} + \left(\frac{dn_e(t)}{dt}\right)_{\text{loss}}, \tag{1.1}$$

where ν is the avalanche coefficient, E is the field strength, the middle term on the right-hand side corresponds to the generation of new free electrons, based on the different phenomena described above, and the right term to the losses due to effects like reabsorption or diffusion.
Once this free electron density exceeds a threshold N_{th}, whose value depends on the chosen definition, a plasma has formed. Using this threshold, can be used to find thresholds for the laser parameters above which the laser causes the formation of a plasma. The main parameter that use for this is the laser intensity I which is related to the field strength by $I \propto E^2$. Additionally, the parameter of the fluence is used, which is the laser energy per unit area and related to the intensity by $I = F/\tau$, where τ is the laser pulse duration.

The easiest case when trying to find the ionization threshold is, where the initial free electrons are independent of the laser itself, for example within metals or in the presence of surface defects [29]. Since the initial free electron density can already be higher than the arbitrary set threshold that defines the plasma (e.g. ^{197}Au has, with a density of $19.3\,\mathrm{g\,cm^{-3}}$ [30], a free electron density of $5.9 \cdot 10^{22}\,\mathrm{cm^{-3}}$), it is more practical to speak of a damage threshold instead. To exceed either threshold definition, damage, or plasma, the deposited energy per time must be larger than the energy per time that is lost due to diffusion. Empirically, this leads to a pulse duration dependency of $F_{th} \propto \sqrt{\tau}$ [31] or in terms of laser intensity

$$I_{\text{th, long pulse}} \propto 1/\sqrt{\tau}. \tag{1.2}$$

When the pulse duration is short enough the diffusion losses become negligible and the damage fluence becomes independent of the pulse duration resulting in the empirical scaling law of [31]

$$I_{\text{th, conductor, short pulse}} \propto 1/\tau. \tag{1.3}$$

For conductors, empirical studies have shown that the transition between both scaling laws occurs at pulse durations around 100 ps to 1 ns [31].

The second case to consider is insulators. In the long pulse regime, empirical studies have shown the same scaling of the threshold fluence with the pulse duration as for conductors [28, 29] (compare eq. 1.2), meaning that a shorter laser pulse will ignite a plasma at higher peak intensities. In the context of insulators the transition of this scaling law is however valid down to pulse durations of $\tau > 10\,\mathrm{ps}$.
For shorter pulse lengths a transition in the scaling law occurs, also for insulators. Due to the fast drop of field strength after the temporal peak, where ionization processes occur, the avalanche has little time for build-up.

This means that in this case the first generation of electrons must be the main source of the required free electron densities to call the material a plasma and the threshold asymptotically approaches the region where only the direct ionization is present [29].

An interesting implication of the transitions in scaling laws when approaching lower pulse durations, which is valid for insulators as well as conductors, is that materials can withstand short pulses of a higher intensity than that of longer laser pulses of the same intensity [29, 32]. This means that when trying to characterize the instant of ionization during a laser-matter interaction, we must not only take the intensity at different times into account, but also the duration of the relevant features and the material at hand.

This brief introduction to laser-induced ionization processes is followed by an introduction to the formation of such a plasma and how it influences the interaction of the laser with the material, for field strengths far above the ionization threshold.

1.1.2. Formation of the Preplasma

The previously discussed ionizing effects mark the starting point, when the laser field strength exceeds the ionization threshold of materials. Now, physical effects are considered with field strengths far beyond that of the binding between ions and electrons in an atom. The consequence of this is, that the plasma formation will likely not happen at the peak of the temporal intensity, but prior to this. This causes something that is commonly referred to as a preplasma formation prior to the peak laser field-strength. For numerous applications it is necessary for the peak field-strength to arrive in a plasma of precisely controlled conditions - be it due to requirements on the pre-expansion [33, 34] or on pre-heating [35]. For this reason it is necessary to exactly control the formation of the preplasma and understand how it changes the parameters of the material.

During the formation of the plasma, the atoms in the target material are ionized and the charged particles are accelerated by the temporally oscillating electric field of the laser

$$\vec{E}_L = \vec{E}_{L,0} e^{i(\omega_L t - k_0 x)}. \tag{1.4}$$

Accordingly, the force applied by the laser to a single electron can be described by the Lorentz force [36]

$$m \frac{\partial^2}{\partial t^2} \vec{x} = -q_e \Big(\vec{E} + \frac{\partial \vec{x}}{\partial t} \times \vec{B} \Big). \tag{1.5}$$

By inserting eq. 1.4 into eq. 1.5 and neglecting the effect of the magnetic field, the movement of the electrons can be formulated as

$$\vec{x} = \frac{q_e}{m\omega_L^2} \vec{E}_{L,0} e^{i(\omega_L t - k_0 x)}. \tag{1.6}$$

The Maxwell equations [36] can be used in order to understand the consequences of this interaction

$$\vec{\nabla} \vec{E} = 0, \qquad \vec{\nabla} \vec{B} = 0, \tag{1.7}$$

$$\vec{\nabla} \times \vec{E} = -\frac{\partial}{\partial t} \vec{B}, \qquad \vec{\nabla} \times \vec{B} = -q_e n_e \mu_0 \frac{\partial}{\partial t} \vec{x} + \mu_0 \epsilon_0 \frac{\partial}{\partial t} \vec{E}. \tag{1.8}$$

By combing the two equations 1.8 with each other and with eq. 1.6, a wave equation

$$-\Delta\vec{E} + \frac{1}{c^2}\frac{\partial^2}{\partial t^2}\vec{E} = \frac{q_e^2 n_e}{c^2\epsilon_0 m}\vec{E}, \tag{1.9}$$

can be formulated, where $1/c^2 = \mu_0\epsilon_0$. Inserting eq. 1.4 into this wave equation yields the dispersion relation

$$c^2 k_0^2 = w_L^2 - \frac{e^2 n_0}{\epsilon_0 m}. \tag{1.10}$$

The latter term in this relation is commonly referred to as the plasma frequency [37]

$$\omega_p = \sqrt{\frac{n_e q_e^2}{\epsilon_0 m}}. \tag{1.11}$$

The general behavior of the interaction between laser and plasma can be understood when further calculating the refractive index η_P of the plasma [38]

$$\eta_P = \sqrt{1 - \frac{\omega_P^2}{\omega_L^2}}, \tag{1.12}$$

which becomes imaginary for $\omega_P > \omega_L$. In this case, when the laser frequency is smaller than the plasma frequency, the plasma is called overdense, and the laser can not penetrate the plasma and is instead reflected.

Since the plasma frequency is a function of the free electron density we can use eq. 1.11 to define a critical plasma density n_c, where the plasma frequency equals the laser frequency

$$n_c = \frac{\epsilon_0 m_e \omega_L^2}{q_e^2}, \tag{1.13}$$

up to which the laser can propagate before it is reflected.

For high field strengths, this limit is increased by the fact that the movement of the electrons becomes relativistic. The required field strength for this can be approximated by finding the absolute maximum velocity of the electron, using eq. 1.6

$$\left|\frac{\partial\vec{x}}{\partial t}\right| \approx \left|\frac{q_e\vec{E}_0}{m_e\omega_L}\right|. \tag{1.14}$$

When expressing this classical maximum electron velocity now in units of the speed of light c we find a parameter a_0 that can be used to define the degree of relativity

$$a_0 = \left|\frac{q_e E_0}{m_e c\omega_L}\right|. \tag{1.15}$$

In order to reach an a_0 of unity, where we can assume that the interaction is relativistic, a field strength amplitude of

$$E_0 = \frac{\omega_L m_e c}{q_e} \approx \text{TW/m} \tag{1.16}$$

is required, for a laser wavelength around 1 µm. Thus, when considering field strengths of the TW/m order or higher, it is necessary to adapt the critical density [39]

$$n_{c,\gamma} = \frac{\epsilon_0 \gamma m_e \omega_L^2}{q_e^2}, \tag{1.17}$$

with the Lorentz factor

$$\gamma = \sqrt{1 - \frac{v^2}{c^2}}. \tag{1.18}$$

Since the intensity of the laser increases over time up to the peak intensity, the density where the laser is reflected also changes according to eq. 1.17.

The shape of the preplasma during the interaction with the peak field-strength is strongly conditioned by the temporal profile of the laser itself. Once the laser intensity is high enough to induce a preplasma, this plasma begins to expand due to the thermal effects, resulting in a spatial density profile that decreases from overdense near the target to underdense. The laser further deposits energy in the preplasma due to absorption processes, altering the thermal expansion of the plasma [39].

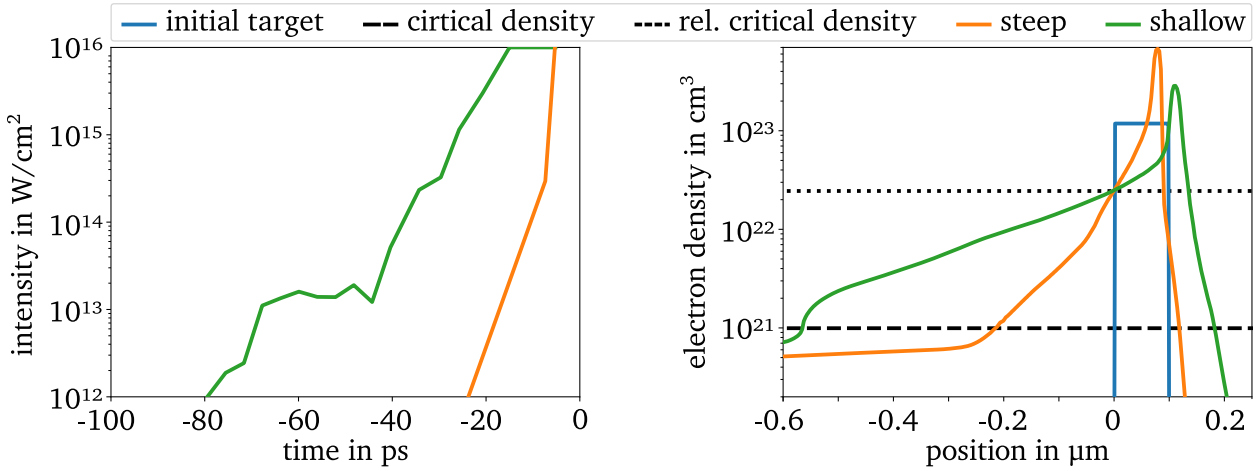

Figure 1.1.: Exemplary temporal profiles of an ultra-high intensity laser (left). Hydrodynamic simulations using the Flash2D code of the corresponding preplasma expansion of a 100 nm target, performed with the assistance of P. Boller.

Hydrodynamic simulations using the software Flash2D [40] of the effect of different temporal profiles on the preplasma can be seen in fig. 1.1. On the left hand side we see three possible temporal profiles, with different slopes increasing towards the peak. The depicted part of the temporal profile starts at 10^{12} W/cm^2 and ends at 10^{16} W/cm^2. The starting intensity corresponds to approximately one order of magnitude above the expected ionization threshold for a laser feature on the few tens of ps regime, which is expected at a fluence of 5-10 J/cm^2 for dielectric materials [29]. Including the order of magnitude difference serves as a margin to assume that the target is fully ionized during the interaction. The upper limit indicates the intensity region where the main interaction starts which provides an estimate of the conditioning of the starting parameters depending on the slope of the temporal profile. This limit also marks the end of the region where the heating process is dominated by inverse Bremsstrahlung and other processes take over [41], that are not considered in the hydrodynamic code.

During the simulated interaction between the three laser profiles and a 100 nm thick Polystyrene (C_8H_8) target a preplasma forms. A lineout, at the point of incidence of the laser, in the direction of the surface normal, of the results from the two simulations are shown on the right-hand side, as the electron density over the position from the initial target position. All lineouts have been shifted to set the spatial position where the density increases over the relativistic critical density to zero.
The blue line indicates the target prior to the interaction with the laser with a chosen solid density of $10^{23}\,\mathrm{cm}^{-3}$.
In green, we can see the electron density after the interaction with the shallower of the temporal profiles. The simulations indicate a steep increase of the density at around $-0.56\,\mu\mathrm{m}$, at the critical density, which is indicated as a dotted horizontal line. Beyond that the electron density further increases and peaks above the solid density at around $0.11\,\mu\mathrm{m}$. This is a common phenomenon caused by the shock wave due to the laser radiation [39]. The distance between the shock wave and the critical density of around $0.67\,\mu\mathrm{m}$ can be interpreted as the length of the pre-expanded plasma.
The length of the preplasma simulated for the steeper of the laser profiles, indicated in orange, is over a factor of two shorter than this, with $0.29\,\mu\mathrm{m}$. The impact of the steepness of the temporal profile can be further emphasized when comparing, the steepness of the free electron density, often referred to as the scale length, at the relativistic critical density. This value decreases by almost a factor of three from $0.146\,\mu\mathrm{m}$ to $0.054\,\mu\mathrm{m}$ for the shallower and steeper temporal profile, respectively.

As mentioned before, many applications of high-intensity lasers require steepest gradients, negligible deposition of energy in the preplasma or precise knowledge and tuning of the preplasma conditions [42, 19, 43, 20, 44].
An example for such an effect is relativistic transparency, which occurs when the electron density drops below the relativistic critical density (compare eq. 1.17) shortly before the peak intensity arrives. With precise timing of the onset of this effect the target can become fully transparent for the laser, which can be exploited for particle acceleration [45]. For this application, as for many others, it is desirable to shoot extremely thin targets in the nanometer to hundreds of nanometer range. However, if the plasma forms to early, the electron density might already have decreased below the critical density, before the peak intensity arrives at the target. In this case the plasma becomes just transparent, and not relativistic transparent. Or in other words, the target is destroyed without us being able to research relativistic transparency.

For this application, as for many others it is sufficient to adjust the target thickness [12] or the plasma scale length [46] in order to control the interaction. However, different applications like ion acceleration via Radiation pressure acceleration, rely on the interaction of the laser pulse with a very thin target with a low pre-expansion of the plasma [20].

Generating laser pulses that are temporally clean enough for such demanding applications is challenging and an ever-relevant research topic. Due to the ever-increasing peak intensities and field strengths, required in order to unlock new regimes of physics to research, our demand on the temporal contrast must also be ever-increasing.
But before discussing my contribution on ways to generate laser pulses that are temporally clean enough for experiments with highest intensities we must understand how we can achieve these highest intensities. This will be the topic of the next section.

1.2. Parameters and Developments of High-Intensity Laser Systems

There are three different ways to increase the laser intensity on-target I_{max}: reducing the illuminated surface area A, reducing the temporal duration of the pulse τ, and increasing the energy in the laser pulse E

$$I_{\text{max}} = \frac{E}{\tau \cdot A} \tag{1.19}$$

The area can be reduced by employing a focusing element, e.g. a lens, prior to the target, that decreases the aperture size from σ_{NF} in the Near-Field (NF) at the lens to σ_{FF}, in the Far-Field (FF), which is positioned one focal length f after the lens, following [47]

$$\sigma_{\text{FF}} = \frac{\lambda f}{\pi \sigma_{\text{NF}}}, \tag{1.20}$$

Regarding the temporal pulse length a drastic decreased is notable since the development of the laser, which was originally a cw-laser. Using a technique called active mode-locking, which was demonstrated in 1985 [48], it is now possible to reduce the pulse duration to a few tens of fs. Nowadays, it is possible to reduce the temporal pulse length even further with different techniques that rely on non-linear optical effects, e.g. post-compression [49]. The generation of higher-harmonics of the laser pulse is the latest of these paradigm shifting techniques which now enables the generation of pulses with durations of a few attoseconds [50]. However, this latest technique has not yet arrived in the setup of ultra-intense laser facilities, which for now all remain on the fs-scale.

The last parameter that can be optimization in order to get the highest intensity is the laser energy. Here, the implementation of the so-called master oscillator power amplifier is what enabled increasingly high pulse energies [51]. In this setup the laser pulse is generated at low energies, but already with a ns-long duration and amplified in consecutive stages. The energy of the laser pulses quickly became large enough to damage materials when passing through them, which hindered the further increase of the energy. Since, as discussed in sec. 1.1.1, the damage threshold of materials scales with the laser intensity, the laser intensity can not be increased further without damaging the laser chain.
Two different workarounds for this fundamental problem have become standard and integral parts of all ultra-high-intensity laser facilities. Both rely on decreasing the intensity locally in the amplification chain and increasing it again on target. Those techniques rely again on the parameters that define the laser intensity, the illuminated surface area, and the temporal duration.
By increasing the beam size, using telescopes, the intensity, and fluence in the material can be locally decreased before focusing the laser onto the target again.
The second technique that locally decreases the intensity for the amplification process is called Chirped-Pulse Amplification (CPA) and relies on temporally stretching the pulse and recompressing it prior to the target [52].

1.2.1. Chirped-Pulse Amplification: Principles, Configurations and Spectral Phase Dynamics

The temporal elongation of the pulse that is necessary for the local decrease in intensity is achieved by using dispersion and/or diffraction, which are wavelength-dependent. Originally, the dispersion of glass was used, by passing the pulse through a considerable length of fiber [52]. The wavelength-dependent

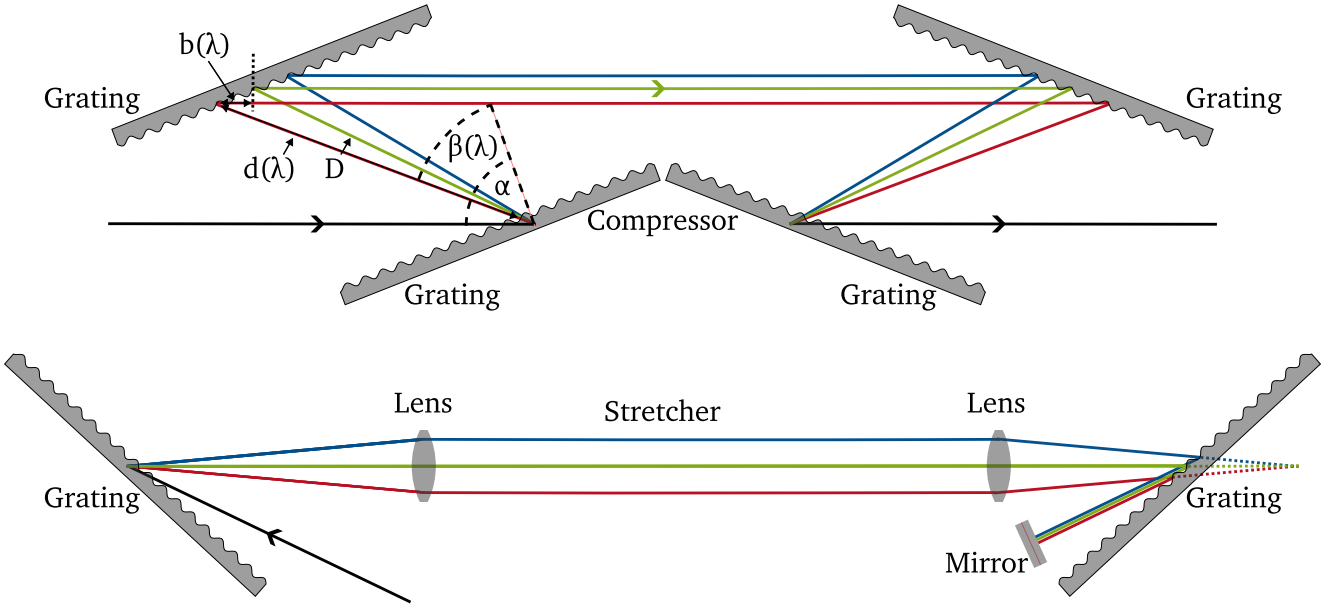

Figure 1.2.: Beam path through a grating-based pulse compressor (top) and a grating-based pulse stretcher (bottom, both in double-pass configurations. The distances b and d indicate the wavelength-dependent path difference. The colored dashed line shows the image of the first grating.

group velocity of light in the medium causes the higher wavelengths in the spectrum to exit the fiber earlier than the lower wavelengths [53]. While all wavelengths entered the fiber at the same time, as intended for a mode-locked pulse, the wavelengths are now to a first degree linearly distributed in time/space. In this context, we speak of a chirp, which gives the name of the technique, chirped pulse amplification.

Nowadays, high-intensity laser facilities rely on diffraction rather than dispersion in a medium for the stretching [54]. In such setups, diffraction gratings are employed in order to introduce a wavelength dependent path length that counteract each other. The setups can be distinguished into two configurations where either the lower or the higher wavelengths travel the shorter distance, respectively.

Depending on the order in which those two are employed one stretches and the other compresses the pulse [55]. Two explanatory setups that visualize this method are depicted in fig. 1.2. On the top, we see the setup that is commonly used for compression. At the first grating, the beam is diffracted in an angle β [47]

$$\sin(\beta) = m\lambda g - \sin(\alpha), \tag{1.21}$$

which is a function of the line density g, the diffraction order m, the angle of incidence relative to the surface normal α and the wavelength λ, which provides the necessarily dispersion. The next grating is parallel to the first one and, since β and α are interchangeable in eq. 1.21, all wavelengths are diffracted in the angle α from the second grating. However, while all wavelengths are parallel after the second grating, they are spatially distributed - a Spatio-Temporal Coupling (STC) commonly referred to as spatial chirp [56]. Thus, it is common practice to either employ a second pair of gratings that introduce the same path difference again, thereby compensating for the wavelength-dependent lateral displacement, or place a folding mirror at the end of the setup and traverse back through the system. Both methods are equivalent as such a double-pass introduces the same path difference. However, some laser facilities skip this part and simply focus the beam onto the target with spatial chirp present in the NF [57].

The image on the bottom of fig. 1.2 shows the counterpart, which is commonly used for stretching. In this so-called Martinez stretcher, which was first introduced in the 1980s [58], a telescope is employed between the gratings. This way the gratings can be moved in front and after the image of the first grating, effectively changing the sign of the introduced dispersion. By placing the second grating between the focal spot and the second focusing element, the dispersion of the compressor can be compensated.

While this was one of the first stretcher setups, it is generally not used for CPA laser systems nowadays. In 1990 the setup was adapted by placing a folding mirror in the Fourier plane of the telescope, which makes the setup easier to align and less prone to alignment errors [59].
The next historical step in the development was the switch to all-reflective optics, since the lens based telescope was limited to pulse lengths above 100 fs due to chromatic aberrations that are introduced for the large bandwidths that are required for shorter pulses [59]. Thus, in 2000 a novel stretcher setup was introduced that substituted the lenses with reflective optics like spherical mirrors or parabolas [59]. However, this setup still introduces aberrations of lower order and is thus still not ideal for largest bandwidths. This is the reason why most modern laser facilities nowadays use an Öffner triplet [60], which is aberration corrected and all reflective. What all mentioned designs share, however, is that they are folded in the Fourier plane.

So far the considered parameters were dispersion and path differences. However, it is useful to describe those effects using the spectral phase of the traversing laser pulse. For this context, the laser beam is described as an electric field in the spectral domain

$$E_0(\omega) = \sqrt{I(\omega)}e^{i\phi(\omega)}, \tag{1.22}$$

which has a real amplitude and a complex phase term, where $I(\omega)$ is the spectral intensity as a function of the angular frequency $\omega = 2\pi c/\lambda$ and ϕ is the spectral phase.
As indicated in fig. 1.2, the wavelength - and thereby the spectral phase - is connected to the path difference L in a compressor by

$$L(\lambda) = b(\lambda) + d(\lambda), \tag{1.23}$$

where b and d are chosen such that $b = 0$ and $d = D$ for the central wavelength λ_c, where D is commonly referred to as the grating distance (not to confuse with the perpendicular grating distance, which is measured along the grating normal). Using trigonometry yields

$$d(\lambda) = D\frac{\cos\beta_c}{\cos\beta(\lambda)}, \tag{1.24}$$

where β_c corresponds to $\beta(\lambda_c)$ and

$$b(\lambda) = [d(\lambda)\sin\beta(\lambda) - D\sin\beta_c]\sin\alpha. \tag{1.25}$$

In order to calculate the spectra phase introduced by such a setup we need to add a phase that is specific to the diffraction from a grating, as discussed by Treacy [61]. For an intuitive understanding of the source of this additional phase it is necessary to have a closer look at the diffraction pattern from a grating, as depicted in fig. 1.3. There, the path difference between the incoming and outgoing waves can be seen. The condition for constructive interference is that this path difference is a multiple of 2π. Thus, for the spectral phase, we need to add a phase of $2\pi \cdot l$, where l is the number of lines the point of incidence of the wavelength P_λ and the center P_c.

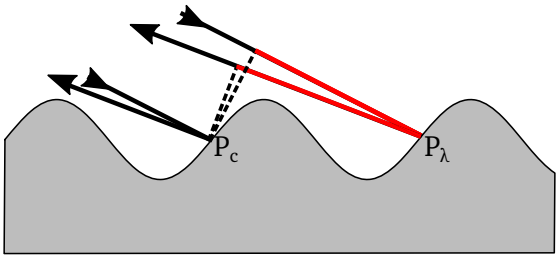

Figure 1.3.: Schematic of the diffraction of a plane wave from a grating. The dashed lines are perpendicular to the propagation direction of incoming and outgoing waves. The red lines indicate the path difference between the two lines of the grating.

The number of lines can be substituted by the line density times the distance between the point of incidence and the center $\overline{P_\lambda P_c}$, which is in turn related to $b(\lambda)$ by the sine of the angle of incidence

$$2\pi l = 2\pi \frac{g b(\lambda)}{\sin\alpha}. \tag{1.26}$$

Thus the accumulated phase in the compressor becomes

$$\phi(\lambda) = \frac{2\pi}{\lambda} L(\lambda) - \frac{2\pi g b(\lambda)}{\sin\alpha}. \tag{1.27}$$

Inserting the optical length L into this equation yields the spectral phase after the compressor

$$\phi(\lambda) = \frac{2\pi}{\lambda} D \cos(\beta_c - \beta(\lambda)). \tag{1.28}$$

Conveniently, the same equation follows for the stretcher, obviously with an inverted sign, where the grating distance D measures between the image of the first grating and the point where the central wavelength is incident on the second grating.

Now, coming back to the insight that during laser plasma experiments we want the laser intensity to increase with a slope that is as steep as possible, we see that spectral phases cause specific wavelengths to arrive at the target at different points in time, which is detrimental to the experiment and thus to be avoided. Here, the temporal profile often shows characteristic shapes, that can be attributed to the different coefficients of the phase when expressing it as a polynomial in a Taylor series.

$$\phi_{\text{Taylor}} = \Phi_0 + \Phi_1(\omega-\omega_0) + \frac{\Phi_2}{2!}(\omega-\omega_0)^2 + \frac{\Phi_3}{3!}(\omega-\omega_0)^3 + \frac{\Phi_4}{4}(\omega-\omega_0)^4 + \ldots \tag{1.29}$$

The first term is commonly referred to as the Carrier Envelope Phase (CEP) and gives the actual state of the oscillation in a beam. This coefficient is irrelevant for most laser systems since the laser will undergo many oscillations while the intensity is significant. It becomes, however, relevant when the pulse duration is only a few cycles long [62].
The second term is the linear phase. When again considering the phase as an optical path difference or time delay between the different frequencies, it becomes evident that the path difference introduced by such a phase is independent of the frequency

$$\phi(\omega) = \frac{\omega-\omega_0}{c} L(\omega) \stackrel{!}{=} \Phi_1 \cdot (\omega-\omega_0) \Rightarrow L = const, \tag{1.30}$$

which means that all frequencies are delayed in position and time and arrive at the target earlier or later, but still with the same temporal relation to each other. Thus, a linear phase in the spectral domain corresponds to a shift in the temporal domain.
A similar analogy can be made for the quadratic phase, which causes a delay between the frequencies.

$$\phi(\omega) = \frac{\omega - \omega_0}{c} L(\omega) \stackrel{!}{=} \frac{\Phi_2}{2!}(\omega - \omega_0)^2 \Rightarrow L \propto \omega. \tag{1.31}$$

It turns out that such a quadratic phase causes the frequencies to be linearly distributed in time, which is called a spectral chirp. This elongation of the pulse is the driving factor in pulse stretching.

The impact of higher orders phase terms onto the temporal profile cannot be described in a comparably intuitive way, but feature distinct characteristic shapes nonetheless. Thus, fig. 1.4 includes calculations of the temporal profiles that are subject to the phase coefficients up to the fourth order. All calculations are made by assuming the spectrum to be an ideal Gaussian and calculating the Fourier transform of eq. 1.22. In this figure the impact of the first five spectral phase coefficients are depicted, all normalized to the maximum intensity of the Fourier transform of the spectrum with a spectral phase that is zero, commonly referred to as the Fourier Transform Limit (FTL) of the spectrum. This shows the expected behavior for the first three coefficients. The third and fourth order cause slopes in the temporal profile where the intensity rises slower that expected, but the peak intensity stays roughly unaffected.

Further to note is that the intensity is depicted in a logarithmic scale and the pulse still has intensity at many times its pulse duration in the presence of higher-order phase terms. This emphasizes how relevant it is to perfectly recompress the pulse after CPA when considering the ultra-high intensities that are present during laser-plasma experiments. As discussed before such a decrease in the slope of the temporal profile is detrimental to many laser-based applications and is to be avoided. However, over so many orders of magnitude, all laser facilities around the world still show significant energy beyond their temporal duration, even with the best efforts in recompression.
A discussion of the reasons for this phenomena is part of the next section, which presents the current state-of-the-art for highest intensity laser systems.

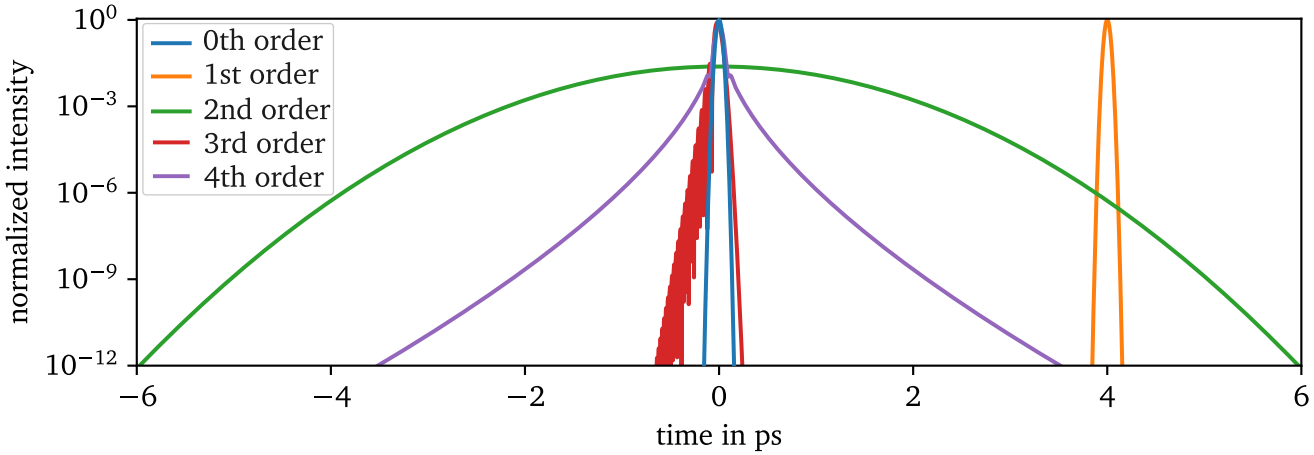

Figure 1.4.: Impact of the first five orders of the spectral phase on the temporal profile of a Gaussian spectrum. All profiles are normalized to the maximum of the FTL.

1.2.2. Historical Milestones to the State-of-the-Art in High-Intensity Laser Facilities

As we have seen lasers have come a long way since the 1960s. Here, the state-of-the-art of research laser facilities are discussed. Since lasers have diverse applications, it is important to distinguish the parameters in which they excel. In research it is common to differentiate mainly between high-energy and high-intensity lasers.

High-Energy Lasers

The first category typically uses relatively long pulse durations of the order of a few nanoseconds [39]. These pulse lengths allow for an increase of the energy to kJ with beam diameters in the tens of centimeter regime. Increasing the energy even further sets requirements for an increase of the surface, otherwise we risk damaging the optical elements. Unfortunately, manufacturing optical elements with such sizes is challenging. Thus, facilities like the National Ignition Facility (NIF) [63] that strive for the highest energies split the large surface over many optical elements. Thus, they use several identical amplification lines, seeded by the same pulse source, in conjunction with a single shot. Furthermore, this has the advantage of increased flexibility in the experimental setup.
This is realized at NIF with about 192 individual laser lines, which equals an increase in the surface area of the same factor. Consequently, this allows them to increase the total laser energy in the system from the kJ regime by roughly the factor of laser beams, which ends up at around 4.2 MJ [64] or, after tripling the frequency, at around 1.8 MJ [65]. Another prominent facility in this category is the Laser MegaJoule (LMJ) in Bordeaux. With its 176 flashlamp-pumped ND:Glass laser arms in a multi-pass amplification system it is designed to deliver 1.5 MJ on target in the third harmonic of the laser wavelength (1053 nm, meaning 351 nm on target), with pulse lengths between 0.3 ns and 25 ns [66].
Those laser facilities are used for research in fields like ICF, where a pellet is compressed by laser ablation pressure until the density and temperature inside allow for fusion to occur [15, 16]. Here, highly precise control of the lasers is required, since any imperfections in the setup will cause instabilities to occur, or otherwise hinder the onset of fusion [65].

High-Intensity Lasers

The central characteristic of the other extreme is the maximization of the laser intensity or laser power. The high powers that are achieved in such facilities exceed the PW level since the year 1999 when the Nova PW laser was commissioned, which was the world's first laser to operate in this regime. While it utilized Nd:Glass for the amplification, similar to the LMJ, it only achieved 680 J, but due to the short pulse lengths and focusing they reported power levels of 1.5 PW [67] and intensities larger than $7 \cdot 10^{20}\,\mathrm{Wcm}^{-2}$ [68]. Only five years later, the Vulcan laser became the first user facility to operate at powers in the PW-class. [67]. Due to the usage of Nd:Glass, with its low thermal conductivity [69], the repetition rate of those lasers was quite low. This changed with the BELLA laser in 2013, which utilizes frequency-doubled Nd:YAG pump lasers for the large aperture amplifiers rather than flash lambs, thereby reducing the thermal load per shot. With this the BELLA laser became the first 1 Hz repetition rate facility that operates at the >PW level [70, 67].
The next game changer that came online was the ELI-NP facility in 2019. By increasing the energy to around 250 J after the compressor, with a compressed pulse length of 21.7 fs, they reportedly achieved peak powers of 10.2 PW [71]. When focusing these high-power laser beams using parabolic mirrors this corresponds to irradiances in the range of 10^{22} to $10^{23}\,\mathrm{Wcm}^{-2}$ [71].
The current world record holder in terms of laser intensity is however the CoReLS facility, where reports claim laser intensities over $10^{23}\,\mathrm{Wcm}^{-2}$ [72].

For reference, the field strengths at ELI-NP and CoReLS are the field strengths that are present in nuclei, which is a threshold for many novel research topics in the regimes of nuclear photonics [73] and strong-field quantum electrodynamics, including vacuum birefringence and pair production in intense electric fields [74].
Currently, a new facility, the Station of Extreme Light (SEL) is being commissioned, which is designed to achieve peak powers of 100 PW, which again surpasses the current world record by an order of magnitude [75, 76].
Beyond that, the pursuit for even higher intensities continues, with research being done on novel concepts for lasers that could reach the exawatt-class level in the future [77].

As discussed in sec. 1.1.2, the matter conditions during the interaction with the peak field-strength of the laser pulse - and therefore the laser-matter interaction itself [39] - is greatly conditioned by the temporal profile of the laser intensity. However, to the best of my knowledge, all laser facilities currently feature a rise time that is not bandwidth limited over the resolvable dynamic range, as illustrated in fig. 1.5. This figure depicts the rise of the intensity of a selected few laser facilities over time. Considering the peak intensities of these facilities it is evident that all depicted laser facilities still have significant intensities above the ionization threshold prior to the arrival of the main pulse and will therefore cause the formation of a preplasma.

When considering how the peak intensity of world-class laser systems has increased over the past decades and how we expect it to increase further, it is intuitive to see that even perturbations in the temporal profile that were previously below the ionization threshold of target materials become more and more relevant and the demand on the temporal quality of the laser pulse increases.
Reducing the perturbations in the temporal profile, which is the central objective of this thesis, is a difficult task with ever-increasing demands and challenges that requires us to tackle all kinds of features in the temporal profile. Those features originate from different parts in the laser chain and feature different pulse lengths. The next section explores those distinct effects, giving an overview over their origin, the challenges they impose and ways to avoid and remove them.

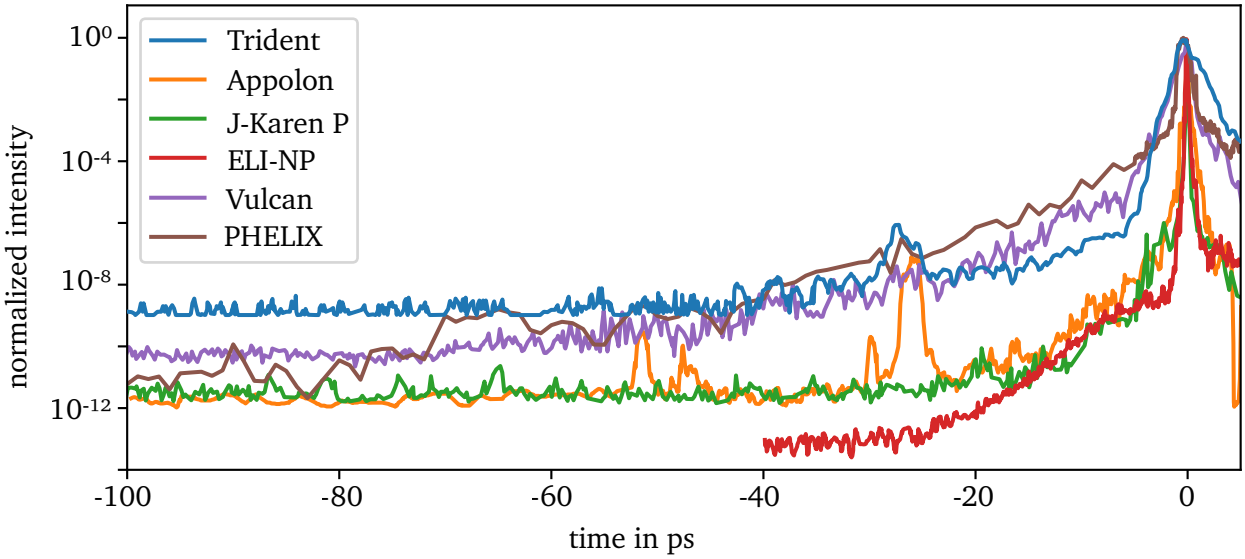

Figure 1.5.: Temporal profiles over time of laser facilities around the globe [78, 79, 80, 73, 81].

1.3. Key Mechanisms of the Temporal Contrast in High-Intensity Laser Systems

A commonly established term to describe the temporal profile over many orders of magnitude is temporal contrast. It is defined as the ratio between the peak intensity and the intensity at a certain time. There are numerous effects that can degrade the temporal contrast of a laser pulse and this section discusses the most important.
The impacts of those effects are schematically depicted in fig. 1.6. The most important feature is obviously the peak intensity, which is positioned at the time zero. But the intensity already slowly starts to rise prior to this, to a pedestal that consists of incoherent noise. The slow rise to this plateau is caused by temporal gating effects, such as Pockels cells in the beam path, that imprint their rise time into the temporal profile while cutting away the residual laser intensity in the few ns- window that electric switches allow. The next feature that can be seen are several pre- and post-pulses, which are replica of the pulse. The last feature that we can see is what is often referred to as the coherent pedestal in the ps-range, or the slow rising edge of the laser pulse. Each of these effects is discussed below, in more detail.

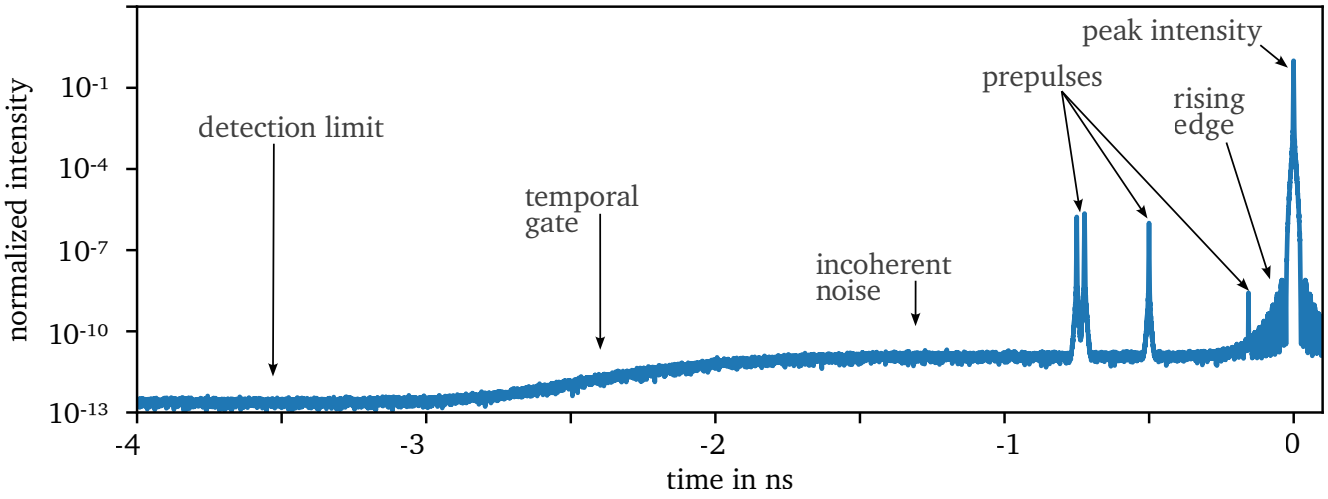

Figure 1.6.: Example temporal profile of a CPA laser system featuring several temporal-contrast conditioning effects.

1.3.1. Formation of the Incoherent Plateau in the Nanosecond Regime

There are two major effects that can contribute to the generation of the incoherent plateau, depending on the laser design, being Amplified Spontaneous Emission (ASE) [82] and Parametric Fluorescence (PF) [83].

Both effects rely on the amplification of random noise in an amplification chain. If this takes place in an non-linear crystal it is called PF, which is an quantum effect that can be attributed to vacuum fluctuations in non-linear amplification stages [83]. It is typically introduced into the beam in processes like Optical Parametric Amplification (OPA). In those the amplification process is a direct energy transfer between pump signal and the seed signal, with some of the energy going into the generation of an idler. The responsible non-linear effect is Difference Frequency Generation (DFG), which is a three-wave mixing process. Such amplification methods can be employed either prior to stretching or after the stretching.

The benefit of the first case is that the pump pulse length can be restricted to the duration of the seed pulse length, which temporally gates the generation of PF. This is typically referred to as ultrafast Optical Parametric Amplification (uOPA). When employing the amplification after the stretching it is called Optical Parametric Chirped-Pulse Amplification (OPCPA). In this case, the incoherent noise is generated over the complete duration of the stretched pulse length, which is typically of the order of ns. While the amplified pulse can be recompressed in the compressor, the PF can not, due to its lack of phase correlation. This results in the discussed incoherent pedestal that can be observed in the temporal profile.

In an active laser medium, there is an additional source of random photons that can be amplified, in which case this noise is called ASE. The origin of these photons is strongly related to the generation of laser pulses itself. During the generation of a laser pulse, a population inversion is achieved in the laser medium, meaning that more electrons are in an excited state than in the ground state [47]. This is commonly done by 3- or 4-level systems [47]. From this excited level, there are two relevant mechanisms for the electron to fall to the ground state. The first is stimulated emission, which is used for lasing. In this case, the electron is relaxed back to the ground state due to the interaction with a passing photon. Since the ground state is less energetic than the excited state the difference energy is emitted in the form of a photon - which in the case of the stimulated emission has the same properties as the stimulating photon. Thus, coherent radiation is generated as necessary for the laser.
The second effect, and source of ASE, is a spontaneous one and depends on the life time of the excited state. At some point each electron will fall back to the ground state on its own, emitting a photon in the process. In contrary to the stimulated emission this photon has random properties. Nevertheless, some of those random photons have the same direction as the stimulated photons, they simply lack the phase correlation. They in turn cause stimulated emission with other excited electrons in all consecutive amplification mediums and are amplified in the process. Thus the name, ASE. Since this effect is not temporally gated by any pump pulse the length of the corresponding plateau depends on the life time of the active medium.

However, in most cases, the first increase in intensity that begins the incoherent plateau is artificially introduced in the laser chain by employing additional temporal gating. Since this temporal gating is employed while the pulse is temporally stretched, the length of the plateau is limited by the stretched pulse duration in the ns-regime.

There are several ways to reduce the intensity of the incoherent plateau on-target with new once still emerging. They can be categorized into either, generating less noise during the laser chain, removing it from the pulse prior to the Main-Amplifier (MA) and removing it after the MA.

For the first category it can be beneficial to take work load of amplification methods based on active laser materials and instead employ OPA, since in the former ASE is generated, which scales linear with the gain of the system. In the latter PF is generated which has been shown to have a weaker scaling [84].

For the second category, the cleaning prior to the MA, Cross-Wave Polarization (XPW) [85] can be used. In this setup a short laser pulse is directed through a non-linear crystal, where due to four-wave mixing processes the polarization is rotated [86]. Since this non-linear effect is highly intensity dependent, the amount of rotation is as well. Thus, by placing the crystal between two polarizers the high-intensity parts of the pulse can be separated from the lower-intensity part of the spectrum. With this technique laser facilities like Apollon are able to improve their temporal contrast by over two orders of magnitude [87]. It is however to note that this techniques has its limitations. After the stretching the incoherent ASE plateau temporally overlaps with the main peak and the intensity does not significantly change during the 1-2 ns of pulse duration. Using an intensity dependent cleaning technique does thus only work prior to the stretching or after the compression.

It is thus common to employ XPW as late as possible in the laser chain, where the beam still fits through crystals with manufacturable sizes and intensities that are below the damage threshold of the material. Hence, often an extra stretcher and compressor are build at strategic points in the laser chain [88].

The last category is the cleaning after the MA and after the compression. For this, concepts like saturable absorber are often employed [89], which absorb parts of the laser beam until they are saturated, thereby removing energy prior to the peak intensity. A similar approach are the so-called plasma mirrors [90]. Those elements have low reflectivity until the intensity on them increases above the ionization threshold and a plasma forms. After this quick process the laser is reflected on the critical density of the plasma, with has a better reflectivity. These elements are often employed in the intermediary field between the focusing element and the focal spot, where the intensity on the mirror can be fine tuned by slight changes in the longitudinal position. Laser facilities like CoReLS have build dedicated setups of telescopes that focus the beam down, and collimate it again after it was reflected from two plasma mirrors in the intermediary field [91]. Even though, this is an intrinsic single-shot method that throws away significant parts of the energy, it is established as one of the go-to solutions for temporal-contrast improvements.

1.3.2. Pre- and Post-Pulse Generation in High-Intensity Laser Systems

The second feature in the temporal profile after the constant ASE plateau that are discussed in this section are pre- and post-pulses. They are often introduced in cavities where the laser pulse is amplified over many round trips [92]. Since the release of the pulse is often done using the polarization rotation provided by a Pockels cell and a polarizer, each round trip produces pre-pulses with relative energies levels that correspond to the efficiency of the polarizer and the energy of the beam in the respective pass. Since those pre-pulses pass through all following amplification stages and are focused on the target prior to the main pulse they can easily already start the formation of a preplasma. A second case in which beam duplicates are introduced is when the pulse is transmitted through a medium and the beam is reflected twice or more on the inside of the plan-parallel element. In those cases the duplicate arrives at the target later than the peak intensity and the so-called post-pulse does very little to impact the laser-matter interaction.

While in a first approximation the introduction of post-pulses seems to be uninteresting, it turns out that they are often transformed into pre-pulses, making them again detrimental to the experiments. This conversion takes place as a nonlinear effect in the amplification stages after the pulse is stretcher. Due to the temporal stretching parts of the main pulse and the post-pulse temporally overlap and can create a new pulse using nonlinear effects [93]. These pulses often feature a temporal distance to the mean pulse that has the same value as the generating post-pulse, just with an inverted sign. However, recent research suggests that those pulses may get shifted temporally depending their temporal overlap with the main peak in the medium [80].

Often, the best approach to remove pulse duplicates from the temporal profile is a thorough investigation of their origin and the implementation of workarounds. If, for example, it turns out that a replica is generated in a transmissive element the duplicate might be removed by employing a wedged optic rather than a plan-parallel one.

However, often in laser systems pre-pulses are still present. Since those feature a smaller duration than the ASE they give a higher damage threshold for target materials, as discussed in sec. 1.1.1. It is thus often sensible to define the ASE contrast and the pre-pulse contrast independent from each other, since the requirements on them differ.

1.3.3. The Rising Edge

In the past years considerable progress has been made in regard to the ASE- and pre-pulse-contrast. However, with every improvement of the ASE-contrast the visibility of the last feature increases. Even when reducing ASE and pre-pulse contrast many orders of magnitude below the ionization threshold - the slow rising edge will eventually start the formation of a preplasma.

Previous research, over twenty years ago, indicated that the rising edge stems from surface defects in the pulse stretcher which are, due to the spectral dispersion on the surfaces, translated into the spectral phase [94], which deteriorates the temporal profile. Almost ten years later, in the year 2008, a first analytical description of this effect was published [95]. There, the authors used a Fourier decomposition of the surface imperfections called the Power Spectral Density (PSD) in order to describe the height distribution of the surface imperfections. While not explicitly stated this already implies that each surface imprints an individual rising edge into the temporal profile, with a magnitude that scales with the PSD of the respective surface. While this still neglects several effects such as the spatial extension of the laser beam and instead describes the laser as an one-dimensional line, it is already capable of describing the phenomenological behavior. The general dependencies were experimentally verified later on, identifying either the gratings [96] or the mirrors [79] as the culprit, which dominates the rising edge formation.

An extension of the analytical model, which introduced the spatial extension of the beam into the considerations, was formulated in 2012 [97], where the authors investigated STC effects that are introduced during the scattering on the optical elements where the beam is spectrally dispersed. This model is quite capable of describing the rising edge directly after the introduction of the noise by the surface imperfections. However, it comes short when trying to consider propagation effects such as diffraction. It is thus more relevant for the description of the impact of the compressor than that of the stretcher, where the beam still has most of the beam path to the target ahead of it. The authors later on proposed a stretcher setup that would validate their theory [98]. While to the best of my knowledge they did not publish such a validation their analytical model allows the same statement as before, that each surface interaction while the beam is spectrally dispersed introduces a new set of spectral phase noise. Their analytical model also already predicts that for two identical surfaces, the interaction with a larger beam size will lead to less phase noise and thus a better temporal profile.

In accordance to that, a work from 2019 [99] suggests that optical elements in the Fourier plane, where the beam size is smallest, are especially detrimental to the rising edge. Since, as discussed during the introduction of the CPA schema in sec. 1.2.1, most CPA laser systems utilize a folding mirror in the Fourier-plane, this is a shared problem in the community. The authors investigated the effect of phase and amplitude effects of the imperfect optical elements using ray-tracing. That the folding mirror in the Fourier-plane is the dominating factor in the rising edge is now widely recognized in the high-intensity laser community, which facilities advancing the use of ultra-polished folding mirrors in Öffner stretchers, like the Apollon laser [79] and J-KAREN-P [100]. Due to the scaling of the rising edge with the PSD temporal-contrast improvements between one and three orders of magnitude were thereby demonstrated. Other facilities completely removed the folding mirror and tested unfolded stretchers based on two concave spherical mirrors [101, 102].

Similar to the other effects, the approaches to reduce this feature can be categorized into either generating less noise or removing it afterwards. For the latter category, the same strategies work as for the incoherent pedestal, e.g. saturable absorbers and plasma mirrors. So far, the available techniques to generate less rising edge in the first place are restricted to the mentioned omitting of the folding mirror in the Fourier plane and improving the surface quality of this mirror.

1.4. Central Thesis Objective

The central goal of this thesis is to develop techniques that allow us to improve the temporal contrast even further. In particular this work focuses on the development of novel techniques to reduce the rising edge. The aimed for approach is avoiding the generation of the rising edge as much as possible and gaining control over its shape.

In order to do so it is necessary to understand the rising edge even better. Thus, the next chapter (cha. 2) will derive its origin more thoroughly. In this context the chapter presents an analytical approach that I have developed in the frame of this thesis, to describe the formation of the rising edge. The considered effects are separated in spectral-phase effects in sec. 2.1 and spectral-amplitude effects in sec. 2.2. Based on theses models several hypothesis concerning the behavior of the rising edge are derived. One major influence parameter discussed in this context is the conditioning of the rising edge by the spatial properties of the beam in sec. 2.3.

Then, cha. 3 provides the experimental validation of these hypotheses. In this frame, the design of a stretcher set-up dedicated to this experimental validation is presented.

Afterwards, cha. 4 is dedicated to the implementation and tests of the stretcher setup the in a CPA laser system, namely the Petawatt Hoch-Energie Laser für SchwerIoneneXperimente (PHELIX) facility, where this thesis was conducted. The chapter starts with a general overview of the PHELIX laser chain in sec. 4.1 and its parameter prior to the pulse stretching in sec. 4.2. The next sections are each dedicated to one central part of the PHELIX laser chain, each discussing the impact of this component on the rising edge in the temporal contrast. The first components are the available stretchers at PHELIX in sec. 4.3, followed by general elements in the beam line, such as spatial filters in sec. 4.4. Then, sec. 4.5 considers the impact of the beam shaping that is done at the serrated aperture. The last component of the CPA laser chain are the grating-based pulse compressors that are available at PHELIX. Section. 4.6 discusses their impact on the rising edge, before the investigation of the impact of the available detectors in sec. 4.7. The conclusion of this chapter in sec. 4.8 is a comparison between the expected rising edges based on the different approaches that I have developed in this thesis to corresponding measurements of the temporal contrast.

The discussion, found in cha. 5, summarizes the findings of this thesis and discuss their implications. This includes a discussion of the validated implications of the analytical model in sec. 5.1 and implications of this work for high-intensity laser systems in sec. 5.2. This chapter further readdresses the hydrodynamic simulations done in this introduction and discuss in their context the implications of this work for laser-plasma experiments in sec. 5.3.

This work closes in cha. 6 with a brief outlook on future developments in the field.

2. The Origin of the Rising Edge: Analytical Modeling

In order to reduce the rising edge in CPA laser systems a phenomenological comprehension is important but not sufficient. We additionally need a way to predict and describe rising edges based on a mathematical model. The development of such a model is the subject of this chapter. The introduction of this work already provided an overview over the efforts in the past decades towards such a model and here my addition to these efforts are explained, being the conditioning of the rising edge by the spatial profile of the laser pulse and diffraction effects during beam propagation.

Fundamentally, there are many different effects that introduce rising edges in the temporal profile and they can be categorized into either phase effects or amplitude effects. Effects that influence the amplitude of the laser can have many sources. The most prominent is clipping on the edge of optical elements, but also damages on optical surfaces or dust particles.

Phase effects can generally be interpreted as changes in the optical path length. For the description of this effect the developed model assumes that during a reflection from an optical element the height profile $H(x)$ is imprinted into the phase of the laser due to the path difference that individual parts of the beam undergo.

Both, amplitude effects and phase effects are normally just a spatial issue, but when the laser pulse is spectrally dispersed, e.g. in the pulse stretcher and compressor of CPA laser systems, they are directly imprinted into the spectral phase and spectral amplitude of the beam. The mapping on the considered surface can be calculated using the dispersion of the gratings based on eq. 1.21. For all calculations in this thesis, the mapping between the angular frequency of the laser ω is assumed to be linear over the position on the optical element x

$$x = a_\omega \omega + b_\omega. \tag{2.1}$$

which is a small approximation, as long as the opening angle $|\beta(\lambda_{\text{max}}) - \beta(\lambda_{\text{min}})|$, is small, where the bandwidth of the laser is $|\lambda_{\text{max}} - \lambda_{\text{min}}|$.

This is visualized in fig. 2.1: the incoming laser beam is spectrally dispersed over the axis x and the surface with a free aperture S features various different steps, with can be described by a height profile $H(x)$. Thus, the spectral amplitude that is not incident on the mirror is removed from the beam. For spectral-phase effects, each wavelength undergoes a slightly different optical path length and thus, features a slightly different phase, and energy is pushed out of the peak intensity into the wings that we call the rising edge.

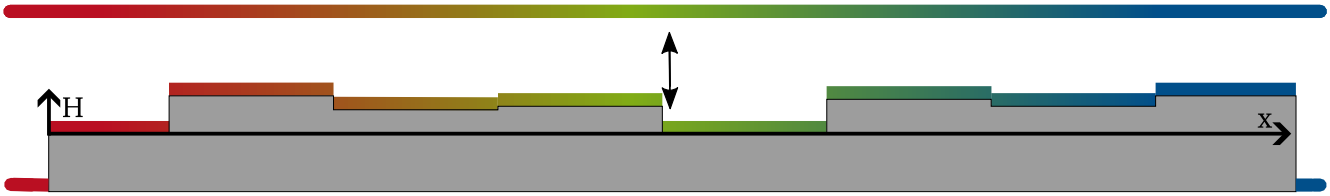

Figure 2.1.: Normal reflection of a spectrally dispersed beam from a mirror disturbed by multiple step functions.

The starting point for my analytical model for both effects is a general undisturbed electrical field in the spectral domain of a short laser pulse

$$E_0(\omega) = \sqrt{I(\omega)}e^{i\phi(\omega)}, \tag{2.2}$$

which consists of an amplitude $\sqrt{I(\omega)}$ and a spectral phase $\phi(\omega)$. This field is perturbed by a term $P(\omega)$, which is either a spectral phase perturbation or an amplitude transfer function, depending on the considered effect.
An important distinction to the model developed by C. Dorrer and J. Bromage in 2008 [95] is that the presented model further incorporates a spatial profile $f(x)$, which is distributed over an optical element according to eq. 2.1. With this the field becomes

$$E(x,\omega) = f(x - a_\omega\omega - b_\omega)P(x)E_0(\omega), \tag{2.3}$$

where the constant b_ω is only an offset which the model neglects in the following considerations.

This approach is similar to the model developed by J. Bromage *et al.*. in 2012 [97], which is, as mentioned, more suitable to describe the conditioning in the pulse compressor. However, the model presented in this chapter is designed to focus on the effects in the stretcher, which are presumably the currently dominating factor for most CPA laser facilities [99]. In order to do so it addresses beam diffraction and propagation effects throughout the laser chain. These effects can be interpreted as a narrow spatial frequency filter, where the parts of the beam that are scattered out of the intended beam path do not arrive at the detector and can thus not contribute to the temporal intensity profile. Analytically, this means that the electric field in the spatial frequency domain is multiplied by a gate $\tilde{R}(k)$, which is for now assumed to be a Dirac-delta $\delta(k)$. The Fourier transform of this equation, denoted by $\mathfrak{F}$

$$E(x,\omega) = \mathfrak{F}\Big[\tilde{R}(k)\cdot\tilde{E}(k,\omega)\Big], \tag{2.4}$$

which is equivalent to the transition into the spatial domain, can be separated into the convolution of the individual Fourier transforms, using the convolution theorem [103]

$$E(x,\omega) = R(x) \circledast \Big[f(x - a_\omega\omega)P(x)E_0(\omega)\Big], \tag{2.5}$$

where $\circledast$ denotes the convolution. Using the assumption that $\tilde{R}(k) = \delta(k)$ yields that $R(x)$ becomes unity and the field becomes

$$E(x,\omega) = 1 \circledast f(x - a_\omega\omega)P(x)E_0(\omega) = \int 1\cdot f(x - a_\omega\omega)P(x)E_0(\omega)dx. \tag{2.6}$$

The convolution is then equivalent to the integration over the complete spatial domain

$$E(\omega) = \int f(x - a_\omega \omega) P(x) dx E_0(\omega) \tag{2.7}$$

meaning that the perturbation of the signal at the detector at the end of the laser chain exhibits no spatial dependency. Another interpretation of this is, that this is the signal a spatially integrating detector will measure when the complete signal is transmitted to the detector. Phenomenological, the impact of the disturbance P is spatially conditioned by the spatial profile $f(x)$.

This consideration of spatial frequency filtering emphasizes the previously made assumption that the surface can be interpreted as multiple step functions, since all parts of the beam that are scattered in such a way that their trajectory changes from the ideal path, are removed in the spatial frequency filter. In other words, since all parts of the beam that are scattered with a change in direction are assumed not to arrive at the detector, the surface can be considered step-like.

In the following two sections eq. 2.7 is used in order to derive analytical equations for the temporal profile, first for spectral phase perturbations and then for a spectral amplitude transfer functions.

2.1. Spectral-Phase Effects

When considering spectral-phase effects the perturbation term that describes the additional optical path is

$$P(x) = e^{\delta\phi(x)}, \tag{2.8}$$

with the perturbative spectral phase $\delta\phi(x)$. Since the phase is assumed to be a perturbation and thus the spectral phase to be small compared with unity the perturbation can be linearized. This simplifies eq. 2.7 to

$$\begin{aligned} E_{\mathrm{SP}}(\omega) &= \int f(x - a_\omega \omega)(1 + i\delta\phi(x)) dx E_0(\omega) \\ &= E_0(\omega) + i \int f(x - a_\omega \omega) \delta\phi(x) dx E_0(\omega). \end{aligned} \tag{2.9}$$

The first term is equivalent to the case without spatial conditioning since the spatial profile $f(x)$ is normalized. After the Fourier transform into the temporal domain and after using the convolution theorem

$$\tilde{E}_{\mathrm{SP}}(t) = \tilde{E}_0(t) + i \left[\int \int e^{i\omega t} f(x - a_\omega \omega) \delta\phi(x) d\omega dx \right] \circledast \tilde{E}_0(t), \tag{2.10}$$

the spatial profile and the phase perturbation term can be separated using the substitution $x' = x - a_\omega \omega$

$$\tilde{E}_{\mathrm{SP}}(t) = \tilde{E}_0(t) + i \left[\int e^{-i \frac{x'}{a_\omega} t} f(x') \frac{dx'}{-a_\omega} \int e^{i \frac{x}{a_\omega} t} \delta\phi(x) dx \right] \circledast \tilde{E}_0(t). \tag{2.11}$$

These individual integrals can then be interpreted as Fourier transforms between the spatial domain and the spatial frequency domain since the quotient of time and dispersion coefficient corresponds to a spatial frequency $k = t/a_\omega$.
With this, the shape of the temporal profile can be calculated, by employing the absolute square of the temporal field

$$I_{\mathrm{SP}}(t) = I_0(t) + \frac{1}{a_\omega^2}\left|\left(\tilde{f}(t/a_\omega)\tilde{\delta\phi}(t/a_\omega)\right) \circledast \tilde{E}_0(t)\right|^2 - \frac{2}{a_\omega}\mathbf{Im}\left(\tilde{E}_0(t)\left[\left(\tilde{f}^*(t/a_\omega)\tilde{\delta\phi}^*(t/a_\omega)\right) \circledast \tilde{E}_0^*(t)\right]\right). \tag{2.12}$$

As a simplification the imaginary part is dropped, assuming that the multiplication by the field quickly decreases toward zero for times larger than the pulse length of the undisturbed pulse E_0. This results in the intensity profile

$$I_{\mathrm{SP}}(t) = I_0(t) + \frac{1}{a_\omega^2}\left|\left(\tilde{f}(t/a_\omega)\tilde{\delta\phi}(t/a_\omega)\right) \circledast \tilde{E}_0(t)\right|^2. \tag{2.13}$$

The convolution can be removed by assuming that the variation of $\tilde{f}\tilde{\delta\phi}$ is small on the time scale where the undisturbed profile is different from zero

$$I_{\mathrm{SP}}(t) = I_0(t) + \frac{1}{a_\omega^2}\left|\left(\tilde{f}(t/a_\omega)\tilde{\delta\phi}(t/a_\omega)\right)\right|^2\left|\int \tilde{E}_0(t-t')dt\right|^2. \tag{2.14}$$

An investigation of the validity of this approximation can be found in app. A.1.
In the next step, the temporal intensity profile is simplified to

$$I_{\mathrm{SP}}(t) = I_0(t) + \frac{\epsilon_s}{a_\omega^2}\left|\tilde{f}(t/a_\omega)\tilde{\delta\phi}(t/a_\omega)\right|^2, \tag{2.15}$$

since the absolute square of the integral over the undisturbed field is a constant ϵ_s.
Using the mapping between the position and angular frequency of the laser from eq. 2.1 allows the description of the introduced perturbative spectral phase $\delta\phi(x)$ as

$$\delta\phi(\omega) = \frac{4\pi}{\lambda_0}H(a_\omega\omega + b_\omega). \tag{2.16}$$

This can in turn be related to the PSD of the surface using the Fourier transformation of the height profile

$$PSD(k) = \left|\tilde{H}(k)\right|^2\Delta k, \tag{2.17}$$

which can be measured with a spatial frequency resolution of Δk and mapped to the time domain using the relation between spatial frequency and time $k = t/a_\omega$. An explanation of the calculation steps necessary to find this quantity can be found in app. A.2.
Combining eq. 2.15, eq. 2.16 and eq. 2.17 leads to an equation that can be used to predict the rising edge in a pulse stretcher while considering that the spatial beam size causes a conditioning effect in the spectral phase

$$I_{\mathrm{SP}}(t) = I_0(t) + \frac{16\pi^2\epsilon_s}{a_\omega^2\lambda_0^2\Delta k}\left|\tilde{f}(t/a_\omega)\right|^2\mathrm{PSD}(t/a_\omega). \tag{2.18}$$

Thus, the temporal profile can approximated as the addition of a rising edge to the undisturbed profile

$$I_{\mathrm{SP}}(t) = I_0(t) + I_{\mathrm{RE}}(t/a_\omega). \tag{2.19}$$

It is to be noted that the slope of the rising edge scales with the dispersion coefficient, according to this model. An important implication of this becomes clear when considering two interactions that are identical in every regard but only differ in the dispersion coefficient. In this situation, the model predicts that the setup employing the smaller dispersion coefficient achieves a steeper rising edge. A discussion on how this can be utilized to correlate the compressed pulse length of a laser system to the achieved rising edge contrast is provided app. A.3.

2.1.1. Consecutive Spectral-Phase Effects

Considering several consecutive surfaces that imprint their imperfect surface profile into the spectral phase of the laser requires inserting the field E_{SP} perturbed by the first surface as the input field E_0 for the next surface. This is further complicated depending on the distance and the amount of spatial frequency averaging between the two considered surfaces. The development of an analytical model capable of this is still pending. Instead, the calculations in this thesis rely on the assumption that the introduced rising edge behaves additive

$$I_{\mathrm{SP,conc}}(t) = I_0(t) + I_{\mathrm{RE},1}(t/a_{\omega,1}) + I_{\mathrm{RE},2}(t/a_{\omega,2}) + ... \tag{2.20}$$

2.1.2. Surface Quality: Amplitude Manipulation of the Rising Edge

Since the PSD goes linear into the rising edge I_{RE}, any scalar change of the PSD changes the rising edge by the same factor. It is important here to realize that this only affects the amplitude of the rising edge, but does not change its shape.

This is supported by the independent work of different laser facilities [79, 100], where the dominating mirror was substituted with an equivalent mirror with improved surface quality. They observed a change in the amplitude of the rising edge that is comparable to the order of magnitude of the improvement of the surface quality.

It is of interest here, that the optical element in the Fourier plane was the limiting element in the stretcher and not the gratings or the telescope. The reason for this lies in the in-stretcher beam size and will be discussed in sec. 2.3.

2.2. Spectral-Amplitude Effects

After having derived a model for the introduction of the rising edge based on spectral-phase effects this section considers spectral-amplitude effects. In this section, I develop an analytical model that is capable of describing the impact of spectral clipping, damages on optical elements in the stretcher and compressor, and dust particles on these surfaces.

The influence of these effect on the laser pulse can be expressed by a spatial transfer function in the stretcher $T(x)$. For spectral clipping this is a top-hat that has the value of unity over the free aperture of the considered element and zero everywhere else. For a damage an inverted top-hat can be employed, which is unity everywhere except at the damage. The dust particles can be treated similarly, where each particle is an inverted top-hat with a width that corresponds to the size of the particle.

The start of the analytical calculation is again eq. 2.7, but with the perturbation

$$P(x) = T(x). \tag{2.21}$$

The spectral field for amplitude effects E_A is then

$$E_A(\omega) = \int f(x - a_\omega \omega) T(x) dx E_0(\omega). \tag{2.22}$$

and for the temporal field follows via Fourier transform and the convolution theorem

$$\tilde{E_A}(t) = \left[\tilde{T}(t/a_\omega)\tilde{f}(t/a_\omega)\right] \circledast \frac{\tilde{E}_0(t)}{-a_\omega}.$$

Therefore, the intensity profile due to the spectral-amplitude effects is again the absolute square of the temporal field

$$I_A(t) = \left| \left[\tilde{T}(t/a_\omega)\tilde{f}(t/a_\omega)\right] \circledast \frac{\tilde{E}_0(t)}{-a_\omega} \right|^2. \tag{2.23}$$

For numerical calculations, however, it is more convenient to remove convolutions using the convolution theorem to express the influence of the spectral clipping on the intensity profile as

$$I_A(t) = \left| \mathfrak{F}^{-1}\left(E_0(\omega) \cdot F\left[\tilde{f} \cdot \tilde{T}\right] \right) \right|^2. \tag{2.24}$$

For calculations at the beginning of the laser chain, like for the stretcher, it is often reasonable to assume the incident spectral phase of the beam to be flat, which allows us to assume that the spectral field is simply the square root of the intensity. With this, eq. 2.24 becomes a tool to quickly estimate the rising edge caused by an arbitrary amplitude perturbation, only relying on the input of a spectrum, the spatial beam profile on the respective surface, and the spatial transfer function.

It is also possible to choose the perturbation as $P(x) = e^{\delta\phi}(x) \cdot T(x)$ which incorporates both, spectral amplitude and spectral-phase effects. While such consideration is useful for a more complete understanding of the mechanisms, they have so far not yielded an equation capable of describing the rising edge, akin to eq. 2.18 and eq. 2.24. For completeness these considerations are included in app. A.4.

2.2.1. Consecutive Spectral-Amplitude Effects

It is possible to calculate the effect of spectral amplitude perturbations for consecutive surfaces by inserting the spectral field after the interaction back as the input during the next interaction.

$$E_{A,2}(\omega) = \int f_2(x' - a_{\omega,2}\omega)T_2(x')dx' E_{A,1}(\omega) \tag{2.25}$$

$$= \int f_2(x' - a_{\omega,2}\omega)T_2(x')dx' \int f_1(x - a_{\omega,1}\omega)T_1(x)dx E_0(\omega), \tag{2.26}$$

or more generally

$$E_{A,N}(\omega) = E_0(\omega)\Pi_{n=1}^{N} \int f_n(x - a_{\omega,n}\omega)T_n(x)dx. \tag{2.27}$$

This approach implies, however, full spatial frequency filtering between the two interactions. This can be assumed to be fulfilled when considering two separated setups in the laser chain, e.g. the first clipping process taking place in the stretcher and the second in the compressor.
When instead considering two interactions that take place prior to the spatial frequency filtering, e.g. both surfaces are in the stretcher, using

$$E_{A,N}(\omega) = E_0(\omega) \int \Pi_{n=1}^{N} f_n(x - a_{\omega,n}\omega)T_n(x)dx. \tag{2.28}$$

provides a better approximation. An example calculation of the temporal profile conditioned by consecutive spectral clipping is provided in app. A.5

2.2.2. Influence of Spectral Dips on the Temporal Profile

The calculations for spectral-amplitude effects are not only valid for spectral clipping but in general for spectral-amplitude effects, like damages on the optical elements in the stretcher or dust particles on the surfaces, which have an deteriorating effect on the temporal profile [99].

These spectral-amplitude effects cause spectral dips and thereby change the FTL of the laser pulse. The analytical model developed in this section can be used to describe this process by inserting a perturbation $P(x)$ into the beam that is an inverse top-hat. This results in a spectral transmission of the element that is one, except for the position of the damage, where the transmission drops to a depth d.

I have conducted a parameter study on this topic using eq. 2.24, with the results that the dip indeed introduces a rising edge, with the shape being conditioned by the width and depth of the dip, as well as the size of the laser beam on the considered surface.
The width of the damage does not change the slope of the rising edge, but only the frequency of the oscillation.
The depth of the spectral dip does not influence the oscillation frequency, but only changes the amplitude of the rising edge.
For the influence of the beam size on the surface it is clear that this dominates the slope of the rising edge. This is intuitive, since for larger beam sizes the hard edges of the dip are smoothed out. In the limit of an infinite beam size the effect of the damage would be completely removed, which must result in the FTL of the undisturbed profile. This stands in agreement with the parameter study, where a larger beam size produces a steeper rising edge.

A depiction of the parameter study, which makes these relations apparent is included in app. A.6.

2.3. Spatial Conditioning Effects

As previously stated, spatial effects are normally not a concern for the temporal profile of a laser pulse. They only become relevant whenever STC is introduced, which is the case for spectral-phase effects and spectral-amplitude effects, as discussed in sec. 2.1 and sec. 2.2, respectively.

This section discusses how spatial effects condition the rising edge formation, starting by an investigation of the impact of the beam size of an ideal Gaussian in sec. 2.3.1. Afterwards, sec. 2.3.2 generalizes this to the impact of the beam shape. Then, sec. 2.3.3 takes into account that spatial modulations in the beam path are affected by propagation effects, which changes the beam shape on optical elements.

2.3.1. Conditioning of the Rising Edge by the Beam Size of an Ideal Gaussian

An important implication of the derived analytical descriptions of the rising edge in eq. 2.18 and eq. 2.24 is that the slope of the rising edge increases with increasing beam size when assuming that the spatial profile $f(x)$ is a Gaussian.

For spectral-phase effects that have become apparent during the parameter study for damages on the surface (compare sec. 2.2.2).
For spectral-phase effects, on the other hand, the statement is a direct conclusion from the analytical description in eq. 2.18. In order to realize this, it is necessary to consider the shape of the Fourier transform of the spatial profile $\tilde{f}(t/a_\omega)$ for a Gaussian:
the Fourier transform of a Gaussian is again a Gaussian but with a width that inversely scales with the width of the original Gaussian. Thus, an increased beam size of $f(x)$ results in a decreased width of $\tilde{f}(t/a_\omega)$. A narrower $\tilde{f}(t/a_\omega)$ in turn results in a faster amplitude reduction of the disturbance and a cleaner temporal profile.

A further implication, and one of the main statements this thesis makes, is that this scaling with the beam size is the reason why the folding mirror in the Fourier plane of a stretcher dominates the rising edge of most CPA laser systems. After the grating the beam is spectrally dispersed, so each wavelength is incident on the first focusing element of the telescope in a slightly different angle and on a slightly different position. As a result each wavelength will have a focal spot on the folding mirror, but on a slightly different transversal position. This resulting focal line has the largest aspect ratio of all interactions in the CPA laser chain. The dispersion coefficient is similar to the value on other surfaces in the setup, but the beam size of each wavelength is decreased.

In order to emphasize the difference between the impact of optical elements in the NF and in the FF, the corresponding Fourier transformed beam profiles $\tilde{f}(t/a_\omega)$ are calculated.

For the NF this is given by the Fourier transform of the spatial profile in the NF, which can be explicitly calculated for a Gaussian beam profile

$$\tilde{f}_{\mathrm{NF}}(t/a_\omega) = \int_{-\infty}^{\infty} e^{-\frac{x^2}{2\sigma_{\mathrm{NF}}^2} - ixt/a_\omega} dx \propto e^{-\frac{\sigma_{\mathrm{NF}}^2 t^2}{2a_\omega^2}} \tag{2.29}$$

In this case, it is evident that the steepness increases with increasing in-stretcher beam size σ_{NF}.

For the FF $\tilde{f}_{\text{FF}}(t/a_\omega)$ we need to first find the spatial profile in the FF $f_{\text{FF}}(x')$. This can either be found by explicit solving of the Fourier transform, or by exploiting that the shape is again a Gaussian with a width given by eq. 1.20

$$f_{\text{FF}}(x') \propto e^{\frac{x'^2}{2\sigma_{\text{FF}}^2}} = e^{-\frac{\pi^2\sigma_{\text{NF}}^2}{2f^2\lambda_0^2}x'^2}, \tag{2.30}$$

with the focal length f and the central wavelength λ_0. This allows the calculation of $\tilde{f}_{FF}(t/a_\omega)$ using one more Fourier transform

$$\tilde{f}_{\text{FF}}(t/a_\omega) \propto e^{-\frac{f^2\lambda_0^2t^2}{2\pi^2\sigma_{\text{NF}}^2a_\omega^2}}. \tag{2.31}$$

This equation shows the previously mentioned key implication, that the slope of the rising edge caused by an optical element in the FF increases with increasing in-stretcher beam size σ_{NF}. In fact, the rising edge caused by optical elements in the NF and FF show an opposed dependency on the in-stretcher beam size.

2.3.2. Conditioning of the Rising Edge by the Beam Profile

Besides the ideal Gaussian beam profile it is also important to discuss the more general case of non-ideal beams and how they condition the rising edge. Derivations from the ideal Gaussian are mostly perturbations, in the spatial phase (aberrations) and spatial amplitude modulations. For the latter, a prominent example is spatial clipping due to the finite size of optical elements. The influence on the spatial profile of both kinds of perturbations can be expressed as $f_{\text{P}}(x) = f(x) \cdot P(x)$.
In order to describe the impact of these more general spatial profiles, it is necessary to repeat the previous calculations for the special case of an ideal Gaussian, this time for $f_{\text{P}}(x)$.

Analogously to the unperturbed case, the perturbed NF profile $\tilde{f}_{\text{NF,P}}(t/a_\omega)$ is calculated using the Fourier transform of the now complex, perturbed spatial profile $f_{\text{NF,P}}(x)$

$$\tilde{f}_{\text{NF,P}}(t/a_\omega) = \mathfrak{F}_{x\to t/a_\omega}\Big[f_{\text{NF,P}}(x)\Big](t/a_\omega). \tag{2.32}$$

For optical elements in the FF, the Fourier transform must be employed twice. The first Fourier transform is again from the NF position x to the position in the FF x'. The second Fourier transform is from the spatial position in the FF x' to t/a_ω

$$\tilde{f}_{\text{FF,P}}(t/a_\omega) = \mathfrak{F}_{x'\to t/a_\omega}\Big[\mathfrak{F}_{x\to x'}\Big(f_{\text{NF,P}}\Big)(x)\Big](t/a_\omega). \tag{2.33}$$

Explicitly solving both integrals simplifies this equation to

$$\tilde{f}_{\text{FF,P}}(t/a_\omega) = \int\int e^{-ix't/a_\omega} e^{i\frac{x'x}{f\lambda_0}} f_{\text{NF}}(x)P(x)dxdx' \tag{2.34}$$

$$= \int \delta\Big(-\frac{t}{a_\omega} + \frac{x}{f\lambda_0}\Big) f_{\text{NF}}(x)P(x)dx \tag{2.35}$$

$$\propto f_{\text{NF}}\Big(\frac{f\lambda_0 t}{a_\omega}\Big)P\Big(\frac{f\lambda_0 t}{a_\omega}\Big)., \tag{2.36}$$

which implies that the spatial perturbation P is directly imprinted into the temporal profile.
In the following these general functions are used to calculate the impact of spatial-phase perturbations, called defocus, and the amplitude effect of spatial clipping.

Impact of Defocus on the Rising Edge Formation

The first case is, since the model is one dimensional, implemented as a quadratic spatial phase $\phi = a \cdot x^2$ with the amplitude a. The effect has an analogous result to a spectral phase described by eq. 1.31 but in the spatial domain. Thus, the defocus leads to an increase of the beam size

$$\tilde{f}_{\text{NF,P}}(t/a_\omega) = \int f_{\text{NF}}(x) e^{ia \cdot x^2} e^{ixt/a_\omega} dx. \tag{2.37}$$

Analogously to spectral phases (compare fig. 1.4), other polynomial orders beside the considered second order can hence be expected to lead to similar changes of shape in the rising edge as their spectral phase counterparts in the undisturbed temporal profile. E.g. third order effects will according to these calculations cause an asymmetry in the rising edge, described by eq. 2.18.
This is a novel implication that predicts a conditioning of the introduced rising edge by the spatial phase on the considered surface.

In the FF the same spatial phase has, according to the model, no impact on the rising edge, since it is again a pure phase effect after the two Fourier transforms in eq. 2.36, which is removed by the absolute square in eq. 2.18.

Impact of Spatial Clipping on the Rising Edge Formation: Near-Field

For the amplitude effect of spatial clipping, I consider the finite size of an aperture x_c, which can be expressed as a top-hat $P(x) = T(x)$. When such an aperture is positioned in the NF or somewhere in the laser chain that is imaged onto the optical element, where the rising edge is introduced, the rising edge is expected to follow

$$\tilde{f}_{\text{NF,P}}(t/a_\omega) = \int f_{\text{NF}}(x) T(x) e^{ixt/a_\omega} dx = (\tilde{f} \circledast \tilde{T})(t/a_\omega), \tag{2.38}$$

where the convolution theorem allows the separation of the equation into two distinct Fourier transforms that can be calculated analytically. The Fourier transform of the undisturbed profile has been discussed before and can be found in eq. 2.29. The Fourier transform of an aperture, which can be mathematically described as a top-hat, is equivalent to a sinc-function

$$\tilde{T}(t/a_w) = \int_{-\infty}^{\infty} T(x) e^{-i\frac{xt}{a_\omega}} dx = \frac{2a_\omega}{t} \sin \frac{x_c t}{2a_\omega}. \tag{2.39}$$

Accordingly, the rising edge in eq. 2.29 in the presence of an NF aperture conditioned by the convolution of the undisturbed profile with a sinc-function. This has to the best of my knowledge, no appealing analytical solution, but can be numerically computed for explicit results when predicting the rising edge.

Analytical simplifications are however possible in the edge cases.
For small apertures, the sine can be approximated as being linear and the sinc function is approximately constant. In this case, the perturbation can be removed from the convolution, leaving an integral over the spatial profile. In this case the spatial conditioning is removed from eq. 2.18, resulting in the model developed by Dorrer and Bromage [95].

For large apertures in comparison to the beam size the top-hat is constant for all positions where the spatial Gaussian has relevant energy, which results in the unperturbed case.

This discussion of spatial perturbations allows the following conclusion: according to the developed analytical model an increase of the beam size in the NF can degrade the temporal contrast caused by the optical element in the NF when this increases the energy that is clipped on the aperture from a negligible to a considerable level.

Impact of Spatial Clipping on the Rising Edge Formation: Far-Field

The same calculation can be repeated, with a spatial aperture in the NF and a perturbed optical element in the FF, according to eq. 2.36. Analytically, this results in a sharp decline in the rising edge, at

$$t_c = \frac{a_\omega x_c}{2 f \lambda_0}. \tag{2.40}$$

Depending on the beam size and the perturbation P, the relative intensity of the rising edge is for large apertures already below any detection limit and sharp decline is negligible since the top-hat is constant for all relevant times.

For small apertures in the NF the rising edge converges against zero, which is intuitive since in the limit the beam in the NF is a diffraction limited spherical wave originating from the aperture, which would correspond to a large beam in the FF.

While the model produces realistic results for those two extremes, it can not deliver meaningful results for cuts at relevant times, since the analytical approximations that lead to eq. 2.18 are no longer valid. The referred to approximation is that the variation of $\tilde{f}\tilde{\delta}\tilde{\phi}$ is small during the duration of the undisturbed pulse, which the model uses to remove these terms from a convolution with the undisturbed temporal profile and find eq. 2.13. This assumption can not be true when the sharp drop of a top-hat occurs during relevant times. Further implications and limits imposed by this approximation are discussed in app. A.1.

Impact of Retrospective Spatial Clipping on the Rising Edge Formation

It is also theoretically possible for spatial apertures to introduce a rising edge when employed after the interaction with the perturbed surface since there is mathematically no fundamental difference between the order of operation. This requires that the field on the perturbed optical element, described by eq. 2.3, translates to an output field of

$$E_{\text{out}}(x, \omega) = f(x) P(x + a_\omega \omega + b_\omega) E_0(\omega), \tag{2.41}$$

where all frequencies are spatially recombined. This removes the frequency dependency from the spatial profile f and transfers it into the perturbation P. According to the fundamental assumption of the analytical model, free beam propagation transitions this field to eq. 2.7, due to the spatial frequency filtering employed by self-diffraction. Nonetheless, it is reasonable to assume that eq. 2.41 is still valid for short distances after the perturbed surface and especially in the image plane of the considered surface.

Under this assumption, subjecting the output field to the spatial aperture $T(x)$ results in a field E_{after} of

$$E_{\text{after}}(x,\omega) = E(x,\omega) \cdot T(x) = f(x)P(x + a_\omega\omega + b_\omega)T(x)E_0(\omega). \tag{2.42}$$

This is equivalent to employing the same spatial aperture prior to the perturbed element, which results in the previously introduced spatial profile on the perturbed optic $f_T(x) = T(x)f(x)$ and thus the field

$$E_{\text{prior}}(x,\omega) = f(x)T(x)P(x + a_\omega\omega + b_\omega)E_0(\omega). \tag{2.43}$$

2.3.3. Impact of Free Propagation on the Spatial Conditioning

A core aspect of the derived analytical models is spatial frequency filtering during propagation effects. Due to the same propagation effects spatial filters employed in the laser chain can not be expected to arrive unchanged at perturbed surface. This becomes especially clear when considering spatial clipping on a hard edge, which introduces high spatial frequency components.
Thus, it is necessary to differentiate between the beam profile at the position of spatial conditioning $f(x,0)$ and at the position where the rising edge is introduced $f(x,\Delta z)$, separated by a distance Δz.

In the frame of this thesis, propagation effects are implemented based on Fresnel Diffraction [104]. In this theory, the propagation of a laser by a distance Δz results in a FF phase-term $\tilde{H}(k,\Delta z)$. Thus, the beam profile at the position Δz can be expressed by first calculating the FF profile prior to propagation $\tilde{f}(k,0)$, applying the complex phase-term $\tilde{H}(k,\Delta z)$ and then calculating the corresponding NF profile $f(x,\Delta z)$. This yields, the beam after propagation by a distance Δz as [104]

$$f(x,\Delta z) = \mathfrak{F}^{-1}\Big[\tilde{f}(k,0) \cdot \tilde{H}(k,\Delta z)\Big](x). \tag{2.44}$$

The rising edge scales with the absolute square of the Fourier transform of the beam profile on the surface (compare eq. 2.18) which is

$$|\tilde{f}(k,\Delta z)|^2 = |\tilde{f}(k,0) \cdot \tilde{H}(k,\Delta z)|^2 = |\tilde{f}(k,0)|^2. \tag{2.45}$$

According to this, the intensity profile in the FF does not depend on the propagation over the distance Δz between the measurement point of the spatial profile and the optical element. Since the rising edge caused by spectral-phase effects scales depends on the intensity profile in the FF the rising edge is also independent of the position of the measurement point.

This becomes relevant when considering the introduction of an aperture at a position prior to the optical element, since it implies that the rising edge is independent of the positioning of the aperture. The phenomenological reasoning behind this is that the rising edge is conditioned by the profile in the FF, which is analytically positioned at an infinite distance from the NF. Thus, the distance between the aperture and the FF is always infinite and the FF profile is independent of the positioning of the aperture.
It is to note, that this approach is chosen in such a way that it does not consider beam divergence, which increases the beam size. The reason for this is that the impact of a change in the beam size was previously discussed in sec. 2.3.1

3. Experimental Validation of the Rising Edge Conditioning by the Spatial Beam Profile

The previous chapter provides a novel analytical model predicting the rising edge. This model has led to several analytical implications for the conditioning of the rising edge, that are tested and validated in this chapter.
In order to validate that the rising edge is dominated by the optical element in the Fourier plane of stretchers and that the beam size conditions the sloop of the rising edge, I have designed and executed an experimental campaign in which I employed a stretcher design that can be used in a folded and an unfolded configuration [1]. This allows an isolation of several parameters of the setup and thereby the validation of the analytical model. The setup is explained in sec. 3.1, followed by the prediction of the rising edge for this setup based on cha. 2 and ray-tracing. In sec. 3.3 a comparison between these predictions and actual measurements is presented. The chapter ends with a brief conclusions on the origin of the rising edge in sec. 3.4.

3.1. Experimental Setup of a Dispersion-Free Stretcher with Rapid Folding Adaptability

Observing changes in the temporal profile of a laser pulse requires a measurement device with a large enough dynamic range to resolve the rising edge and a laser pulse with a high enough intensity to operate the measurement device. A further requirement is that the initial laser pulse is close to the FTL over the measured dynamic range, without a rising edge. The used laser system starts with a Ti:Sa oscillator at 1040 nm with a bandwidth of approximately 16 nm, a pulse length of around 170 fs and a repetition rate of 76 MHz (Mira 900f, Coherent [105]). This laser is amplified to around 100 μJ using OPA [106] with a pump pulse that was generated by an in-house build frequency doubled regenerative amplifier operating at 10 Hz, which was the prototype for the regenerative amplifier described by Y. Zobus [107]. The parametric amplification decreased the bandwidth to approximately 6.2 nm and the repetition rate to 10 Hz, with the 76 MHz background of the Mira oscillator at around 1-2 nJ per pulse.
The measurement device used to resolve the temporal profile of this pulse is a commercially available device called Sequoia (Amplitude) [108], which operates fully in the NF. With the achieved energy the Sequoia was capable of resolving a dynamic range of nine orders of magnitude. Section 4.7 discusses this third-order cross-correlator in more detail.

A schematic of the configurations of the experimental setup is depicted in fig. 3.1. The first configuration of this setup is a bypass of the stretcher, which can be used to verify that the laser front-end has a clean temporal profile, without signs of a rising edge.

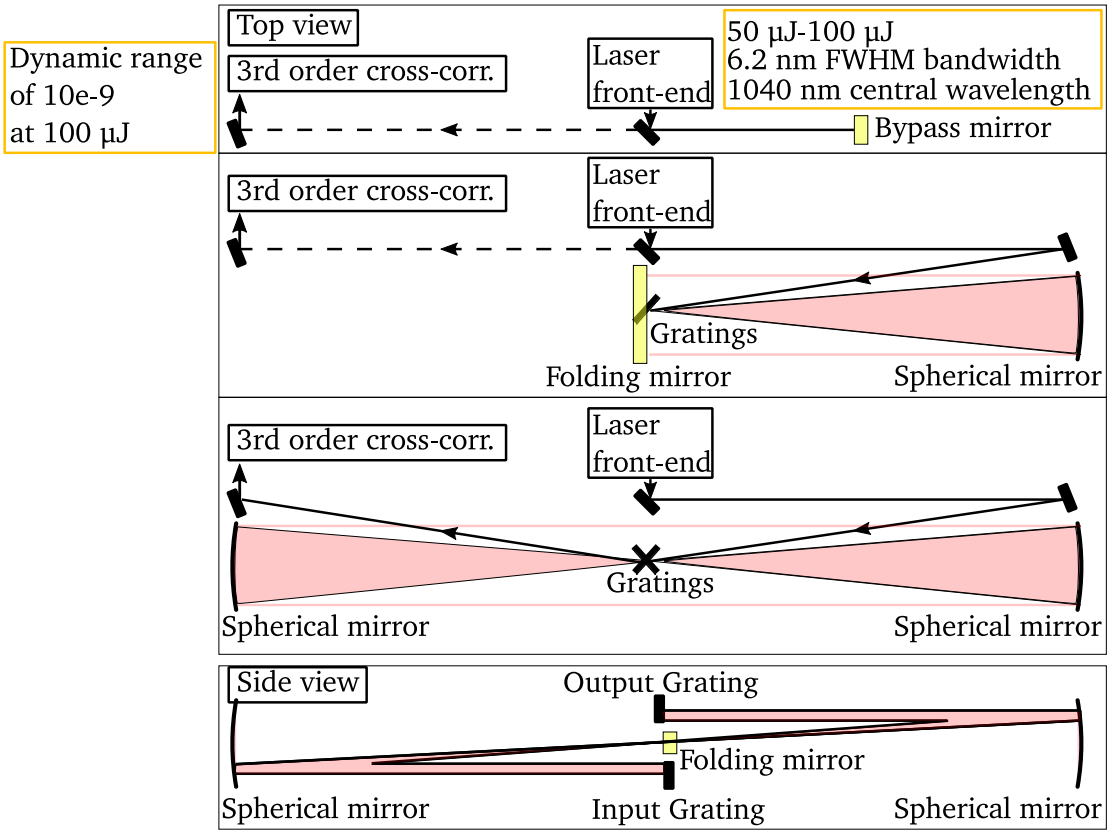

Figure 3.1.: Setup configurations used for the experimental validation of the conditioning of the rising edge caused by the beam size. The first three views are a bypass configuration, used to verify that the injected pulse does not feature a rising edge, a folded configuration, and an unfolded configuration. The bottom view is the side view.

The second configuration is a folded design that uses a diffraction grating with a line density of 1740 l/mm, a spherical mirror with a radius of curvature of 3.048 m and an aperture of 152.4 mm and a dielectric folding mirror with a coated aperture of 135 mm. The beam is incident on the grating, which spectrally disperses it. After this, the beam is reflected by the spherical mirror which is positioned one focal length apart from the grating. The spatial separation from the incoming beam is realized by a combination of tilting the spherical mirror and choosing a point of incidence on the mirror below the center. The folding mirror is positioned directly above the grating, also at a distance of one focal length from the spherical mirror. It is also slightly tilted in such a way that the beam can be separated from the incident beam after traversing back through the stretcher.

The third configuration, being the unfolded design, is as close to equivalent to the folded design as technically feasible. It employs a second, identical spherical mirror and a second grating, with identical grating constant. Switching between both setups is made simple and reproducible, as only the folding mirror has to be removed from or placed in the setup.

Since the grating distance (compare fig. 1.2) is set to zero in this stretcher, the dispersion coefficient a_ω (compare eq. 2.1) on the gratings vanishes and they do not contribute to the rising edge. The combination of this and the quick changeability between folded and unfolded configurations allows for an isolated investigation of the influence of the folding mirror.

The setup furthermore incorporates a removable magnification telescope that allows for quick changes of the beam size by factor of approximately six. This allows the investigation of the conditioning by the beam size that is predicted by eq. 2.18. In the following, the configuration with the magnification telescope and without the magnification telescope are referred to as the large beam (lb) configuration and the small beam (sb) configuration, respectively.

The topic of the next section is the estimated degradation of the temporal profile for this setup. This includes an estimation of the aberrations introduced in the stretcher, based on ray-tracing, an estimation of the impact of spectral clipping and a prediction of spectral-phase effects based on eq. 2.18.

3.2. Prediction of the Rising Edge in the Proof-of-Principle Setup

A characterization of the system is necessary for the estimation of the rising edge. This includes a spatial characterization of the input beam profile, as well as a spectral characterization of the beam before and after the stretcher, in order to identify the spectral bandwidth and the clipping wavelengths.
For spectral-phase effects, a further required parameter is the PSD of all relevant surfaces. The corresponding measurements and calculations are provided in app. A.2.
The last parameter is the dispersion coefficient a_ω on each surface. This parameter does not require dedicated measurements and can be calculated analytically using the specifications of the components, extracted from the ray-tracing or calculated from the optical element sizes and the measured clipping wavelengths in the setup. This is the parameter discussed in the following.

3.2.1. Calculation of the Dispersion Coefficients on the Stretcher Optics

The dispersion coefficients on each surface are given by the geometry of the stretcher. This particular setup employs gratings with a line density of 1740 l/mm $\pm$ 1 l/mm, spherical mirrors with a radius of curvature of R =3.048 m $\pm$ 0.03 m and an aperture of S =152.4 mm$\pm$ 1.5 mm diameter and a flat mirror with a coated area of 135 mm $\pm$ 0.5 mm x 40 mm. With this, the bandwidth that fits on the mirrors can be calculated using basic trigonometry and the diffraction equation (eq. 1.21). A visualization of the relevant part of the setup with the individual values can be found in fig. 3.2.

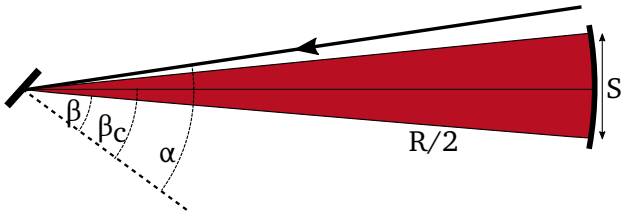

Figure 3.2.: After the first hit on a grating under the incident angle α relative to the grating surface normal the beam is diffracted at a diffraction angle β. The optical axis of the system is chosen in such a way that it is equivalent to the path of the central wavelength λ_c, corresponding to the diffraction angle β_c. The grating is positioned in the focal length $R/2$ of the spherical mirror with a clear aperture S.

Trigonometric considerations of this setup yield

$$\sin(\beta_c - \beta_1) = \frac{S}{R} \qquad \sin(\beta_c - \beta_2) = -\frac{S}{R}, \tag{3.1}$$

where β corresponds to the angle relative to the grating normal after diffraction, and the subscripts $c, 1, 2$ correspond to the central wavelength and the longest and shortest wavelengths that still hit the surface, respectively. Then, the reflected bandwidth corresponds to the difference between the clipping wavelengths $\Delta\lambda = \lambda_2 - \lambda_1$. In order to calculate this bandwidth, the diffraction angles can be substituted by the diffraction equation for gratings, see eq. 1.21. The angles of the clipping wavelengths can be calculated using the known distance between the focal point to the edges of the mirror due to the relation $\sin\beta_{1,2} = S/R$ since the gratings are positioned at half the radius of curvature in this setup.

$$\Delta\lambda = \frac{\sin(\beta_c + \arcsin(S/R)) - \sin(\beta_c - \arcsin(S/R))}{mg} = \frac{2S}{mgR}\cos\beta_c \tag{3.2}$$

For an incident angle of $\alpha = 69\,^\circ \pm 2\,'$ this gives a bandwidth on the spherical mirrors $\Delta\lambda_{\text{sphere}}$ and the flat folding mirror $\Delta\lambda_{\text{flat}}$ of

$$\Delta\lambda_{\text{sphere}} = 27.6\,\text{nm} \pm 0.41\,\text{nm} \qquad \Delta\lambda_{\text{flat}} == 24.6\,\text{nm} \pm 0.29\,\text{nm}. \tag{3.3}$$

The clipping wavelength after the folding mirror in the Fourier plane of the setup was calculated using the assumption that the wavelengths are collimated after the first spherical mirror. This value is slightly smaller than for the spherical mirror, due to the smaller free aperture of the folding mirror in the Fourier plane.

With the transmitted wavelengths known, the dispersion coefficient can be calculated using the small angle approximation, which yields that the angular frequencies are linearly distributed over the optical element

$$a_\omega = \frac{S}{\Delta\omega} = \frac{S\lambda_c^2}{2\pi c\Delta\lambda} = 3.15\,\text{mfs} \pm 0.17\,\text{mfs}. \tag{3.4}$$

The dispersion coefficient on the folding mirror has the same value if we assume that the grating is positioned at half the radius of curvature of the spherical mirror and that the wavelengths propagate parallel to each other after the first spherical mirror.
It is further important to note, that the dispersion coefficients vanishes on the surface of the gratings, resulting in a vanishing rising edge according to eq. 2.18 for the grating. This is intuitive, since each wavelength experiences the same spectral phase modulation, implying that the influence of the gratings can be neglected for the Proof-of-Principle (PoP).

3.2.2. Predicting the Rising Edge in the Proof-of-Principle Setup: Spectral Clipping

This chapter covers the expected impact of spectral clipping on the stretcher optics based on sec. 2.2. This estimation requires the measurement of the transfer function for each optical element $T(x)$, the spatial beam profile $f(x)$ and the undisturbed temporal profile $\tilde{E_0}(t)$.

The top-hat transfer function can be defined according to the dispersion coefficient and the transmitted bandwidth, calculated in the previous section. However, in the actual setup the aperture of the spherical mirror was not fully utilized, in order to accommodate beam separation. This introduces a slight difference between unfolded and folded configuration.

For the former, the only necessary separation is before and after the beam is incident on the spherical mirror, which is in this setup realized by a tilt of the spherical mirror and an offset of 25 mm with respect to the center of the free aperture. For the folded design a further separation is necessary, between the in-going and out-going beam. This is realized with a tilt of the folding mirror in the Fourier plane. For this setup, the resulting offset on the sphere is approximately 50 mm.

The measurement of the transmission through the stretcher is depicted in fig 3.3, together with vertical grey lines at the clipping wavelengths according to eq. 3.4. The vertical purple lines indicate the measured clipping wavelengths. The thickness of these lines corresponds to the uncertainty, determined as the area where the smoothing due to the beam size can be seen. This yields measured transmitted bandwidths of

$$\Delta\lambda_{\text{folded}} = 19.9\,\text{nm} \pm 0.5\,\text{nm}, \qquad \Delta\lambda_{\text{unfolded}} = 26.1\,\text{nm} \pm 0.3\,\text{nm},$$

for the folded and unfolded (bottom) configuration, respectively.
The difference to the expectations of almost 5 nm in the folded design and 1.6 nm for the unfolded setup fit well to the effect of the introduced offsets o on the spheres according to

$$o = \sqrt{\frac{S^2}{4} - \frac{S'^2}{4}} = \sqrt{\frac{S^2}{4} - \left(\frac{mgR\Delta\lambda}{4\cos\beta_c}\right)^2}, \tag{3.5}$$

where S' is the effective aperture size of the sphere.
Using this equation yields, offsets of 52.8 mm and 25.2 mm, in the folded and unfolded configuration, respectively, with fits well to the specified values of 50 mm and 25 mm.

Since this setup is designed to provide the temporal measurements necessary to validate the theoretical model described by eq. 2.18, it is necessary that no parameters that condition this equation are changed when switching between the folded and the unfolded configuration.
While the clipping wavelengths differ, the previous consideration have shown that this is caused by the offset on the sphere. Thus, the important parameters of a_w does not change. In accordance to that, the validation of the theoretical model is not compromised by this difference, as long as the impact of the spectral clipping does not dominate the rising edge.

At first glance, it looks like the clipping that can be seen in the spectrum might be expected to have a large impact on the spectrum since it occurs at roughly 6.7% of the peak intensity in the spectrum. However, it is important to realize that the depicted spectrum does not uniformly contribute to the signal in the cross-correlator. Rather, only the small central portion of the spectrum that is amplified in the uOPA process does.
The calculation of this signal is done by first recording the complete signal, which is the addition of the Mira oscillator with its high repetition rate and low energy per shot and the uOPA signal with its low repetition rate and higher energy per shot. For the second measurement the temporal overlap between Mira and the pump is detuned, yielding the pure Mira spectrum. The subtraction of both signals must thereby result in the uOPA signal, which can be seen more clearly on the right-hand side of fig. 3.3. For this PoP, it is sufficient to fit a Gaussian distribution onto this curve, which results in an Full Width Half Maximum (FWHM) of 6.2 nm.

The fit to the data is necessary in order to estimate the shape of the temporal profile, since the 16bit dynamic range of the employed spectrometer (HR2000+, OceanOptics) does not provide the FTL over the required nine order of magnitude for the characterization of the temporal contrast.

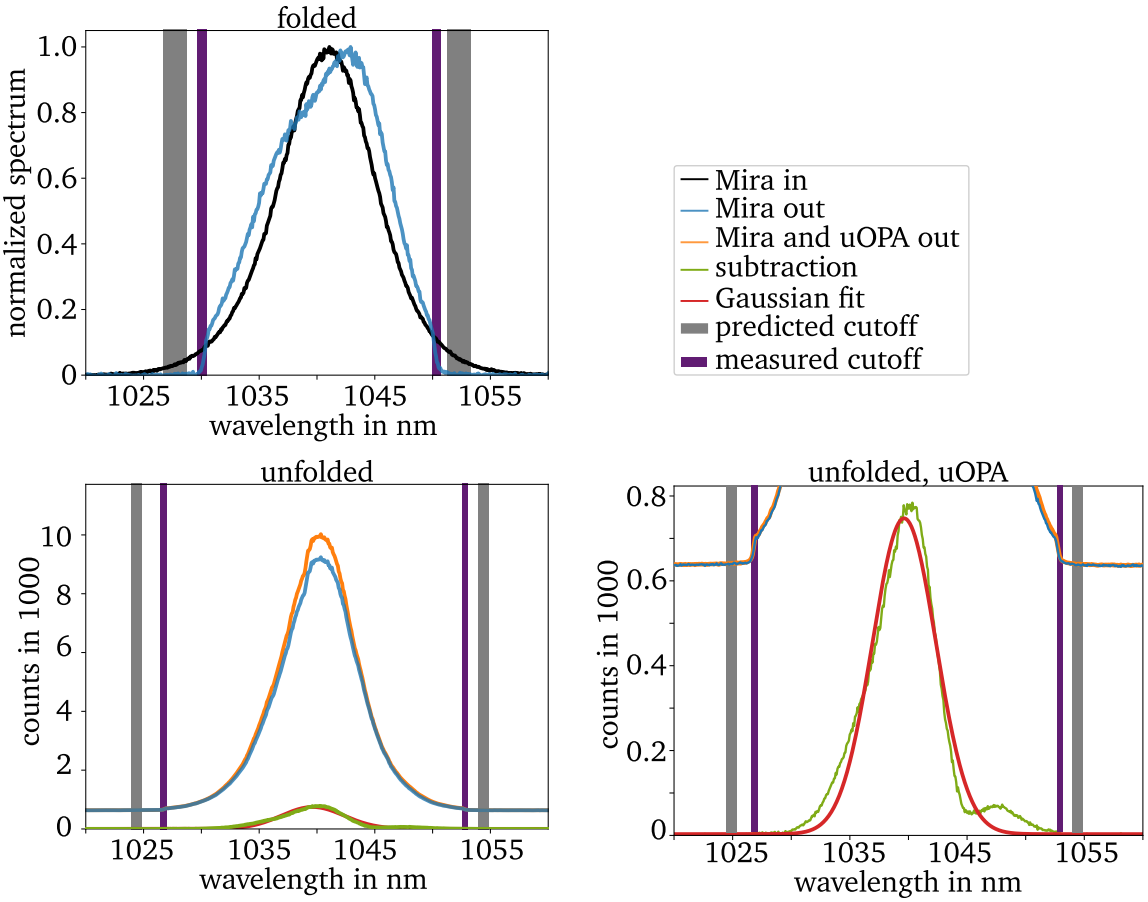

Figure 3.3.: Spectrum of the laser pulses used for the PoP. On the top left side, the spectrum of the Mira laser oscillator is depicted before and after passing through the folded stretcher design. The vertical lines mark the predicted and measured clipping wavelengths, with the thickness of the line corresponding to the respective uncertainty. On the bottom left the transmission spectrum for the unfolded configuration can be seen. Additionally, the plot includes the measurement of the uOPA spectrum, which is the subtraction of the Mira signal with the uOPA signal and the pure Mira signal. For clarity, the uOPA spectrum is again depicted in the right, over the relevant area, as well as the fit of a Gaussian onto that spectrum.

With this, the first two components necessary for the estimation of the rising edge caused by spectral clipping according to eq. 2.24 are acquired, being the undisturbed profile $\tilde{E}_0(t)$, which is approximated as the square root of the FTL of the Gaussian fitted onto the OPA spectrum and the measured transfer function $T(\lambda)$. Thus, the last remaining quantity that must be measured is the spatial profile $f(x)$.

The profile was measured at the stretcher input with a CCD camera (Basler, acA1920-40gm). Similar to the measurements of the spectrum, this requires subtracting extracting the OPA signal by subtracting the Mira signal.

In this context, only the one dimensional profile is relevant, since the spectral clipping only takes place in the plane of diffraction of the grating. Furthermore, the analytical model developed in cha. 2 only relies on the one dimensional profile. Thus, the dimension perpendicular to the diffraction plane of the grating is neglected.

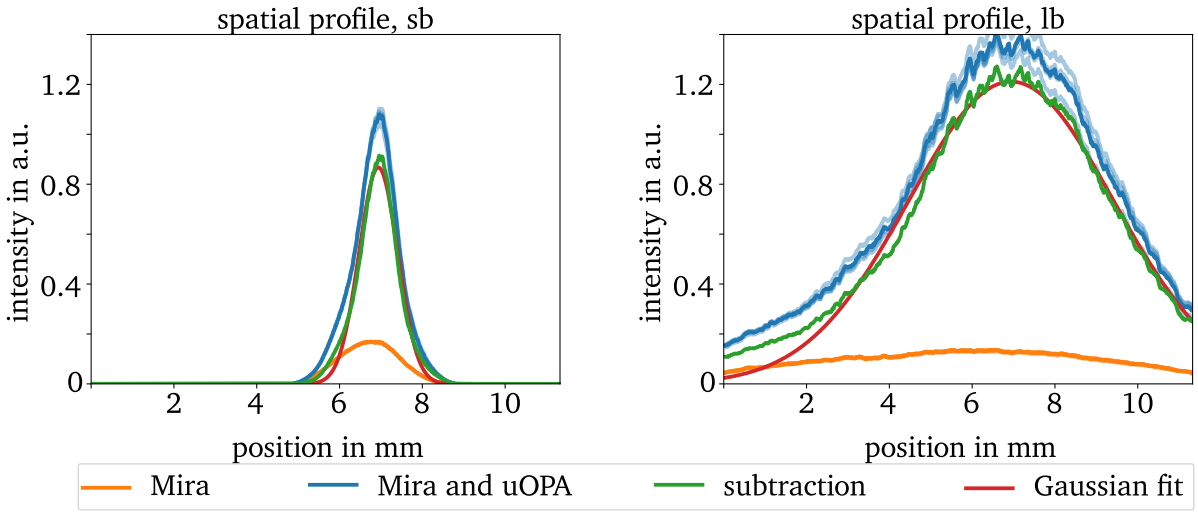

Figure 3.4.: Spatial profile of the laser pulses used for the PoP. Included are measurements of the Mira signal with and without uOPA, as well as the subtraction of both and a Gaussian fit to the subtraction. All measurements were executed at a position near the stretcher entrance, for the sb (left) and the lb (right). All measurements have been averaged over the y-axis of the camera.

For the calculation of the beam profile this was realized assuming that the beam profile is an ideal, two dimensional Gaussian and averaging the two dimensional measurements over the y-axis. This gives again a Gaussian distribution with the same size as before. The lineouts, calculated from the measurements, are shown in fig. 3.4, as well as the corresponding Gaussian fits.

From these measurements at the location of the camera, the beam size at the optical elements of the stretcher can be calculated using Gaussian beam propagation [109]. For this calculation, a measurement of the defocus is required, which was done using an Shack-Hartmann-Sensor (SHS) [110]. Considerations concerning the uncertainty that this measurement device introduces to the calculations of the beam size can be found in app. A.7.
Beyond beam propagation effects, the beam size in the diffraction plane is further increased by the projecting during the diffraction from the grating, depending on the incident angle. Incorporating both gives an estimate of the beam size on the surface of the sphere and an estimate of the radius of curvature of the wavefront at this position. The impact of the defocus at this position is mainly a longitudinal displacement of the focal position. During the alignment, the precision with which the folding mirror was positioned in the Fourier Plane was approximately one Rayleigh length. Thus, even when the defocus at the sphere is large, the beam size on the mirror is assumed to be between the diffraction-limited spatial profile at the sphere and a magnification of $\sqrt{2}$, which corresponds to propagation of one Rayleigh length.
The estimated beam sizes at the respective surfaces are,

$$\mathrm{FWHM}_{\text{sphere, sb}} = 2.33^{+0.38}_{-0.43}\,\mathrm{mm}, \quad \mathrm{FWHM}_{\text{sphere, lb}} = 10.66^{+2.85}_{-2}\,\mathrm{mm}, \tag{3.6}$$

$$\mathrm{FWHM}_{\text{flat, sb}} = 216.13^{+148}_{-34}\,\mu\mathrm{m}, \quad \mathrm{FWHM}_{\text{flat, lb}} = 47.3^{+35.0}_{-10.0}\,\mu\mathrm{m}, \tag{3.7}$$

where the uncertainties on the spherical mirror are calculated from the uncertainty of the SHS, and the uncertainty on the flat folding mirror are calculated by a combination of the uncertainty in the NF and a Rayleigh length of propagation.

The temporal profiles calculated based on the measurements in this section are shown in fig. 3.5.
The best contrast is, as to be expected, provided by the largest beam size in the unfolded design, where spectral clipping only takes place in the NF.
From there on the contrast decreases with decreasing beam size on the optical surfaces, reaching its worst point for the smallest beam size, which is again produced by the lb configuration, but this time in the FF. This is the expected behavior since a larger beam size in the NF produces a smaller focal spot in the FF.
The investigations further consider the impact of spatial clipping on the coupling mirrors, according to sec. 2.3.2. For the lb, the smallest free aperture in relation to the beam size is a 50 mm diameter mirror, prior to the stretcher. For the sb the smallest free aperture in relation to the beam size is a 25 mm diameter mirror, prior to the magnification telescope. However, neither have a measurable impact on the observed temporal contrast introduced by spectral clipping, according to the calculations.

With this the first source of temporal-contrast degradation is studied. The next steps are the computation of the influence of the other two considered effects, being spherical aberrations and degradation due to the PSD. After that, a comparison between all three influences will ascertain the dominant effect for each configuration, culminating in a comparison with experimental data.

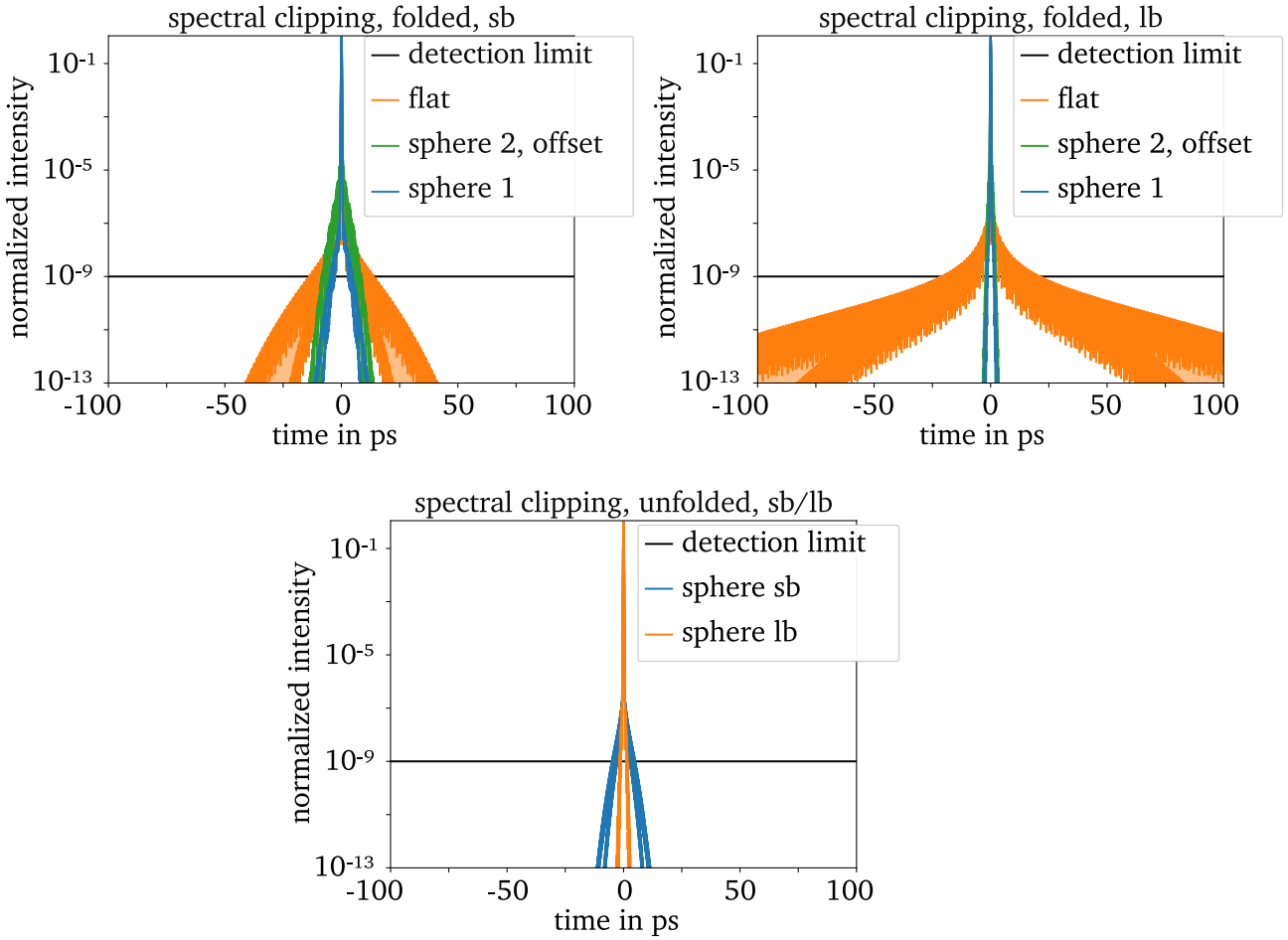

Figure 3.5.: Expected temporal profiles influenced by spectral clipping, for the lb and the sb, for the folded (top) and unfolded (bottom) configuration. The uncertainties of the beam sizes are incorporated as the shaded area between the upper and lower limits.

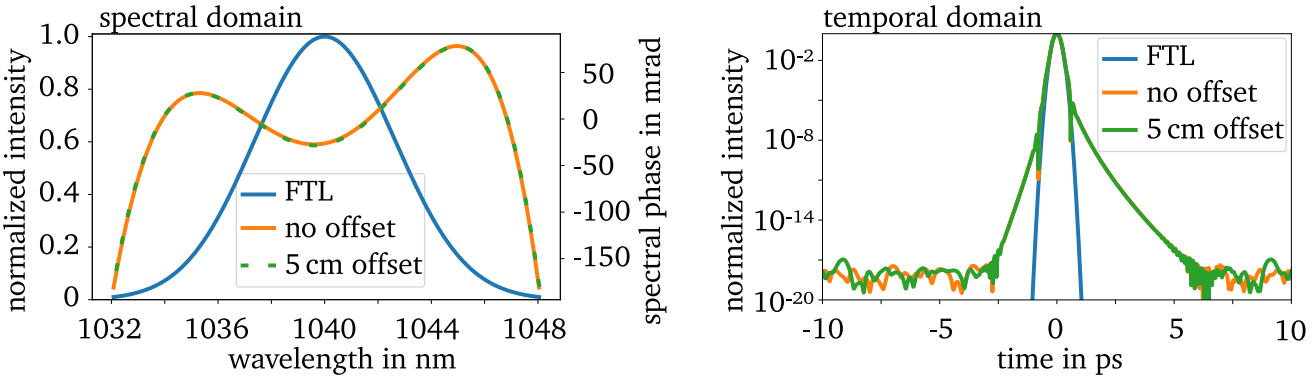

Figure 3.6.: Spectral (left) and temporal (right) profile of a pulse after passing through the unfolded stretcher configuration (compare fig. 3.1), calculated by ray-tracing. Included are the results for a simulation where all rays stay in the dispersion plane of the grating (orange) and a simulation where the rays leave the diffraction plane of the grating due to an offset of 5 cm of the spherical mirrors (green).

3.2.3. Predicting the Rising Edge in the Proof-of-Principle Setup: Spherical Aberrations

It is clear that aberrations in optical systems lead to a degradation of the beam parameters. In this section, ray tracing is used in order to estimate how these aberrations translate into the temporal profile.

Due to spherical aberrations introduced by the spherical mirrors, not all parts of the beam (from now on the individual parts are referred to as rays) will recombine on the same spot after the stretcher telescope. Instead, rays that are further away from the optical axis before the second spherical mirror are reflected in such a way that they pass through the optical axis further behind the ideal focal spot. This results in a waist, rather than that all rays recombine in a single point. The deviation from the ideal beam path changes the path length of the individual rays from the idealized telescope.

The employed ray-tracing, where each ray corresponds to one wavelength, determines the expected deviation of the spectral phase caused by this path difference. This approach can be further enhanced with the integration of the beam size by using multiple rays for each spectral component. However, the chosen approach only relies on one ray per spectral component, since the conditioning of the spatial profile of the beam is covered in the consideration of the PSD (compare eq. 2.18).

As the unfolded and folded stretcher configurations of the setup are, in the context of ray-tracing, physically equivalent, it is sufficient to simulate one of them. In fig. 3.6 the beam after such a stretcher is depicted in the spectral domain (left) and the temporal domain (right). Both plots include the results for a setup that is solely in two dimensions and, as this is nonphysical since the rays can not pass through the gratings without interaction, the results for a three-dimensional case, where the spherical mirrors are offset enough to accommodate separation of the beams. In this case, the offset of the center of curvature of the mirrors is 5 cm, which approximately replicates the setup of the experimental campaign. While in the real setup the separation is realized by a combination of tilt and offset of the spherical mirror, both approaches are physically equivalent for spheres.

In the simulated setup, the second grating was moved by 0.9 mm from the ideal focal plane in the two dimensional case and 1.13 mm in the three dimensional case in order to compensate the fourth-order phase term by a second-order phase term, resulting in a characteristic "m"-shape in the spectral phase.

With this compensation the spectral phase difference between outer and inner parts of the spectrum is reduce, which results in a shorter pulse duration.

The simulation corroborates that such a stretcher design introduces aberrations into the spectral phase. In this specific case, the contrast degradation is restricted to a 2 ps range around the maxima, over 18 orders of magnitude. Comparing this to the effect of clipping in fig. 3.5 shows, that for this specific PoP setup and this bandwidth, the impact of the aberrations can be neglected. Hence, so far the clipping seems to dominate.
The last temporal-contrast degrading effect investigated in this section, is the imprinting of the PSD into the spectral phase of the pulse, which will be discussed in the next section.

3.2.4. Predicting the Rising Edge in the Proof-of-Principle Setup: Spectral-Phase Effects

The expected rising edge caused by spectral-phase effect is calculated based on eq. 2.18 for the individual surfaces in the stretcher. Besides the laser parameters, which have been part of previous sections, this further requires a characterization of the PSD of each considered surface. This was realized using a confocal microscope and a detailed description of the required calculations from the surface measurement to the PSD can be found in app. A.2.

The resulting rising edges are depicted in fig. 3.7. Additionally to the uncertainty of the PSD, the effect of the uncertainty of the spatial beam size are incorporated.

As expected, the calculations predict that for the lb size the rising edge introduced on the flat mirror in the FF has the largest magnitude of all calculated configurations. This is consistent with the discussed effect of the greatly decreased beam size in the FF and thus decreased spatial averaging in the spectral phase.
Generally, comparing the slope of all calculated rising edges with the beam sizes on the surface (compare eq. 3.6 and eq. 3.7), directly shows the expected correlation between the calculated rising edge and the beam size.
This can also be observed for the lb on the spherical mirror, where the rising edge is almost completely restricted to the undefined region around the main peak, when neglecting spatial apertures. When however considering spatial apertures, a drastic change in the temporal profile can be observed, which results in the slow rising edge visible in fig. 3.7. Both cases, with and without aperture, are included in fig. 3.7, in order to emphasis the difference between both considerations.

The incorporation of spatial clipping is analogous to sec. 3.2.2, with the relevant free apertures being 50 mm for the lb and 25 mm for the sb.
This has no notable effect on the rising edge for the sb size, due to the large ratio between free aperture and beam size. If further has no impact for the flat mirror in the FF. According to eq. 2.40, the impact of the FF element is expected to occur at around 132 ps, which is above the considered time interval.

In order to find the actual expected rising edge for each stretcher configuration, it is necessary to compare the different effects and surfaces and consolidate them into one rising edge, which follows in the next section.

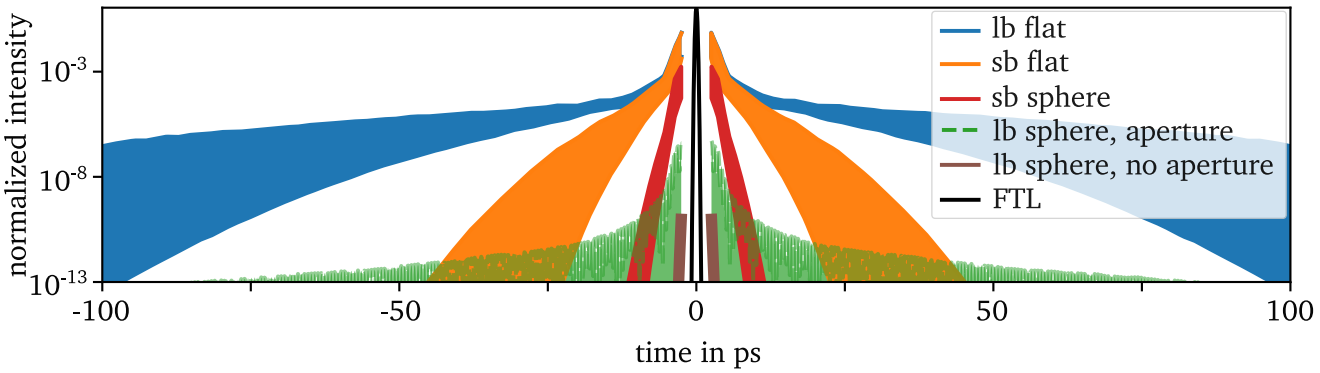

Figure 3.7.: Rising edge calculated for the different surfaces and beam sizes of the PoP setup. The shaded areas indicate uncertainties based on the measurements of the PSD and the beam size.

3.2.5. Predicting the Consolidated Rising Edge in the Proof-of-Principle Setup

The three previous sections calculated the rising edge caused by each surface considering the effects of spectral clipping, the imprinting of the PSD into the spectral phase, and the expected rising edge due to spherical aberrations in the stretcher. Now, the analysis below compares the magnitude of each effect and expected temporal profiles for each configuration.

For a system fully dominated by spectral-amplitude effects, this can be realized eq. 2.28 for consecutive clipping in one setup.

When the system is fully dominated by spectral-phase effects the presented calculations assume that the rising edge of the complete system is the addition of the impact of each surface, according to eq. 2.20, which results in

$$I_{\text{folded}} = 2 \cdot I_{\text{sphere,NF}} + I_{\text{flat,FF}} \tag{3.8}$$

$$I_{\text{unfolded}} = 2 \cdot I_{\text{sphere,NF}}. \tag{3.9}$$

For a system fully dominated by spherical aberrations the combination is not necessary, since the ray-tracing treats the system as a whole.
The expected rising edge for these three possibilities are depicted in fig. 3.8. According to these calculations, spectral-phase effects (denoted as PSD in the plot) dominate for all configurations. This revelation simplifies the process of finding a consolidated rising edge for the complete setup substantially. Due to the markedly dominance of the PSD effect over the other effects it is equivalent to neglecting the other effects individually on each surface, or as a whole from the beginning.

Before moving on to a comparison with measurements, a discussion more detailed of the expectations is necessary. To be more specific, it is evident in this Figure, that the temporal-contrast degradation due to the PSD dominates for the folded configuration of the discussed setup for both beam sizes (top left and top right). For the unfolded configuration with the sb size the PSD also dominates between 10 ps, where the intensity breaches the expected detection threshold of nine orders of magnitude. The effect of clipping becomes comparable in magnitude for times further from the peak than 10 ps. However, the absolute magnitude of both effects is far below any detection limit by then.

For the lb size in the unfolded design, the model expects the temporal-contrast degradation by the PSD to be visible only up to around 5 ps. Even though the calculations predict the steepness of the slope to decrease for times further from the peak, a measurement of this feature would require a larger dynamic range than the Sequoia (and the available energy) allows. What is to note here is, that no lower limit of the impact of the PSD can be seen in this configuration. This is due to the uncertainty imposed by the diffraction of the spatial clipping on the coupling mirrors prior to the stretcher. In the case that, due beam diffraction, the sharp feature in the beam profile becomes smoothed over the short propagation distance, spherical aberrations and spectral clipping start to dominate the rising edge.

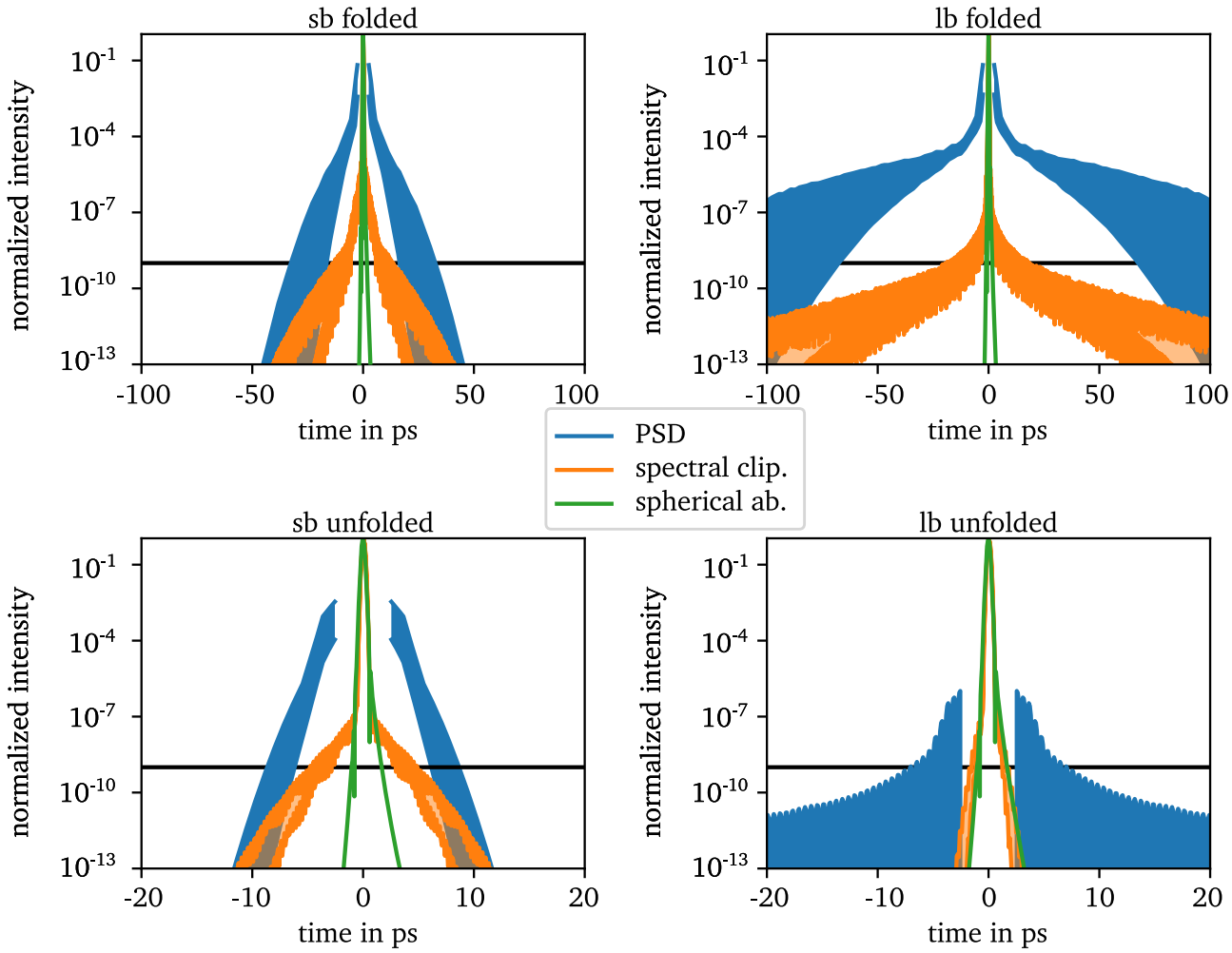

Figure 3.8.: Rising edge calculated for the folded and unfolded design with an lb size and an sb size of the PoP setup. The shaded areas indicate uncertainties based on the measurements. The blue curves are calculated using the PSD, the orange curves represent the effect of consecutive spectral clipping, and the green curves represent the impact of the spherical aberrations.

3.3. Comparing the Rising Edges Measured with the Proof-of-Principle Setup to the Predictions

Before comparing the calculated rising edges to measurements is possible it must be considered that Sequoia measures the cross-correlation

$$I_{\mathrm{cc}} = I \circledast I^2. \tag{3.10}$$

rather than the actual temporal intensity profile (for more information on cross-correlators see sec. 4.7). For comparability, the consolidated rising edges from sec. 3.2.5 are used to calculate the corresponding temporal profiles and then the cross-correlation signal of those temporal profiles, according to eq. 3.10.

For the first step the temporal profile is calculated according to eq. 2.20 by adding the predicted rising edges to the FTL. The rising edge is however not yet defined for times close to the peak, where the model does not predict the impact of the PSD. In order to avoid this, the assumption is made that the rising edge is monotonously increasing. Then, based on this the rising edge is estimated, by assuming that the rising edge is constant in the undefined region. For these temporal profiles the cross-correlation signal is calculated based on eq. 3.10.

The comparison to the measured temporal profiles, depicted in fig. 3.9, yields two main insights.

The first insight is, that the temporal profile of this setup is limited by the mirror in the Fourier plane, which is consistent with previous research based [99, 79, 102, 100] and to the implications of the analytical model, discussed in sec. 2.3.1.

The second insight is, that the rising edge caused by the PSD of a surface does indeed scale with the beam size on that surface.
In the folded design, where the beam is dominated by the optical element in the Fourier plane, the rising edge is worse for the larger beam size. This stands in agreement with the analytical model and predictions, since a larger beam size in the NF corresponds to a smaller spot in the focal plane. This means that less spatial averaging takes place in the Fourier plane for the large NF beam size and a worse (meaning a slower declining) rising edge can be expected and observed during the measurement.

When comparing the measurement results to the predicted rising edges, a good qualitative agreement can be found. The steepness of the rising edge, which scales with the beam size, fits well between prediction and measurement for the lb. The magnitude is overestimated in the predictions, as well as the slope for the sb. A reasonable explanation for the observed discrepancies in the magnitude is an overestimation of the PSD. The discrepancy in the slope for the sb can be caused by discrepancies between the actual beam sizes on the respective optical elements and the expected beam sizes. Since the folded stretcher is dominated by the mirror in the FF, the discrepancy in the slope corresponds to an overestimation of the NF beam size.
For the unfolded design, the qualitative agreement between prediction and simulation is that the smaller beam produces the worse rising edge. In terms of the slope, a disagreement can be observed for the smaller beam size, where the predictions overestimate the steepness of the slope. This substantiates the hypothesis that the sb size in the NF is overestimated.
For the lb size, the predictions show almost perfect agreement between theory and experiment over the observable dynamic range and in the temporal constrains. This is a considerable improvement of the temporal contrast in comparison to the sb, and especially to rising edge measured for the folded design. The remaining rising edge is well described by spatial clipping on the mirror prior to the stretcher. Thus, the expected temporal contrast can be further improved, when removing the spatial clipping prior to the stretcher.

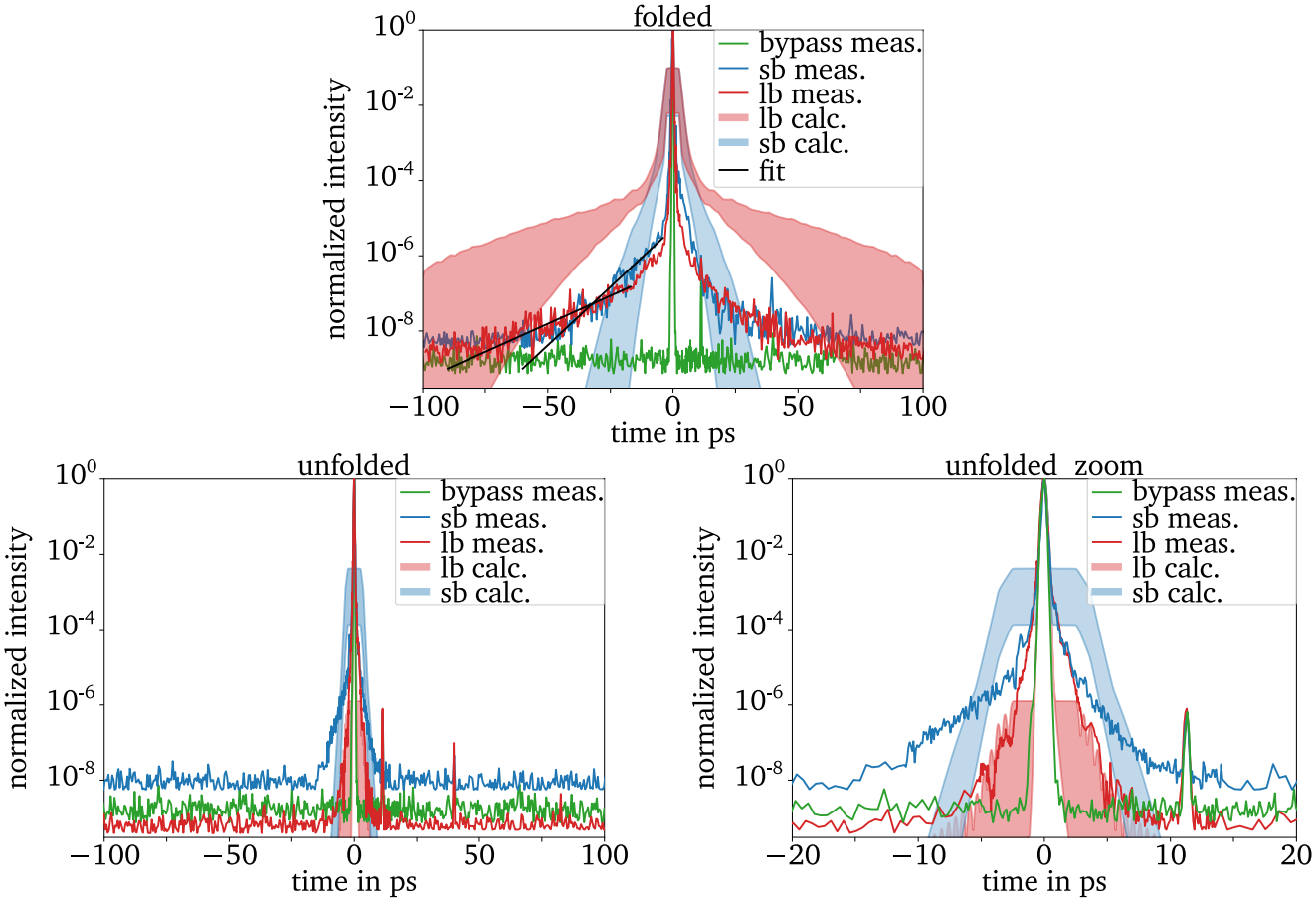

Figure 3.9.: Measured temporal profiles after the folded (top) or the unfolded stretcher (bottom left) with a zoom-in (bottom right), together with the corresponding predicted rising edges and their areas of uncertainty (shaded area). Additionally included is a fit to the rising edge for the folded design, to emphasize the dependency of the slope on the beam size. The noise level is given by the dynamic range of the cross-correlator, which differs between measurements.

3.4. Conclusion to the Origin of the Rising Edge

This chapter validated that the analytical model developed in cha. 2.1 is capable of predicting the formation of a rising edge. Using a zero-dispersion stretcher, that is quickly adaptable between a folded and unfolded configuration, enabled isolating the effect of the folding mirror in the Fourier plane of the stretcher and identifying it as the origin of the strongest observed rising, of all configuration. This validates that the folding mirror in the stretcher dominates the rising edge. The setup further featured an adjustable in-stretcher beam size. This was used in this chapter to validate the implication of the analytical model that the in-stretcher beam size conditions the slope of the rising edge.

This only validates the analytical model theory for the simple setup, where the stretcher does not stretch, no gratings contribute to the rising edge, the beam parameters are not influenced by the gain of amplification stages and no compressor is used. Thus, after the successful PoP, I adapted and rebuilt this setup for usage at a more complex system. This is the topic of the next chapter.

4. Improving the Temporal Contrast of the PHELIX laser system

After successfully validating that the in-stretcher beam size can be utilized in order to manipulate the steepens of rising edges and the successful demonstration that the folding mirror dominates the rising edge, the same stretcher system from the PoP is employed in the laser chain of a CPA laser system. The stretcher is build as an addition to the PHELIX laser system, since this thesis is part of a strive at PHELIX for an improved temporal contrast.

The next section, sec. 4.1, briefly introduces the laser facility, with a primary focus on the temporal contrast. A characterization of the beam parameters prior to the stretchers is provided in sec. 4.2. This enables the prediction of the rising edge introduced in the PHELIX stretchers, which are the topic of sec. 4.3.
Beyond this, other components of the laser chain are investigated in the context of their contribution to the rising edge at PHELIX. The first and second investigated parts are spatial apertures. First, spatial apertures close to the stretcher are investigated, in sec. 4.4, followed by an investigation of the impact of a serrated aperture in sec. 4.5. Subsequently, the impact of the compressors at PHELIX is estimated in sec. 4.6. The last investigated effect is the impact of the available cross-correlators, in sec. 4.7. Afterwards, combined expected temporal profiles are compared to measurements in sec. 4.8. The chapter ends in sec. 4.9, with a conclusion on the achieved rising edge contrast improvement at PHELIX.

4.1. Overview of the PHELIX Laser-Chain

The beam path of PHELIX, depicted in fig. 4.1, is seeded by the same oscillator model as the one employed for the OPA system in the PoP (Mira 900f, , Coherent). As mentioned in sec. 3.1, this oscillator emits laser pulses with approximately 1-2 nJ and an FTL pulse duration of 170 fs, at a repetition rate of 76 MHz. Since the PHELIX uses Nd:Glass MA the central wavelength of the oscillator is tuned to 1054 nm in order to fit the amplification profile. This is a small difference to the PoP, where the oscillator was operated at 1040 nm, which is closer to the center of the emission profile of the Ti:Sa crystal in the Mira and thus more stable and more energetic.

The next step in the laser chain is also comparable to the PoP, as again the beam is amplified using uOPA. The PHELIX system features a more sophisticated two-staged setup that amplifies a 10 Hz subset of the laser pulses. An upgrade to this design has been build, which provides around 1 mJ. This uOPA system is, similar to this thesis, part of the temporal-contrast improvements at PHELIX and is due for implementation in the laser chain at the next available time slot. The expected improvement of the pre-pulse contrast is from below $2.8 \cdot 10^{-8}$ to $6.2 \cdot 10^{-11}$, while keeping the ASE contrast at $4.9 \cdot 10^{-13}$ [111].

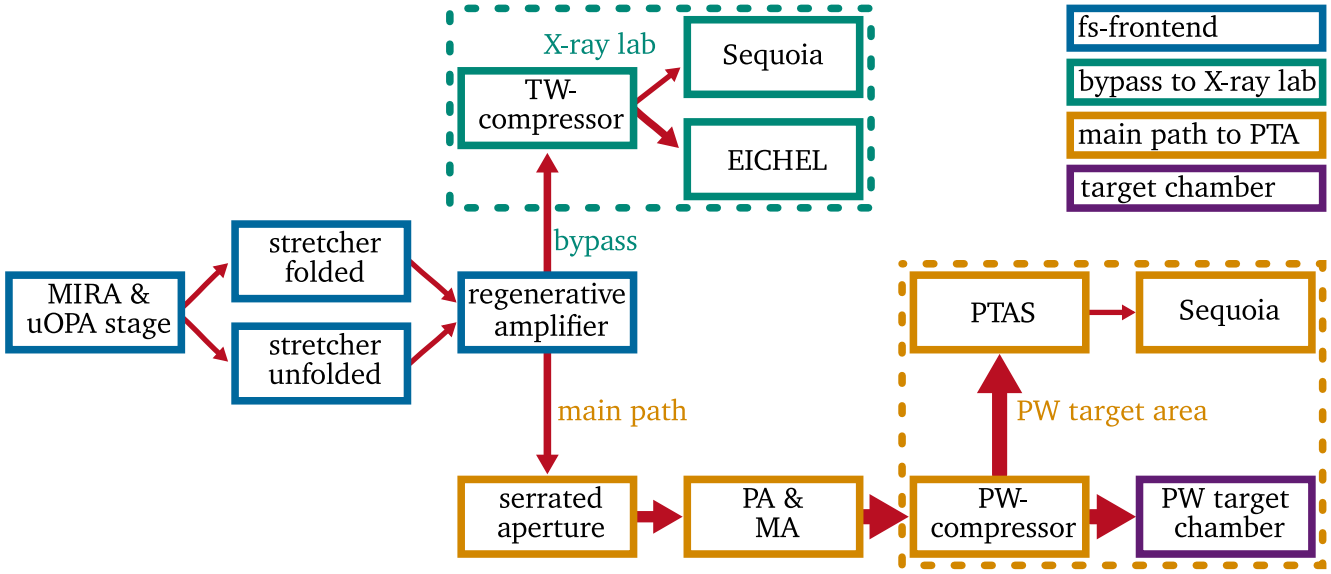

Figure 4.1.: Schematic setup of the PHELIX laser chain. Components of the fs-frontend are indicated in blue. The bypass beam path, leading to the measurement point in the X-ray lab is indicated in teal and the main beam path of the PHELIX laser chain is indicated in orange, leading to the measurement point after Petawatt Target Area Sensor (PTAS) in the Petawatt Target Area (PTA). The PW target chamber, where experiments at PHELIX are set up, is indicated in purple. The thickness of the arrows indicates the magnification between the components (not to scale).

After the uOPA stage, the pulse is stretched to approximately 2 ns, using a folded Banks stretcher design [59]. Since this stretcher is used substitutionally to the stretcher design from the PoP, the Banks stretcher design is from now on referred to as the "folded" stretcher and to the PoP stretcher as the "unfolded" stretcher, since this is the configuration in which it is employed during the experimental campaign.

Succeeding the stretching, the laser pulse is amplified in the Ti:Sa crystal of a regenerative amplifier in a ring configuration. After passing through the ring regenerative amplifier, a Pockels cell is used to eject the pulse, which by then has an energy of around 18 mJ. The measurements and calculations discussed in app. A.8 suggest that this component does not limit the temporal contrast, in the frame of this work.

In the main configuration of PHELIX the beam is then guided through a serrated aperture and a spatial frequency filter, in order to achieve a uniform amplification in the subsequent stages.

The beam is then amplified in the Pre-Amplifier (PA) stage with a gain of around 400, in Nd:Glass rods of varying size. Even though the beam is temporally stretched, within these amplification stages it is necessary to reduce the fluence, which is done by magnifying the beam over four telescopes between the amplification stages from a size of 7 mm at PA input to approximately 60 mm at the end of the PA stage. The beam size after the PA can be adjusted by switching between several available serrated apertures at the start of the PA.

After this stage, the beam is injected into a double-pass of the MA stage. This consists of a magnification to an aperture of around 240 mm and passing through five flash lamp pumped Nd:Glass slabs. The pumping of those slabs deposits a considerable amount of energy not usable for the amplification. Therefore, the Glass heats up, which leads to a deformation of the wavefront. While considerable effort is being made in

the frame of the THRILL project to employ a water cooling system [112, 113], the amplifiers are currently still air cooled, which limits the repetition rate to around one shot every 90 minutes. In the measurements discussed in this thesis, the rods are not actively pumped; instead, they are passively traversed, similar to the rods in the PA.

After main amplification the beam is recompressed in the PW-compressor. This grating compressor, with two gratings with a clear aperture of 807 mm, leaves the beam temporally compressed but spatially chirped. To provide highest intensities the PHELIX facility is currently testing an adaptive optic loop with a deformable mirror prior after this compressor which is capable of flattening the wavefront and enabling highest intensities in focus [114].

In the last step, the beam is focused by an off-axis parabola onto a target in the PW target chamber. With best effort the facility has reported laser intensities of $1.4 \cdot 10^{21}\,\mathrm{Wcm}^{-2}$ on target [115].

There are several places in the laser chain that allow a measurement of the temporal contrast.
The first is in the PHELIX target chamber. Measurements conducted at this position are closest to the temporal contrast during peak-intensity experiments. However, the measurement at this position is impractical, since the operation as a user facility does currently now allow for a permanent setup at this point.
The next best measurement point in terms of comparability to the temporal contrast during peak-intensity experiments is after the PTAS. This setup is designed to utilize leakage light, demagnify and attenuate it, before characterizing its spatial characteristics [114]. Using this as a measurement point necessitates the removal of the leakage mirror, in order to utilize the full available energy for the temporal contrast measurements. In this configuration laser energies of 1.5 mJ after PTAS are measured, which is sufficient for temporal characterization.
Since temporal-contrast measurements at PTAS require substantial workload, a third measurement point is frequently used at PHELIX. In this configuration the beam is picked of directly after the regenerative amplifier, and guided to another experimental area, with a separate compressor. This measurement location is referred to as the X-ray lab, with a TW-compressor. The assumption here is that the contrast at this measurement location is equivalent to measurement points after the PW-compressor. An assumption that is only valid when the temporal contrast is limited by something prior to the bypass, e.g. the pulse stretcher.

In the following sections, the individual components are discussed in more detail with an emphasis on their impact on the rising edge contrast. The first relevant components in the laser chain are the stretchers, since previous measurements have shown that pulses generated by uOPA do not feature a rising edge (compare fig. 3.9).
Estimating the rising edge caused by the stretcher requires a characterization of the beam after the uOPA, which is the topic of the next section

4.2. Characterization of the Laser Parameters at the fs-frontend

The relevant parameters for the rising ede formation in the stretchers are the spectrum, which is presented first, and the spatial profile. The ratio of the Mira background and the uOPA is more than a factor of 10 better at PHELIX compared to the PoP, due to a stronger amplification of the PHELIX uOPA. This allows for a more precise characterization of the system.

The measured spectrum after the uOPA stage can be seen in fig. 4.2, where the Gaussian fit to the uOPA signal gives a width of 9.2 nm, which is 50% larger than the used bandwidth in the the PoP.

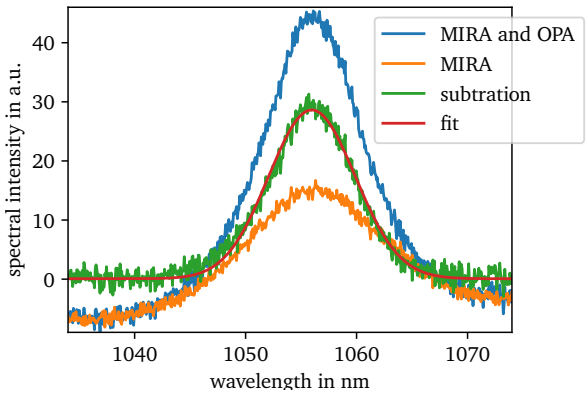

Figure 4.2.: Measurement of the uOPA spectrum as the difference between the signal with uOPA and Mira and the pure Mira signal.

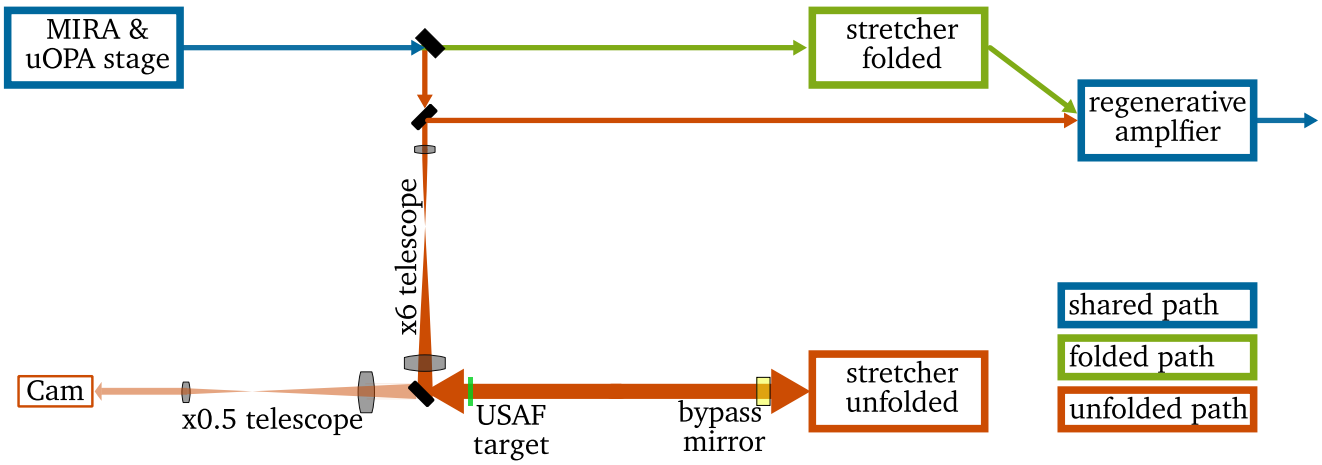

Figure 4.3.: Beam path from the uOPA front end through the folded and unfolded stretcher. Additionally included are the magnification telescope prior to the unfolded stretcher, the demagnification telescope for the reference stage, as well as an optional USAF target and bypass mirror, for the spatial characterization of the input beam in the reference stage.

After the uOPA, two different beam paths can be selected, as shown in fig. 4.3. The first path traverses the folded stretcher and, after a double-pass, the regenerative amplification stage. The second traverses the same magnifying telescope as during the PoP, with a magnification of six. Again, this telescope can be removed, allowing an lb and sb configuration of the unfolded stretcher.

The spatial characterization for the beam in both stretchers is done at the reference stage which operates on the leakage light from a turning mirror prior to the unfolded stretcher. In this stage, the beam is first demagnified by a factor of two, in order for the beam in all configurations to fit on the chip of a camera and an SHS. For the measurement of the beam size a zero-degree mirror was positioned on a quick-release mount close to the input of the unfolded stretcher, directing the beam back through the turning mirror onto the reference stage. For clarity a schematic of the beam path is included in fig. 4.3.

Again, the Mira signal is subtracted from the total signal which leaves the uOPA signal. After subtracting the Mira beam profile from the signal, a Gaussian profile is fit to the data, providing a beam size for the lb and the sb configuration at the camera. This beam size is calibrated to the position of the stretcher input

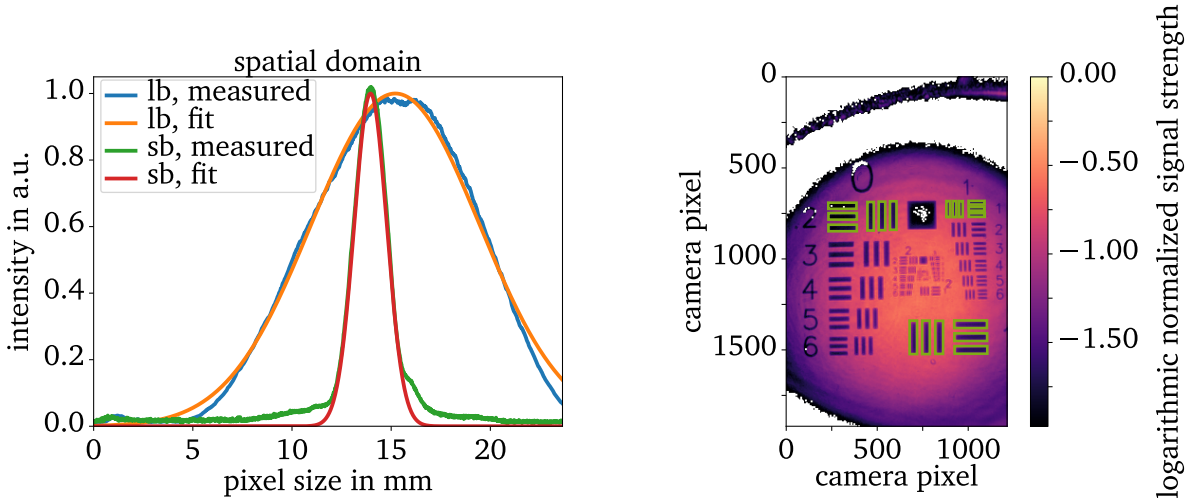

Figure 4.4.: Left: Measurement of the spatial profile of the uOPA signal for the sb and the lb, as well as a Gaussian fit. Right: Image of the USAF target, with green squares indicating the areas selected for calibration of the pixel size.

using the magnification of the reference telescope. For improved precision, a USAF target is imaged onto the chip of the camera, and the effective pixel size is calibrated using the well-known size of its features. With this technique, the beam sizes of the uOPA output after passing through either of the two telescopes are

$$\sigma_{\mathrm{sb}} = 1.16\,\mathrm{mm}, \qquad \sigma_{\mathrm{lb}} = 6\,\mathrm{mm}. \tag{4.1}$$

The measurement with the corresponding Gaussian fits can be seen in fig. 4.4, together with the calibration of the USAF-target.
The chosen positioning of the zero-degree mirror results in a distance between USAF target and zero-degree mirror that equals half the distance between USAF target and the first spherical mirror in the unfolded stretcher. This ensures that the beam size on the latter equals that on the USAF target. The beam size in the folded stretcher is expected to be the same as the sb beam size in the unfolded stretcher, to a good approximation, due to the comparable length of free propagation.

With this, the parameters of the beam that are relevant to the rising edge formation in the stretchers are characterized and the beam is guided into either of two stretchers.

4.3. The PHELIX Pulse Stretchers: Addition of an Unfolded Design

In the current experiment mode for users at PHELIX, the laser pulse is guided through the folded Banks stretcher at PHELIX [116]. In the frame of this thesis, I have added an additional, unfolded stretcher to the front-end of PHELIX which can be used substitutionally to the folded one. The switch between both is as simple as putting in two quick-release mounts and switching between two timing settings for pulse-pickers in the laser chain. Both stretchers and their impact on the rising edge are discussed in the following, starting with the folded design.

4.3.1. Established Stretcher at PHELIX: The Folded Design

Upon entering the stretcher which can be seen in fig. 4.5, the beam is incident on a gold grating with a line density of 1740 l/mm with an angle of incidence of 72.5°. This grating is positioned 1 m from the focal spot of a spherical mirror with a 5.6 m radius of curvature and a free aperture of 304.8 mm. After the grating, the beam is reflected from the spherical mirror, with an offset from the center of 4.5 cm, for separation from the incident beam. The beam then reflects from a folding mirror in the intermediary field (1.48 m from the sphere), a folding mirror in the Fourier plane (2.8m from the sphere), and again from the first folding mirror in the intermediary field (1.48 m from the sphere). Then, the beam is reflected again from the same spherical mirror and diffracted by the same grating. In a double-pass configuration with a rooftop mirror for vertical displacement at the end, the beam propagates in the inverted direction through the stretcher.
With this setup, the effective grating distance is 4 m. After traveling through this stretcher the beam has roughly a pulse duration of 2 ns.
While the optical surface quality of the components in this stretcher is specified in terms of peak-to-valley, no PSD measurements are currently available. Moreover, the measurements are not feasible, since this would effectively shut down experiments at PHELIX for the duration of the measurement. Thus, the calculation of the expected rising edge relies on estimates of the PSD.

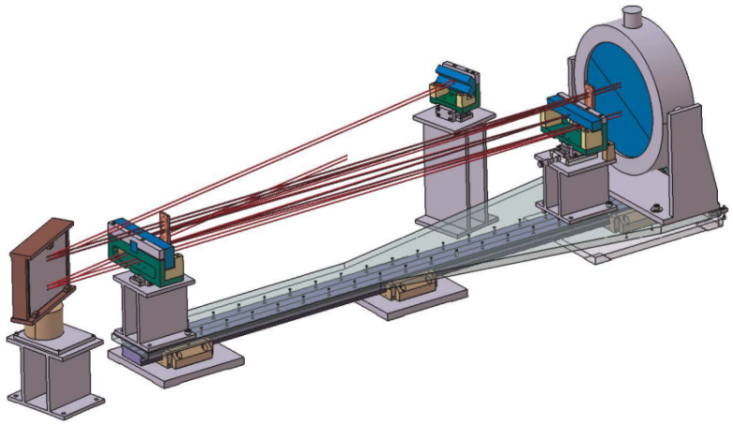

Figure 4.5.: Schematic of the folded stretcher setup at PHELIX [116].

4.3.2. The Temporal-Contrast-Optimized, Unfolded Design at PHELIX

Substitutionally to the folded stretcher, the beam can be guided through a modified version of the unfolded stretcher design from the PoP setup, which is shown in fig. 4.6.

The gratings are moved closer to the spherical mirrors of the telescope, in order to match the effective grating distance of 4 m after a double-pass, to the folded design and the compressors.
After the first grating, the beam is reflected from the first spherical mirror, which is tilted backward in order to provide an angle between the reflected beam and the table plane of 4.6°. This is necessary since the radius of curvature of the spherical mirrors is relatively small with 3.048 m. Since the grating distance requires 1 m per pass and grating, this leaves little space between the grating and the sphere. To be precise, the chosen distances with respect to the spheres are $p_{g1} = 34\,\mathrm{cm}$ and $p_{g2} = 62\,\mathrm{cm}$.

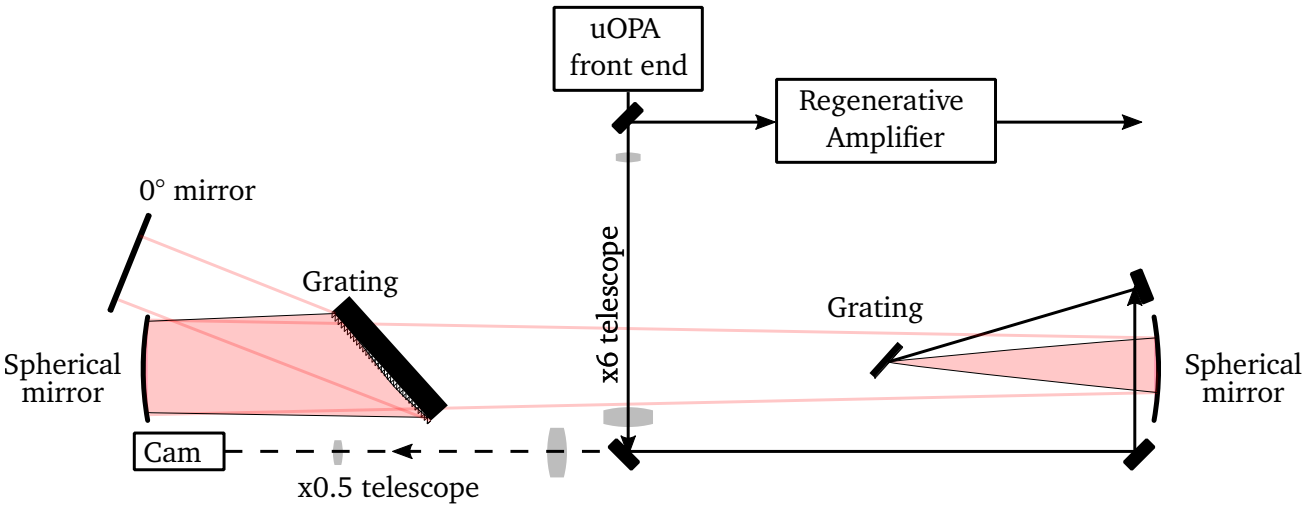

Figure 4.6.: Schematic of the unfolded stretcher setup at PHELIX (top view).

Due to spatial restrictions in the geometry, both gratings have been shifted in the direction of the first spherical mirror, which reduces the necessary elevation of the large grating above the table. This does not change the sum of the grating distances and thus the introduced dispersion, but it changes the beam sizes on several surfaces and is thus important to keep in mind, as this alters the rising edge.
After passing above the first grating and below the second grating, the beam is reflected from the second spherical mirror, which results in a horizontal propagation plane again.
The beam is then diffracted from the second grating, which features a clear aperture of 220 mm x 165 mm. In contrary to the PoP-setup, the beam is spectrally dispersed on the subsequent 0°-mirror, for the double-pass. Here, the well-characterized folding mirror is employed, which was previously used in the Fourier plane.

For the separation of the in- and outgoing beam, two setups were tested. One utilized a tilt of the double-pass mirror, and the other a Faraday-rotator and a polarizer. Both ways may, according to the considerations in the PoP, have a minor impact on the temporal profile, either due to spatial clipping on the small rotator window or due to changes in the spectral clipping on the stretcher telescope. During the experimental campaign, tilt and Faraday-rotator were tested and the temporal profiles were compared, showing no noticeable difference.
The fact that there was no noticeable difference in the rising edge for the Faraday-rotator and the tilt already in itself indicates that the system is not limited by spectral clipping in the unfolded stretcher or by free apertures that are bigger than the 5 mm of the Faraday-rotator. The in-depth analysis of this effect is presented in the next subsection, which discusses the expected rising edges for both stretchers.

4.3.3. Estimation of the Rising Edges from the Stretcher Designs at PHELIX

As before, this section discusses the impact of aberrations, spectral clipping, and the PSD and compares their magnitude in order to identify the dominating effect and predict the rising edge. The first investigated effect is aberrations, based on ray-tracing of the setups.

Investigation of the Spherical Aberrations Caused by the PHELIX Stretchers using Ray-Tracing

In the context of ray-tracing both stretcher designs are similar. The various folding mirrors in the folded design do not contribute to the aberrations and can thus be disregarded in the calculation. Since the grating constants are the same, the angle of incidence of both systems must also be the same in order to achieve the same spectral phases. During the alignment of the unfolded stretcher great attention was payed to that, which results in an estimated angle match uncertainty of 5'.

Hence, the main difference between both systems in the context of ray-tracing is the radius of curvature of the spherical mirror. Another second-order difference is the different offset from the center of the sphere. Due to the larger radius of curvature in the folded design, only an offset from the center of 4.5 cm is necessary for the separation from the input beam, while the smaller radius of curvature in the unfolded design requires an offset of 7 cm.

The resulting spectral phases of the ray-tracing is depicted in fig 4.7 for both stretchers, together with the temporal profiles. The used spectrum is the Gaussian fit calculated from the measurements in sec. 4.2.

The simulations predict that the unfolded design produces a cleaner temporal contrast than the folded design. This indicates that a smaller radius of curvature is desirable in a stretcher design, when limited by the spherical aberrations. It further indicates that the dependency on the radius of curvature has a stronger impact than the small offset necessary to separate the beam. The effect itself can be explained by the strong increase of spherical aberrations, which scales with the distance from the central wavelength [47].

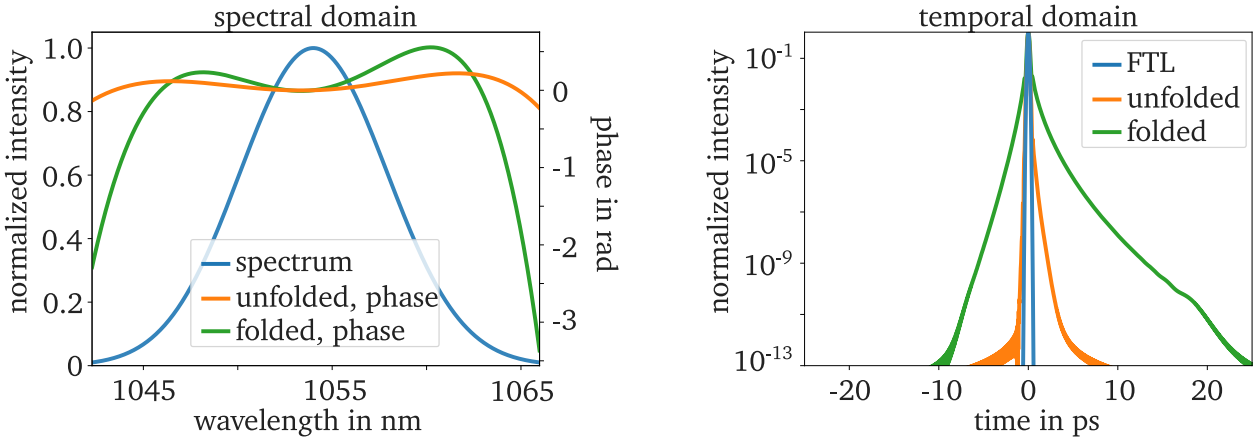

Figure 4.7.: Influence of the additional spectral phase that is introduced due to the spherical aberrations in the folded and unfolded stretcher setup at PHELIX, calculated using ray-tracing. On the left-hand side, the spectrum and the spectral phase can be seen and on the right-hand side, the corresponding temporal profile is depicted.

Investigation of the Impact of Spectral Clipping in the PHELIX Stretchers on the Temporal Contrast

In order to estimate the rising edge caused by spectral clipping, the calculations for the PHELIX stretchers follow the same procedure as for the PoP in sec. 3.2.2. The acquisition of the required parameters is explained in app. A.9 and the parameters themselves are summarized in tab. A.1.

The considered spectral shape of the pulse is a Gaussian with a bandwidth of 9.2 nm, as measured in sec. 4.2. This provides the means to calculate the expected rising edge caused by spectral clipping for each surface. They are summarized in fig. 4.8, with the clipping in the folded stretcher on the bottom and in the unfolded stretcher on the top, with the sb size on the top left and the lb size on the top right.

In the unfolded design, the expected impact of spectral clipping is dominated by the effect of the second spherical mirror.
For the folded design the rising edge is dominated by the folding mirror, where the beam size is smallest.

The temporal-contrast degradations found for the unfolded design with the sb size and the folded design are already considerable. But it is not clear yet if this dominates the rising edge at PHELIX before comparing it to the impact of the PSD, which is calculated in the next section.

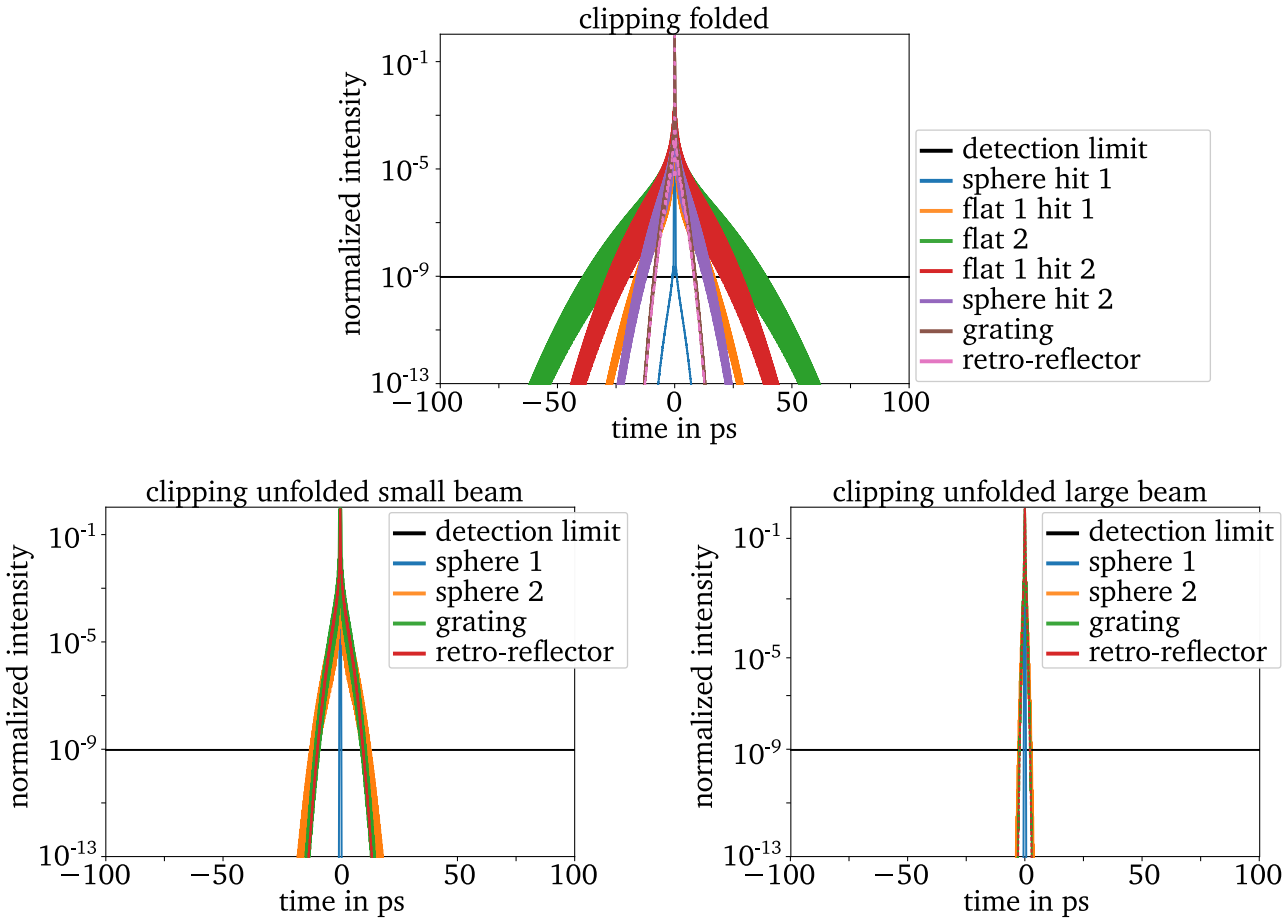

Figure 4.8.: Expected impact of spectral clipping in the unfolded (bottom) and folded (top) stretcher design at PHELIX. The impact of spectral clipping in the unfolded design is shown for the sb size (left) and the lb size (right). Each line in the respective plots corresponds to one interaction with a surface, as denoted in the legend, where the different interactions are sorted according to the successive order of the optical elements. Additionally included is the detection limit of the Sequoia device that was used during the PoP, as a reminder of the resolvable region. The second pass through the system is not displayed since it produces equivalent temporal profiles.

Predicting the rising edge caused by the PSD and the conditioning of this rising edge by the spatial beam profile on each surface is done analogously to the prediction during the PoP (compare sec. 3.2.4). For the unfolded design the calculation is almost equivalent, with the only differences being the different dispersion coefficients, slightly different beam sizes and the impact of the second grating and zero-degree mirror.

Unfortunately, no measurement of the PSD of the grating surface is available, as previously stated. The same statement holds for the folded design, where the PSD of the spherical mirror, the two folding mirrors, the roof-top mirror and the grating are required. The used assumptions in order to approximate the PSD of these surfaces are discussed in app. A.10. This results in the flat and spherical mirrors featuring PSDs of comparable orders of magnitude. In contrast, the PSDs for the gratings are two to three orders of magnitude larger than those of the mirrors.

The corresponding rising edges causes by the PSD are calculated and displayed in fig. 4.9.
For the unfolded design (bottom), again a dependency on the in-stretcher beam size is expected. The expected contribution from the spherical mirror is consistent with the expectations during the PoP, for the sb (left) and the lb (right). Both feature fast declining rising edges, which becomes shallower for the lb further from the center, due to spatial clipping. The same behavior can be observed for the grating, but at a larger magnitude, due to the larger PSD.

The considered free apertures are again the 45° turning mirror prior to the stretcher, with a free aperture of 50 mm and 25 mm, for the lb and the sb, respectively. Additionally included is the expected rising edge of the grating for a larger free aperture (80mm mirror), in order to emphasize that with larger turning mirrors this design should be capable of producing even cleaner temporal profiles.
For the sb the rising edge remains steep, with the smallest free aperture of 25 mm, not limiting the profile. The smallest ratio between free aperture and FWHM is a factor of three larger than for the lb.

For the folded design (top), the smallest considered aperture is also 25 mm. In this context, it is to note that the intermediate folding mirror poses a special case in this consideration that requires that the beam profile conditioned by the aperture on this surface is calculated using Fresnel diffraction (compare sec. 2.3.3).
Nonetheless, there is no visible impact of spatial clipping in the rising edge caused by the PSD. This is not surprising, considering the comparable beam size to sb in the unfolded stretcher.
However, the stretcher is expected to introduce a large temporal-contrast degradation, due to the folding mirrors. In this configuration, the dispersion coefficient during the second reflection from the intermediary folding mirror is slightly larger than during the reflection from the actual folding mirror. This causes the rising edge introduced in the intermediary field to be stronger than the one introduced in the actual Fourier-plane. This is within the area of uncertainty of the beam size and beam profile, since with an increasing NF beam size the FF beam size decreases. This in turn results in an increase of the the rising edge caused by this surface. As a result, the maximum predicted rising edge ends up approximately the same.

For the following corroboration of the effects two one temporal profile caused by each stretcher eq. 2.20 is used to accumulate the effect of the PSD.

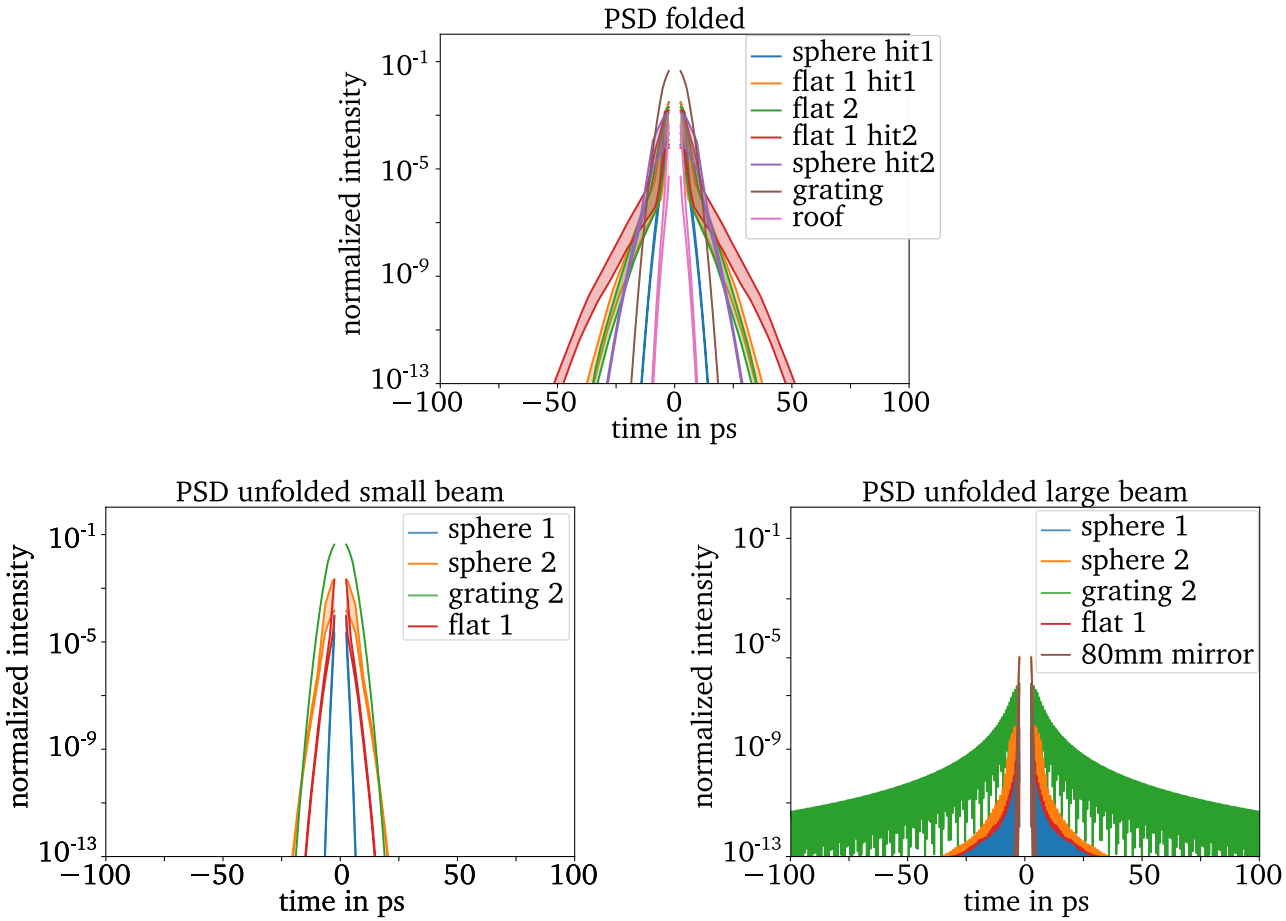

Figure 4.9.: Expected impact of the PSD in the unfolded (bottom) and folded (top) stretcher design at PHELIX. The effect of the PSD in the unfolded design is shown for the sb (bottom, left) and the lb (bottom, right). Each line in the respective plots corresponds to one interaction with a surface, as denoted in the legend, where the different interactions are sorted according to the successive order of interaction. The second pass through the system is not displayed since it produces equivalent temporal profiles. Additionally included for the lb in the folded setup, is the expected rising edge with an increased size of the coupling mirror from 50 mm to 80 mm.

Estimation of the Rising Edges Introduced by the PHELIX Stretchers

Now, after calculating the temporal-contrast degradation caused by spherical aberrations, spectral clipping, and the PSD of the surfaces they can be combined into a single temporal profile that comprises all these effects and may be expected to result from the propagation through the PHELIX stretchers. The combination of these effects is again done with assumptions.

In a first step, the complete impact of each setup is calculated using, eq. 2.20. Equivalent to that, the complete effect of spectral clipping is calculated based on, eq. 2.28.

For the combination of spectral clipping and the PSD, the comparable magnitude of both effects is a problem since it is, unclear how they interact, as discussed in app. A.4. It is possible that they interact positively, meaning that the spectral clipping removes wavelengths that experience an especially large shift from

the peak intensity and thus contribute strongly to the rising edge. But the opposite is also possible, that the spectral clipping removes wavelengths that are mainly in the temporal peak, thereby reducing the energy in the peak of the temporal profile and reducing the temporal contrast. Due to the lack of a better approximation, the presented analysis for now neglects the interaction between both and assumes they overlap.

Under this assumption, the combination of the three rising edges caused by spectral clipping, spherical aberrations, and the summed PSD is achieved by overlaying the three profiles and calculating the maximum value at each position as the value of the combined rising edge. Equivalent to the calculation of the complete expected rising edge of the PoP setup in sec. 3.3, the effect of the PSD is not defined at times close to the peak intensity. I thus again use the assumption that the rising edge caused by the PSD is constant in the undefined region.

Comparing the different effects with each other, as depicted in fig. 4.10, provides the insight that for the folded design the effect of spectral clipping and the PSD differ from each other only marginally for times further from the peak intensity than 10 ps. Both effects are dominated by the folding mirrors. Towards the peak intensity the effect of the PSD dominates, but this is the region, where the estimation of the PSD becomes less reliable.

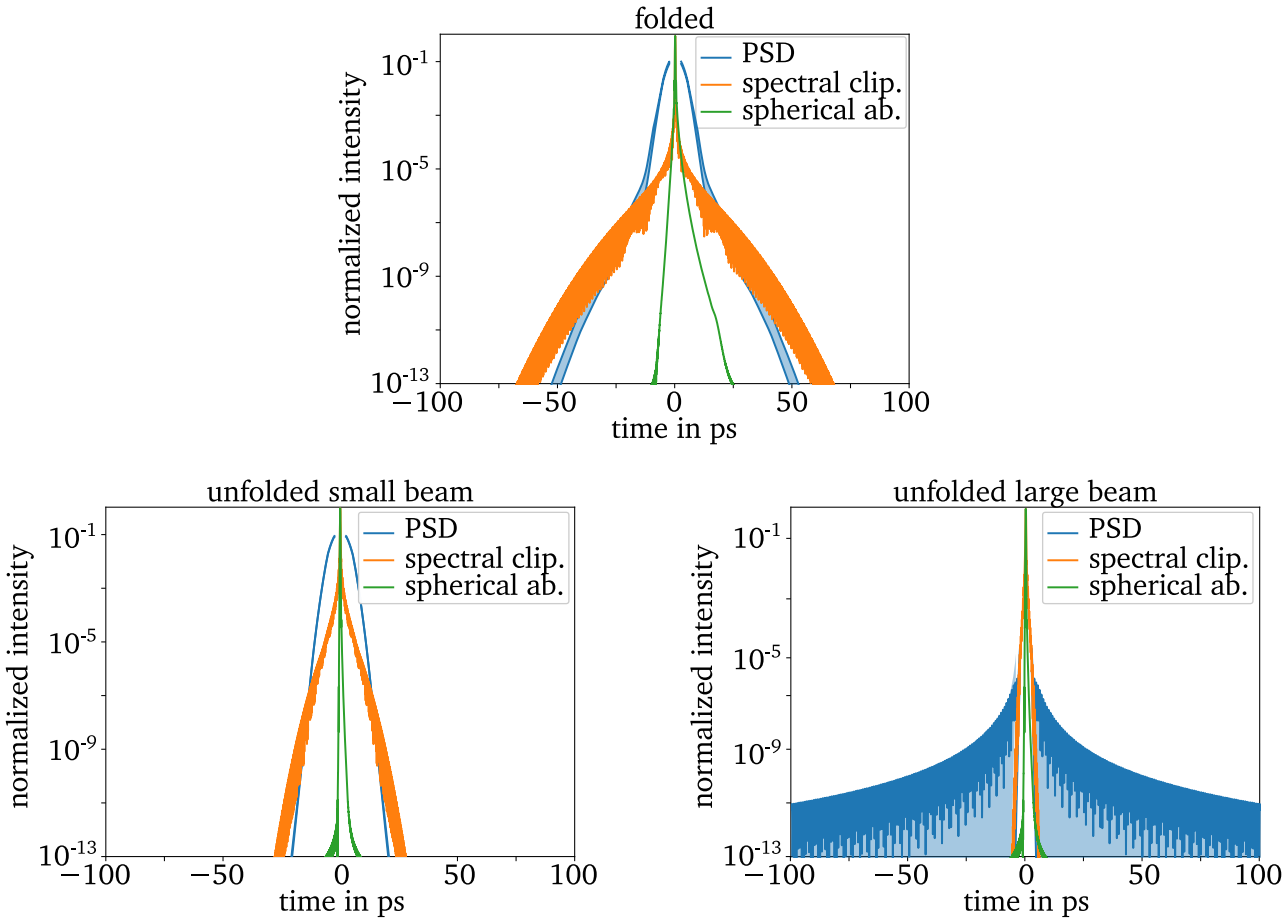

Figure 4.10.: Summary of the expected rising edges for the folded (top) and unfolded (bottom) stretcher setup at PHELIX, for the sb size configuration (left) and the lb size configuration (right). For each setup, the rising edge introduced to the laser by the PSD (blue), spectral clipping (orange), and spherical aberrations (green) are depicted.

A similar behavior is present for the unfolded design (sb), where the effect of the PSD is slightly stronger than spectral clipping close to the peak intensity, but at larger times this switches and spectral clipping dominates. For the lb in the unfolded design, the effect of the PSD dominates, due to the spatial clipping on the turning mirror prior to the stretcher.

Comparing the different setups with each other shows a strong dependency on the in-stretcher beam size for the unfolded design. While the expected temporal profile is better close to the peak intensity for the lb, than for the sb, this changes due to the concave shape of the rising edge in the case of the lb. Hence, at around 25 ps and nine orders of magnitude below the peak, the rising edge caused by the lb is expected to be worse than for the sb. Additionally, an improved temporal contrast over the first 13 orders of dynamic range is expected, when using the unfolded design with the sb size in comparison with the folded stretcher. Besides the scientific insights gained from this, this already promises an improvement for experimental campaigns at PHELIX that heavily rely on the temporal contrast, once this stretcher setup is established for users.

Ideally, these estimations should now be compared with measurements of the temporal profile after the

stretcher. However, it would be impossible to discern the deteriorating effects caused by the stretcher from the undisturbed laser pulse since the pulse is temporally stretched. As discussed during the introduction of the PHELIX laser chain (compare sec. 4.1) the stretchers are followed by a regenerative-amplification stage and either the TW-compressor or by a serrated aperture, passive PA stage, a passive MA stage, the PW-compressor and several telescopes for demagnification. The measurement of the temporal contrast is only possible after either of these beam paths, where the pulse is recompressed. The fact that some of these components might further degrade the temporal contrast, makes it difficult to discern the impact of the stretcher, especially for the improved contrast provided with the unfolded stretcher, where it is not clear which component limits the contrast. Thus, considerable effort is made in the following sections to estimate the impacts of the subsequent components, in order to identify the dominating factor and adequately predict the temporal profile at the measurement points.

Before discussing the impact of these stages in the following sections the following analysis quickly jumps ahead and compares the temporal contrast curves calculated in this section with measurements made after the TW-compressor, which is the current default measurement point for the temporal contrast at PHELIX. These measurements, which can be seen in fig. 4.11, were executed with an in-house built cross-correlator called Enhanced Intensity Cross-correlator for High Energy Lasers (EICHEL) [92]. The measurements with the folded stretcher (red) show a good agreement with the predictions, considering the strong sensitivity of the beam size and the accuracy with which these beam sizes were determined.

For the unfolded design, however, there are several features that require a discussion. The first is, that the temporal contrast is in the first 40 ps considerably worse in the measurements than predicted. This indicates an additional, not considered source of temporal-contrast degradation, that the following sections investigate.

The second insight is, that there is no measurable dependency on the in-stretcher beam size found in the measured temporal profiles for the unfolded stretcher. This further supports that there is an unknown source of temporal-contrast degradation outside of the stretcher since cha. 3 validated that the beam size conditions the rising edge in the stretcher. In other words, this shows that the PHELIX contrast with the unfolded stretcher is not directly limited by the stretcher.

The third and last feature is, that after 50 ps the rising edge for all three curves shows a good agreement with the effect of the spatial clipping in the lb, where the ratio of beam size to the free aperture is 3.5 (compare sec 4.3.3). This indicates that at some point in the laser chain, that all beam paths cross, and where all beams have the same beam size, a spatial clipping process occurs with a ratio of beam size to free aperture of around 3.5. An alternative explanation for this agreement between the measured curves is a previously unconsidered effect that introduces a similar rising edge.

Since we see a change of slope in the measurements between 40-50 ps for the unfolded stretcher it is likely that the rising edge is limited by two different effects. The first effect dominates between the peak and 40 ps with a so far unknown source, likely outside of the stretcher. In the following, this is referred to as the "fast feature", due to the steeper slope than the second "slow feature", which dominates at times further from the peak than 40 ps. The following sections, discuss the remaining components in the laser chain in order to identify the source of these features.

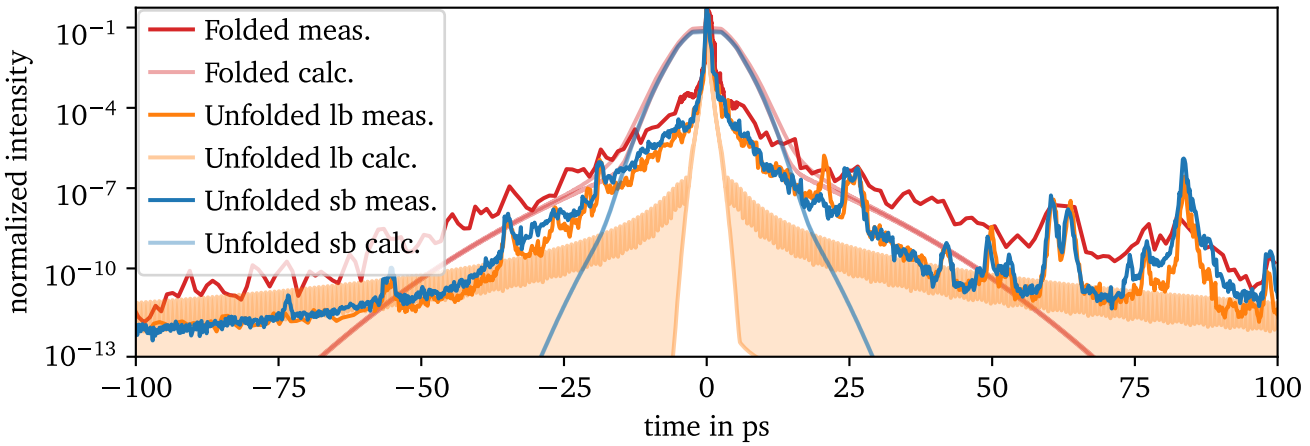

Figure 4.11.: Comparison between the measured temporal profiles in the X-ray lab with the EICHEL and the expected introduced rising edges by the stretchers.

4.4. Impact of Spatial Beam Modulations on the Temporal Contrast

As our model predicts that the temporal contrast is conditioned by the beam profile, via the Fourier transform of the beam on the considered optical element, it might be interesting to evaluate the effect of the beam shape on the temporal contrast. The most favorable beam profile for contrast purposes follows a Gaussian spatial distribution. While this might be hard to maintain experimentally, it is interesting to test our theory by altering the beam profile to manipulate the temporal contrast.

4.4.1. Impact of Spatial Clipping by a Slit on the Temporal Contrast

One easy way to alter the beam shape is by using a slit of variable width located in the beam path. The previous considerations employed similar spatial filters for the coupling mirrors into the stretcher as a top-hat function with a width given by the mirror size (compare sec. 3.2.4). This conditioned the temporal contrast dramatically, by changing the spatial profile on the stretcher optics (compare sec. 2.3.2).

The previous section showcased that this has an impact on the rising edge calculated for the lb in the unfolded stretcher. Since this effect depends on the beam size in comparison to the size of the spatial top-hat, the model predicts that a rising edge of the calculated magnitude is introduced for a ratio between the spatial filter size and the FWHM of the beam of $50\,\mathrm{mm}/(\sqrt{2}\cdot 10\,\mathrm{mm}) = 3.5$. The factor $\sqrt{2}$ is specific for turning mirrors that are positioned under 45° to the beam.

This allows the assumption that a spatial filter introduces a similar rising edge when employed on a beam with a different size than lb, as long as the ratio between the top-hat and the Gaussian beam profile is comparable. Using this yields the required size of the spatial top-hat filter for the sb of $3.5\cdot 1.9\,\mathrm{mm} = 6.6\,\mathrm{mm}$, which analytically results in a similar rising edge.

In fig. 4.12 (right) corresponding rising edges are depicted, based on spectral-phase effects according to eq. 2.18. The parameters for the calculation are chosen according to the second spherical mirror in the unfolded stretcher with the sb. Additionally included is the same calculation, with a spatial aperture of 1.5 mm, which produces a rising edge with a larger magnitude, but comparable slope.

For the experimental validation of this, I have implemented an 1.5 mm slit prior to the stretcher, oriented in such a way that it employs a top-hat in the dispersion plane of the gratings.

In fig. 4.12 (left) three corresponding temporal-contrast measurements are depicted. The first measurement, without the slit, gives a reference. For the second measurement, I placed the slit in the image plane of the second spherical mirror. This ensures that the beam profile on the slit is as close to the beam profile on the sphere, as technically feasible. In the last measurement, the slit is placed 1.5 m prior to the image plane. According to eq. 2.45, where $\Delta z = 1.5\,\mathrm{m}$, this does not condition the formation of the rising edge. However, this theory does not consider that the beam is smaller after the slit than before and will thus diverge faster. Accordingly, the beam size in the image plane is larger than the model predicts. As a result, the rising edge is expected at a lower magnitude for the second position.

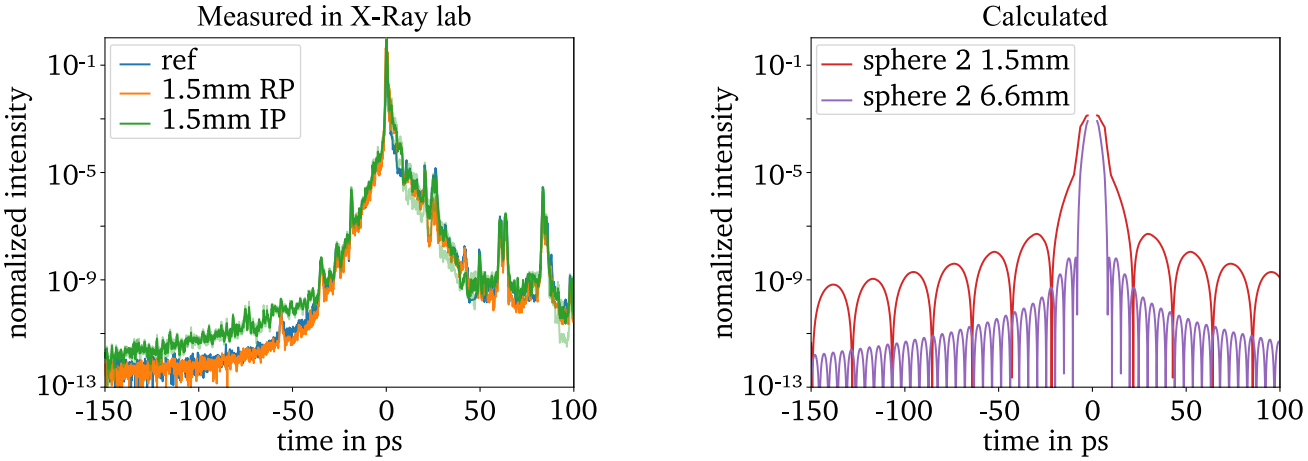

Figure 4.12.: Measurements (left) of the temporal contrast after the unfolded stretcher, with a 1.5 mm slit in the image plane (IP) of the second spherical mirror, in a random plane prior to the stretcher, and a reference measurement without a slit. Additionally included are calculations (right) of the expected rising edge according to eq. 2.18 for slits of 1.5 mm size, which corresponds to the measurements and of 6.6 mm size which corresponds to the theoretical necessary size to explain the measured rising edge for the sb. All measurements were executed after the TW-Compressor with the EICHEL.

The first thing to note, when comparing the measurements with each other, is that the measurements show a clear temporal-contrast degradation in the temporal range from -150ps to -50ps when employing the slit. This is a clear validation of the theory that top-hat apertures condition the rising edge formation.

However, the discrepancy can only be observed for the placement of the slit in the image plane. For the random plane, any difference to the reference measurement is overshadowed by the remaining temporal features in the reference. This is consistent with the expected impact of beam divergence.

Further insight can be gained by comparing the predicted rising edges to the measurements. Employing the calculated slit size of 6.6 mm in the analytical model, provides a good agreement to the slow feature observed in the reference, as expected. For the 1.5 mm slit, however, the analytical model results in an overestimation of the rising edge. The conclusion that can be drawn from this is, that it is likely that the impact of the other aperture sizes is also overestimated. Accordingly, it is likely that a smaller ratio between free aperture and FWHM of the beam than 3.5 is necessary to explain the slow feature in the reference.

4.4.2. Impact of Spatial Filtering by an Inverse Top-Hat on the Temporal Contrast

Spatial apertures like slits, pinholes, and finite-sized mirrors are not the only elements that change the beam profile. Another class of such spatial filters are small damages on optical surfaces, that introduce an inverse top-hat to the spatial beam profile.

I have artificially introduced such a perturbation to the input beam prior to the unfolded stretcher by placing various needles in the beam path. The temporal-contrast measurements for this study were executed after the PTAS with the Sequoia.

It is further to note, that the employed beam size for this measurement differs from the other measurements presented in this thesis. All other configurations are categorized as either sb or lb, which correspond to magnifications prior to the stretcher of x1 and x6, respectively. For this measurement, a magnification of x4 was employed. However, since this offers no meaningful insights or improvements, no further measurements with this magnification are presented in this manuscript.

The reasoning for the changed measurement point and in-stretcher beam size is that in the previous section, the comparably large rising edge in the reference limited the ability to observe the spatial conditioning. Thus, for this investigation, the configuration providing the best temporal contrast is used, in order to overcome these limitations. While this approach necessitates a preemptive mentioning of the differences in the rising edge between the X-ray lab and the PTAS, it should be noted that these will be fully elaborated in sec. 4.8, for the sake of a cohesive argument, after a thorough discussion of the impact of the remaining components.

The benefit of this approach becomes clear when comparing the measurements in fig. 4.13 with each other. The observable difference is restricted to the area between $-25\,\mathrm{ps}$ and $-5\,\mathrm{ps}$, where the rising edge is subject to the fewest additional disturbances, e.g. pre- and post-pulses. For this reason, a zoom-in into this temporal region is depicted on the right. In this area, no impact of the slit was observed in the previous section. While this might be due to the different nature of the employed filter, it is more likely that this is caused by the improved rising edge in this temporal region, in comparison to the measurements in the X-ray lab. A downside of this measurement point is that potential differences at times further from the peak than $-50\,\mathrm{ps}$ can not be observed, due to the limited dynamic range.

Again, the needle is placed in the image plane of the second spherical mirror in the unfolded stretcher and in the random plane 1.5 m prior to the image plane. For the placement of the needle in the image plane a clear degradation of the temporal contrast, compared to the reference, can be observed.

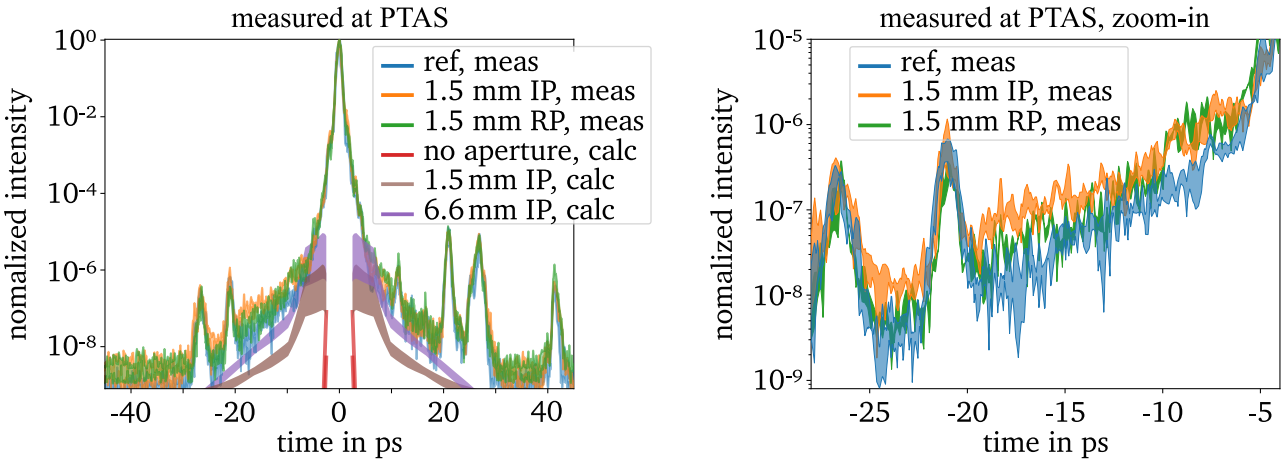

Figure 4.13.: Measurements of the temporal contrast after the unfolded stretcher, with a 400 µm needle in the image plane (IP) of the second spherical mirror, in a random plane prior to the stretcher, and a reference measurement without a needle. Additionally included are simulations of the expected rising edge according to eq. 2.18 for slits of 400 µm size, which corresponds to the measurements and of 1 mm size. All measurements were executed after PTAS with the Sequoia. The plot on the right-hand side shows a zoom-in into the area where a systematical difference between the measurements is visible. The peak-to-valley variations between multiple measurements are indicated as a shaded area.

Measuring the rising edge with the needle in the random plane yields a slightly degraded rising edge in comparison to the reference. The worsening is however less pronounced than for the placement in the image plane. However, even with the improved reference contrast, the systematic difference is too small to conclude the validity of eq. 2.45.

Additionally included in this figure, are the corresponding predicted rising edges based on eq. 2.18. The first is the reference, without spatial clipping effects, in red.
The second calculation corresponds to the employed needle size of 400 µm. The predicted rising edge for the 400 µm needle shows a qualitative agreement to the observed rising edge but underestimates the magnitude.
The third calculation allows the estimation of whether this quantitative difference can be explained by a size difference. As it turns out, the analytical model implies that a larger needle indeed causes a higher rising edge, but only up to 1 mm, beyond which the magnitude does not further increase. Instead, oscillations become visible in the rising edge.

Nonetheless, the mathematical model predicts the rising edge well, especially considering additional sources of uncertainty like the PSD, the double-pass, and the other optical elements in the stretcher (especially the second grating). This leads me to the conclusion that damages in the hundreds of µm-range are a possible limiting factor of the current temporal contrast in the PTA when using the unfolded stretcher design. On this point it is crucial to keep in mind that spatial modifications in the beam do not intrinsically change the temporal profile - they do so only in combination with STC, e.g. the noise introduced by the PSD of the stretcher optics.

4.5. Impact of the Serrated Aperture on the Temporal Contrast

After the regenerative amplification stage the beam, which is at this point to a good approximation of an ideal Gaussian shape, is magnified to a beam size of FWHM = 3.8 mm. Subsequent to this magnification, the beam can follow one of two available beam paths. The first is a bypass to the TW-compressor and the X-ray lab and the second is the main path, through a serrated aperture, a spatial frequency filter, the PA, MA, and the PW-compressor before concluding in the PTA. This section is dedicated to the spatial conditioning in the main path, before discussing the two available compressors in sec. 4.6.

When traversing the main beam path, the beam is spatially clipped on a serrated aperture. The serrated shape ensures that the diffraction artifacts from the clipped edges are high spatial frequency features that can be removed by spatial frequency filtering, e.g. with an aperture in the FF of a lens. At PHELIX the serrated aperture is designed in such a way, that when employing it in combination with the spatial frequency filter and with the radially dependent gain profile in the amplification stages the spatial beam profile becomes as close as possible to a top-hat on the PW-compressor gratings. This ensures a homogeneous distribution of fluence on this surface and thus allows for a higher total energy.

This section provides the calculations of the impact of this component on the beam profile in the PW-compressor in order to adequately estimate the impact of this component on the rising edge when discussing the PW-compressor in sec. 4.6.1.

I have investigated the impact of three different configurations, with the first being a reference setup, where an empty substrate was employed instead of a serrated aperture. The other two configurations are two serrated apertures, referred to as A1 and A11, with inner and outer diameters of

$$D_{\text{inner, A1}} = 6.9\,\text{mm} \qquad D_{\text{outer, A1}} = 8.3\,\text{mm}, \tag{4.2}$$

$$D_{\text{inner, A11}} = 5.9\,\text{mm} \qquad D_{\text{outer, A11}} = 7\,\text{mm}. \tag{4.3}$$

The spatial profile prior to the serrated apertures, as well as an indication of the contours of the serrated apertures is shown in fig 4.14 (left).

After all three configurations, the beam undergoes spatial frequency filtering with an aperture of 1.1 mm in the focus of a lens with a focal length of $f = 273\,\text{mm}$. The beam then propagates through the PA and MA (more information in app. A.11), before entering the PW-compressor. The impact of the serrated aperture on the spatial profile at the compressor input f_{Comp} can be described by

$$f_{\text{comp}}(\bar{x}) = \mathfrak{F}^{-1}\left(\mathfrak{F}\Big[f(x)\cdot T_{\text{SA}}(x)\Big](k)\tilde{T}_{\text{FF}}(k)\right)(\bar{x}). \tag{4.4}$$

This equation incorporates several steps, starting with applying the serrated aperture $T_{\text{SA}}(x)$ to an undisturbed spatial Gaussian $f(x)$. Then, the signal in the FF is calculated, using the Fourier transform of the NF signal, and the spatial frequency filter $\tilde{T}_{\text{FF}}(k)$ is applied. In the last step, the inverse Fourier transform is used, to translate the beam back into the NF. The spatial coordinate $\bar{x}$ in the NF after this step includes the magnification in the PA of $m_{\text{PA}} \approx 7.9$ and the MA of $m_{\text{MA}} \approx 3.8$, such that $\bar{x} = m_{\text{MA}} \cdot m_{\text{PA}} \cdot x \approx 30x$. This yields magnified serrated aperture sizes at the PW-compressor input of

$$D_{\text{inner, A1, PW}} = 207\,\text{mm} \qquad D_{\text{outer, A1, PW}} = 249\,\text{mm}, \tag{4.5}$$

$$D_{\text{inner, A11, PW}} = 177\,\text{mm} \qquad D_{\text{outer, A11, PW}} = 210\,\text{mm}. \tag{4.6}$$

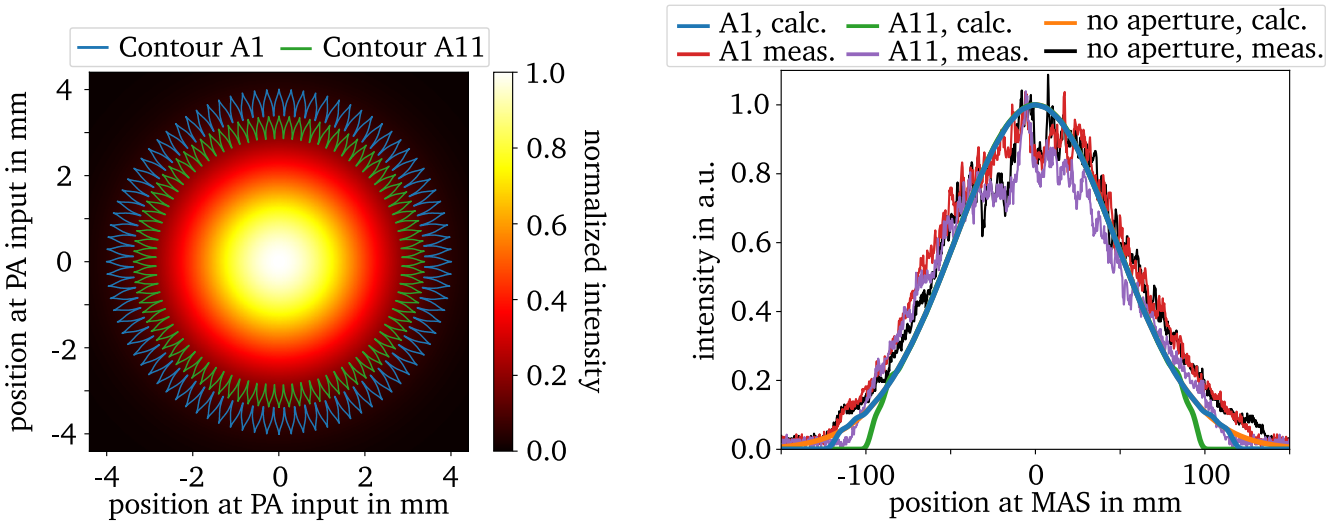

Figure 4.14.: Left: spatial NF profile of the beam at the PA input, with the two contours indicating the shape of the serrated apertures, A1 and A11. Right: measured and calculated lineouts of beam profiles for the two serrated apertures at the Main Amplifier Sensor (MAS), together with a reference without serrated aperture. All lineouts are taken at the center of gravity of the respective data sets, along the axis of the grating dispersion in the PW-compressor.

A lineout along the center of gravity of the resulting spatial profile at the compressor input is depicted in fig. 4.14 (right), for all three configurations.
Additionally included are measurements of the beam profile at a calibrated imaging system of the MA output onto a camera at the MAS. A similar calibrated sensor is available that images the surface of the second grating in the PW-compressor on a camera chip. It is however to note, that the beam is spectrally dispersed in this image. Thus, the measurements are executed at the MAS for comparison to the calculated lineouts. Each lineout was again taken along the center of gravity, along the axis that is parallel to the dispersion axis of the compressor gratings.

It is to note, that the beam without the serrated aperture is spatially clipped on the rods of the PA, which introduces sharp edges in the measured lineout. The lineout measured with the serrated aperture A1 features an identical edge on one side, at around $-120\,\mathrm{mm}$. This indicates that on this side, the beam is not conditioned by the serrated aperture A1, but also spatially clipped on the rods in the PA. The lineout with the serrated aperture A11 is fully dominated by the serrated aperture but features a slightly broader profile and less pronounced clipping edges.

The otherwise good agreement between the measured lineouts and the calculated lineouts allows the use of the latter for further calculations that rely on the spatial profile in the compressor, with less noise than the measurement. This becomes especially important when employing this spatial profile for the estimation of the rising edge caused in the PW-compressor, which is the subject of sec. 4.6.

4.6. Impact of the PHELIX Pulse Compressors on the Rising Edge

The source of the rising edge in CPA system has been debated for over two decades. While this is mostly due to the stretcher [79, 102, 1], as the previous parts of this thesis demonstrated, some arguments have also been made that pointed into the direction of the compressor [117, 118]. It is obvious that the same spectral phase introduction happens on the surfaces in the compressor as in the stretcher and the same spectral clipping processes occur. However, since the temporal contrast is mainly of interest during high-intensity experiments the beam size in compressors is generally large. This is especially true for the PW-Compressor at PHELIX with a beam diameter of around 240 mm, which is around a factor of 100 bigger than in the stretcher and less so for the TW-compressor with an FWHM of around 4 mm. This section explores how this influences the temporal-contrast formation according to the previously developed model. Since the previous section discussed the beam path up to the PW-compressor, this is the first discussed compressor.

4.6.1. Impact of the Petawatt Compressor on the Temporal Contrast

After the serrated aperture, the PA and the MA, the beam is temporally compressed in the PW-compressor. The remaining beam path is depicted in fig. 4.15. During experiments, the beam is directed into the target chamber, where an off-axis parabola is used to focus the beam on a target. In this configuration, leakage light is transmitted into the PTAS for spatial characterization [114]. In this component, several telescopes are used to reduce the beam size. The first of these telescopes consists of two off-axis parabolas, while the remaining telescopes employ lenses.
For temporal-contrast measurements after PTAS the leakage mirror is removed from the beam path and the beam is directed into the Sequoia device after the demagnification.

Due to the single-pass design of the PHELIX PW-compressor, the beam is spectrally dispersed on all remaining surfaces downstream of the first compressor grating. All surfaces thus introduce a rising edge, via spectral amplitude and spectral-phase effects. In order to predict the rising edge, analytical considerations can reduce the considered surfaces to the elements prior to the demagnification of the parabola (compare app. A.12). All other remaining surfaces, besides the second compressor grating, are, for spectral-phase effects, neglected based on the assumption that this component features the largest PSD out of all relevant surfaces. For spectral clipping, all other surfaces are neglected based on the size of the optical elements. This leaves the second grating in the PW-compressor to be considered as a potential source of temporal-contrast degradation, prior to the Sequoia.

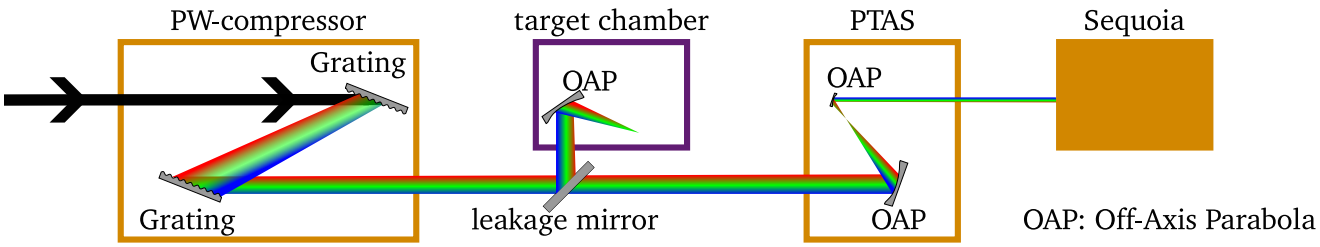

Figure 4.15.: Schematic of beam path in the PW-compressor and the PTA. The leakage mirror is removed for the temporal-contrast measurements.

Estimation of the Influence parameter for the rising edge formation in the PW-Compressor

In order to calculate the impact of the second compressor grating on the rising edge, based on spectral phase perturbations and spectral amplitude perturbations, estimations of the beam profile, the spectral transmission, and the PSD are required.

The beam profile on the second grating, as conditioned by the serrated aperture of choice, was discussed in sec. 4.5. This also included the various spatial clipping processes on the rods in the PA, which further condition the spatial profile and thus the rising edge introduced in the PW-compressor.

For the spectral transmission through the PW-compressor, measurements in the MAS and in the PTA are compared with each other and to the trigonometric calculations. For the latter, it is sufficient to assume a point source on the first grating and calculate the opening angle, between two rays that would hit the edges of the second grating. The transmission bandwidth can then be calculated using the dispersion of the grating, according to eq. 1.21. The calculation only relies on the specifications of the compressor, such as the effective grating distance of 4 m, the free aperture of the grating in the dispersion direction of S =0.807 m, the line density of the gratings g =1740 l/mm, the angle of incidence on the first grating, with respect to the grating normal α =72.5° and the central wavelength λ_c = 1054 nm. The resulting transmission bandwidth through the stretcher is then

$$\Delta\lambda_{\omega,PW} = 26.1\,\mathrm{nm}. \tag{4.7}$$

The dispersion coefficient $a_{\omega,PW}$ on the surface of the second PW-compressor grating can be calculated by inserting this result into eq. 3.4

$$a_{\omega,PW} = \frac{S\lambda_c^2}{2\pi c\Delta\lambda} = 18.3\,\mathrm{mfs}. \tag{4.8}$$

This is approximately a factor of two larger than during the second interaction with the stretcher gratings (compare tab. A.1), which is plausible given that the compressor is designed to compensate for the dispersion introduced in the stretcher with a single-pass, instead of the double-pass that is employed in the stretchers.

Estimation of the impact of spectral clipping for an ideal spectral Gaussian

The spectral clipping bandwidth, which is essentially the transmission profile of a beam with negligible size, on the compressor grating itself turns out to be larger than for the stretchers. Accordingly, the clipping process on this grating produces less disturbance in the temporal profile, when neglecting the beam size, since the hard edge of the clipping is introduced at a lower spectral intensity.

Additionally, the introduced edges in the spectrum are smoother for the interaction in the compressor than for the stretcher, due to the larger beam size. The expected rising edge based on spectral clipping, should therefore be smaller than for the stretchers. This statement is validated by corresponding calculations of consecutive clipping, based on eq. 2.27. For this calculation, the spectral clipping in the stretcher is considered first (compare sec. 4.3.3) and then the spectrally clipped field is used as the input for the spectral clipping process in the PW-compressor.

The results of this are that, for all configurations, the interaction is fully dominated by the stretcher, with no measurable difference to the impact of spectral clipping in the isolated stretchers.

Accordingly, no impact of the PW-compressor and no dependency on the serrated aperture can be expected.

Estimation of the Impact of Spectral-Phase Effects in the PW-Compressor on the Rising Edge

Spatial conditioning plays a crucial role in the consideration of spectral-phase effects on the second PW-compressor grating. Without the consideration of the serrated apertures or other spatial apertures in the beam path, the expected rising edge caused by this effect is negligible, due to the large beam size in the compressor. However, the analytical model predicts that the spatial conditioning causes a notable rising edge to be introduced on this component, as depicted in fig. 4.16.
The corresponding calculations are executed based on eq. 2.18, with the spatial profiles determined in sec. 4.5. The assumed PSD for these calculations is the same as for the stretcher gratings and is discussed in app. A.2.

The calculations of the rising edge show a dependency on the serrated aperture configuration, with the empty substrate producing the worst rising edge. This is due to the hard edges in the spatial profile, introduced by spatial clipping on the rods in the PA.
The smallest serrated aperture A11, produces the best temporal contrast since it provides the smoothest edges.
For the serrated aperture A1, which is slightly larger, the calculations predict a rising edge with a higher magnitude, even though the spatial edge in the profile is at a smaller relative intensity.
It is to note, that the difference between A1 and A11 remains when neglecting the spatial clipping on the PA rods.

Due to relay-imaging, the sharp edges in the considered spatial profiles are transported to the compressor. However, the image of the serrated aperture is positioned a few meters prior to the PW-compressor entrance. Equation 2.45 predicts that the rising edge is independent of such propagation distances. However, the efforts made in sec. 4.4 indicate that free propagation on the meter scale, occurring after the aperture is applied, reduces the impact of spatial apertures on the temporal profile. This suggests that the calculations overestimate the actual introduced rising edge.

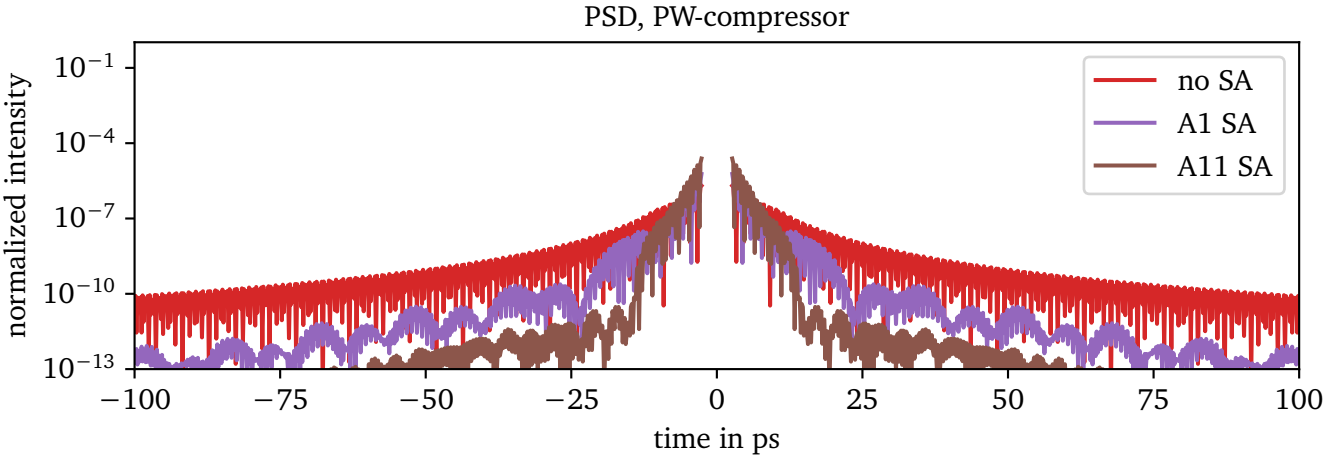

Figure 4.16.: Rising edge introduced by the PSD of the second grating in the PW compressor. The three curves correspond to the spatial conditioning by the three serrated aperture configurations.

Prediction of the expected rising edge by comparison of amplitude and phase effects

To predict a temporal profile after the PW-Compressor, all considered effects are combined. This includes spectral clipping in the stretcher and the compressor as well as the impact of the PSD in both components. The combination is simplified by the fact that the former effect is fully dominated by the stretcher and the latter is assumed to behave additive with other effects. As a consequence, the combined temporal profile can be found by combining the temporal profiles previously presented in sec. 4.3.3 with the impact of the PSD in the compressor, presented in the previous section.

The predicted rising edge is depicted in fig. 4.17, sorted by the stretcher configuration.

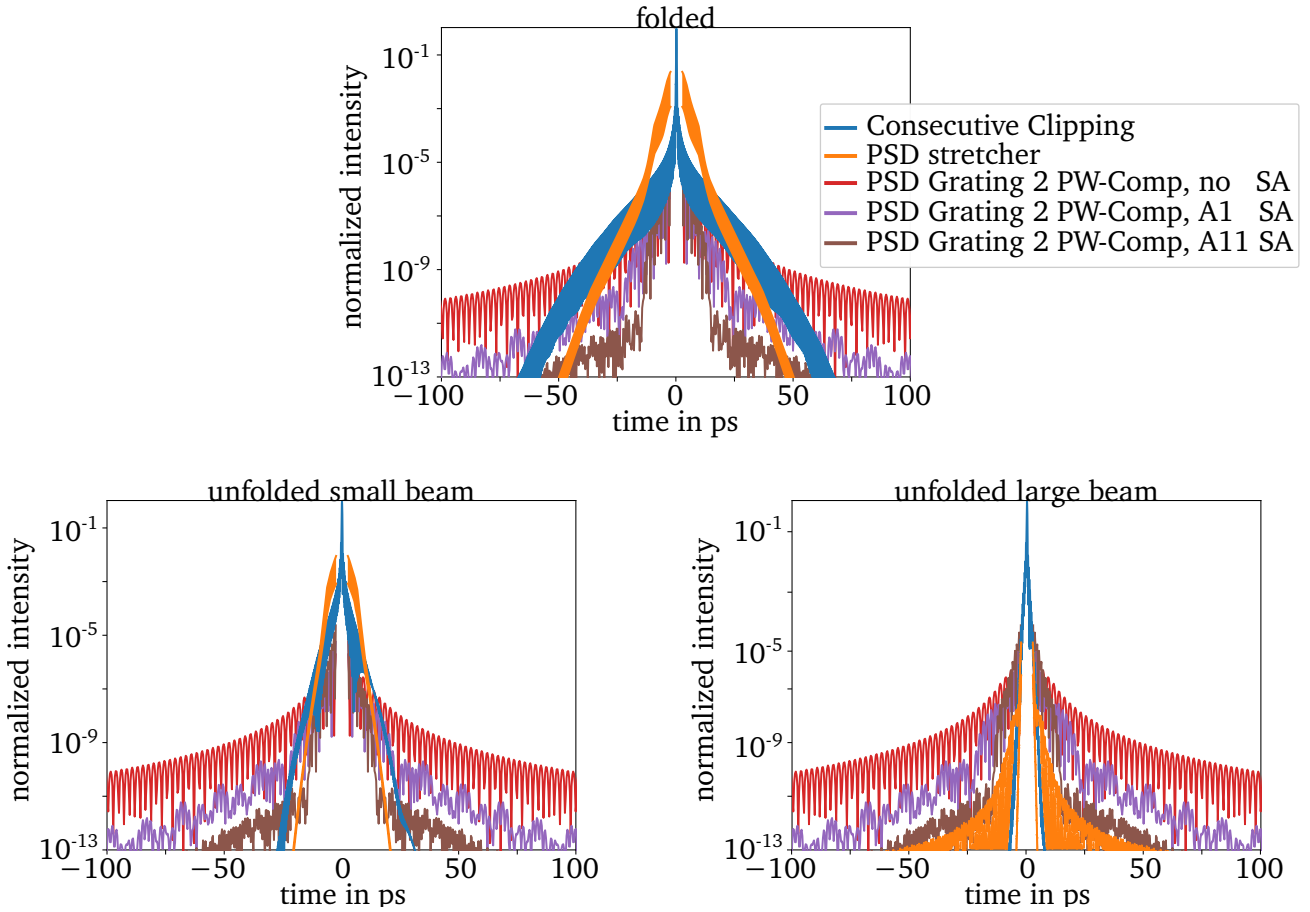

Figure 4.17.: Summary of the expected rising edges introduced in the PW-compressor for beams coming from the folded (top) and unfolded (bottom) stretcher setup at PHELIX, for the small in-stretcher beam size configuration (bottom, left) and the large in-stretcher beam size configuration (bottom, right). The rising edge introduced by the PSD in the PW-compressor is included for the three serrated aperture configurations. Also included are the impact of consecutive spectral clipping in the laser chain (blue), and of spectral-phase effects in the stretcher (orange).

For the folded design the predicted rising edge is dominated by the PSD in the stretcher for times smaller than 15 ps. For larger times it is dominated by spectral clipping. When comparing this to the predictions for the influence of the stretcher itself (fig. 4.11), it is clear that in this temporal region, the rising edge can be expected to be limited by spectral clipping on the folding mirror in the folded stretcher. The dominating effect that overtakes the spectral clipping is the PSD of the second compressor grating, but the magnitude of this slow feature depends on the choice of the serrated aperture. Over the first nine orders of magnitude, however, this is fully dominated by the stretcher, and when employing a serrated aperture (A1 or A11) it is limited by the stretcher for the first twelve orders of magnitude.

For the unfolded stretcher with the sb, the beam is only limited by the stretcher for the first 15 ps. At this point, the predicted rising edge has already declined over eight orders of magnitude, before the slow feature of the compressor takes over. This can be further reduced to nine orders of magnitude at around -20ps when employing the serrated aperture A1 and to twelve orders of magnitude at around -25ps with the serrated aperture A11.

For the unfolded stretcher with the lb, the rising edge is at no relevant point in time expected to be limited by the stretcher. Instead, the rising edge is fully dominated by the second compressor grating in the PW-compressor.

Before comparing this to the corresponding measurements, the remaining relevant elements are discussed, being the other available compressor at PHELIX in the next section and afterward the impact of the available measurement devices.

4.6.2. Impact of the Terawatt Compressor on the Temporal Contrast

The TW-Compressor at the PHELIX facility was originally built for the purpose of a transient X-ray laser for laser spectroscopy of lithium-like ions in the year 2003 [119], giving the corresponding lab its name - X-ray lab. While it was originally intended for usage after amplification of the laser in the PA, it is nowadays mainly used in the bypass configuration, where the beam is picked off after the regenerative amplification stage at the end of the front-end and directed to the TW-Compressor. Unlike the original setup, the compressor is no longer housed in a vacuum chamber; instead, it is exposed to air.

In the compressor, which is depicted in fig. 4.18, one 40 cm large circular grating with a line density of 1480 l/mm is used, under an angle of incidence of α =46.1°. The effective grating distance $D_{\mathrm{TW}} = 3.87\,\mathrm{m}$ necessary for recompression, is achieved in a folded design, first with a horizontal roof-top-mirror and then after the second hit on the grating with a vertical roof-top-mirror in order to provide a separation from the input pulse.

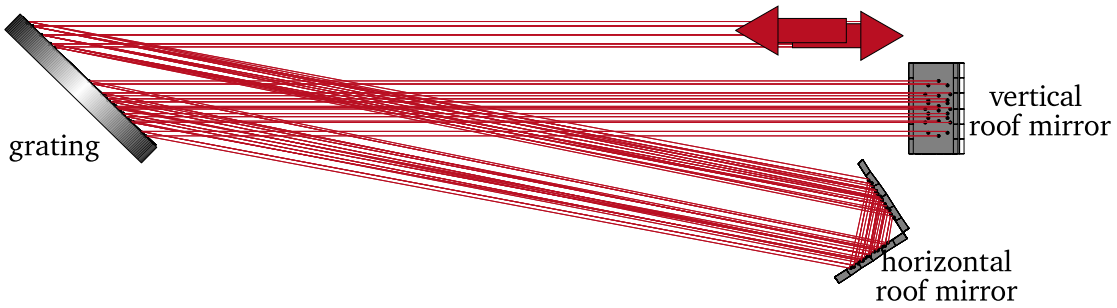

Figure 4.18.: Schematic of the TW-compressor at PHELIX, adapter and translated [119].

Even though the large optical elements support the beam size after the PA, the smaller beam size at the PA input, where the beam is picked off, makes this unnecessary. Thus, 50 mm optics have been placed for the coupling into the compressor, which is sufficient for the beam size of $\mathrm{FWHM_{TW}} = 4\,\mathrm{mm}$. The measurement of this beam size was done with a Basler cam, with a specified pixel size of 5.86 µm. The sum of the measurement in the direction perpendicular to the table is depicted in fig. 4.19 (left), together with the employed Gaussian fit. This is the first key difference to the PW-compressor: the spatial profile is to a good degree Gaussian-shaped.

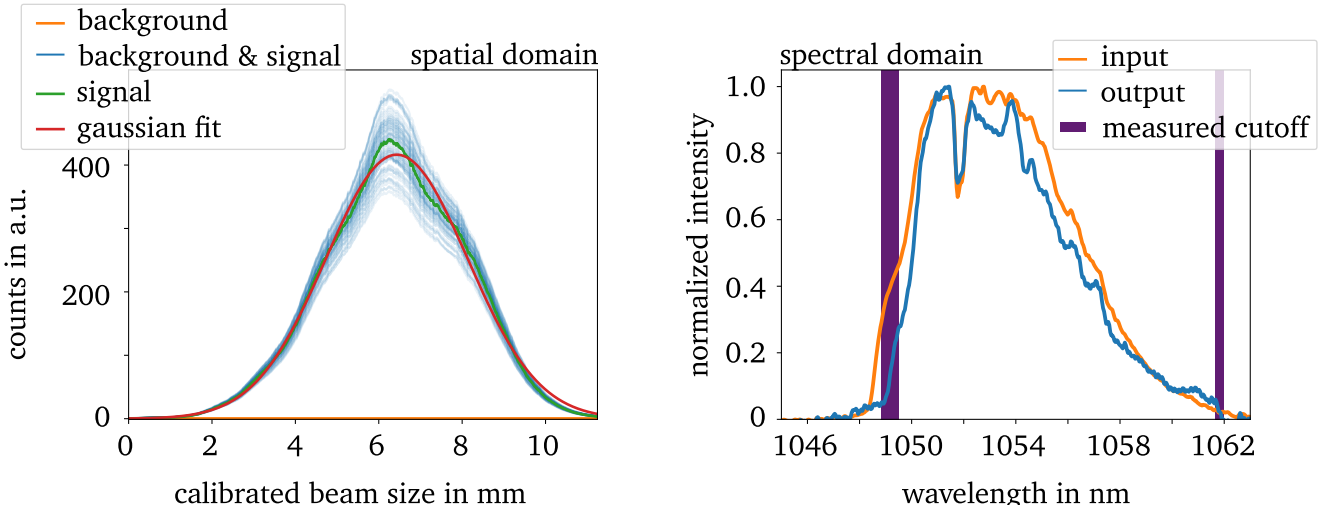

Figure 4.19.: Spatial characterization of the beam in the TW-compressor (left), calculated by subtracting the background from several measurements of the beam profile. The depicted signal is the average of the lineouts along the axis perpendicular to the dispersion of the grating grooves. Further included is a Gaussian fitted onto the signal. On the right, the spectrum is displayed, before and after the TW-compressor. The vertical lines mark the measured clipping wavelengths, with the thickness of the line corresponding to the uncertainty.

Estimation of the impact of consecutive spectral clipping in the TW-compressor on the rising edge

In order to estimate the impact of spectral clipping in this compressor on the temporal contrast the spectral transmission of each element and the corresponding dispersion coefficients must be determined.
Since the beam sizes are assumed to be the same for all interactions and rigorous geometrical calculations or ray-tracing of the setup would be necessary to determine which wavelength clips on which surface exactly, the following analysis instead relies on the assumption that all clipping happens on the surface with the largest dispersion coefficient. This simplified the calculation and gives an upper estimate of the introduced rising edge.
The largest dispersion coefficient can be found during the interaction with the second grating. In order to find the dispersion coefficient on this surface eq. 3.4 is rearranged and the distance S between the clipping wavelengths is eliminated eq. 3.4 in favor of the effective grating distance D

$$a'_\omega = \frac{S\lambda_c^2}{2\pi c \Delta\lambda} = \frac{\lambda_c^2 m g D}{2\pi c}. \tag{4.9}$$

This is independent of the clipping process so far and is only a geometric consideration of the opening angle in a compressor and can thus be calculated for the stated specifications of the TW-compressor.
Since the considerations are for a surface that is perpendicular to the dispersion direction of the central wavelength, it must be scaled to the orientation of the grating by the dispersion angle of the central wavelength β_c, which can be calculated using eq. 1.21 using the specifications of the compressor. This results in a projected dispersion coefficient during the second interaction with the grating in the TW-compressor of

$$a_{\omega,\mathrm{TW,G2}} = a'_{\omega,\mathrm{TW,G2}} / \cos(\beta_{\mathrm{c,TW}}) = 6.2\,\mathrm{mfs}, \tag{4.10}$$

where the dispersion coefficient $a'_{\omega,TW,G2}$ is calculated based on eq. 4.9.
The beam size on this surface can be calculated with a similar projection, by recognizing that the measurement took place in the direction of the central wavelength

$$\mathrm{FWHM}_{\mathrm{TW,G2}} = \frac{\mathrm{FWHM}_{\mathrm{TW}}}{\cos\beta_{\mathrm{c,TW}}} = 7.4\,\mathrm{mm} \tag{4.11}$$

This is exactly the same scaling factor as for the dispersion coefficient and the effect of the projection cancels out.

The clipping wavelengths are determined experimentally, by comparing the spectrum before and after with each other. This is depicted in fig. 4.19 (right), for the beam path through the folded stretcher. This stretcher was chosen since it provides the broadest bandwidth and thus the most precise determination of the clipping wavelengths in the TW-compressor to

$$\lambda_{1,\mathrm{TW}} = (1049.3 \pm 0.3)\,\mathrm{nm} \quad \lambda_{2,\mathrm{TW}} = (1061.8 \pm 0.1)\,\mathrm{nm}. \tag{4.12}$$

The impact of the spectral clipping that results from these considerations is depicted in fig. 4.20. Equivalent to the considerations of the PW-compressor in sec. 4.6.1, the considerations here first assume an idealized spectral input, before considering consecutive spectral clipping (compare eq. 2.27). Due to the smaller beam size and transmission bandwidth, compared to the PW-compressor, the consecutive clipping is, for the TW-compressor, not fully dominated by the stretcher.

Additionally included in the consideration are the spatial filters present in the beam path. In this case, the limiting factor is the 50 mm mirrors that are used to couple into the compressor. The influence of this effect is in this context however negligible.

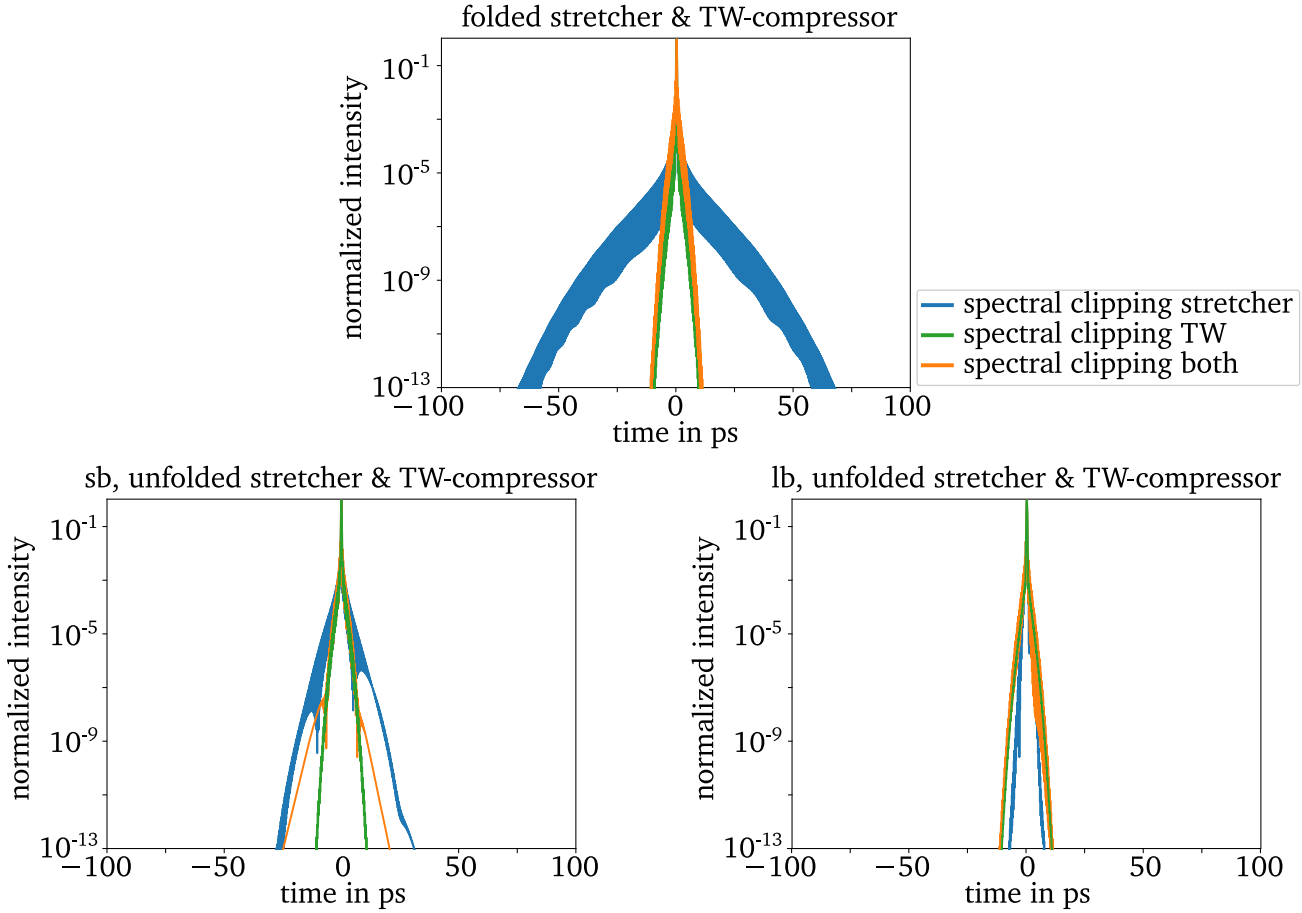

Figure 4.20.: Impact of spectral clipping on the temporal profile after the TW-compressor, sorted by the traversed stretcher configuration. The blue curves correspond to ideal compressors, or in other words to a system where clipping in the stretcher fully dominates the temporal profile. The green curves correspond to an ideal spectral Gaussian at the input of the compressor, without previous spectral clipping. The orange curves are the consecutive spectral clipping in the complete system.

Estimation of the Impact of Spectral-Phase Effects in the TW-Compressor on the Rising Edge

The second considered effect is that of the PSD in the TW-compressor. Since the beam profile can to a good degree be described by a Gaussian that is only slightly spatially clipped prior to the compressor, the expected rising edge is small. However, due to the folded design with ten contributing interactions, we find a steep rising edge with a high offset, as depicted in fig. 4.21. It is important to keep in mind that the calculation of a total rising edge by the addition of the individual rising edges is only an approximation, which might overestimate the total rising edge.

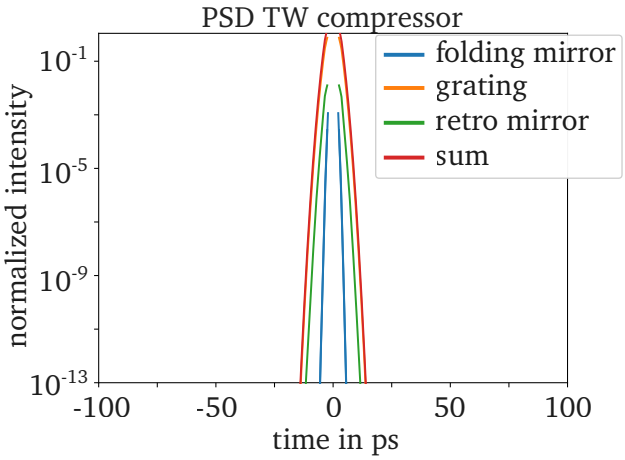

Figure 4.21.: Rising edges introduced by the PSD of the optical elements in the TW-compressor. The total rising edge caused by the TW-compressor is calculated as the addition of the rising edges of the ten individual relevant surfaces.

There is one additional effect, that differentiates the TW-Compressor from the rest of the discussed dispersive elements in the PHELIX laser chain, being the difference in the line density of the grating. Where all other components utilize gratings with a line density of 1740 l/mm, the TW-compressor employs a grating with a line density of 1480 l/mm. However, the impact of this effect on the temporal contrast can be neglected, as discussed in app. A.13.

Comparing the impact of the components in this section as well as the previous sections to experimental measurements of the rising edge after the discussed various possible beam paths requires the measurement of the temporal profile. In the next section, the available devices are discussed, as well as their potential impact on the measured temporal profile.

4.7. Assessing Measurement Device Contributions to the Perceived Rising Edge

At PHELIX a selection of different measurement devices are available that allow for the characterization of the temporal profile of ultra-short laser pulses, such as scanning autocorrelators and various Single-Shot AutoCorrelator (SSAC). Beyond that numerous devices are available that allow for full spectral-temporal characterization of the laser pulse, based on FROG [120] and SPIDER [121]. However, none of these elements is capable of resolving the orders of magnitude in dynamic range that are necessary to study the temporal contrast. For this purpose, cross-correlators are used, such as the Sequoia device which was already used for the PoP (compare cha. 3) and the EICHEL [92], which is an in-house build cross-correlator.

The measurement principle of the two cross-correlators is the same: the incident beam is split into two arms. One of which is frequency doubled using SHG [24] in a non-linear crystal and then recombined with the other arm in a second non-linear crystal, where a Sum-Frequency Generation (SFG) [24] signal is generated. The signal is then measured by a time-integrating detector. By delaying the two arms with respect to each other the temporal pulse profile is sampled.

However, the setup used to realize this principle differs between the two devices, in design, required energy, and resolvable dynamic range. Thus, it can not be assumed a priori that both measure the same physical parameters. This section presents both available cross-correlators, starting with the EICHEL, before comparing them.

4.7.1. The EICHEL Device

In the EICHEL device (compare fig. 4.22, left) the incident laser beam is split into two arms, the first one is frequency doubled using SHG in a 10 mm crystal and focused into a second 15 mm crystal with a cylindrical lens. There, the beam is overlapped with the beam traversing the second arm. This second arm is transmitted through an attenuator wheel before it is also focused into the non-linear crystal with a cylindrical lens. The orientations of the focal lines are parallel to each other and to the table-normal. In order to scan the large temporal range the SHG arm can be delayed. In the crystal, where both arms overlap, an SFG signal is generated at 3ω of the incident pulse. The beam is then directed through a vertical slit parallel to the focal lines, in order to guarantee separation from the 1ω and 2ω light, onto a photo-multiplier.

With this technique, EICHEL is capable of resolving the temporal laser profile over 13 orders of magnitude. To note here is, that the EICHEL is at PHELIX only used after the TW-compressor and not after the PW-compressor, due to the bulky design of the device and the high energy requirement of a few mJ laser energy.

The beam coming from the TW-compressor has, as discussed, roughly an FWHM of 4 mm. Thus, spatial clipping occurs at the limiting free apertures in the device, which turn out to be the SHG (10 mm), SFG (15 mm) crystal and the slit after the SFG crystal. The resulting ratio between aperture sizes and FWHM in the EICHEL are thus around 2.5, for the SHG crystal. For the SFG crystal, the ratio is 3.75, however only in one axis. On the other axis, the ratio is much larger due to the cylindrical lenses.

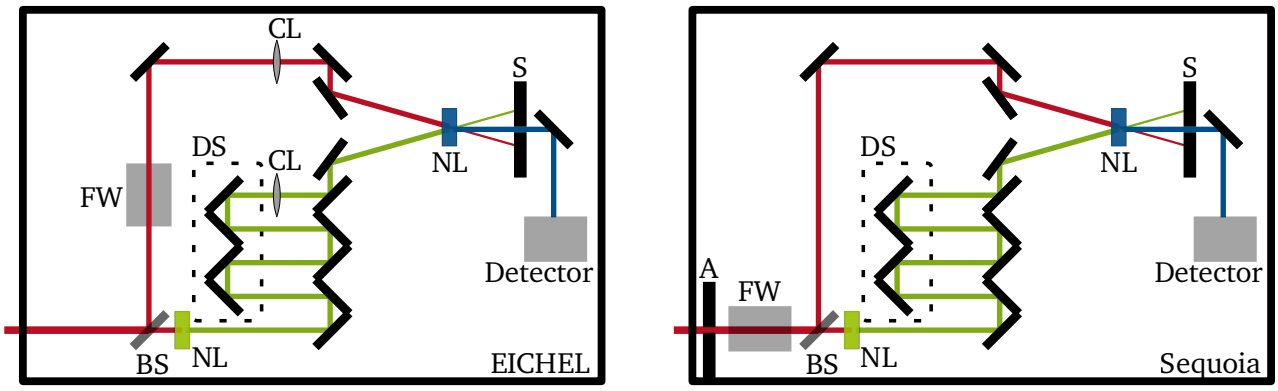

A: Aperture CL: Cylindrical Lens FW: Filter Wheel S: Slit
BS: Beam Splitter DS: Delay Stage NL: Non-Linear crystal

Figure 4.22.: Schematic setup of the EICHEL (left) and Sequoia (right). This is an illustrative example, and not an exact replication of the actual beam paths [92, 108].

4.7.2. The Sequoia Device

In contrary to the EICHEL, the Sequoia is designed to operate fully in the NF, as depicted in fig. 4.22 (right). It further employs the attenuation at the entrance of the device, instead of only in the 1ω arm. The apertures in the Sequoia are smaller with an 10 mm iris at the entrance and 5 mm for both crystals. Similar to the EICHEL device, the SFG signal is separated from the generating arms by an angle and an 1 mm slit.

The device measures the temporal contrast over nine orders of magnitude with energies in the hundreds of µJ to 1 mJ range, for the pulse durations in the hundreds of fs regime. This is the configuration employed for measurements in the X-ray lab and after PTAS, where sufficient energy is available. The beam is demagnified at both measurement locations prior to the Sequoia, by a factor of 3 and 52.8, respectively, in relation to the corresponding in-compressor beam size. This results, in the X-ray lab, in an FWHM of around 1.3 mm and apertures to FWHM ratios of 3.75 and 0.75 for the non-linear crystals and the slit, respectively.

After PTAS, the beam shape is not assumed to be Gaussian, due to the serrated aperture, thus it is a more reliable way to express the beam size at a position according to the size of the edges that the serrated aperture introduces. For the measurement point after PTAS, the demagnification scales the edge of the serrated aperture A11 in the beam to around 3.8 mm (compare fig. 4.14).

The second configuration employs an 1 m focal length lens at the entrance of the device. This puts a focal spot in both arms at a position between the first non-linear crystal and the second non-linear crystal. Due to the corresponding decrease in beam size, the intensity in the crystal increases and it is possible to achieve eight to nine orders of dynamic range with 100 mJ. This is the configuration employed for the PoP in cha. 3. The downside of this configuration is, that the beam size in the SHG crystal changes during the scanning process. However, the necessary path length change in order to scan 100 ps is around 3 cm. Thus, for a focal lens of 1 m the change of beam size in the intermediary field, where the second crystal is located, is also of the order of $3\,\mathrm{cm}/1\,\mathrm{m}$, which is negligible compared to the accuracy of the determination of the beam size.

A downside of Sequoia, when compared to EICHEL, is the mentioned positioning of the attenuator at the detector entrance rather than solely in the 1ω-arm. While for the latter position, the intensity change in the signal is straightforwardly deducible from the optical density of the employed filter, this process is more complicated for the former position. This difference can influence the measured temporal contrast since the intensity change of the SHG signal does not scale linearly with the optical density of the attenuator.

4.7.3. Predictions of the influence of the detectors on the temporal contrast

In both devices, spatial clipping is present, especially when used for Gaussian beams. According to the analytical model, spatial apertures in the beam path can condition the formation of a rising edge (compare sec. 2.3.2). This has been validated in sec. 4.4 for apertures in the image plane of an optical element that introduces a rising edge.
The case of the detectors differs from this since the apertures in the devices are positioned after the relevant optical elements and can thus not change the beam profile on the surface. Nonetheless, the calculations in sec. 2.3.2 predict that spatial conditioning is independent of whether the spatial clipping occurs before or after the rising edge is introduced. This is however only valid as long as no spatial frequency filtering takes place between both interactions. While it is reasonable to assume that sufficient filtering takes place

during the free propagation to prevent the detector apertures from influencing the rising edge, further research is required to disprove this conditioning fully. Thus, the apertures must be incorporated in the predictions of the temporal profile, even though this effect is an overestimation.

The largest ratio between aperture size and input FWHM of the beam is featured by the slits after the SFG crystal. Due to the large ratios, the analytical model will predict a large impact of this spatial clipping process. However, between the input and the slit, two non-linear processes take place that prevent a straightforward estimation of the beam profile at the slit. While the available model does not allow ruling the slit out as a potential source of temporal artifacts, it can also not produce meaningful estimations of this source. Thus, the slits are not included in further analysis. The fact that this slit is positioned close to the focal point of the cylindrical lenses in the EICHEL serves as another reason to discount clipping on this component, for the EICHEL.

The presented analysis further neglects the impact of spatial clipping on the SHG crystal, since the temporal profile of the frequency-doubled signal can be approximated by $I_{2\omega}(t) \approx I_{1\omega}^2(t)$ [24]. The validity of this statement is restricted to intensities where the process is not saturated, which can be assumed to be true for the low intensities of the rising edge. The absolute change in the rising edge of this profile is thus small compared to the corresponding changes in the 1ω signal. Adding to the justification for disregarding the SHG crystal is that only one arm is affected by clipping on this component.

These arguments leave the clipping on the SFG crystal to be considered. For the EICHEL, the crystal is positioned at the focal position of the cylindrical lenses, which diminishes the imposed effect of spatial clipping. This allows neglecting the SFG crystal in the EICHEL. With this, the influences of all apertures in the EICHEL have been discarded.

For the Sequoia, the considerations implement the spatial clipping on the SFG crystal, by applying the the aperture to the beam profiles $f(x)$ which conditions the rising edge, based on spectral-phase effects (eq. 2.18) and spectral-amplitude effects (eq. 2.24). For the measurement location in the X-ray lab, the impact of this spatial clipping is depicted in fig. 4.23.

Included are also the calculations for the reference of an ideal Gaussian that is only conditioned by the 50 mm mirrors at the input of the TW-compressor (compare sec. 4.6.2). The comparison to the reference suggests that the spatial clipping on the SFG crystal greatly increases the expected rising edge for the Sequoia. While this is true for both, spectral amplitude and spectral-phase effects, only the latter shows features above the detection threshold.

The impact of the PW-compressor on the temporal contrast has already been discussed in sec. 4.6.1. In fig. 4.24 these considerations are supplemented by the effect of spatial clipping on the SFG crystal in the Sequoia, for a demagnification between the PW-compressor and the Sequoia of 52.8. Due to the comparably low impact of the Sequoia on spectral clipping and the generally low impact of spectral clipping in the PW-compressor, the analysis is restricted to spectral-phase effects.
Comparing the expected rising edge with and without the detector aperture to each other shows almost no difference, for all serrated apertures. Which is no surprise, since this rising edge is already heavily conditioned by spatial clipping.

After discussing these deteriorating effects, one last effect of the detectors must be taken into account before comparing the expected profiles to the actual measurements with these devices after the various beam paths. This effect is again the cross-correlation of the calculated temporal profiles, as defined in eq. 3.10. The comparison to the measurements is the topic of the next section.

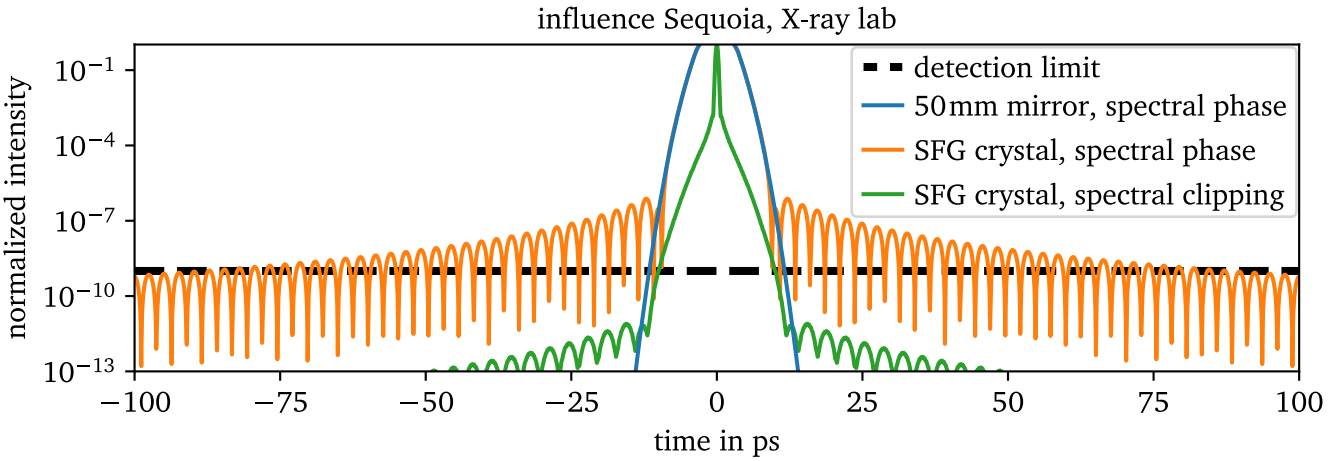

Figure 4.23.: Influence of spatial clipping on the SFG crystal in the Sequoia on the rising edge. The considered mechanisms are spectral-phase effects and spectral clipping (full line) in the TW-compressor. For reference, the spatial clipping process on the 50 mm turning mirrors at the TW-compressor entrance is included. The dashed black lines indicate the resolvable dynamic range of the corresponding device.

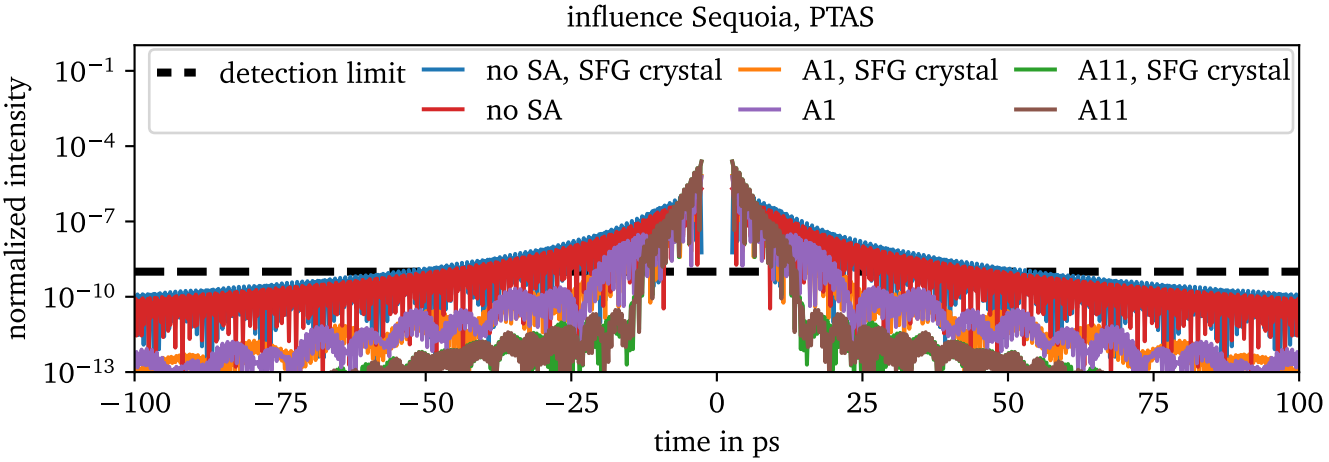

Figure 4.24.: Influence of spatial clipping on the SFG crystal in the Sequoia on the rising edge. The considered mechanism is spectral-phase effects in the PW-compressor. For reference, the expected influence of spectral-phase effects is included, for each serrated aperture configuration (compare sec. 4.5 and sec. 4.6.1). The dashed black lines indicate the resolvable dynamic range of the corresponding device.

4.8. Comparison of Measurement and Predictions: Temporal-Contrast Improvements at PHELIX

The previous chapter has provided the data for the statement that laser pulses generated by Mira and amplified by uOPA, are temporally clean without a rising edge over the measurable range (compare fig. 3.9). Previous sections of this chapter discussed all parts of the PHELIX laser chain that is expected to introduce a rising edge to such a clean temporal profile.
I have built an unfolded stretcher design at PHELIX and sec. 4.3 presents a study of its impact on the temporal contrast as well as the impact of the folded stretcher. This includes numerical and analytical investigations of the impact of spectral clipping on each surface in the stretcher and of the impact of the spectral-phase effects due to imperfections of the stretcher optics. Additionally, investigations based on ray-tracing code, that I developed for this purpose, have provided valuable insights into the impact of spherical aberration introduced by the spherical mirrors in the stretchers.
Afterward, sec. 4.4 presented the impact of spatial apertures on the contrast, and sec. 4.5 predicted the impact of beam shaping in serrated apertures on the contrast. The expected rising edge formation in the compressors and the artifacts introduced in the detectors are presented in sec. 4.6 and sec. 4.6, respectively.

The previous sections provide the means to predict the temporal profiles at the measurement points in the X-ray lab and after PTAS. This section presents and discusses temporal-contrast measurements at those two measurement points and compares them with the corresponding predictions.
The structure for this is as follows:

The first presented comparison is between predictions for the cross-correlation in the X-ray lab and the corresponding measurements with EICHEL. This is a more sophisticated repetition of the comparison made in sec. 4.3.3, supplemented by considerations of the compressor.
Throughout this investigation it becomes evident that the temporal temporal contrast with the folded stretcher is limited by damage to its folding mirror and an experimental investigation of this effect is presented.
Lastly, a comparison is provided between the temporal profiles in the X-ray lab, measured with EICHEL and with Sequoia.

After this discussion of the measurements in the X-ray lab, the results from the measurement point after PTAS are discussed. This starts with a comparison of the temporal contrast provided by the different stretcher configurations when measuring after PTAS. The results further include an experimental investigation of the conditioning by the serrated apertures. Then, a comparison between the predicted cross-correlation traces and the measurements with the Sequoia is made.

The last presented comparison is between measurements executed after the PTAS and in the X-ray lab.

4.8.1. Measurements of the Temporal Contrast in the X-Ray Lab

After predicting the rising edge caused by the stretchers in sec. 4.3.3, fig. 4.11 already showcased one temporal-contrast measurement for each stretcher configuration, in order to emphasize that the stretcher alone is not capable of explaining the measured rising edge.

As a reminder, with these measurements, I have demonstrated that switching to the unfolded stretcher improves the temporal contrast at PHELIX. However, comparing them to the prediction yielded that there is still a discrepancy between the measurement and the predicted rising edge. Besides the discrepancy in

the magnitude of the rising edge, the comparison also allowed the observation of a lack of the expected dependency on the in-stretcher beam size in the measurements. The predictions for the folded design already show a good agreement with the measured temporal profile. While it slightly underestimates the rising edge for larger times, this is within the area of uncertainty of the beam size on the folding mirrors in the stretcher.

Comparing the temporal profiles for each stretcher after the TW-compressor measured with EICHEL

The mentioned temporal-contrast measurements were executed using the EICHEL device after traversing through the regenerative amplifier and the TW-Compressor. The effect of the former has been ruled out in app. A.8 and the effect of the latter has been calculated in sec. 4.6.2. Based on this, the comparison between measurement and prediction is repeated - this time comparing the same measurements to the influence of the remaining beam path as well as the stretcher. An additional change to the previous depiction is that multiple traces are depicted for each configuration, instead of the best achieved temporal contrast.

As visible in fig. 4.25, the folded stretcher and unfolded stretcher with the sb are still expected to dominate over the TW-compressor for all considered configurations, for all relevant times. The only exception is the first 10 ps around the peak, for the unfolded stretcher design with the lb. Only in this configuration, the rising edge introduced by the stretcher is expected to be small enough to make the effect of the compressor visible.

The measurements after traversing the unfolded stretcher feature a kink in the rising edge at around 45 ps, a change of slope that can be attributed to a change in the dominating effect. For now, none of the investigated effects predicts a rising edge that can explain the fast feature at times smaller than 45 ps.

However, a good agreement is found between the measured slow feature and the predictions of the influence of the stretcher with the lb. As a reminder, this curve is limited by spatial clipping on the 50 mm mirrors at the input of the unfolded stretcher, as already stated in sec. 4.3.3.

For the folded design, various measurements are depicted, that have been executed over the course of one year. The systematic differences between the EICHEL measurements can be categorized in the cases "stretcher contrast" and two "winged contrast" configurations, denoted as "measurement config 2" and "measurement config 3". While the behavior of the first category stands in good agreement with the analytical predictions, as we have seen before (compare fig. 4.25), the latter features additional wings. These wings spread out of the stretcher contrast at around 100 ps and only drop below the detection limit at around 250 ps and 400 ps.
During the investigation of this effect, it has become clear that this is caused by a spectral-amplitude effect that can be described using eq. 2.24: damage on the folding mirror in the stretcher. The three cases of the EICHEL trace can be correlated to changes in the beam path. For the best contrast, the "stretcher contrast" the damage on the mirror is least visible in the spectrum. The worst configuration can be correlated to the most prominent dips in the spectrum. The case in-between can be correlated to a slight change in beam size at the stretcher input during maintenance of the frontend. The following discussion presents the measurements and calculations that support the conclusion that the damage on the mirror is causing the rising edge and shows how the observed correlations between the configurations are consistent with the analytical model and the parameter study discussed in sec. 2.2.2.

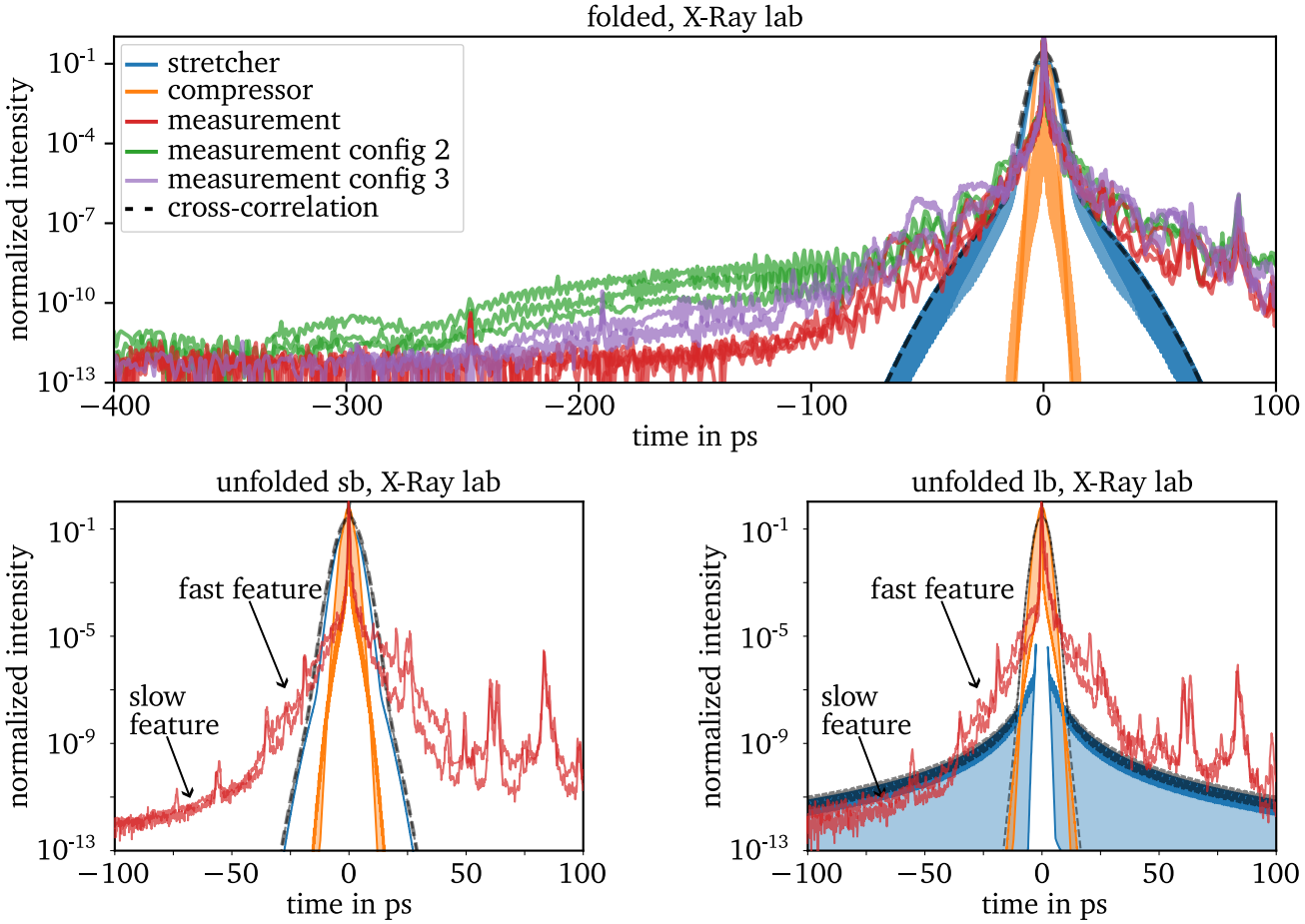

Figure 4.25.: Comparison between the measurements with the EICHEL detector and the influence of the different components of the PHELIX laser chain, sorted by the traversed stretcher setup. The shaded areas indicate the uncertainty, which is for the unfolded stretcher with the lb given by the degree of smoothing in the spatial profile between the aperture and the stretcher optics. Additionally included, are arrows pointing to the slow and the fast feature in the rising edge measured when traversing the unfolded stretcher. The transition between both features happens at a kink at around 45 ps. For the folded stretcher measurements, three different colors indicate different stretcher configurations.

Temporal-Contrast Manipulation by Controlled Introduction of Spectral Dips

After developing the analytical model necessary to calculate the rising edge for spectral amplitude modulation in sec. 2.2, I have already theoretically investigated the impact of spectral dips. The implication of the conducted parameter sweep was, that the width of the damage influences the oscillations in the rising edge and the beam size on the element influences the slope of the envelope.

In order to estimate whether this effect is capable of explaining the wings in the temporal profile of the folded stretcher, I have validated this model. I realized this by introducing dips into the spectrum, at various positions in the folded stretcher and measuring the resulting rising edge and spectrum. The corresponding measurements are depicted in fig. 4.26, where I have placed opaque objects with widths of w =1.3mm

and w =2.1mm, first in front of the folding mirror in the FF. In the reference spectrum on the left, we already see a spectral dip at 1052 nm, which is a known feature at PHELIX and is commonly agreed on being caused by damage on the folding mirror.

Comparing these measurements to the reference measurements, where no such object is employed, validates that such a dip can influence the temporal profile. It further shows the expected dependency on the width, being a change in the oscillation frequency, with an unchanged envelope.

Placing the object in the NF in front of the retro-reflecting mirror instead of the FF has two effects on the analytical description: first, it changes the dispersion coefficient a_ω, which influences both the envelope and the oscillation frequency of the sinc-function (compare eq. 2.39). Second and more important, it changes the beam size on the surface from the hundreds of µm-regime to the mm-regime (compare tab. A.1). As predicted by the analytical model, this increases the slope of the introduced rising edge enough for the effect to vanish behind the rising edge of the reference.

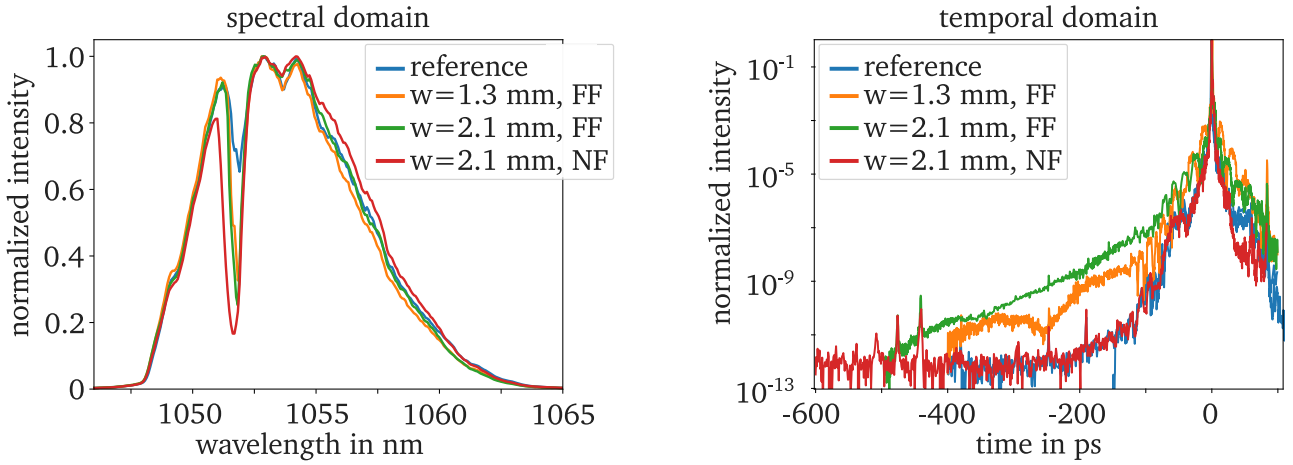

Figure 4.26.: Influence of spectral dips on the spectrum (left) and the temporal profile (right). All measurements were done for the beam path through the folded stretcher and the TW-compressor, with the EICHEL detector. For all measurements but the reference opaque objects with widths of 1.3 mm or 2.1 mm have been placed in the beam path, either at the folding mirror (FF) or at the retro-reflecting mirror (NF).

This proves that spectral dips can impact the temporal contrast, under the right circumstances (being mainly a small beam size). It is thereby strongly indicated, that the observed wings in the temporal contrast (compare fig. 4.27) are attributable to the damage on the mirror in the Fourier plane of the folded stretcher. This is further substantiated by the consistency with the predicted behavior: when increasing the beam size on the surface, the model predicts a drop in the rising edge. This is consistent with the observed change from "measurement config 2" to "measurement config 3", which is correlated to a slight change of the in-stretcher beam size during maintenance of the fs-frontend.

However, the causality is not conclusively confirmed, since this would require removing the damage from the mirror, which is not feasible. While replacing the mirror would have a similar effect, it would still not confirm the causality and is not necessary since the unfolded design omits this specific mirror while providing a better temporal contrast.
The following considerations employ the best effort configurations, where as little spectral clipping on the damage as possible is included.

Comparison of the measured temporal profiles using EICHEL and Sequoia

In this section, the comparison between the temporal profiles measured with EICHEL and with Sequoia is provided, for two purposes. The first purpose is the validation that both devices measure similar traces. The second purpose is the evaluation of the predicted artifacts in the Sequoia trace, according to sec. 4.7.

It is to note that, the comparison is restricted to the dynamic range of the Sequoia of nine orders of magnitude.

The measurements for the unfolded stretcher, which are depicted in fig. 4.27 are conducted parallel to each other. This means, that both devices measured simultaneously, at the same measurement point, only separated by a beamsplitter. However, the scanning process of both devices was not synchronized, so they did not use the exact same laser pulses for the same point in time. Nonetheless, this procedure should ensure comparability between the traces.

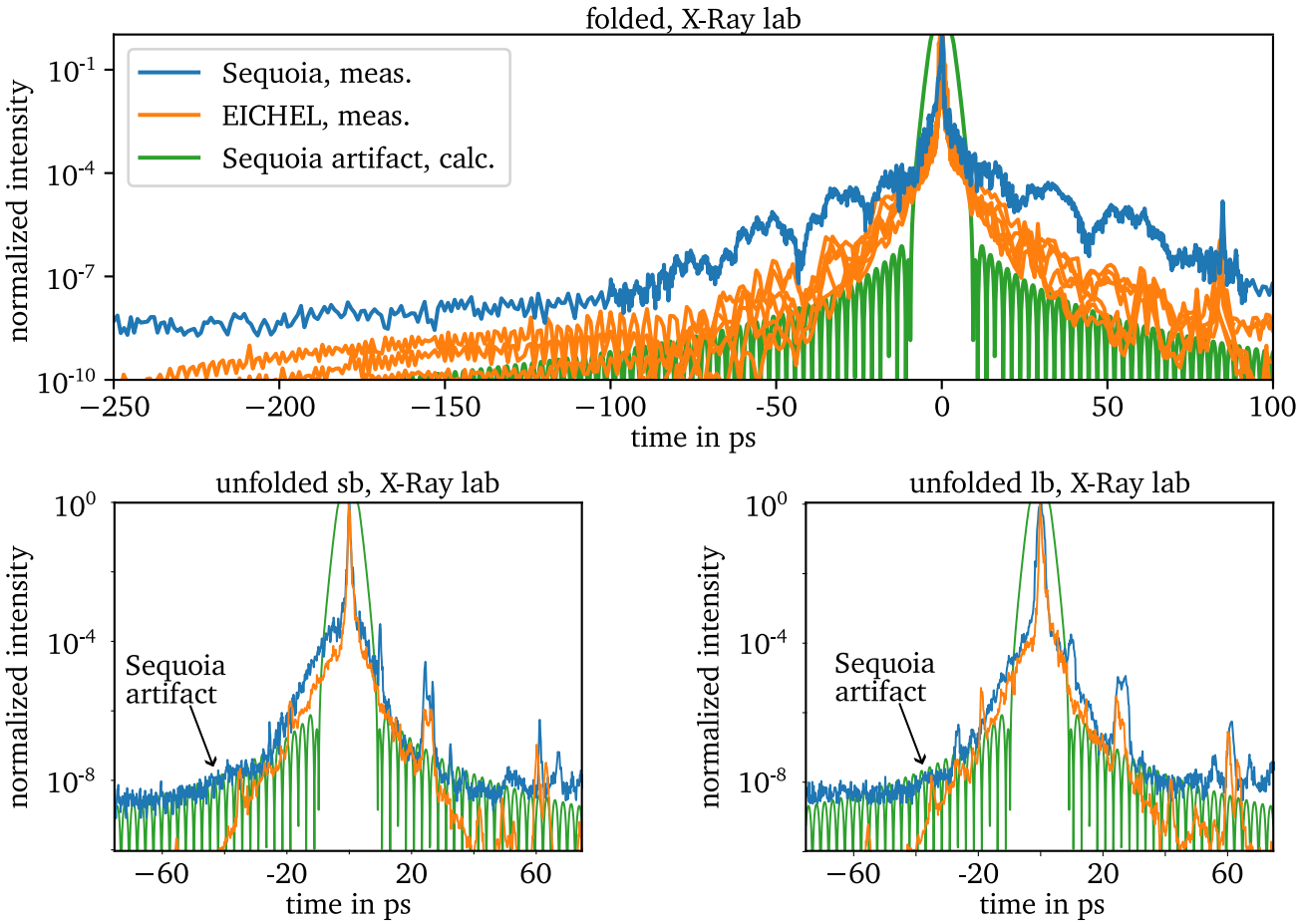

Figure 4.27.: Comparison between the rising edge measured with the EICHEL detector and the Sequoia detector after the beam is stretcher in the folded stretcher (top) or unfolded stretcher with a large in-stretcher beam size (bottom, right) or a small in-stretcher beam size (bottom, left) and recompressed in the TW-compressor. Additionally included is the expected effect of the apertures in the Sequoia, as calculated in sec. 4.7. For the folded design, statistics of the PHELIX contrast are provided, measured over one year.

For the unfolded stretcher, the slope of the rising edge is similar for both devices, indicating a common source of this rising edge. Therefore, it is likely that the cause for the fast feature is outside of the detectors, in a shared part of the beam path.
The traces only differ qualitatively for times further from the peak than 30 ps, where the EICHEL trace drops unchanged, but in the Sequoia trace an additional, slow feature in the rising edge becomes visible, denoted to as "Sequoia artifact" in the figure. Additionally included is the predicted Sequoia artifact, caused by spatial clipping in the detector (compare sec. 4.7). The predicted influence of the Sequoia on the rising edge shows a good agreement with the measurements. It can thus be interpreted as a possible explanation of the differences in the measurements between the detectors. However, the dynamic range in which this difference is visible is small and the implications of the analytical model required for this influence of the devices is yet to be validated or disproved.

While I can report a good agreement for the unfolded stretcher, the measurements for the folded stretcher show a notable difference between the two detectors. It is essential to note that the comparison between the detectors with the folded stretcher relies on a large number of available measurements with the EICHEL, as opposed to a synchronized measurement process. For the EICHEL the large number of available measurements provides a statistical margin of uncertainty that rules out that the discrepancy is caused by a measurement error for the EICHEL measurements. It is, however, possible that the depicted Sequoia trace is caused by a measurement error, e.g. a drop in laser energy during the scanning process has gone unnoticed, which can lead to an overestimation of the wings. If this is the case can be investigated in further research, by repeating the measurement. However, since no such repeated measurements are currently available, it is necessary to consider that this is a real feature that the current analytical predictions fail to explain. As such, this discrepancy is a further indication that the cross-correlators influence the temporal contrast.

4.8.2. Measurements of the Temporal Contrast in the PTA

After investigating the temporal contrast in the X-ray lab, the influence of the stretcher on the temporal contrast measured at the PTA is investigated, as well as the influence of the serrated aperture. Measuring at the PTA is crucial for characterizing the temporal contrast at PHELIX since this is closer to the on-target contrast during experiments. While previous to establishing the unfolded stretcher at PHELIX the contrast was fully limited by the folded stretcher, rendering the contrast equivalent at each measurement position, it would be premature to assume this for the unfolded stretcher as well.

Equivalent measurements to the ones in the X-ray lab are conducted at the PTA after the PTAS, with the Sequoia. The comparison between the measurements for the two in-stretcher beam sizes in the unfolded stretcher and the folded stretcher is depicted in fig. 4.28. Contrary to the measurements done in the X-ray lab, these measurements show clear conditioning by the in-stretcher beam size. They further show an even larger improvement in the rising edge between the folded and the unfolded stretcher. With this, I can report an achieved rising edge contrast at PHELIX of $5.7 \cdot 10^{-10}$ at -30 ps.

Similar to the measurements in the X-ray lab, the measurements with the unfolded stretcher show two distinct features, this time with a transition at -5 ps for the lb an 13 ps for the sb, both at a contrast of six orders of magnitude.

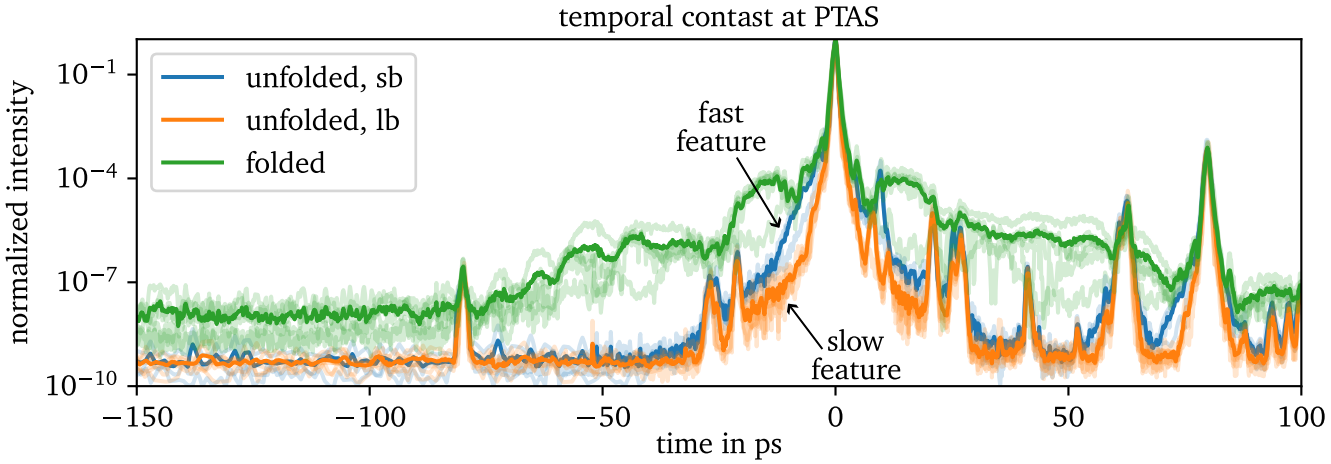

Figure 4.28.: Comparison between Sequoia measurements after the PTAS. Included are several measurements for the beam path through the folded stretcher and the unfolded stretcher with lb and sb, as well as the mean of all measurements for each configuration. The faint lines correspond to statistical measurements, which are averaged to form the prominent line. Additionally included are pointers to the fast and the slow features in the rising edge.

In the following, these measurements are compared to the corresponding predicted profiles in order to identify the limiting factors. Since, by now a large number of different effects that condition the rising edge have accumulated, the variables are narrowed down prior to the comparison. One of the additional variables in the beam path to the PW-compressor, that is expected to condition the rising edge is the serrated aperture configuration (compare sec. 4.5).

Measurements of the Temporal Contrast in the PTA Depending on the Serrated Aperture

The experimental investigation to asses whether the rising edge at PHELIX can be manipulated through the serrated aperture configuration utilizes the beam path through the unfolded stretcher in the lb configuration. Since this configuration provides the cleanest temporal profile (compare fig. 4.28), this selection should maximize the detectability of the conditioning by the serrated aperture.

The results of these measurements for the two serrated apertures A1 and A11 and the empty substrate (no SA) are depicted in fig. 4.29, together with the corresponding predicted rising edges introduced by the PW-compressor, according to sec. 4.6.1.

While the remaining rising edges in these measurements are similar to the predicted rising edges, no dependency on the serrated aperture can be reported in the measurements. For all measured traces the temporal intensity decreases below the detection threshold at around 30 ps. Since the measured rising edge is higher than the expected rising edge for the serrated apertures A1 and A11, it is likely that the influence of the serrated aperture is overshadowed by a more prominent effect.

Further investigations of this effect require either a cleaner contrast, a higher dynamic range than the Sequoia is capable of, or an aperture with a more prominent impact on the rising edge. For now, the presented comparison yields the conclusion that the remaining rising edge at PHELIX is not conditioned by the choice of the serrated aperture, eliminating this variable for further consideration.

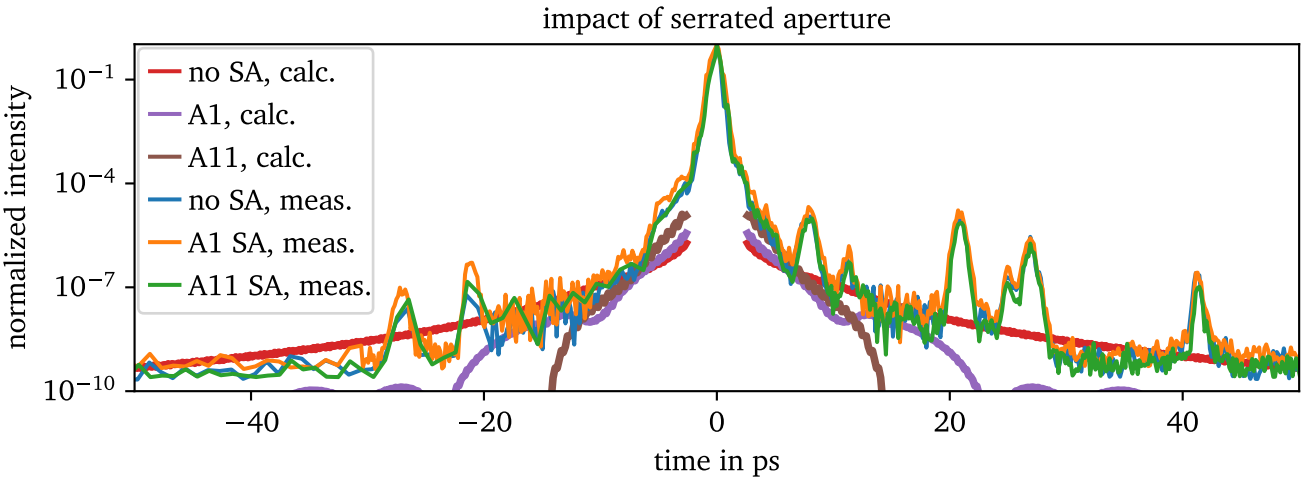

Figure 4.29.: Comparison between the measured rising edge and the predicted rising edge, depending on the choice of the serrated aperture. All measurements are done with the lb in the unfolded stretcher using the Sequoia after the PTAS. For better visibility, the fast oscillations in the calculated curves are smoothed with a narrow moving average.

Comparing the Measured Temporal Contrast at the PTAS to the Predictions

With this, most considered effects in the PW-compressor are ruled out as dominating factors in the rising edge.

The first eliminated effect was that of spectral-amplitude effects in the PW-compressor (compare sec. 4.6.1), as the considerations of consecutive clipping have led to no change in temporal profile.

The second effect that was eliminated is spectral-phase effects in the PW-compressor, due to spatial conditioning by the serrated apertures. In the previous consideration, no conditioning by the serrated apertures was observed. Instead, the measured rising edges have shown a good agreement with the case without a serrated aperture, where the interaction is dominated by spatial clipping on the rods in the PA. Thus, the following considerations neglect the serrated aperture and only employ spectral-phase effects in the PW-compressor for a beam that is spatially clipped on the PA rods.

The last effect that can be ruled out is that of the Sequoia since it made no significant contribution during the prediction for any considered configuration in the PW-compressor (compare fig. 4.24).

Thus, for the PW-compressor only the spectral-phase effects remain, for beams that are spatially clipped on the PA rods.

Besides this, the only other remaining contribution to the expected rising edge is that of the stretcher, which remains unchanged from the considerations in the X-ray lab (compare fig. 4.25).

The comparison of these effects to the corresponding measurements is depicted in fig. 4.30.
In the case of the unfolded stretcher with the sb (bottom left), the fast feature in the rising edge between the peak and ± 13 ps, shows a good agreement to the predicted influence of the stretcher.
For the lb, the fast feature (± 5 ps) is underestimated by all current considerations, indicating an unknown source of the limitation. For the slow features, the rising edge shows a good agreement to the effect of the PW-compressor, with spatial clipping in the PA.

However, the magnitude of this feature changes with the in-stretcher beam size. This fact, which is better visible in fig. 4.28, challenges the notion that the slow feature is caused by the PW-compressor. A possible explanation is that for the sb the temporal contrast is still limited by the stretcher, but for lb the calculations indicate that the temporal contrast is instead limited by the compressor.

The predictions for the folded design underestimate the observed rising edge by two orders of magnitude. This is similar to the discrepancy observed for the folded stretcher between measurements done in the X-ray lab using EICHEL and Sequoia (compare fig. 4.27). A comparison between both measurement locations is provided in the next section.

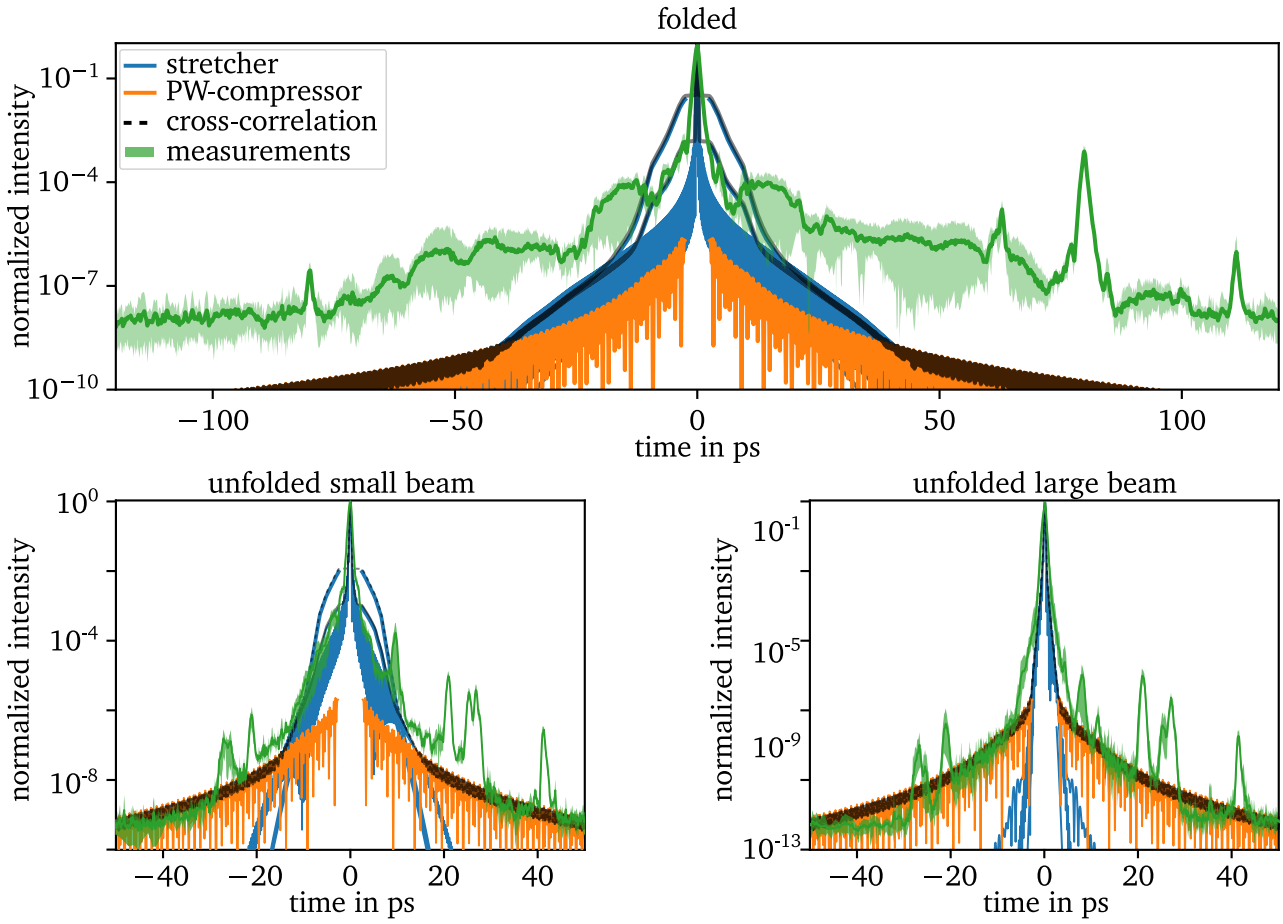

Figure 4.30.: Comparison between the rising edge measured with the Sequoia detector after the PTAS and the expected trace. The expected traces take clipping and PSD effects in the stretcher into account, as well as, the spatial clipping in the PA. Additionally included is the combination of all effects via addition and the corresponding cross-correlation. The measurements are depicted as the mean value over several measurements (full line) and the peak-to-valley of these measurements (shaded area).

4.8.3. Comparison between the Temporal Contrast in the X-Ray Lab and the PTA

Upon discussing the origins of the rising edge for all beam paths and measurement locations, the next step is to compare the two measurement locations to each other, as depicted in fig. 4.31.

Starting with the folded stretcher, the measurements show oscillating features and disturbances in the traces for all three configurations. The Sequoia shows a higher rising edge than the measurements with the EICHEL, as discussed when first showing the measurements of the folded stretcher with the Sequoia in fig. 4.27. It also produces a higher temporal contrast in the X-ray lab than in the PTA.

This relationship between the three measurement configurations is consistent with the measurements done for the unfolded stretcher. All measurements done at the PTA produced rising edges that are better (lb) or equal (sb) to the rising edges measured at the X-ray lab.

For the sb the rising edge measured after the PTAS, is almost identical to the EICHEL measurements in the X-ray lab. Over the resolvable range, the average slope of both traces is similar.
The only notable difference is that the Sequoia trace shows the discussed kink at $-13\,\mathrm{ps}$ and the EICHEL trace shows one, continuous slope. This can either point to different sources of the rising edge or to a measurement artifact.

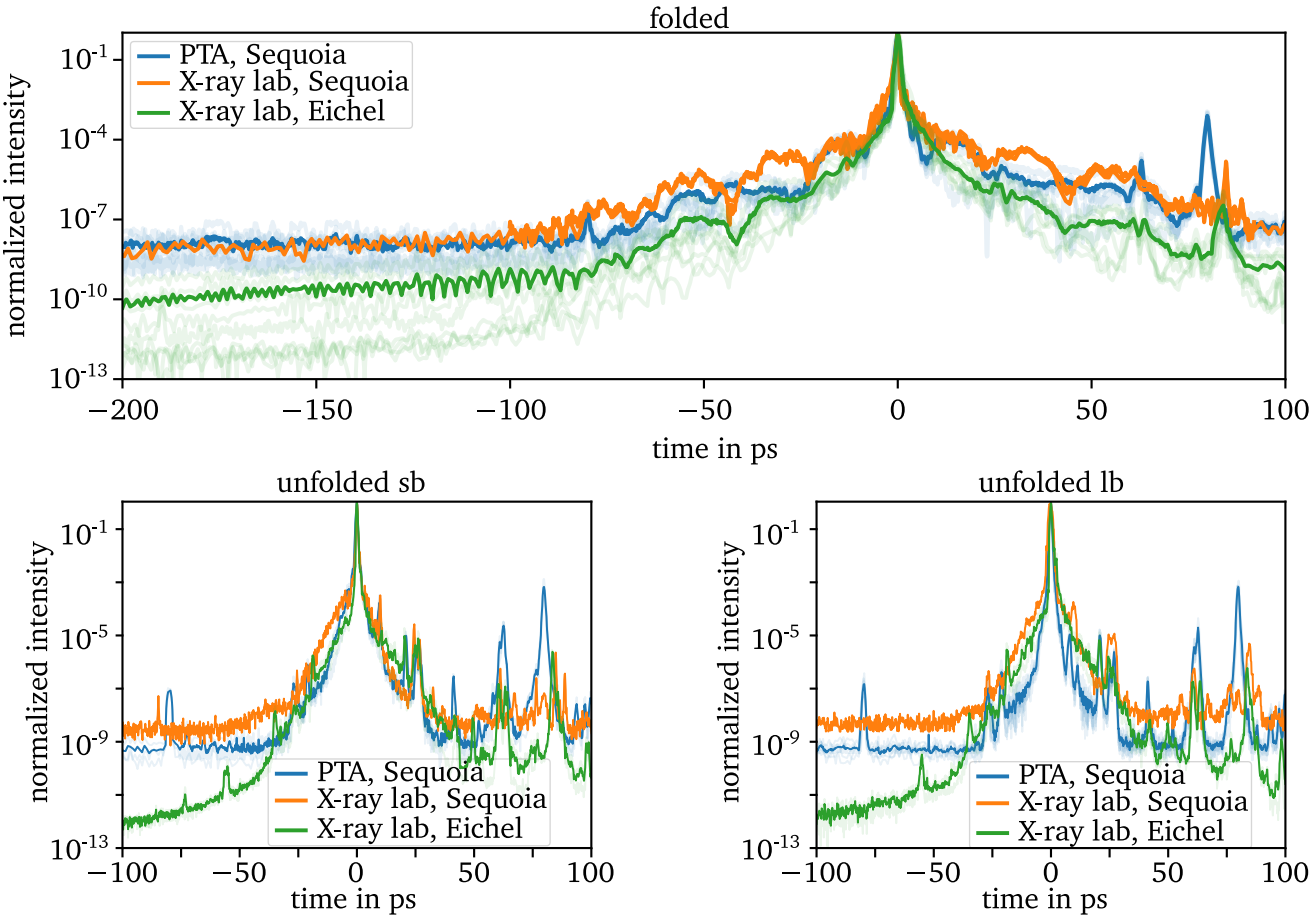

Figure 4.31.: Comparison between EICHEL and Sequoia measurements for all beam paths, sorted by the traversed stretcher configuration.

The measurements in the X-ray lab show a more prominent slow feature (compare fig. 4.25), which previous analysis attributed to the Sequoia. The fact feature is less pronounced in the PTA is consistent with this explanation, since the expected impact of the Sequoia is smaller in the PTA than in the X-ray lab.

A large discrepancy between the different measurement locations is evident in the measurements in the configuration with the lb in the unfolded stretcher. This allows the conclusion that it is no longer valid to assume that temporal-contrast measurements in the X-ray lab represent the temporal contrast in the PTA. It may lead to the speculation that the measurement location in the X-ray lab could be used as an upper-limit measurement for the rising edge contrast. However, this hypothesis is invalidated by the measurements for the folded design. In this case, the measured rising edge at the PTA is larger than the one measured with the EICHEL in the X-ray lab. Consequently, these conflicting outcomes suggest that measurements in the X-ray lab cannot reliably be used to determine an upper limit for the rising edge contrast, across these different configurations.

4.9. Conclusion on the Rising Edge at PHELIX

Over the course of the previous sections, several implications of the rising edge formation have become clear, which lead to conclusions, either directly from the comparison between measurements or by comparison from measurements with the behavior predicted by the analytical model.
This section presents the conclusions that the available measurements and analytical predictions allow.

Spatial clipping is a valid explanation for the slow feature observed in the temporal-contrast curves for the unfolded stretcher
All measurements for the unfolded stretcher show two distinct features. The one with the shallower rising edge, which dominates at times further from the peak intensity, is in the context of this thesis called the slow feature. Comparison between measurements and predictions of the impact of spatial clipping have shown a good agreement to observed slow features.
Examples of this are the calculations of the impact of spatial clipping on a slit in sec. 4.4.1, needles in sec. 4.4.2, a mirror prior to the unfolded stretcher in sec. 4.3.3 and in the Sequoia in sec. 4.8.3.

When employing the sb in the unfolded stretcher, the rising edge at the PTA is still limited by the stretcher
It is evident that the temporal contrast measured at the PTA is still limited by the unfolded stretcher when employing the sb. This becomes clear due to the observed dependency of the rising edge on the beam size. The fact that the rising edge predicted for the stretcher agrees almost perfectly with the measurements corroborates this further.
For the lb, the contrast may not be limited by the stretcher itself any longer, with spatial effects emerging as a possible limiting factor.

The rising edge at the X-Ray lab is not limited by the unfolded stretcher

During the comparison between the measurement locations, a similarity became apparent between the rising edge measured in the X-ray lab with the EICHEL and in the PTA with the Sequoia, for the sb in the unfolded stretcher. This might suggest that those two rising edges are causally connected, with a likely source of the rising edge in the stretcher. This is corroborated by the previous conclusion that this configuration is still limited by the stretcher when measuring in the PTA.

However, over the course of this work, it has become evident that the in-stretcher beam size conditions the slope of the rising edge. I already validated this during the PoP (compare cha. 3) and it has become evident again for the measurements after the PTAS (compare sec. 4.8.2).

The fact that this dependency on the in-stretcher beam size is not present for any measurements in the X-ray lab with the unfolded stretcher provides strong evidence that suggests that the temporal contrast is not limited by the stretcher in this configuration.

Thus, the observed similarity between the curves is discarded as coincidental. Nonetheless, the conclusion that the same stretcher configuration limits the temporal profile in the PTA, together with the similarity of the curves, suggests that the unfolded stretcher in the sb configuration and the TW-compressor are almost equally detrimental to the temporal profile.

Components beside the stretcher begin to shift into attention as limiting factors of the rising edge contrast

A direct conclusion of the previous statement is that we must investigate the impact of other components in order to further improve the rising edge contrast. This thesis has thus, besides the stretcher, begun an investigation of regenerative amplification stages, beam shaping stages like serrated apertures, compressors, and detectors.

Acceptable measurement points for the temporal contrast at PHELIX

For the folded stretcher, it was generally assumed that the rising edge is limited by the stretcher and it is thus irrelevant at which compressor the characterization of the temporal contrast took place. The presented measurements which were conducted in the X-ray lab and the PTAS do not support this assumption, neither for the folded stretcher nor for the unfolded stretcher (compare sec. 4.8.3). For the folded stretcher the observed discrepancy must, however, be reproduced in order to rule out potential measurement errors.

For the unfolded stretcher, the discrepancy is more conclusive, since the temporal contrast is not limited by the stretcher when measuring in the X-ray lab.

Accordingly, the drawn conclusion is that it is not valid to measure the temporal contrast in the X-ray lab in order to estimate the temporal contrast in the PTA. Further, it is not advisable to utilize the measurement point in the X-ray lab as an upper estimate of the rising edge, since the folded stretcher produces a worse rising edge when measuring in the PTA, than when measuring in the X-ray lab with the EICHEL

The temporal contrast at PHELIX is currently not limited by the serrated aperture

The measurements in the PTA did not yield any dependency of the rising edge on the choice of the serrated aperture. Instead, the observed magnitude of the rising edge is currently overshadowing the expected effect (compare sec. 4.8.2).

The conclusion this observation allows is that the temporal contrast is currently not limited by the serrated aperture. However, the analytical model predicts that this dependency becomes visible when further improving the temporal contrast at PHELIX.

5. Discussion

The following discussion summarizes the findings of this manuscript, starting with the implications of the analytical models. These implications are a summary of the most important new physical understandings provided in this manuscript. Beyond this, implications for high-intensity laser systems are presented, which include possible improvements to a CPA laser system in the context of the rising edge contrast and realized improvements at PHELIX. Lastly, the discussion shifts to implications for the research of laser-plasma physics and revisits the hydrodynamic simulations from the introduction of this thesis. The purpose of revisiting the simulations is to illustrate how the achieved improvements of the rising edge influence the preplasma expansion during experiments.

5.1. Implications of the analytical model

In this thesis, I have discussed how the components of a CPA laser chain cause the temporal-contrast degradation that is commonly referred to as the temporal pedestal or the rising edge. The first effect I have studied is the surface disturbance of mirrors. While those are normally a concern for the beam shape and not the temporal profile, the effects become coupled into the temporal domain when the beam is spectrally dispersed during an interaction with the disturbed surface. This effectively imprints the surface disturbance into the spectral phase. A second effect I have studied in this context is spectral clipping, or more generally spectral amplitude modulations.

Based on mainly those two effects, I have expanded on existing models that are designed to predict the rising edge formation in CPA laser systems (compare cha. 2). My contribution to the existing models is that this model for the first time incorporates spatial frequency averaging due to the diffraction of the beam and the spatial conditioning of the beam profile.

I executed the necessary measurements to predict the rising edges introduced by a stretcher with a telescope based on concave spherical mirrors. During a PoP I measured the corresponding temporal traces and validated the developed model (compare cha. 3). Doing so allowed me to validate several implications of the model, which are listed below. Note, that the two last of the listed implications were not validated during the PoP setup but with the setup at PHELIX.

The beam size on the considered surface conditions the slope of the introduced rising edge

The most important implication of my analytical model is that the rising edge scales with the absolute square of the Fourier transform of the beam profile on the considered surface. Thus, a larger beam size on the surface produces a narrower rising edge, for ideal Gaussian beam profiles. In this context, the spatial beam smooths the temporal-contrast-compromising effects. This statement can be made for both, spectral-phase effects and spectral-amplitude effects on the surface.

Spatial clipping conditions the rising edge

The previous statement can be refined by considering other profiles besides the Gaussian. As stated, the rising edge scales with the absolute square of the Fourier transform of the beam profile on the surface, based on the developed model. Thus, the shape of the beam profile is correlated to the rising edge rather than just the beam size. I validated this by manipulating the shape of the beam on a stretcher surface, by employing an aperture and needles in the beam path prior to the stretcher (compare sec. 4.4). The presented study suggests that the previous statement can be adapted to: the Fourier transform of the spatial beam profile is imprinted into the temporal profile of the laser pulse.
This way of phrasing suggests that a larger beam size is not always beneficial for the temporal contrast. Instead, it appears to be desirable to achieve a beam profile on the considered surface, where the Fourier transform exhibits a rapid decrease in intensity, e.g. a Gaussian.

Spectral clipping conditions the rising edge

The main concern of spectral-amplitude effects in CPA systems is that of spectral clipping on the free apertures of the optics. The analytical implication, that any spectral clipping modulates the FTL of the laser pulse, is well understood. In earlier generations of CPA laser systems, it was commonplace to utilize spectral clipping in the Fourier plane of the stretcher to adjust the pulse length [122].
However, it has, to the best of my knowledge, never been observed as the limiting factor of the temporal contrast of high-intensity laser systems. Nor has it been utilized for controlled manipulation of the temporal contrast. In the frame of this work, both were realized (compare sec. 2.2.2). By inserting a needle in the beam path in the stretcher, I was able to introduce a rising edge. I was further able to alter the shape of this rising edge by changing the size of the needle. The observed alterations stand in qualitative agreement with the expected behavior based on the conducted analytical calculations (compare sec. 4.8.1).

5.2. Implication for high-intensity laser systems

The goal of this work is to facilitate laser systems around to globe to perform experiments with the highest demands on the temporal contrast, by improving our current understanding of the rising edge formation. The implications summarized in the preceding section hold substantial relevance in this context, as they allow a purely optical manipulation of the slope of the rising edge. In the following, conclusions are stated for the design of pulse stretchers, that utilize these findings in order to optimize the rising edge. Further, the results of the successful implementation of these design guidelines are summarized, in the form of the achieved rising edge contrast improvements at the PHELIX laser.

The folding mirror in the stretcher limits the rising edge

Most high-intensity laser facilities employ a folding mirror in the Fourier plane, either a flat mirror for Banks designs or a concave mirror for Öffner designs. This is generally the stretcher optic where the beam size for each individual wavelength is the smallest.
In previous studies, the hypothesis was formulated that this element dominates the rising edge formation due to the small on-element beam size, which was substantiated by ray-tracing simulations. Multiple faculties have since then utilized this for temporal-contrast improvements, thereby experimental validating that the rising edge formation is dominated by the folding mirror in the Fourier plane.
The contribution of this work to this field is, besides an analytical model capable of predicting this behavior, evidence to the hypothesis that the folding mirror dominates due to the small on-element beam size.

Unfolding the stretcher is beneficial to the temporal contrast
The previous statement that the folding mirror in the stretcher limits the rising edge contrast, allows the conclusion that omitting this mirror, by employing an unfolded design, can increase the temporal contrast. While this was already previously experimentally validated, this manuscript provides additional reasoning and analytical understanding behind this design choice.

The slope of the rising edge can be manipulated by employing a telescope prior to the stretcher
During the validation of the in-stretcher beam size dependence of the rising edge, it has become evident that a telescope prior to the stretcher can be employed for manipulation of the rising edge. The validity of this novel technique was further demonstrated at PHELIX, where a magnification prior to the stretcher has proven to enhance the temporal contrast.

PHELIX is now capable of achieving an temporal contrast of $5.7 \cdot 10^{-10}$ orders below the peak intensity in 30 ps With this controlled manipulation of the in-stretcher beam size and thus of the rising edge I was able to improve the rising edge contrast at PHELIX to $5.7 \cdot 10^{-10}$ orders of magnitude below the peak intensity in 30 ps.

5.3. Implications for Laser-Plasma Physics

The introduction of this work motivated the necessity for novel techniques for temporal-contrast control by showing the influence of the rising edge on an 100 nm tick target with the help of hydrodynamic simulations (compare sec. 1.1.2). These simulations were executed using distinct rising edges, differentiated by their individual steepness, scaled to the peak intensity of PHELIX. Now, to conclude this thesis, fig. 5.1 shows these simulations again.
While the used temporal-contrast curves were useful to motivate the importance of the rising edge for laser-plasma interactions, they also show the estimated impact of the temporal-contrast improvement on the preplasma expansion at PHELIX. Both curves correspond to different temporal profiles measured in the frame of this work at PHELIX. Since the focus of this work is the rising edge contrast, all pre-pulses in the used temporal profiles were neglected for the simulation.

The shallower of the slopes is a rising edge measured for the folded stretcher with the EICHEL in the X-ray lab. This curve represents the temporal contrast at PHELIX prior to my work. The corresponding simulation produced a significant disturbance of the target conditions, with a preplasma expansion length of 0.67 µm, measured between peak density and critical density, and a scale length of 146 nm at the relativistic critical density.

The steeper curve was measured for the unfolded stretcher in the PTA, with the Sequoia. This is the configuration that provides the best temporal contrast, of the configurations at PHELIX investigated in the frame of this thesis, in the frame of this work. It is further, to the best of my knowledge, the best rising edge contrast achieved with PHELIX, to this day. Contrary to the other curves, the preplasma expansion is almost a factor of three smaller with an expansion length of 0.29 µm and a scale length of 54 nm at the relativistic critical density.

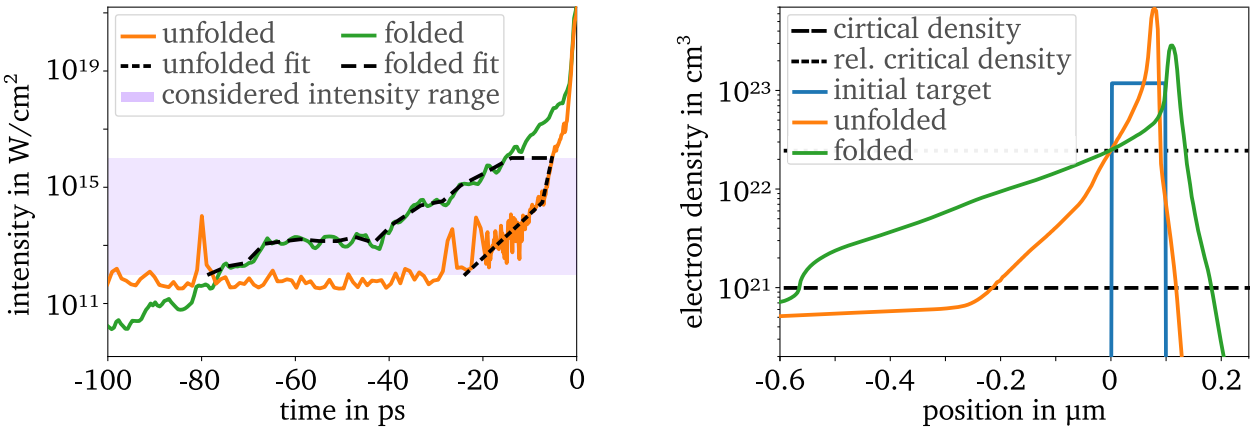

Figure 5.1.: Expected impact of different temporal laser profiles (left) on the target pre-expansion (right) for a thickness of 100 nm. The orange curve shows the temporal contrast using the unfolded stretcher at PHELIX with an Ib size, measured with the Sequoia after the PTAS. The red curve was also measured in the X-ray lab with the EICHEL, but the folded stretcher was traversed instead of the unfolded. All profiles have been upscaled to a peak intensity of $1.4 \cdot 10^{21}$ Wcm^{-2}. The corresponding hydrodynamic simulations using the Flash2D code were performed with the assistance of P. Boller for an intensity range between 10^{12} and 10^{16} W/cm^2, which is indicated by the shaded area in the left-hand side figure. The corresponding simulated free electron densities for the different temporal-contrast conditions are depicted on the right-hand side. Additionally included are the initial density distribution of the 100 nm target, the critical density, and the relativistic critical density. In the plot of the temporal profiles.

The simulations suggest that the preplasma conditions during experiments at PHELIX can in the future be improved, with the upcoming installation of the new front end, and the corresponding pre-pulse and ASE-contrast [111], as well as with a possible transition of the unfolded stretcher into the standard configuration of PHELIX.

While the unfolded stretcher will only become available for users at PHELIX after being transitioned from a test setup to a more robust implementation, a first test of the expected impact in laser-plasma experiments is planned during an experimental campaign. In the frame of this campaign, PHELIX will be used for the generation of a secondary particle source, focusing on the regime of relativistic transparency. A back-reflection diagnostic will be employed, able to measure plasma scale lengths in the sub-micrometer range [123]. It can thus be used to measure the impact of the temporal-contrast improvements with the unfolded stretcher, thereby verifying the expected impact in fig. 5.1. During the experimental campaign, the plasma parameters will be controlled by the introduction of a pre-pulse in order to scan for ideal parameters for the ion acceleration process. In this context, the improved rising edge contrast can improve the precision of the preplasma manipulation.

The insights gained in this thesis, provide the means for laser facilities to improve their rising edge contrast by implementing unfolded stretcher designs and by using telescopes to condition their rising edge. They further provide the means to understand a large portion of rising edge introducing effects.

However, even when these improvements are enough to enable research of effects at the highest intensities, the strive for even higher intensities continues and so must therefore our strive for an ever-cleaner temporal profile. Thus, this thesis ends with an outlook on the field of the rising edge contrast.

6. Outlook

The first aspect discussed in this outlook encompasses potential improvements to the analytical model, in order to predict rising edges more accurately, for smaller times and to test implications that are as of now not validated.
The second aspect is a discussion of additional effects that can be considered in the calculation of the rising edge when the temporal contrast is no longer fully limited by spectral-phase effects. Due to the temporal-contrast improvements achieved in the frame of this thesis, it is necessary to revisit this assumption.

Extension of the model to two spatial dimensions

A potential improvement of the model is the extension of the model to two dimensions. This has already been done, even without the need for assumptions, in previous research [97]. However, this approach does not employ spatial frequency filtering, which is a key component of the model described in this work. This improvement of the model should increase the accuracy of the calculation in general.

Unifying the description of spectral amplitude and Spectral-Phase effects into one equation

In the frame of this work, spectral clipping and spectral-phase effects are treated as fully independent from each other, even though analytical calculations presented in app. A.4 indicate that this is not the case. Advancing the model into one equation for the temporal profile that incorporates both effects could substantially augment our comprehension of the rising edge.

Testing further implications of the analytical model

Besides mathematically improving the analytical model it is also promising to experimentally test unresolved implications of the model. This would provide valuable insight into the model's applicability and fidelity.
One of the concepts validated in this thesis is that a slit in the image plane of the spherical mirror of the stretcher conditions the rising edge. However, in the design used for this validation the beam path of the incoming and outgoing beam overlap at the image plane. Only after the image plane they are sufficiently spatially separated to manipulate them separately from each other.
A so far purely theoretical implication of the analytical model is that spatial clipping can influence the rising edge, even when the spatial clipping occurs after the rising edge is introduced. This statement could be experimentally tested in a similar setup, adapted in such a way that it is possible to employ the slit only in the image plane of the outgoing beam, without influencing the incoming beam.
Another implication of the model, which is also yet to be tested, is that spatial phases condition the shape of the rising edge. This hypothesis is grounded in the implication of the model that the Fourier transform of the spatial profile is imprinted into the temporal profile.

Testing this hypothesis requires a setup where the spatial phase on the surface of stretcher elements can be manipulated without changing the intensity profile of the beam on the surface. This decoupling of the beam size and the spatial phase is required in order to avoid overshadowing a potential impact of the spatial phase with the impact of the beam size.

Incorporation of dust particle distributions in theory and experiment

Previous research based on ray-tracing suggests that spectral-amplitude effects produce a slow rising edge, with a slope increasing towards the peak intensity [99]. This is a familiar feature in many of the measured temporal profiles presented in this manuscript. While it is evident from this manuscript that spatial clipping can be the source of the slow features, they can also be caused by small spectral amplitude perturbations, e.g. absorbing dust particles distributed over the surface [99].
Further research is required to identify the source of this slow feature and eventually eliminate it. In an analogous approach to the incorporation of the PSD for the spectral-phase effects, this can be realized by extending the analytical description of spectral-amplitude effects in such a way that it utilizes a spatially resolved reflectivity measurement of the surface. Under the assumption that this is mainly conditioned by the dust particles on the surface, a numerical representation of the dust particle size and distribution might be sufficient for this task.

Extending the scope of considered elements beyond the stretcher

The achieved improvement of the rising edge introduced in the stretcher enabled measurements of temporal profiles that are in all likelihood no longer limited by the stretcher. This emphasizes that other elements besides the stretcher must be considered for further temporal-contrast improvements.
In the case of PHELIX, this encompasses the consideration of the serrated aperture, spatial clipping in the pre-amplifier, the compressor, and the parabola, with the inclusion of the latter being due to the single-pass design of the compressor.

Closing remarks

In this work, the overarching motivation was that the temporal contrast currently limits many novel applications of ultra-intense lasers. In particular, the rising edge in the temporal profile has gained relevancy over the past years, as it is yet to be fully understood.

The goal of this thesis was to contribute to laser technology in such a way that the generation of the rising edge can be reduced, in order to decrease preplasma expansion and thereby create conditions that facilitate novel experiments. Deepening our understanding of the origin of the rising edge and improving our control over its shape were essential means to accomplish this primary goal. The central insight gained in this thesis is the demonstration of the relationship between the beam size on a stretcher surface and the shape of the introduced rising edge.

Based on this insight, a technique has been developed and demonstrated, which incorporates the dependency of the rising edge on the beam size into a stretcher design for CPA systems. This design omits the folding mirror in the Fourier plane, thereby avoiding the interaction with the smallest beam size. It further incorporates a beam expander to increase the NF beam size on all elements, thereby increasing the slope of the rising edge. This is a novel, purely optical approach to control the temporal contrast of CPA lasers.

As stated in the introduction of this thesis, the achieved peak intensities are ever-increasing, and so are therefore the demands on the temporal contrast. In a future with peak intensities far beyond the current technological limit, it is therefore of paramount importance to focus our attention on the development of techniques that avoid the introduction of the rising edge.

The contribution of this manuscript to laser technology aims at providing such a technique that will facilitate tomorrow's breakthroughs in the research of the interaction between light and matter at the highest intensities.

Bibliography

[1] S. Roeder *et al.*, How the Laser Beam Size Conditions the Temporal Contrast in Pulse Stretchers of Chirped-Pulse Amplification Lasers, High Power Laser Science and Engineering, **10**:e34, 2022, doi:10.1017/hpl.2022.18.

[2] T. H. Maiman, Stimulated Optical Radiation in Ruby, Nature, **187**(4736):493–494, 1960, doi:10.1038/187493a0.

[3] A. L. Schawlow, Spectroscopy in a New Light, Reviews of Modern Physics, **54**(3):697–707, 1982, doi:10.1103/RevModPhys.54.697.

[4] W. Demtroeder, Laser Spectroscopy 1: Basic Principles, Springer, New York, 5th Edition, 2014.

[5] P. A. Franken *et al.*, Generation of Optical Harmonics, Physical Review Letters, **7**(4):118–119, 1961, doi:10.1103/PhysRevLett.7.118.

[6] L. Radziemski *et al.*, A Brief History of Laser-Induced Breakdown Spectroscopy: From the Concept of Atoms to LIBS 2012, Spectrochimica Acta Part B: Atomic Spectroscopy, **87**:3–10, 2013, doi:10.1016/j.sab.2013.05.013.

[7] M. M. Günther *et al.*, Forward-Looking Insights in Laser-Generated Ultra-Intense γ-Ray and Neutron Sources for Nuclear Application and Science, Nature Communications, **13**(1):170, 2022, doi:10.1038/s41467-021-27694-7.

[8] T. Tajima *et al.*, Wakefield Acceleration, Reviews of Modern Plasma Physics, **4**(1):7, 2020, doi:10.1007/s41614-020-0043-z.

[9] A. Macchi *et al.*, Ion Acceleration by Superintense Laser-Plasma Interaction, Reviews of Modern Physics, **85**(2):751–793, 2013, doi:10.1103/RevModPhys.85.751.

[10] A. Kleinschmidt *et al.*, Intense, Directed Neutron Beams from a Laser-Driven Neutron Source at PHELIX, Physics of Plasmas, **25**(5):053101, 2018, doi:10.1063/1.5006613.

[11] J. Norem *et al.*, Triggers for RF Breakdown, Nuclear Instruments and Methods in Physics Research Section A: Accelerators, Spectrometers, Detectors and Associated Equipment, **537**(3):510–520, 2005, doi:10.1016/j.nima.2004.07.289.

[12] N. Dover *et al.*, Enhanced Ion Acceleration from Transparency-Driven Foils Demonstrated at Two Ultraintense Laser Facilities, Light: Science & Applications, **12**(1):71, 2023, doi:10.1038/s41377-023-01083-9.

[13] J. H. Nuckolls, LLNL, Early Steps toward Inertial Fusion Energy (IFE) (1952 to 1962), Technical Report UCRL-ID–131075, 658936, Lawrence Livermore National Lab. (LLNL), Livermore, CA (United States), 1998, doi:10.2172/658936.

[14] S. E. Hunyadi Murph *et al.*, 4 Nuclear Fusion: The Promise of Endless Energy, in M. A. Benvenuto *et al.* (Editors), Green Chemistry, P. 39–62, De Gruyter, 2022, doi:10.1515/9783110706635-004.

[15] J. Nuckolls *et al.*, Laser Compression of Matter to Super-High Densities: Thermonuclear (CTR) Applications, Nature, **239**(5368):139–142, 1972, doi:10.1038/239139a0.

[16] A. B. Zylstra *et al.*, Burning Plasma Achieved in Inertial Fusion, Nature, **601**(7894):542–548, 2022.

[17] F. Krausz *et al.*, Attosecond Physics, Reviews of Modern Physics, **81**(1):163–234, 2009, doi:10.1103/RevModPhys.81.163.

[18] S. Haessler *et al.*, High-Harmonic Generation and Correlated Electron Emission from Relativistic Plasma Mirrors at 1 kHz Repetition Rate, Ultrafast Science, **2022**, 2022, doi:10.34133/2022/9893418.

[19] C. Li *et al.*, Effects of Laser-Plasma Interactions on Terahertz Radiation from Solid Targets Irradiated by Ultrashort Intense Laser Pulses, Physical Review E, **84**(3):036405, 2011, doi:10.1103/PhysRevE.84.036405.

[20] I. J. Kim *et al.*, Radiation Pressure Acceleration of Protons to 93 MeV with Circularly Polarized Petawatt Laser Pulses, Physics of Plasmas, **23**(7):070701, 2016, doi:10.1063/1.4958654.

[21] A. Einstein, Über Einen Die Erzeugung Und Verwandlung Des Lichtes Betreffenden Heuristischen Gesichtspunkt, Annalen der Physik, **322**(6):132–148, 1905, doi:10.1002/andp.19053220607.

[22] A. Kramida *et al.*, NIST Atomic Spectra Database (ver. 5.10), [Online]. Available: https://physics.nist.gov/asd [2023, August 17]. National Institute of Standards and Technology, Gaithersburg, MD., 2022.

[23] M. Göppert-Mayer, Über Elementarakte Mit Zwei Quantensprüngen, Annalen der Physik, **401**(3):273–294, 1931, doi:10.1002/andp.19314010303.

[24] R. W. Boyd, Nonlinear Optics, Academic Press, San Diego, CA, 2nd Edition, 2003.

[25] G. Gamow, Zur Quantentheorie Des Atomkernes, Zeitschrift für Physik, **51**(3-4):204–212, 1928.

[26] L. V. Keldysh, Ionization in the Field of a Strong Electromagnetic Wave, Journal of Experimental and Theoretical Physics, **20**(5):1307–1314, 1965.

[27] N. B. Delone *et al.*, Tunneling and Barrier-Suppression Ionization of Atoms and Ions in a Laser Radiation Field, Physics-Uspekhi, **41**(5):469–485, 1998, doi:10.1070/PU1998v041n05ABEH000393.

[28] D. Du *et al.*, Laser-induced Breakdown by Impact Ionization in SiO2 with Pulse Widths from 7 Ns to 150 Fs, Applied Physics Letters, **64**(23):3071–3073, 1994, doi:10.1063/1.111350.

[29] B. Stuart *et al.*, Nanosecond-to-Femtosecond Laser-Induced Breakdown in Dielectrics, Physical review. B, Condensed matter, **53**(4):1749–1761, 1996, doi:10.1103/PhysRevB.53.1749.

[30] W. M. Haynes, CRC Handbook of Chemistry and Physics, CRC press, 95 Edition, 2014.

[31] B. C. Stuart *et al.*, Optical Ablation by High-Power Short-Pulse Lasers, Journal of the Optical Society of America B, **13**(2):459, 1996, doi:10.1364/JOSAB.13.000459.

[32] A.-C. Tien *et al.*, Short-Pulse Laser Damage in Transparent Materials as a Function of Pulse Duration, Physical Review Letters, **82**(19):3883–3886, 1999, doi:10.1103/PhysRevLett.82.3883.

[33] J. Peebles *et al.*, Investigation of Laser Pulse Length and Pre-Plasma Scale Length Impact on Hot Electron Generation on OMEGA-EP, New Journal of Physics, **19**(2):023008, 2017, doi:10.1088/1367-2630/aa5a21.

[34] P. Varmazyar *et al.*, Effect of Pre-Plasma on the Ion Acceleration by Intense Ultra-Short Laser Pulses, Laser and Particle Beams, **36**(2):226–231, 2018, doi:10.1017/S0263034618000241.

[35] T. R. Desjardins *et al.*, Reducing Direct Drive Preheat with Dopants, High Energy Density Physics, **39**:100937, 2021, doi:10.1016/j.hedp.2021.100937.

[36] D. J. Griffiths, Introduction to Electrodynamics, Pearson, Boston, 4th Edition, 2013.

[37] F. Chen, Introduction to Plasma Physics and Controlled Fusion, Springer International Publishing : Imprint: Springer, Cham, 3rd Edition, 2016, doi:10.1007/978-3-319-22309-4.

[38] P. Gibbon, Introduction to Plasma Physics, CERN Yellow Reports, P. 51 Pages, 2016, doi:10.5170/CERN-2016-001.51.

[39] P. Mulser *et al.*, High Power Laser-Matter Interaction, number 238 in Springer Tracts in Modern Physics, Springer, Heidelberg, 2010.

[40] B. Fryxell *et al.*, FLASH: An Adaptive Mesh Hydrodynamics Code for Modeling Astrophysical Thermonuclear Flashes, The Astrophysical Journal Supplement Series, **131**(1):273, 2000, doi:10.1086/317361.

[41] S. Eliezer, The Interaction of High-Power Lasers with Plasmas, Series in Plasma Physics, CRC Press, Taylor & Francis Group, Boca Raton London New York, 2002.

[42] A. J. Mackinnon *et al.*, Effect of Plasma Scale Length on Multi-MeV Proton Production by Intense Laser Pulses, Physical Review Letters, **86**(9):1769–1772, 2001, doi:10.1103/PhysRevLett.86.1769.

[43] M. Zepf *et al.*, Role of the Plasma Scale Length in the Harmonic Generation from Solid Targets, Physical Review E, **58**(5):R5253–R5256, 1998, doi:10.1103/PhysRevE.58.R5253.

[44] P. Varmazyar *et al.*, Effect of Pre-Plasma on the Ion Acceleration by Intense Ultra-Short Laser Pulses, Laser and Particle Beams, **36**(2):226–231, 2018, doi:10.1017/S0263034618000241.

[45] M. King *et al.*, Perspectives on Laser-Plasma Physics in the Relativistic Transparency Regime, The European Physical Journal A, **59**(6):132, 2023, doi:10.1140/epja/s10050-023-01043-2.

[46] B. Y. Li *et al.*, Experimental Demonstration of Efficient Harmonic Generation via Surface Plasma Compression with Lasers, Physical Review Letters, **128**(24):244801, 2022, doi:10.1103/PhysRevLett.128.244801.

[47] F. Träger (Editor), Springer Handbook of Lasers and Optics: With 163 Tables, Springer Berlin, Heidelberg, 2nd Edition, 2012, doi:10.1007/978-3-642-19409-2.

[48] J. A. Valdmanis *et al.*, Generation of Optical Pulses as Short as 27 Femtoseconds Directly from a Laser Balancing Self-Phase Modulation, Group-Velocity Dispersion, Saturable Absorption, and Saturable Gain, Optics Letters, **10**(3):131, 1985, doi:10.1364/OL.10.000131.

[49] P.-G. Bleotu *et al.*, Post-Compression of High-Energy, Sub-Picosecond Laser Pulses, High Power Laser Science and Engineering, **11**:e30, 2023, doi:10.1017/hpl.2023.10.

[50] G. Sansone *et al.*, Isolated Single-Cycle Attosecond Pulses, Science, **314**(5798):443–446, 2006, doi:10.1126/science.1132838.

[51] C. Guo *et al.* (Editors), Handbook of Laser Technology and Applications: Four Volume Set, Handbook of Laser Technology and Applications, CRC Press, Boca Raton, 2nd Edition, 2021.

[52] D. Strickland *et al.*, Compression of Amplified Chirped Optical Pulses, Optics Communications, **55**(6):447–449, 1985, doi:10.1016/0030-4018(85)90151-8.

[53] E. Hecht, Optics, Pearson Education, Inc, Boston, 5 Edition, 2017.

[54] M. Pessot *et al.*, 1000 Times Expansion/Compression of Optical Pulses for Chirped Pulse Amplification, Optics Communications, **62**(6):419–421, 1987, doi:10.1016/0030-4018(87)90011-3.

[55] I. V. Yakovlev, Stretchers and Compressors for Ultra-High Power Laser Systems, Quantum Electronics, **44**(5):393, 2014, doi:10.1070/QE2014v044n05ABEH015429.

[56] X. Gu *et al.*, Spatial Chirp in Ultrafast Optics, Optics Communications, **242**(4-6):599–604, 2004.

[57] V. Bagnoud *et al.*, Commissioning and Early Experiments of the PHELIX Facility, Applied Physics B, **100**(1):137–150, 2010, doi:10.1007/s00340-009-3855-7.

[58] O. Martinez, 3000 Times Grating Compressor with Positive Group Velocity Dispersion: Application to Fiber Compensation in 1.3-1.6 µm Region, IEEE Journal of Quantum Electronics, **23**(1):59–64, 1987, doi:10.1109/JQE.1987.1073201.

[59] P. Banks *et al.*, Novel All-Reflective Stretcher for Chirped-Pulse Amplification of Ultrashort Pulses, IEEE Journal of Quantum Electronics, **36**(3):268–274, 2000, doi:10.1109/3.825872.

[60] A. Öffner, Unit Power Imaging Anastigmat U.S. Patent 3748015, July 24, 1973.

[61] E. Treacy, Optical Pulse Compression with Diffraction Gratings, IEEE Journal of Quantum Electronics, **5**(9):454–458, 1969, doi:10.1109/JQE.1969.1076303.

[62] D. J. Jones *et al.*, Carrier-Envelope Phase Control of Femtosecond Mode-Locked Lasers and Direct Optical Frequency Synthesis, Science, **288**(5466):635–639, 2000, doi:10.1126/science.288.5466.635.

[63] J. A. Paisner *et al.*, The National Ignition Facility Project, Fusion Technology, **26**(3P2):755–766, 1994, doi:10.13182/FST94-A40246.

[64] J.-M. G. D. Nicola *et al.*, Recent Laser Performance Improvements and Latest Results at the National Ignition Facility, in High Power Lasers for Fusion Research VII: SPIE Lase, Jan 28-Feb 3, 2023, San Francisco, California, United States, volume PC12401, P. PC1240103, SPIE, 2023, doi:10.1117/12.2655251.

[65] C. A. Haynam *et al.*, National Ignition Facility Laser Performance Status, Applied Optics, **46**(16):3276–3303, 2007, doi:10.1364/AO.46.003276.

[66] J.-L. Miquel *et al.*, The Laser Mega-Joule : LMJ & PETAL Status and Program Overview, Journal of Physics: Conference Series, **688**(1):012067, 2016, doi:10.1088/1742-6596/688/1/012067.

[67] C. N. Danson *et al.*, Petawatt and Exawatt Class Lasers Worldwide, High Power Laser Science and Engineering, **7**:e54, 2019, doi:10.1017/hpl.2019.36.

[68] M. D. Perry *et al.*, Petawatt Laser Pulses, Optics Letters, **24**(3):160–162, 1999, doi:10.1364/OL.24.000160.

[69] A. A. Kuzmin *et al.*, Large-Aperture Nd:Glass Laser Amplifiers with High Pulse Repetition Rate, Optics Express, **19**(15):14223–14232, 2011, doi:10.1364/OE.19.014223.

[70] W. P. Leemans *et al.*, BELLA Laser and Operations, in Proceedings of PAC2013, Pasadena, CA USA THYAA1, P. 1097, JACoW, 2013.

[71] C. Radier *et al.*, 10 PW Peak Power Femtosecond Laser Pulses at ELI-NP, High Power Laser Science and Engineering, **10**:e21, 2022, doi:10.1017/hpl.2022.11.

[72] J. W. Yoon *et al.*, Realization of Laser Intensity over 10^{23} W/cm^2, Optica, **8**(5):630–635, 2021, doi:10.1364/OPTICA.420520.

[73] S. Gales *et al.*, The Extreme Light Infrastructure—Nuclear Physics (ELI-NP) Facility: New Horizons in Physics with 10 PW Ultra-Intense Lasers and 20 MeV Brilliant Gamma Beams, Reports on Progress in Physics, **81**(9):094301, 2018, doi:10.1088/1361-6633/aacfe8.

[74] V. Zamfir *et al.*, Extreme Light Infrastructure Nuclear Physics (ELI-NP), Europhysics News, **50**(2):23–25, 2019, doi:10.1051/epn/2019204.

[75] E. Cartlidge, The Light Fantastic, Science, **359**(6374):382–385, 2018, doi:10.1126/science.359.6374.382.

[76] P. Yujie *et al.*, Overview and Status of Station of Extreme Light toward 100 PW, Reza Kenkyu, **49**(2):93–96, 2021.

[77] K. D. Chesnut *et al.*, Ideal Spatio-Temporal Pulse Distribution for Exawatt-Scale Lasers Based on Simultaneous Chirped Beam and Chirped Pulse Amplification, Optics Express, **31**(4):5687–5698, 2023.

[78] R. P. Johnson *et al.*, Techniques for Pre-Pulse Contrast Improvement on the 0.5 Ps, 80 J, "C" Beamline of the Trident Laser, in CLEO: 2011 - Laser Science to Photonic Applications, CLEO: 2011 - Laser Science to Photonic Applications, 01-06 May 2011, Baltimore, MD, United States, volume b, P. 1–2, IEEE, 2011.

[79] L. Ranc *et al.*, Improvement in the Temporal Contrast in the Tens of Ps Range of the Multi-PW Apollon Laser Front-End, Optics Letters, **45**(16):4599–4602, 2020, doi:10.1364/OL.401272.

[80] H. Kiriyama *et al.*, Enhancement of Pre-Pulse and Picosecond Pedestal Contrast of the Petawatt J-KAREN-P Laser, High Power Laser Science and Engineering, **9**:e62, 2021, doi:10.1017/hpl.2021.51.

[81] L. E. Bradley *et al.*, Comparing Temporal Contrast Measurements Taken in the Vulcan Front-End and Target Area Petawatt, Central Laser Facility Annual Report 2019-20, P. 37, 2020.

[82] V. V. Ivanov *et al.*, Amplified Spontaneous Emission in a Ti:Sapphire Regenerative Amplifier, Applied Optics, **42**(36):7231, 2003, doi:10.1364/AO.42.007231.

[83] S. E. Harris *et al.*, Observation of Tunable Optical Parametric Fluorescence, Physical Review Letters, **18**(18):732–734, 1967, doi:10.1103/PhysRevLett.18.732.

[84] V. Bagnoud *et al.*, High-Dynamic-Range Temporal Measurements Ofshort Pulses Amplified by OPCPA, Optics Express, **15**(9):5504–5511, 2007, doi:10.1364/oe.15.005504.

[85] A. Jullien *et al.*, 10^{-10} Temporal Contrast for Femtosecond Ultraintense Lasers by Cross-Polarized Wave Generation, Optics Letters, **30**(8):920–922, 2005, doi:10.1364/OL.30.000920.

[86] N. Minkovski *et al.*, Nonlinear Polarization Rotation and Orthogonal Polarization Generation Experienced in a Single-Beam Configuration, JOSA B, **21**(9):1659–1664, 2004, doi:10.1364/JOSAB.21.001659.

[87] D. N. Papadopoulos *et al.*, The Apollon 10 PW Laser: Experimental and Theoretical Investigation of the Temporal Characteristics, High Power Laser Science and Engineering, **4**:e34, 2016, doi:10.1017/hpl.2016.34.

[88] M. P. Kalashnikov *et al.*, Double Chirped-Pulse-Amplification Laser: A Way to Clean Pulses Temporally, Optics Letters, **30**(8):923–925, 2005, doi:10.1364/OL.30.000923.

[89] J. H. Sung *et al.*, Enhancement of Temporal Contrast of High-Power Femtosecond Laser Pulses Using Two Saturable Absorbers in the Picosecond Regime, Applied Physics B, **116**(2):287–292, 2014, doi:10.1007/s00340-013-5687-8.

[90] C. Thaury *et al.*, Plasma Mirrors for Ultrahigh-Intensity Optics, Nature Physics, **3**(6):424–429, 2007, doi:10.1038/nphys595.

[91] S. G. Lee *et al.*, Double Plasma Mirror System for the 4 PW Ti: Sapphire Laser at CoReLS, in 1st Asia-Pacific Conference on Plasma Physics, Chengdu, China, P. 18–23, AAPPS DPP, 2017.

[92] V. A. Schanz *et al.*, High Dynamic Range, Large Temporal Domain Laser Pulse Measurement, Applied Physics B, **125**(4):61, 2019, doi:10.1007/s00340-019-7172-5.

[93] N. V. Didenko *et al.*, Contrast Degradation in a Chirped-Pulse Amplifier Due to Generation of Prepulses by Postpulses, Optics Express, **16**(5):3178–3190, 2008, doi:10.1364/OE.16.003178.

[94] V. Bagnoud *et al.*, Influence of Optical Quality on Chirped-Pulse Amplification: Characterization of a 150-Nm-Bandwidth Stretcher, JOSA B, **16**(1):188–193, 1999, doi:10.1364/JOSAB.16.000188.

[95] C. Dorrer *et al.*, Impact of High-Frequency Spectral Phase Modulation on the Temporal Profile of Short Optical Pulses, Optics Express, **16**(5):3058–3068, 2008, doi:10.1364/OE.16.003058.

[96] C. Hooker *et al.*, Improving Coherent Contrast of Petawatt Laser Pulses, Optics Express, **19**(3):2193–2203, 2011, doi:10.1364/OE.19.002193.

[97] J. Bromage *et al.*, Temporal Contrast Degradation at the Focus of Ultrafast Pulses from High-Frequency Spectral Phase Modulation, JOSA B, **29**(5):1125–1135, 2012, doi:10.1364/JOSAB.29.001125.

[98] J. Bromage *et al.*, A Cylindrical Öffner Stretcher for Reduced Chromatic Aberrations and Improved Temporal Contrast, in CLEO: Conference on Lasers and Electro-Optics, 6–11 May 2012, San Jose, California, United States, P. CM4D.4, Optica Publishing Group, 2012, doi:10.1364/CLEO_SI.2012.CM4D.4.

[99] V. A. Schanz *et al.*, Picosecond Contrast Degradation by Surface Imperfections in Chirped-Pulse-Amplification Stretchers, JOSA A, **36**(10):1735–1742, 2019, doi:10.1364/JOSAA.36.001735.

[100] H. Kiriyama *et al.*, Laser Output Performance and Temporal Quality Enhancement at the J-KAREN-P Petawatt Laser Facility, Photonics, **10**:997, 2023, doi:10.3390/photonics10090997.

[101] X. Lu *et al.*, Suppressing Temporal Pedestal in Nd:Glass Laser Systems by Avoiding Far-Field Spectral Phase Noise, IEEE Journal of Selected Topics in Quantum Electronics, **24**(5):1–6, 2018, doi:10.1109/JSTQE.2017.2785291.

[102] X. Lu *et al.*, Reducing Temporal Pedestal in a Ti:Sapphire Chirped-Pulse Amplification System by Using a Stretcher Based on Two Concave Mirrors, Optics Letters, **46**(21):5320–5323, 2021, doi:10.1364/OL.435145.

[103] Y. Katznelson, An Introduction to Harmonic Analysis, Dover Books on Advanced Mathematics, Dover publ, New York, 2nd corr. Edition, 1976.

[104] A. Forbes (Editor), Laser Beam Propagation: Generation and Propagation of Customized Light, CRC Press, Taylor & Francis Group, Boca Raton, 2014.

[105] Coherent, MIRA 900f Laser Oscillator Data Sheet.

[106] R. Baumgartner *et al.*, Optical Parametric Amplification, Quantum Electronics, IEEE Journal of, **15**:432–444, 1979, doi:10.1109/JQE.1979.1070043.

[107] Y. Zobus *et al.*, Versatile, Compact Chirped Pulse Amplifier Pump System for Ultrafast Optical Parametric Amplifiers, Optics Express, **31**(3):5002–5015, 2023, doi:10.1364/OE.477610.

[108] Amplitude Technologie, Sequoia User's Manual Version 5.0.

[109] J.-C. Diels *et al.*, Ultrashort Laser Pulse Phenomena Fundamentals, Techniques, and Applications an a Femtosecond Time Scale, Elsevier Inc., 2nd Edition, 1996.

[110] B. C. Platt *et al.*, History and Principles of Shack-Hartmann Wavefront Sensing, Journal of Refractive Surgery, **17**(5):573–577, 2001, doi:10.3928/1081-597X-20010901-13.

[111] Y. Zobus *et al.*, Millijoule Ultrafast Optical Parametric Amplification as Replacement for High-Gain Regenerative Amplifiers, High Power Laser Science and Engineering, **11**:e48, 2023, doi:10.1017/hpl.2023.30.

[112] M. Patrizio, Development of an Actively Cooled Large Aperture Laser Amplifier at the GSI Helmholtzzentrum, Ph.D. thesis, Technische Universität, Darmstadt, 2020, doi:10.25534/tuprints-00011959.

[113] Work Packages – THRILL Project, https://www.thrill-project.eu/workpackages/ (Accessed: 07.06.2023).

[114] J. Ohland, Design and Setup of a Post-Compressor Adaptive Optics Loop at PHELIX, Ph.D. thesis, 2022, doi:10.26083/tuprints-00021995.

[115] J. Ohland *et al.*, Ultra-Compact Post-Compressor on-Shot Wavefront Measurement for Beam Correction at PHELIX, High Power Laser Science and Engineering, **10**:1–9, 2022, doi:10.1017/hpl.2022.9.

[116] D. Javorková, The CPA System for the PW Peak Intensity at PHELIX, Ph.D. thesis, Comenius University Bratislava, Bratislava, 2007.

[117] K. Osvay *et al.*, On the Temporal Contrast of High Intensity Femtosecond Laser Pulses, Laser and Particle Beams, **23**(3):327–332, 2005, doi:10.1017/S0263034605050469.

[118] Z. Li *et al.*, Further Development of the Short-Pulse Petawatt Laser: Trends, Technologies, and Bottlenecks, Laser & Photonics Reviews, **17**(1):2100705, 2023, doi:10.1002/lpor.202100705.

[119] P. Neumayer, Ein transienter Röntgenlaser zur Laserspektroskopie an Lithium-ähnlichen Ionen, Ph.D. thesis, Technische Universität, Darmstadt, 2004, doi:https://tuprints.ulb.tu-darmstadt.de/id/eprint/452.

[120] R. Trebino, Frequency-Resolved Optical Gating: The Measurement of Ultrashort Laser Pulses, Springer Science + Business Media, New York, 2000.

[121] C. Iaconis *et al.*, Spectral Phase Interferometry for Direct Electric-Field Reconstruction of Ultrashort Optical Pulses, Optics Letters, **23**(10):792, 1998, doi:10.1364/OL.23.000792.

[122] A. Dubietis *et al.*, Powerful Femtosecond Pulse Generation by Chirped and Stretched Pulse Parametric Amplification in BBO Crystal, Optics Communications, **88**(4):437–440, 1992, doi:10.1016/0030-4018(92)90070-8.

[123] J. Hornung *et al.*, Time-Resolved Study of Holeboring in Realistic Experimental Conditions, Nature Communications, **12**(1):6999, 2021, doi:10.1038/s41467-021-27363-9.

[124] A. V. Oppenheim *et al.*, Discrete-Time Signal Processing, Prentice Hall, Upper Saddle River, N.J, 2nd Edition, 1999.

[125] A. L. Camus *et al.*, Impact of Compression Grating Phase Modulations on Beam Over-Intensities and Downstream Optics on PETAL Facility, Optics Express, **30**(5):7426–7440, 2022, doi:10.1364/OE.449397.

[126] L. Yu *et al.*, Investigation of the Temporal Contrast Evolution in a 10-PW-level Ti:Sapphire Laser Facility, Optics Express, **27**(6):8683–8695, 2019, doi:10.1364/OE.27.008683.

[127] K. Burdonov *et al.*, Characterization and Performance of the Apollon Short-Focal-Area Facility Following Its Commissioning at 1 PW Level, Matter and Radiation at Extremes, **6**(6), 2021.

[128] V. Bagnoud, Étude et Réalisation d'une Chaîne Laser Femtoseconde Kilohertz Térawatt : Étude de l'accord de Phase Spectrale, Amplification de Puissance En Présence de Charge Thermique, Ph.D. thesis, Bordeaux 1, 1999.

[129] N. Jha *et al.*, Temporal Contrast Improvement in Chirped Pulse Amplification Systems by a Four-Grating Compressor and by Spectral Modifications, Optik, **125**(10):2261–2266, 2014, doi:10.1016/j.ijleo.2013.10.078.

[130] Sellmeier, Zur Erklärung Der Abnormen Farbenfolge Im Spectrum Einiger Substanzen, Annalen der Physik, **219**(6):272–282, 1871, doi:10.1002/andp.18712190612.

[131] Refractive Index of CRYSTALS - Sapphire, https://refractiveindex.info/?shelf=3d&book=crystals&page=sapphire (accessed: 07.13.2023).

[132] R. H. Byrd *et al.*, A Limited Memory Algorithm for Bound Constrained Optimization, SIAM Journal on Scientific Computing, **16**(5):1190–1208, 1995, doi:10.1137/0916069.

[133] C. Zhu *et al.*, Algorithm 778: L-BFGS-B: Fortran Subroutines for Large-Scale Bound-Constrained Optimization, ACM Transactions on Mathematical Software, **23**(4):550–560, 1997, doi:10.1145/279232.279236.

[134] A. Major *et al.*, Dispersion of the Nonlinear Refractive Index in Sapphire, Optics Letters, **29**(6):602–604, 2004, doi:10.1364/OL.29.000602.

[135] J. S. Hayden *et al.*, Advances In Glasses For High Average Power Laser Systems, in H. Weber (Editor), 1988 International Congress on Optical Science and Engineering, P. 36, Hamburg, Germany, 1989, doi:10.1117/12.950070.

Acknowledgments

Zum Ende dieser Arbeit möchte ich mich bei all denen bedanken, die mich unterstützt haben.

Allen voran bei meinem Doktorvater, Vincent, der sich immer Zeit für mich genommen hat. Dabei hast Du mir das Gefühl gegeben, dass Du mit voller Aufmerksamkeit da bist und Dich in meine Probleme reindenkst. Danke, dass Du mit angepackt hast und mir gezeigt hast, dass Dir mein Projekt wichtig ist.

Mein besonderer Dank gilt Johannes. Von meinem ersten Tag an hast Du mir kein einziges Mal das Gefühl gegeben, dass ich zu viel von Dir verlange. Ich schätze deine Meinung nach wie vor sehr: Wenn du sagst, dass etwas gut ist wie es ist, dann kann ich nachts ruhig schlafen.

Mit wenigen Menschen habe ich so angenehme, reflektierte Gespräche wie mit Dir, Jonas. Bei jedem Thema habe ich mich von Dir verstanden gefühlt. Danke, für dein offenes Ohr.

Yannik, dich den Experten zu nennen ist nicht ausreichend. Es ist unfassbar, wie sehr Du dich in Sachen reinarbeitest, wenn ich dich um Hilfe bitte. Immer wenn ich zu Dir komme, um gemeinsam Probleme zu lösen, packst Du mit an. Selbst bei den schwierigsten Sachen mit vier Rädern und einem Stuhl.

Ich möchte mich bei meinem Kommilitonen, Arbeitskollegen und Freund Pascal bedanken. Vom ersten Tag des Studiums bis zum letzten Tag meiner Dissertation sitzen wir Seite an Seite. Danke, für deine Freundschaft und deine Unterstützung.

Auch bei Haress möchte ich mich bedanken, für die tolle Zeit im gemeinsamen Büro.

Bei Christian möchte ich mich dafür bedanken, dass Du dich für mich verantwortlich gefühlt hast. Bis zum letzten Tag weiß ich nicht, ob Du mir vertraust, dass ich hinbekomme, was ich anpacke, oder ob es Dir einfach egal ist, wenn bei dem Versuch alles kaputt geht. Ganz egal was es ist, Du hast mir damit das Selbstvertrauen und die Rückendeckung gegeben, Dinge selbst in die Hand zu nehmen.

Bei Zsuzsanna möchte ich mich bedanken, dafür, dass Du mich bei meinen Messungen so tatkräftig unterstützt hast.

Mein Dank gilt der PHELIX Crew. Dafür, dass Ihr mich unterstützt habt, wo Ihr nur konntet. Für die Zeit, die Ihr euch genommen habt und für das Vertrauen, dass Ihr mir entgegen gebracht habt.

Diese Arbeit hat viel Zeit gekostet - und nicht nur meine. Auch die von meinen Kollegen, die sie Korrektur gelesen haben. Danke dafür, Pascal, Johannes, Yannik, Jonas, Philipp und Vincent.

Zu guter Letzt möchte ich meiner Frau Lisa danken. Du bist der Grund warum ich mich darauf freue was jetzt kommt.

Education

Master of Science (Physics)

28.03.2018 - 16.03.2020

Technical University of Darmstadt
Karolinenplatz 5
64289 Darmstadt
Germany

Thesis: Design of a SPIDER for time-resoled plasma characterization

Bachelor of Science (Physics)

01.10.2014 - 27.03.2018

Technical University of Darmstadt
Karolinenplatz 5
64289 Darmstadt
Germany

Thesis: Gütefaktoren von supraleitenden Beschleunigungsstrukturen des S-DALINAC

General University Entrance Qualification

05.06.2014

Wilhelm-Knapp-Schule
Frankfurter Straße 39
35781 Weilburg an der Lahn
Germany

A. Appendix

A.1. Limits of the Analytical Approximations for Spectral-Phase Effects

The analytical model that I developed in sec. 2.1 relies on several approximations, that I have all mentioned when employing them during the derivation.

The approximation that I discussed here is the statement that the variation of $\tilde{f}\tilde{\delta\phi}$ is small during the duration of the undisturbed profile. This was used in the steps from eq. 2.12 to eq. 2.13 in order to pull the terms out of the convolution,

$$\left(\tilde{f}(t/a_\omega)\tilde{\delta\phi}(t/a_\omega)\right) \circledast \tilde{E}_0(t) \approx \tilde{f}(t/a_\omega)\tilde{\delta\phi}(t/a_\omega) \int \tilde{E}_0(t)dt = \tilde{f}(t/a_\omega)\tilde{\delta\phi}(t/a_\omega), \tag{A.1}$$

where I used the normalization of the undisturbed profile for the last step. For the discussion of the validity of this approximation, all three of the terms in this function are considered.

Concerning the undisturbed field $\tilde{E}_0(t)$, the assumption could become invalid when the duration of the pulse increases, or in other words when the incident beam already contains considerable energy on the time scale of the rising edge, e.g. in the case of a previously deteriorated pulse. Thus, we see that this model is best applicable when the rising edge is dominated by a single effect on a single surface.

Secondly, I want to discuss the case when the beam profile dominates the multiplication $\tilde{f}\tilde{\delta\phi}$, e.g. $\tilde{\delta\phi}$ is approximate constant for relevant times. In this case, the validity depends on the spatial and temporal shape of the beam. For the interaction with a surface in the NF, an initially FTL temporal field

$$E_0(t) = \exp\left(\frac{-t^2}{\sigma_{\text{FTL}}^2} - i\omega t\right), \tag{A.2}$$

is convoluted with a spatial Gaussian shape (compare eq. 2.29), where σ_{FTL} is the FTL pulse duration and $i\omega t$ is the oscillation of the field. This convolution can be analytically calculated and only requires the Slowly-Varying Envelope Approximation (SVEA), to remove the oscillation of the field from the convolution

$$\begin{aligned}
|\tilde{f}(t/a_\omega) \circledast \tilde{E}_0(t)|^2 &\propto \left| \exp\left(\frac{-t^2\sigma_{\text{x,NF}}^2}{a_\omega^2}\right) \circledast \exp\left(\frac{-t^2}{\sigma_{\text{FTL}}^2} - i\omega t\right)\right|^2 \\
&\overset{\text{SVEA}}{\approx} \left| \int \exp\left(\frac{-t'^2\sigma_{\text{x,NF}}^2}{a_\omega^2}\right) \exp\left(\frac{-(t-t')^2}{\sigma_{\text{FTL}}^2}\right) dt' \right|^2 \\
&\propto \left| \exp\left(-\frac{t^2}{a_\omega^2/\sigma_{\text{x,NF}}^2 + \sigma_{\text{FTL}}^2}\right)\right|^2 .
\end{aligned} \tag{A.3}$$

When comparing that to the approximated case

$$\begin{aligned}
|\tilde{f}(t/a_\omega) \circledast \tilde{E}_0(t)|^2 &\approx \left|\tilde{f}(t/a_\omega)\right|^2 \cdot \left|\tilde{E}_0(t)\right|^2 \\
&= \left|\exp\frac{-t^2\sigma_{\text{x,NF}}^2}{a_\omega^2}\right|^2 \left|\int \exp\frac{t'^2}{\sigma_{\text{FTL}}^2} dt'\right|^2 \\
&\propto \left|\exp\left(-\frac{t^2\sigma_{\text{x,NF}}^2}{a_\omega^2}\right)\right|^2
\end{aligned} \tag{A.4}$$

it becomes clear that the approximation is only valid if $\sigma_{\text{FTL}}^2 \ll a_\omega^2/\sigma_{\text{x,NF}}^2$ such that

$$a_\omega^2/\sigma_{\text{x,NF}}^2 + \sigma_{\text{FTL}}^2 \approx a_\omega^2/\sigma_{\text{x,NF}}^2. \tag{A.5}$$

The influence of the spatial profile on the validity of this approximation has already been discussed at the end of sec. 2.3.2, with the result that a sinc-function on a surface will cause a sharp edge in $\tilde{f}(t/a_\omega)$, which contradicts this approximation.

The last term I want to consider is the surface disturbance itself. This term dominates when the Fourier transform of the spatial profile on the surface is a broad, slowly varying function, e.g. when the beam profile is a narrow Gaussian or even a one-dimensional Dirac-peak. In this case the same assumption allowed Dorrer *et al.* [95] to simplify the convolution to $|\tilde{\delta\phi}(t'/a_\omega)|^2$ in the following steps:

$$\begin{aligned}
&|\tilde{\delta\phi}(t/a_\omega) \circledast \tilde{E}_0(t)|^2 = (\tilde{\delta\phi}(t/a_\omega) \circledast \tilde{E}_0(t)) \cdot (\tilde{\delta\phi}^*(t/a_\omega) \circledast \tilde{E}_0^*(t)) \\
=& \int\int \tilde{\delta\phi}(t'/a_\omega) \cdot \tilde{\delta\phi}^*(t''/a_\omega)\tilde{E}_0(t-t')\tilde{E}_0^*(t-t'')dt'dt'' \\
\approx& \int\int \tilde{\delta\phi}(t'/a_\omega) \cdot \tilde{\delta\phi}^*(t''/a_\omega)\tilde{I}_0(t-t')\delta(t'-t'')dt'dt'' \\
=& \int \tilde{\delta\phi}(t'/a_\omega) \cdot \tilde{\delta\phi}^*(t'/a_\omega)\tilde{I}_0(t-t')dt' \\
=& \int |\tilde{\delta\phi}(t'/a_\omega)|^2\tilde{I}_0(t-t')dt' \\
\approx& |\tilde{\delta\phi}(t'/a_\omega)|^2 \int \tilde{I}_0(t-t')dt' \\
=& |\tilde{\delta\phi}(t'/a_\omega)|^2.
\end{aligned} \tag{A.6}$$

A.2. Characterizing the Power Spectral Density of the Stretcher Optics

In order to estimate the influence of the PSD on the rising edge, it is necessary to characterize the surface of all relevant optical elements. In this appendix, I present the corresponding measurements of spherical mirrors employed in the telescope of both stretchers that have been developed for this thesis. I further present analogous measurements of the flat, dielectric folding mirror which was employed in the Fourier plane in the PoP setup, and as a 0°-mirror for the double pass of the unfolded stretcher at PHELIX.

The spatial resolution requirements on the measurements are deduced, using the mapping between spatial frequency and time, given by the previously calculated dispersion coefficients $t = 2\pi a_\omega k$.
Since we are only interested in a time region up to a hundred picoseconds, a spatial resolution of $dx = 1/k_{\text{max}} = 2\pi a_\omega / t_{\text{max}} \approx 0.2\,\text{mm}$ is sufficient. For the lower temporal limit, the temporal resolution must accommodate the prediction of fast-declining rising edges, for interactions with large beam sizes. Since the analytical calculation relies on approximations that the undisturbed temporal field is already close to zero, the characterization of the PSD down to a limit of a few ps is sufficient.

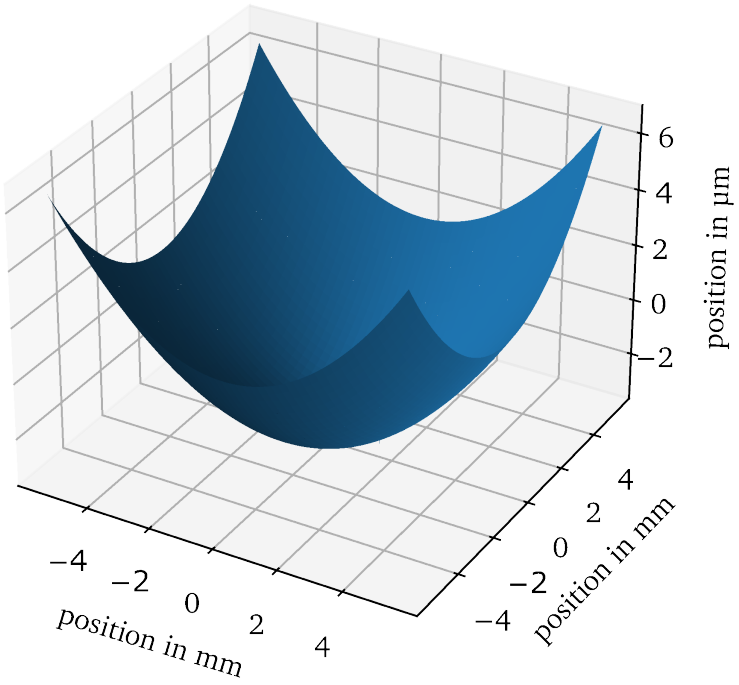

Figure A.1.: Surface measurement of the spherical mirror used for the PoP by a confocal microscope.

The measurements were conducted at CEA-CESTA, France, using a confocal microscope (New View 7300) with two different magnifications, x1 and x0.5. The spatial resolutions of 11.6 µm and 23 µm, respectively provide a temporal window that is over one order of magnitude larger than necessary. The spatial window sizes, with a diameter of 21.9 mm for the x1 magnification and a 10.9x10.9 mm sized rectangle for the x0.5 magnification, provide a temporal resolution down to 0.9 ps and 1.8 ps, respectively, which fulfills the

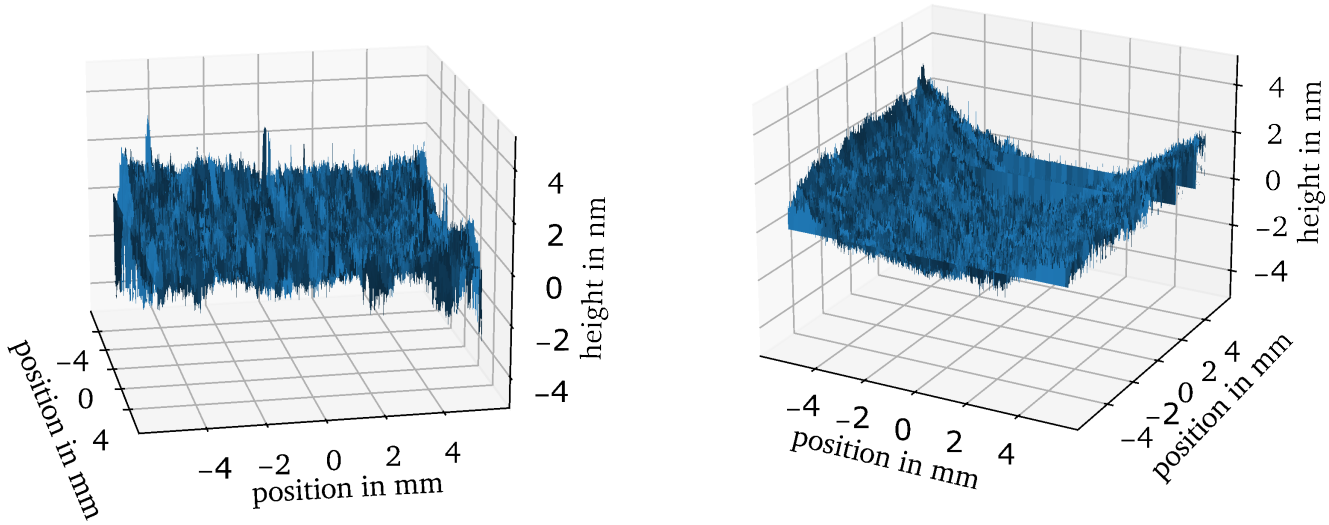

Figure A.2.: Surface measurement of the spherical mirror (left) and flat mirror (right) used for the PoP by a confocal microscope, post-processed by subtraction of a fitted sphere (only for the spherical mirror) and removing of hot pixels.

stated requirement for this study.

In fig. A.1 the raw surface measurement of the spherical mirror is depicted. Since my theoretical model, which was presented in sec. 2.1, relies on the one-dimensional PSD in the direction of the grating dispersion, it is sufficient to calculate the one-dimensional PSD. In the first step to extract the 1D- PSD from the raw data, I removed a calibration measurement of a well-characterized probe surface. This removes the aberrations of the measurement device itself from the data. Afterward, I line-wise removed the spherical shape for the spherical mirror; obviously, this was not necessary for the flat mirror.

Without the spherical shape, the actual disturbances in the surface can be seen in fig. A.2. To further refine the image, hot pixels are removed from the images, which increases the accuracy of the PSD calculation by removing high-frequency artifacts of the measurement device. Such hot pixels are likely caused by absorbing particles on the surface, that the device is not capable of resolving. Since my analytical model for the rising edge does not incorporate absorbing particles, the information that is lost at these points is not relevant to the analysis.

Since the calculation of the PSD involves the Fourier transform of the surface, I applied a Hann-Window to the data in order to suppress edge effects [124]

$$W(x) = \frac{1}{2}\left[1 - \cos\left(\frac{x}{\Delta x}\right)\right]. \tag{A.7}$$

This was realized by multiplying each lineout by an offset cosine with its maximum at the center of the image and a frequency that is the reciprocal of the spatial window size Δx. With this configuration, the

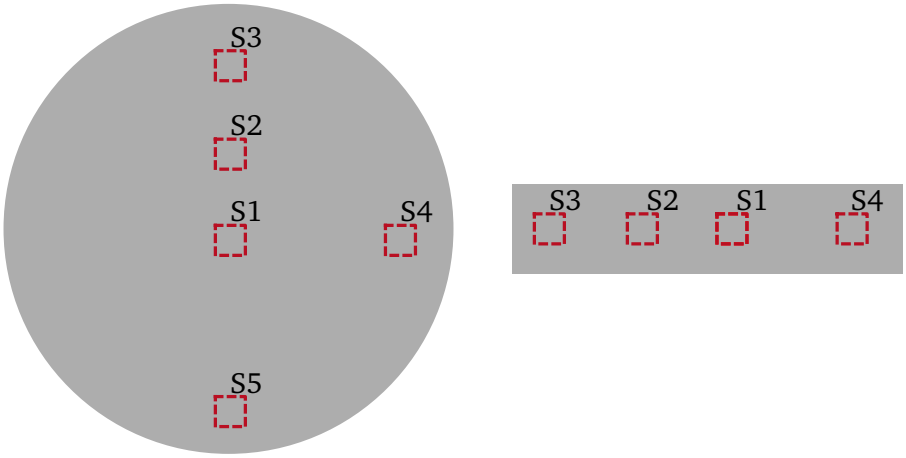

Figure A.3.: Selected measurement areas (S) on the spherical aluminum mirror (left) and the flat dielectric mirror (right).

Hann-window reaches its absolute minimum of zero at the edges of the window.

Then, the one-dimensional PSD can be calculated from the individual lines by

$$PSD(k) = |\tilde{z}(k)|^2 \cdot \Delta k, \tag{A.8}$$

where $\tilde{z}$ corresponds to the Fourier transform of the surface lineout. The multitude of lineouts that are available due to the two-dimensional surface measurement was used as statistics, resulting in an averaged measurement of the one-dimensional PSD. The resulting PSD is symmetrical around the zero-frequency. Adding the negative part to the positive part provides a more straightforward description, by only concentrating on the positive frequencies while preserving all necessary information.

To further improve the accuracy of the measurement four different regions of the mirrors were measured, as schematically indicated in fig. A.3, and the PSD in both directions were calculated. Depending on the polishing method, the anticipated PSD is either isotropic for the flat mirror, or in the case of the sphere I expect two different PSD. These two PSD correspond to two orthogonal directions on the mirror surface: the radial direction and the tangential direction. The data from the measurement, as depicted in fig. A.4 suggested that the PSD is homogeneous for both mirrors since no correlation depending on the direction can be found. Instead, we observe uncorrelated discrepancies that suggest that a statistical uncertainty dominates the measurement rather than a systematical error in the manufacturing process. This statistical discrepancy is larger for the flat mirror, which is understandable since the surface is dielectric, meaning that the reflection takes place on many different surface layers, which is not optimal for the used measurement device. The spherical mirror on the other hand is easier to characterize since all wavelengths are reflected on the thin, highly-opaque aluminum coating. It is further to note here that the flat mirror exhibits a systematically better surface quality (over all relevant points lower PSD) than the spherical mirror. This seems intuitive since the manufacturing process is more complex for spherical surfaces.

Additionally included in the Figure is a temporal axis, that was calculated for an $a_\omega = 3.15\,\mathrm{m}\cdot\mathrm{fs}$, which according to the calculations in sec. 3.2.1 represents the mapping between angular frequencies of the laser and the position of the spherical mirrors in the PoP setup.

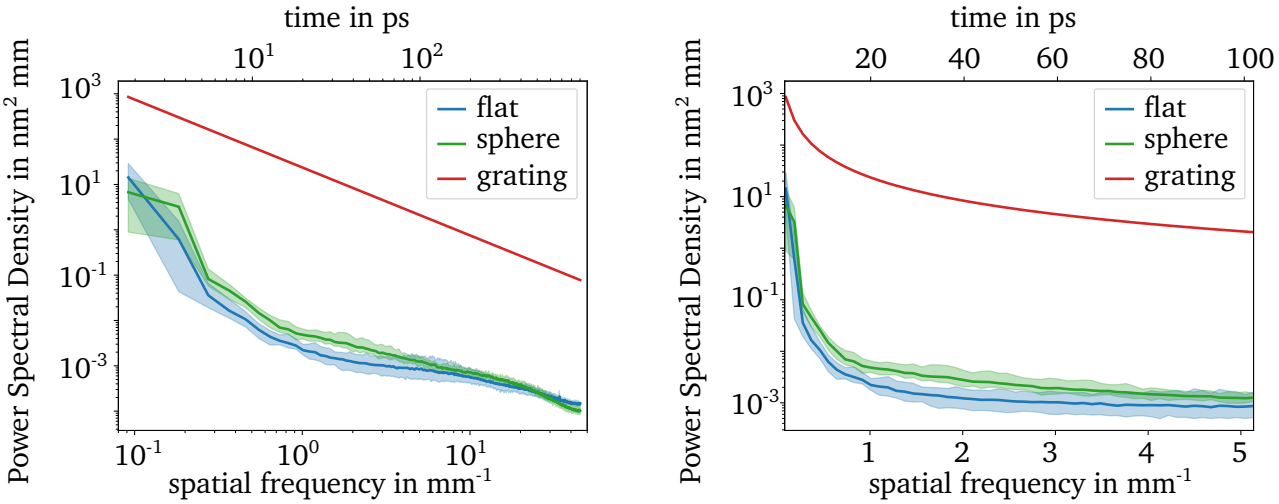

Figure A.4.: PSD calculated from the measurements, for the spherical mirror and the flat mirror. All measurements were evaluated in the x- and y-direction, for the two objectives with the magnifications of $x1$ and $x0.5$, as well as for the different measurement positions on the respective mirror. The full lines indicate the mean PSD for all configurations and the shaded area indicates the Peak-to-Valley (PtV)-variation for all configurations. On the left-hand side, the measurements are shown in a double logarithmic scale, as usual for PSD measurements. On the right-hand side, the x-axis is depicted in a linear scale, as usual for temporal-contrast curves, over the relevant time scale for the rising edge. For both measurements two x-axis are included, the spatial frequency scale on the lower axis and the time axis calculated for a dispersion coefficient of 3.16 mfs on the upper x-axis. Additionally included is an estimate of the PSD of a typical grating based on [125].

While not necessary for the characterization and calculations during the PoP, the gratings are relevant in cha. 4. However, no measurements of the gratings are available. Thus, I have included a rough estimate of the PSD of a typical grating extracted from the results of [125]. This shows that the PSD of gratings can be expected to be two to three orders of magnitude higher than that of flat, dielectric elements and curved, metallic surfaces.

A.3. Compressed Pulse Length: Its Determinants and Correlations to the Temporal Contrast

An effect that can be observed when comparing the rising edge of different CPA laser facilities around the world is, that laser systems with shorter pulses seem to have steeper rising edges (compare fig. 1.5). Another way to visualize this is by depicting the time duration it takes for the rising edge of each laser facility to increase from an arbitrary level to the peak intensity, over the pulse duration, as shown in fig. A.5. For this plot, I have chosen a threshold-temporal-contrast level of eight orders of magnitude, since this is still within the dynamic range of all considered measurements. The facilities ELI-NP, SULF 10 PW, Apollon, and J-Karen-P all feature rising edges with roughly the same steepness and roughly have the same pulse duration of a few tens of fs, with a contrast of eight orders of magnitude a few ps prior to the peak intensity. On the other hand, facilities like Vulcan, Trident, and PHELIX feature considerably longer pulse durations of 980 fs and the later two of 500 fs and more shallow rising edges.

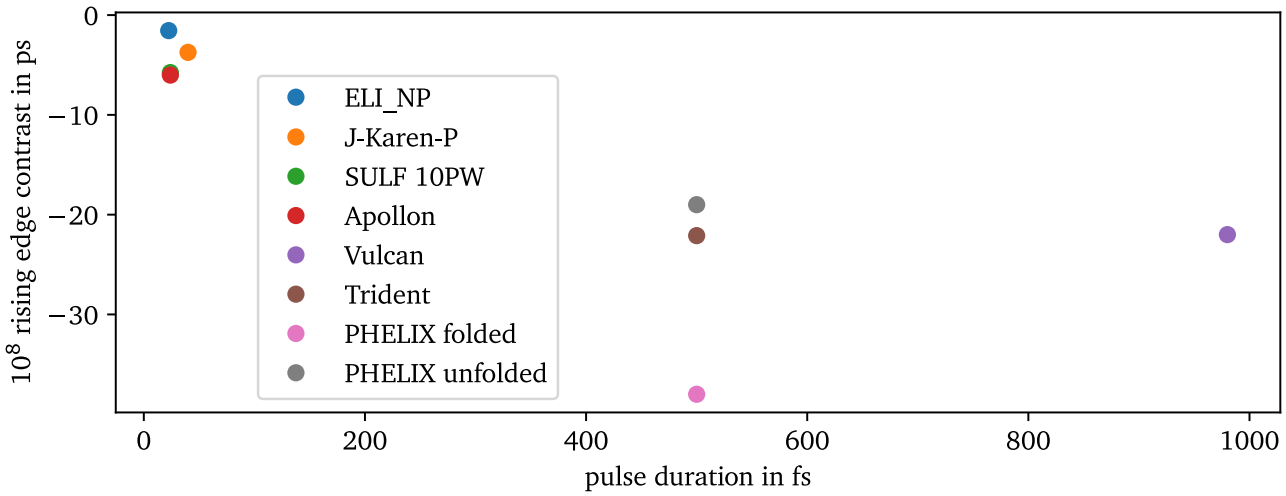

Figure A.5.: Time duration between the peak intensity and the first time the relative intensity decreases to eight orders of magnitude below the peak, over the temporal duration of the various CPA laser facilities. The pulse lengths used for this plot are 21.7 fs (ELI-NP [71]), 30 fs (J-Karen-P [67]), 24 fs (SULF 10 PW [126]), 24 fs (Apollon [127]), 980 fs (Vulcan [81]) and 500 fs (Trident [78] and PHELIX). The rising edge contrast values have been extracted from fig. 1.5 and from fig. 4.28, for the unfolded stretcher with the lb size.

The depicted correlation between pulse duration and slope of the rising edge stands in agreement with the analytical model and is presumably caused by a change in the dispersion coefficient a_ω, that maps the angular frequency to the position on the surface.

For spectral-amplitude effects, the perturbation remains unchanged, but the dispersion coefficient changes the clipped wavelengths on the edges of an optical element or the bandwidth removed by damage on an optical element. Thereby, the chosen dispersion coefficient directly influences the shape of the rising edge caused by spectral-amplitude effects.

For spectral-phase effects, the mapping can be expressed more explicitly as a linear relationship between the spatial frequencies k and the time axis t. Thus, an increase of the dispersion coefficient of a factor of two expands the time axis by a factor of two, according to eq. 2.18. Or specifically, a spatial frequency k, as expressed in the PSD(k) now does not shift laser energy from $t = 0$ to $t = a_\omega k$ but to $t = 2a_\omega k$, pushing the disturbances further away from the peak, and decreasing in the steepness of the rising edge.

In order to explain why the dispersion coefficients are generally larger for laser systems with longer pulse durations on target, I will give a short introduction to stretcher and compressor design:

The pn-target pulse duration behaves anti-proportional to the on-target bandwidth, as evident by the explicit Fourier transform of a Fourier-transform limited spectral Gaussian pulse into the temporal domain

$$I(t) = \left| \int e^{-\frac{(\omega-\omega_0)^2}{2\sigma_\omega^2} - i\omega t} d\omega \right|^2 \propto \left| e^{-\frac{\sigma_\omega^2 t^2}{2}} \right|^2 \qquad \Rightarrow \sigma_t = \frac{1}{\sigma_\omega}. \tag{A.9}$$

For Nd:Glass systems, an ideal Gaussian with an FWHM of a few nm can be compressed to around 500 fs. However, Ti:Sa systems achieve tens of fs on target, which requires a bandwidth FWHM of 50-100 nm on target.

For identical stretcher and compressor setups a decrease in the bandwidth first results in a shorter temporal pulse duration after the stretcher, which can be approximated by

$$\Delta\tau_s \approx \Phi'' \cdot \Delta\omega \tag{A.10}$$

for large quadratic phases Φ'' of the stretcher. This in turn can be derived [128] by adding a purely quadratic phase prior to the Fourier transform in eq. A.9 and then assuming large quadratic phases.

According to eq. A.10, laser systems with narrower bandwidths must employ larger quadratic phases to reach the same stretched pulse duration.
Typically, laser facilities settle for stretched pulse durations of a few ns, regardless of the compressed pulse duration they achieve. Since the energy in the pulse is limited by the size of the last compressor grating, where the pulse is already recompressed and thus the damage threshold is independent of the employed stretching, there is little reason to increase the pulse beyond the few ns mark.

Thus, systems with larger bandwidths can rely on stretcher and compressor designs with reduced introduce dispersion, in comparison to systems with smaller bandwidths.
Implementing a reduction in dispersion is possible by adjusting the parameters of the stretcher and compressor, as discussed in sec. 1.2.1, being the incident angle α, the line density of the gratings g and the grating distance D. Each change has the same effect on the dispersion coefficient: an increase in the employed dispersion increases the dispersion coefficient on the surfaces in the stretcher and compressor and thus decreases the slope of the introduced rising edge.

The fourth parameter that influences the dispersion of the system is the number of passes. This parameter is intentionally left out of consideration as its influence on the rising edge is more complicated and covered in sec. 2.1.1.

A.4. Combination of Amplitude and Spectral Phase Averaging Effects by the Spatial Beam profile

The model I have developed in cha. 2 is capable of predicting the rising edge introduced by spectral-amplitude effects or by spectral-phase effects.
There have to the best of my knowledge been no investigations on how these two effects condition each other. This appendix provides calculations on how these amplitude and phase effects interplay. The approach is for now limited to the spectral-amplitude effect of spectral clipping on the edges of the considered optical element.
For this calculation, a perturbation term is defined as

$$P(\omega) = T(x) \cdot e^{i \cdot \delta\phi(x)}, \tag{A.11}$$

where the top-hat function $T(x)$ describes the spectral clipping on the finite-sized optical elements, as in sec. 2.2, and $\delta\phi$ the surface distortion as in sec. 2.1.

When we start the calculation of the temporal profile with this modified perturbation term we can use the same linearization of the phase perturbation as in sec. 2.1

$$E(\omega) = \int f(x - a_\omega\omega) T(x) e^{i \cdot \delta\phi(x)} dx E_0(\omega) \tag{A.12}$$

$$= \int f(x - a_\omega\omega) T(x) (1 + i\delta\phi(x)) dx E_0(\omega) \tag{A.13}$$

$$= \int f(x - a_\omega\omega) T(x) dx E_0(\omega) + i \int f(x - a_\omega\omega) T(x) \delta\phi(x) dx E_0(\omega). \tag{A.14}$$

Here, the integral over the first term equals the field after E_A isolated spectral clipping (see eq. 2.22). For the second term, a strategic mathematical manipulation can be used to separate the influence of clipping in a distinct term. For this manipulation, I drag the impact of the top-hat into the limits of the integral, which is possible since the contribution of the term is zero everywhere the top-hat is zero. For the further calculation, I use that the integral of a symmetric function $g(x)$ can be separated into the integral over an aperture and the remaining part

$$\int_{-\frac{x_C}{2}}^{\frac{x_C}{2}} g(x) dx = \int_{-\infty}^{\infty} g(x) dx - 2 \int_{\frac{x_C}{2}}^{\infty} g(x) dx. \tag{A.15}$$

Accordingly, the disturbed spectral field can be formulated as

$$E(\omega) = E_A(\omega) + E_{\text{SP}}(\omega) - 2i \int_{\frac{x_C}{2}}^{\infty} f(x - a_\omega\omega) \delta\phi(x) dx E_0(\omega) dx E(\omega) \quad = E_A(\omega) + E_{\text{SP}}(\omega) - E_{\text{RA}}(\omega). \tag{A.16}$$

This equation now consists of three parts: the isolated spectral-amplitude effect E_A (eq. 2.22), the isolated spectral-phase effect E_{SP} (eq. 2.9) and the interplay between both effects $-E_{\text{RA}}(\omega)$. The additional term can be understood as the part of the beam that would contribute to the spatial smoothing of the PSD if it was not removed by the spectral clipping, which is why I denote this term as the Removed Averaging (RA) in the subscript.

So in the case of an ideal spatial Gaussian, which features a fast declining function $\tilde{f}$ in the isolated cases, this term is detrimental to the temporal profile. The reasoning behind this statement is that the wavelength, which is incident on the very edge of the optical element, is only smoothed by half the Gaussian.
However, when the clipped wavelengths would have experienced a strong phase shift, in the isolated spectral phase case, removing them might prove to be beneficial to the rising edge.
It is thus dependent on the specific configuration if this term is beneficial or detrimental to the temporal contrast. Therefore, it cannot be simply neglected in the context of an upper estimate.

For further calculation a Fourier transform is applied, in order to find the temporal profile corresponding to the field in eq. A.16

$$\tilde{E}(t) = \tilde{E}_A(t) + \tilde{E}_{\mathrm{SP}}(t) - \tilde{E}_{\mathrm{RA}}(t). \tag{A.17}$$

The temporal profile is then given by the absolute square of this field

$$I(t) = I_A(t) + I_{\mathrm{SP}}(t) - I_{\mathrm{RA}}(t) + 2Re(E_A E^*_{\mathrm{SP}}) - 2Re(E_A E^*_{\mathrm{RA}}) - 2Re(E_{\mathrm{SP}} E^*_{\mathrm{RA}}), \tag{A.18}$$

where $I_{\mathrm{A}}(t)$ and $I_{\mathrm{SP}}(t)$ are equivalent to eq. 2.24 and eq. 2.18, respectively. Besides these the isolated spectral-phase effect and the isolated amplitude effect, several mixing terms appear.
The mixing terms with the removed averaging effect are specific to this combined configuration. However, the mixing between spectral-amplitude effects and spectral-phase effects $2Re(E_A E^*_{\mathrm{SP}})$ is comparable to the term appearing in the isolated consideration of the spectral-phase effects in eq. 2.12. In that context, it was possible to simply neglect this mixing term, by realizing that the multiplication by a fast declining function $E_0(t)$ is zero for all relevant times. Unfortunately, this is no longer true in the presence of spectral clipping, especially when both effects have a comparable impact on the temporal profile. With this, I can reinforce the previously made statement, that the validity of this analytical description decreases when the incident temporal profile has already deteriorated to the statement that the validity of the model decreases in the presence of other relevant temporal-contrast-deteriorating effects, even on the same surface.
In summary, I find that the combined effect of amplitude effects and spectral-phase effects on the temporal profile consists mainly of the addition of the temporal profiles of the isolated effects $I_A(t)$ and $I_{\mathrm{PSD}}(t)$, with additional mixing terms that correspond to the energy that would contribute to the STC due to the phase noise, but is removed due to clipping $I_{\mathrm{RA}}(t)$, $2Re(E_A E^*_{\mathrm{RA}})$ and $2Re(E_{\mathrm{PSD}})$ and lastly the coupling between both effects $2Re(E_A E^*_{\mathrm{SP}})$ for all wavelengths.

A.5. Spectral Clipping on two Consecutive Surfaces

This appendix provides an example calculation of the consecutive spectral clipping process described by eq. 2.27. The underlying assumption is that full spatial frequency filtering occurs between the clipping process, meaning that no STC are present during the second interaction. The aim of this is to demonstrate that under the right circumstances, a second spectral clipping process can improve the rising edge, rather than degrade it further.

The temporal profiles for this example can be seen in fig. A.6, where I use an ideal spectral Gaussian as the input of the first element. During this first interaction the beam is spectrally clipped with a small beam size of 80 µm, which results in a hard edge in the spectrum (right) at around 1045 nm and 1062 nm. The corresponding temporal profile to this clipping process shows a considerable deterioration from the FTL, with a contrast of eight orders of magnitude within the first 100 ps before the peak.

The second clipping process is centered between 1050 nm and 1057.5 nm and takes place with a larger beam size of 40 mm (green). The edge that this process introduces in the spectrum reduces the energy of the first edge so much that it can be neglected. The consequence for the temporal profile is that the rising edge from the first interaction is completely removed from the temporal profile and instead, we see a steeper rising edge due to the larger beam size.
However, this rising edge features a slightly higher intensity at times close to the peak than the temporal profile after the first interaction. Nonetheless, this is a considerable improvement when considering that ultra-high intensity lasers feature peak intensities, where the rising edge after the first surface would have been sufficient to ignite a plasma during an experiment.
In a second case, I have increased the beam size during the second interaction to 60 mm (green). This causes the spectral intensity at the wavelength of the first clipping process (1045 nm and 1062 nm) to drop by around six orders of magnitude. The result of this reduction is that the rising edge caused by the first surface is still visible in the temporal contrast, albeit reduced by roughly five orders of magnitude.

From the previous example, we can infer, that even hard edges in the spectrum introduced early in the laser chain might be removed later on, thereby potentially improving the temporal contrast. Furthermore, this is an indication that cases exist, where an increase of the beam size on the second component might be detrimental to the rising edge rather than beneficial.
A typical case where such consecutive clipping processes occur is the combination of stretcher and compressors in a CPA laser chain.

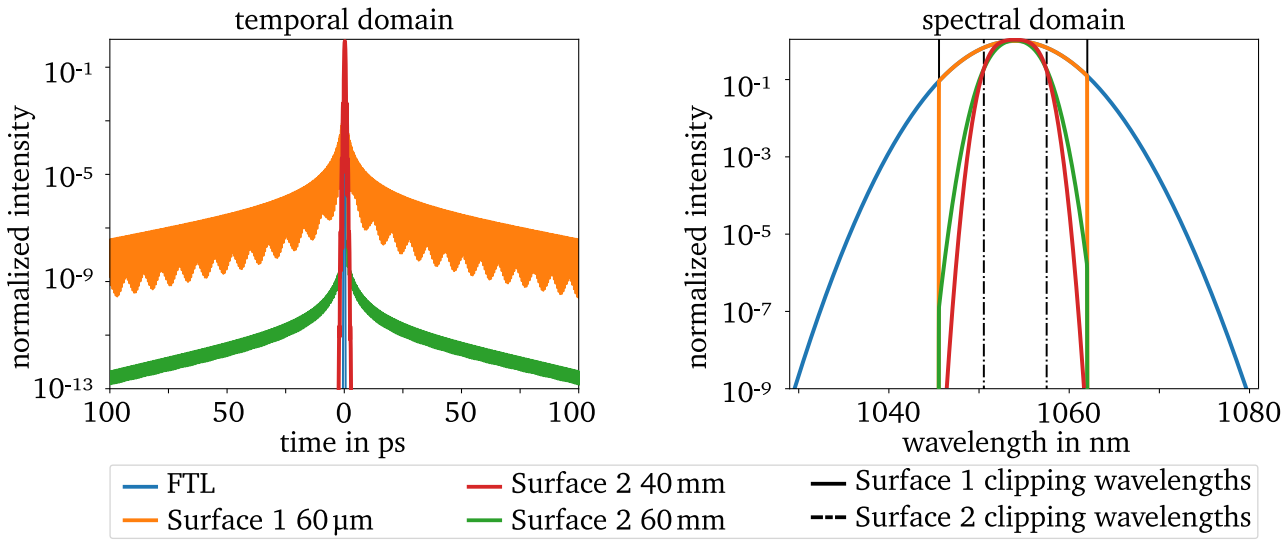

Figure A.6.: Spectral clipping on two consecutive surfaces. Temporal profile (left) and spectrum (right) of an ideal spectral Gaussian after spectral clipping on a first surface, with a small FWHM of 80 µm (orange) and then on a second surface with either a larger beam size with an FWHM of 40 mm (red) or an even larger beam size of 60 mm (green). The black vertical lines in the spectrum mark the clipping wavelength of the first optical element (full line) and the second optical element (dashed line).

A.6. Parameter Study on the Rising Edge Introduced by Spectral Dips

In fig. A.7 a parameter study is depicted on the influence of spectral dips on the rising edge, calculated using eq. 2.24. This is equivalent to damage on an optical surface in the stretcher and an inverse top-hat can be used to describe the impact of this damage on the laser. The scanned parameters are different widths w of the inverse top-hat, depths d of the inverse top-hat, and beam sizes on the considered element σ. For all parameters, the influence on the spectrum is depicted (left), as well as the resulting temporal profile (right). The resulting temporal profile can be described by an envelope and an oscillation, with each parameter having an effect on only one of the two aspects.

The calculations suggest, that the width of the damage does not change the slope of the rising edge, but only the frequency oscillation. This can be understood by comparing this rising edge to the analytical description of a sinc-function (compare eq. 2.39), where it is evident that the width of the top-hat only influences the oscillation frequency of the sine and not the envelope.

The depth of the spectral dip does not influence the oscillation frequency, but only changes the offset of the rising edge.

For the influence of the beam size on the surface, the simulations indicate that this dominates the slope of the rising edge. This is intuitive since for larger beam sizes the hard edges of the dip are smoothed out. For a limit of a large width, the effect of the damage would be completely removed, which must result in the FTL of the undisturbed profile. This stands in agreement with the depicted curves, where a larger beam size produces a steeper rising edge.

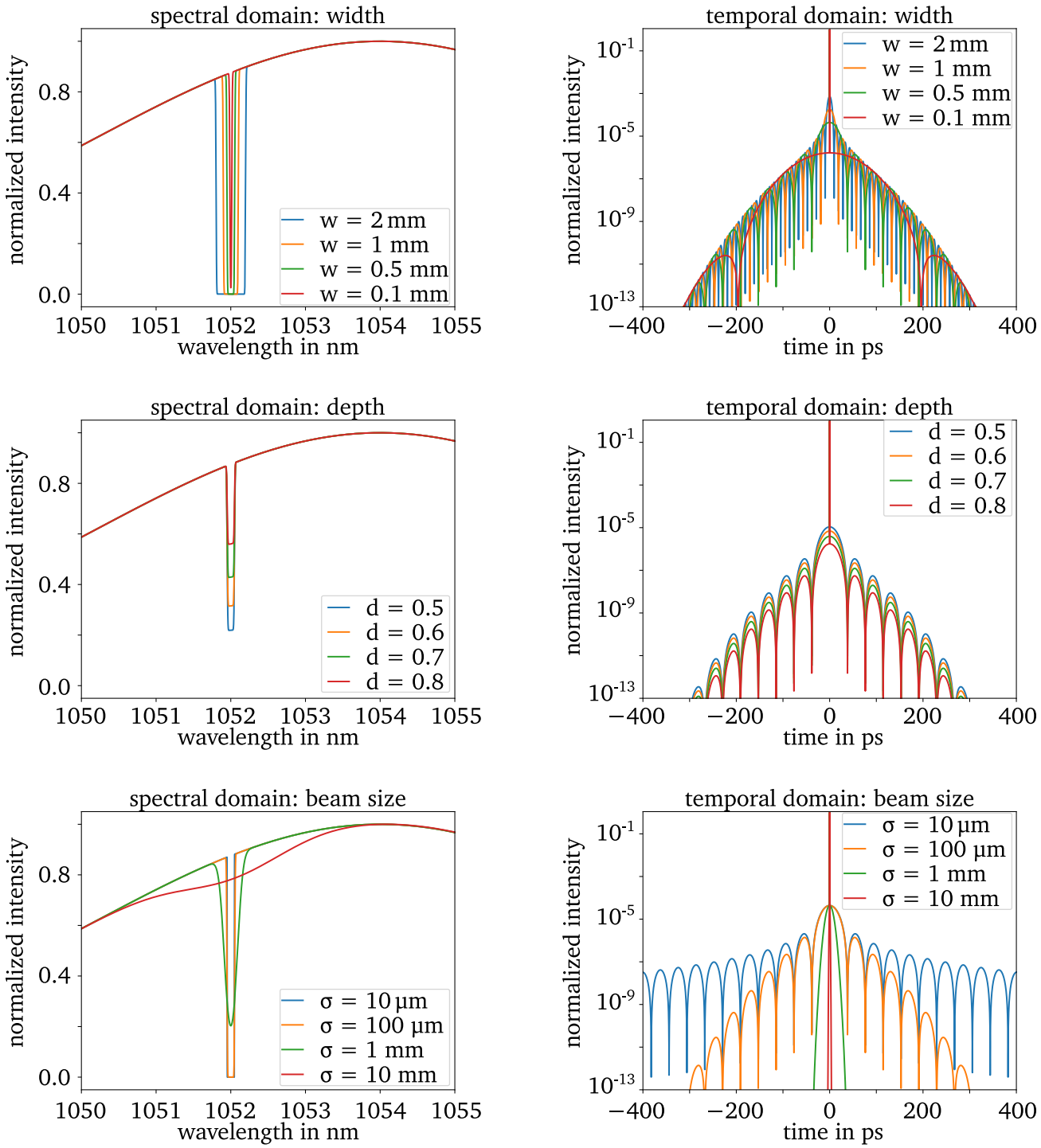

Figure A.7.: Influence of spectral dips in the spectrum (left) on the temporal profile (right). Considered are the influence parameters of, width w (top), depth d (middle), and beam size σ (bottom). While varying one parameter the remaining parameters were left constant at w_c=0.5 mm, d_c=0, σ_c=100 µm. The considered spectrum is an ideal Gaussian, centered at 1054 nm with a width of 9.2 nm.

A.7. Uncertainties of the SHS

For the estimation of the beam size during the PoP in sec. A.9 I used a measurement of the wavefront with an SHS. However, the accuracy of the measurement is limited, due to the uncertainty of the pitch of the utilized micro-lens array. This uncertainty has the impact that the device outputs that the wavefront is flat when the focal spots on the camera are spaced according to the specified pitch.

We can calculate how a defocus would affect the position of the focal points of the micro-lens array and from that estimate the accuracy of the device. Since I am considering the beam profile to be one dimensional I will do the same for the defocus, but this is expandable to 2D. Let us assume a spatial phase of the shape $\phi_{\mathrm{x}} = a(x - x_0)^2$. This can be transitioned from a phase into the spatial domain by multiplication by $\lambda/(2\pi)$.

The effect of a pitch error is, that the focal spot on the CCD-chip is shifted by the ratio of the pitch error to the actual pitch $\Delta p/p$. Using that the beam after the lens will propagate perpendicular to the inclination of the wavefront at each beamlet lets us use trigonometry to connect this displacement on the chip to the phase

$$\frac{\Delta p}{p} = f \tan\left(\frac{d}{dx}\frac{\lambda}{2\pi}\phi_{\mathrm{x}}(x)\right) \approx f\frac{\lambda}{2\pi}2a(x - x_0) = \frac{fa\lambda}{\pi}, \tag{A.19}$$

with the approximation that the displacement is small compared to the focal length. For the used SHS with a focal length of f =11mm, a pitch of p =250 µm and a pitch uncertainty of $\Delta p = 0.5$ µm, according to manufacturer specifications, this results in a phase coefficient of $a = 5 \cdot 10^5$. Or in more intuitive terms, for the wavelength of λ =1040 nm this results in a PtV of the wavefront of

$$PtV = a(pN)^2/(2\pi) \approx 0.5\lambda \tag{A.20}$$

for an SHS with 20 lenses along the considered axis, meaning $N = 10$ focal spots between peak and valley, each with a spacing of the pitch p. A visualization of this systematic error can be found in fig. A.8, where we see that the focal spots end up with a spacing on the CCD chip that is equivalent to the expected pitch, but only due to the defocus. A flat wavefront would however cause the focal spots to be spaced with the actual pitch. It is to note here, that while I have chosen to calculate the uncertainty introduced for the pitch uncertainty of the micro-lens array, the same can be done for the pitch of the camera pixels, resulting in comparable uncertainty. In summary, the pitch uncertainty causes us to believe that the beam is collimated at the position of the SHS, while in reality, it has a defocus, which we have to consider for the Gaussian beam propagation when calculating the beam size on the respective optical elements in the stretcher.

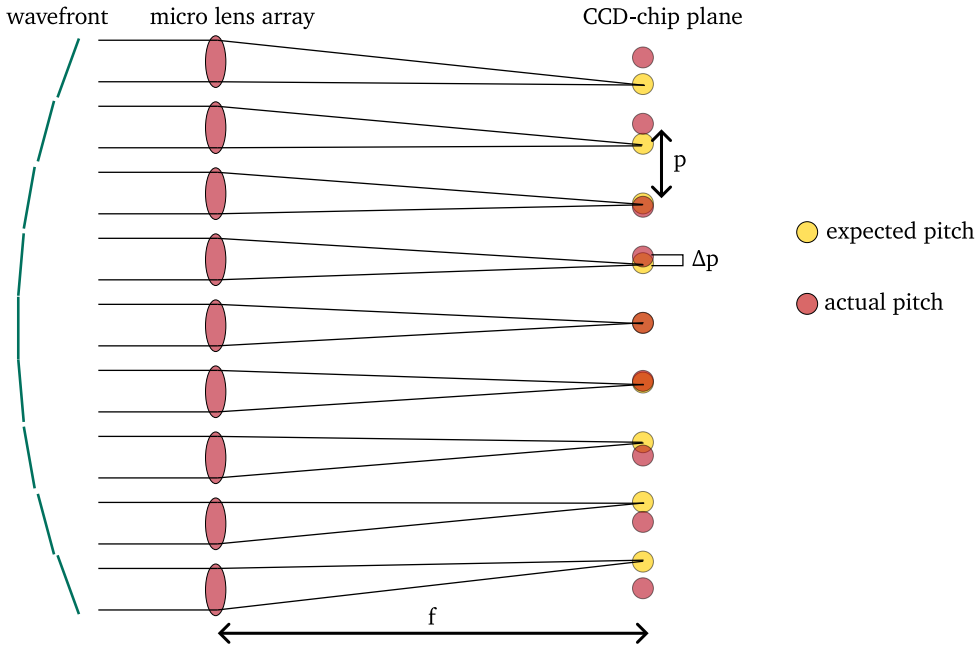

Figure A.8.: Schematic of the systematic defocus introduced when using an absolute reference pitch in an SHS. The discrepancy between the expected pitch and the actual pitch causes us to introduce a defocus into the beam during alignment.

A.8. Impact of the Regenerative Amplification at PHELIX on the Rising Edge

A ring regenerative amplification stage is used at PHELIX for amplification of the temporally stretched pulse. In this appendix, I consider the effect of the linear and non-linear index of reflection of the Ti:Sa crystal employed in this device. The conclusion of this study is that the rising edge at PHELIX is currently not expected to be limited to the device.

After either of the stretchers, the beam is transmitted through a Pockels Cell (PC) and a DAZZLER, before being coupled into a ring regenerative amplification stage.

There the beam traverses 66 times for the unfolded stretcher through a Ti:Sa crystal with a free aperture of 10 mm and a length of 25.4 mm, where it is amplified from an energy of around 200 µJ to around 20 mJ, meaning with a gain of approximately $G = 100$. For now, I assume that the Gain profile is a rectangular function with values of one outside the 7 mm diameter of the pump beam, and G inside the diameter of the pump. After each round-trip the beam hits a leaky mirror and the transmitted light is directed onto a photodiode. The trace on this photodiode is depicted in fig. A.9, where each peak corresponds to one round trip. The amplitude of the peak behaves linear with the pulse energy and, since the energy after the last round trip is known, the amplitude can be scaled to the energy of the pulse after each round trip. The regenerative amplifier converts the mode of the beam to the Eigenmodes of the cavity, which in this case is a TEM00 mode, the so-called Gaussian mode. The parameters of the cavity define the waist of the beam to approximately 0.8 mm and with an approximate pulse length of 1.5 ns the trace can be further scaled from the energy to the intensity in the crystal. Using a logistic fit to the scaled trace provides the signal intensity for each pass.

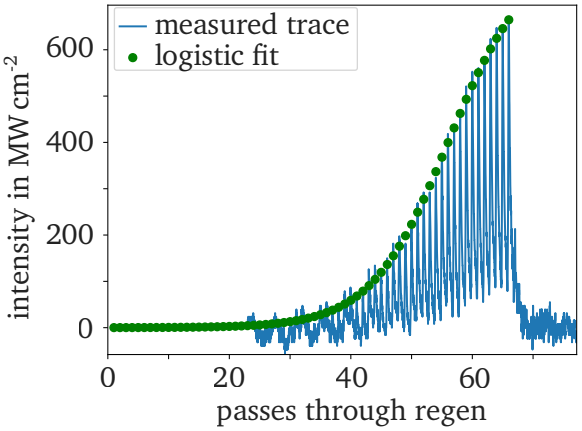

Figure A.9.: Photo diode signal of the transmission through a leaky mirror in the PHELIX ring regenerative amplification stage. The signal strength is linearly mapped to the intensity for the parameters of the seed in the amplification medium. Due to the finite dynamic range of the data set the intensity of the additional passes that happen at low intensity are extrapolated by fitting a logistic function to the trace.

In the following, I calculate how the refractive index of the Ti:Sa influences the rising edge. In this context, I distinguish between the linear index of refraction and the non-linear index of refraction, which becomes relevant at high laser intensities.

Impact of the linear refractive index in the Regenerative Amplifier on the Temporal Contrast

Besides energy, the seed pulse also gains spectral phase during the propagation due to the material dispersion of Ti:Sa. The spectral phase introduced by this must be compensated by the stretcher and compressor, which is at PHELIX done by directing the beam through the complete beamline and into an SSAC. Then the grating distance and the input angle of the stretcher are adjusted while leaving the central frequency on the optical axis of the stretcher. This alignment procedure allows us to compensate second and third-order phase terms, in theory perfectly. However, since these are only two degrees of freedom we are only able to compensate these first two phase terms and not higher-order phase terms. This leaves a residual spectral phase ϕ_{material} that reduces the compressibility of the laser pulse and deteriorates the temporal contrast

$$\phi_{\text{res}} = \phi_{\text{stretcher}}(\alpha, D) + \phi_{\text{material}} + \phi_{\text{compressor}}. \tag{A.21}$$

Since other research suggests that the introduced fourth-order phase from the material dispersion in the regenerative amplifier is responsible for the rising edge [129], I calculated the impact on the spectral phase of this using the Sellmeier coefficients [130] for Sapphire [131], and a total distance traversed through the medium given by the number of passes and the length of the crystal $66 \cdot 25.4\,\text{mm} = 1.7\,\text{m}$. Then I found the stretcher configuration that best minimizes the mean square error of the residual phase ϕ_{res} using a numerical solver based on the Limited-memory Broyden-Fletcher-Goldfarb-Shannon with Bounds method [132, 133], by adjusting the two available degrees of freedom. In an 1%-1% area around the peak of the spectral intensity, the resulting phase is of the order of 100 mrad and has almost no impact in the temporal contrast, for the spectrum at PHELIX. This rules out the linear refractive index of Ti:Sa as

the source of the rising edge. It is however to note that this effect is bound to become relevant for larger bandwidths and that the refractive index is not purely linear.

Impact of the non-linear refractive index in the Regenerative Amplifier on the Temporal Contrast

When the intensity is high enough the non-linearity of the refractive index becomes relevant, which is in the case of sapphire $2.8 \cdot 10^{-16}\,\mathrm{cm}^2/\mathrm{W}$ [134]. Due to this non-linearity, the laser accumulates an additional phase that is called the B-Integral which can be approximated with

$$B(t) = \frac{2\pi}{\lambda} n_{2,\mathrm{Sapphire}} I_{\mathrm{max}} I(t) dz, \tag{A.22}$$

which uses the upper estimate that the intensity is constant over the length of the crystal.

In order to calculate the impact of this phase on the laser pulse after the regenerative amplifier, an iterative approach is necessary with one iteration corresponding to one pass through the crystal. For the first step, we need the temporal profile of the stretched laser pulse, which is non-trivial.

Even though the model developed in this thesis describes the impact of the spectral-phase deteriorations on the temporal profile of the compressed pulse, it provides little information about the fields that correspond to this intensity profile. In theory, any rising edge can be produced by either pure amplitude effects (e.g. spectral clipping), pure spectral-phase effects (e.g. PSD), or a combination of both. The case of pure spectral clipping allows us to find the electric field amplitude $\tilde{E}_0(t) = \sqrt{I_A(t)}$. In order to add the effect of the PSD in the form of a spectral phase I am again using an upper estimate, by neglecting the spatial averaging in the PSD and instead assuming that the beam on each surface is a line. This allows us to use the PSD to calculate a random height profile by inverting eq. 2.17 and define the incident field into the crystal as

$$E(\omega) = E_A(\omega) \cdot e^{i4\omega/c \cdot H(\omega/a_\omega)}, \tag{A.23}$$

where $E_A(\omega)$ is the FTL of $\tilde{E}_A(t)$. For the dispersion coefficient a_ω I used the value found for the second interaction with the spherical mirror, for both stretchers (compare tab. A.1). The spectrally clipped field corresponds to the considerations in sec. 4.3.3. Then, in an iterative process, I insert the temporal field from this as the Fourier transform of eq. A.23 into eq. A.22, which I add as a temporal phase to the temporal field.

After the 66 passes the accumulated B-Integral over the temporal position in the stretched pulse is depicted in fig. A.10 (bottom, left) together with the temporal profile after recompression (top) and the spectrum/spectral phase after recompression (bottom, right). In the last, I only included the calculations for the beam traversing through the folded stretcher, in order for the plot to remain clear. The difference between the incoming and outgoing beam for the recompressed temporal profiles is fairly below the uncertainty of the calculated traces and can be thus neglected.

Similar to the linear dispersion a solution for the stretcher configuration exists, that minimizes the remaining phase. But in all three cases, the required position change of the stretcher grating that would compensate for the minuscule amount of spectral phase is of the order of 200 µm, which is again fairly below the alignment accuracy of the stretcher.

In summary of the considerations on the regenerative amplification, the impact of the linear and nonlinear refractive index on the rising edge can be neglected.

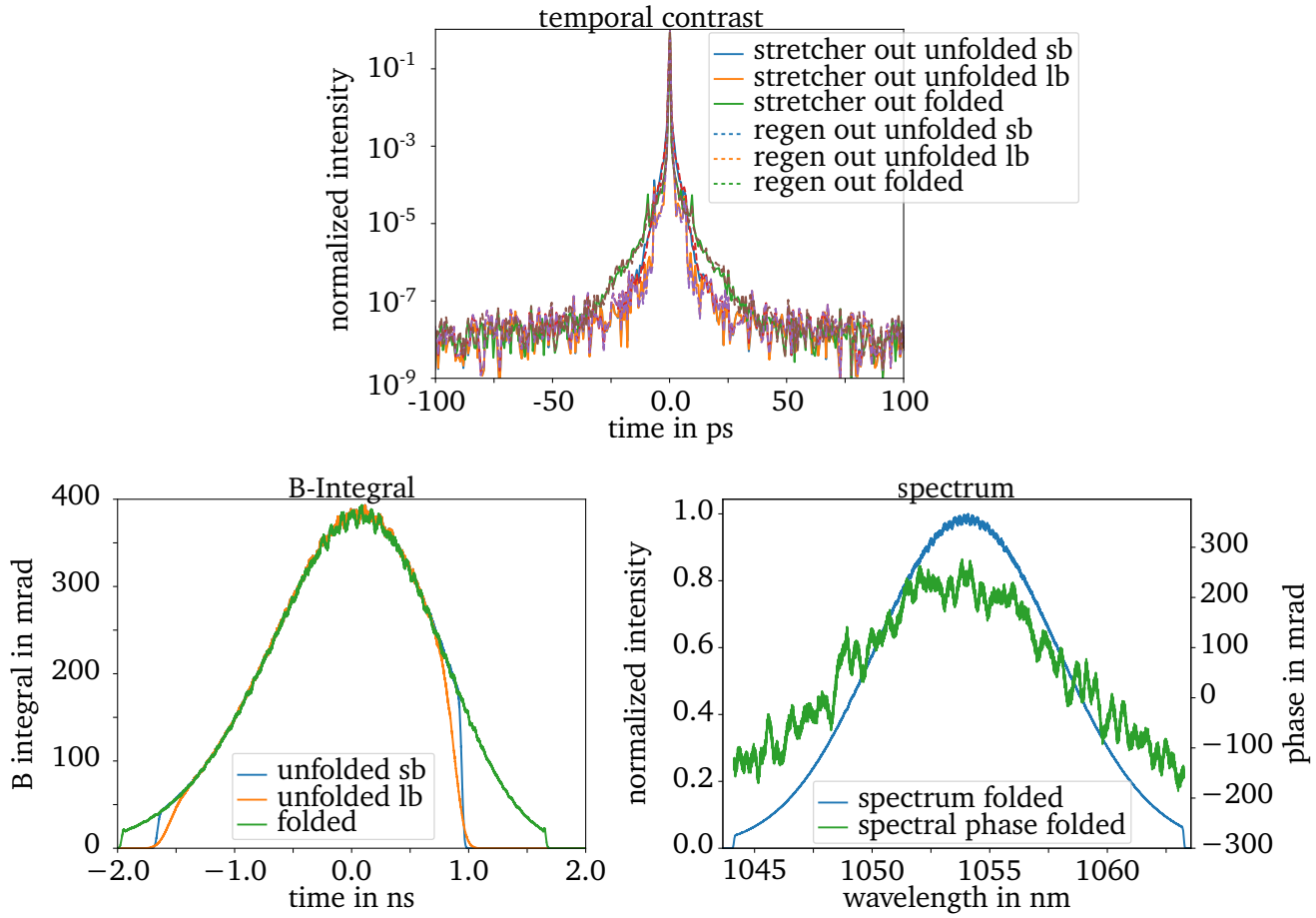

Figure A.10.: Accumulated B-integral of the disturbed, stretched beam after passing through the ring regenerative amplification stage at PHELIX (bottom, left), for the unfolded design with a smaller (blue) or larger (orange) in-stretcher beam size and for the folded design (green). Due to the large stretching, all frequencies are mapped linearly over time and the temporal intensity resembles the spectral profile, with the spectral phase being expressed as high-frequency oscillations in the signal. Since the B-integral scales linearly with the temporal intensity, the B-integral also resembles the spectral profile (bottom, right). Depicted on the top are the disturbed temporal profiles after recompression with and without the B-integral, for all three stretcher configurations.

A.9. Overview of the Stretcher Parameters at PHELIX

An overview of the parameters necessary to determine the impact of spectral clipping and spectral-phase effects of the stretcher setups during the test at PHELIX, described in cha. 4, is presented in this section. The clipping wavelengths for each configuration are measured and the transfer function for each surface is specified. The transfer functions are given by the clear aperture of all optical elements used and the dispersion on each surface. They are summarized in tab. A.1, together with all the other parameters necessary for the calculation of spectral phase and amplitude effects, such as the number of interactions, the position of the element, the transmission bandwidth, beam size on the optical element and dispersion coefficient a_ω.
Additionally included in this table are the beam sizes at the individual positions. For the unfolded design two beam sizes are given, referring again to sb and lb. For the folded stretcher, the spatial beam size of the uOPA output is used, which is equal to sb. The beam sizes in the Fourier plane are calculated using eq. 1.20, and the beam size in the intermediary field is calculated using the opening angle between the FF and the NF

$$\sigma_{\text{interm}} = 2\sigma_{\text{NF}} z_{\text{interm}} / R \tag{A.24}$$

For both setups, all beam sizes are adjusted to take into account the projection onto and from the grating. This results in a slightly larger beam size on the sphere than measured on the camera and a considerably larger beam size on the grating.

The last row of the table shows the dispersion coefficient. While the calculation of the transferred bandwidth and the dispersion coefficient is possible analytically, similar to sec. 3.2.1, I have used the ray-tracing simulation from the investigation of the spherical aberrations in these two setups to determine them. The validity of this approach is based on the PoP, where the approach provided a good agreement to the analytical calculation. I have also included the number of reflections from each surface in a "number" column, for the calculation of the impact of the PSD.

Element	Number	Position	Aperture	Transmission	Beam size (FWHM)	a_ω
Folded						
Sphere	2	NF	305 mm	1029.2 nm-1075.2 nm	1.9 mm	3.89 mfs
	2			1042.7 nm-1064.5 nm		8.21 mfs
Flat 1	2	interm.	219 mm	1040.6 nm-1066.3 nm	1.4 mm	5.03 mfs
	2			1044.6 nm-1062.8 nm		7.07 mfs
Flat 2	2	FF	190 mm	1044.5 nm-1063.0 nm	0.85 mm	6.06 mfs
Grating	2	NF	350 mm	1041.2 nm-1064.1 nm	4.1 mm	8.99 mfs
Roof top	1	NF	110 mm	1040.6 nm-1064.5 nm	1.2 mm	2.70 mfs
Unfolded						
Sphere 1	2	NF	152 mm	1009.3 nm-1088.1 nm	1.9 mm & 10.0 mm	1.13 mfs
Sphere 2	2	NF	152 mm	1045.5 nm-1062.0 nm	1.9 mm & 10.0 mm	5.46 mfs
Grating 2	2	NF	220 mm	1048.0 nm-1062.2 nm	4.1 mm & 21.1 mm	9.00 mfs
Flat	1	NF	130 mm	1048.6 nm-1066.2 nm	1.2 mm & 6.3 mm	2.68 mfs

Table A.1.: Parameters used for the stretcher setups at PHELIX, with the corresponding setup, the name of the optical element, the number of interactions of the beam with the element, and the position, where "interm." represents the intermediary field between NF and FF. In this instance, the relevant intermediary element is positioned at a distance of 1.48 m from the spherical mirror with a radius of curvature of 5.6 m. In the unfolded design, the radius of curvature is 3.048 m. Further included in the table is the size of the coated aperture of each element. The spectral transmission bandwidth of each element and the dispersion coefficient a_ω on each element are calculated by ray-tracing the system. The beam size has been measured in the NF and used to calculate the beam size on all other elements. For the intermediary field, the assumption was used that the intermediary field and the NF are far away from the FF, which implies a linear dependency between both beam sizes. Additionally taken into consideration is the beam-size change due to the projection on the considered surface. For the unfolded design, an additional configuration with a magnifying telescope is available, resulting in a second beam size.

A.10. Estimating the Power Spectral Density for the Components at PHELIX

In order to estimate the rising edges caused by spectral-phase effects, an assumption concerning the PSD of the employed surfaces must be made, since measurements only the spherical mirror and flat mirror in the unfolded design are available (compare app. A.2).
This assumption is that the shape of the PSD solely depends on the kind of optical element. This means that the PSD shape of all flat mirrors is the same, as well as the PSD shape of the spherical mirrors and that of the gratings. Furthermore, I assume that the magnitude of the PSD can be scaled by the specified surface roughness. The corresponding surface qualities in terms of PtV for both setups are summarized in tab. A.2. Accordingly, the scaled PSDs are

$$PSD_{\text{sphere,folded}} = 0.4 \cdot PSD_{\text{sphere,unfolded}}, \qquad PSD_{\text{flat, folded}} = 0.7 \cdot PSD_{\text{flat, unfolded}},$$

where $PSD_{\text{flat, unfolded}}$ and $PSD_{\text{sphere, unfolded}}$ available from measurements discussed in app. A.2.
Even less is known about the PSD of the employed gratings, since no measurements of their PSD are currently feasible. For this analysis, I have settled on using measurements of comparable gratings [125], as depicted in fig. A.4. This rough estimation involved extracting specific data points on the measured curves

and interpolating between those points to obtain a comprehensive data set. This shows that we can expect the PSD of the gratings to be two to three orders of magnitude larger than the flat and spherical mirrors over the relevant range.

Element	Surface PtV
Folded	
Sphere	$\lambda/20$
Flat 1	$\lambda/20$
Flat 2	$\lambda/20$
Roof top	$\lambda/20$
Unfolded	
Sphere 1	$\lambda/8$
Sphere 2	$\lambda/8$
Flat	$\lambda/14$

Table A.2.: Surface quality of the optical elements used in the stretchers, in PtV. All values are based on manufacturer specifications.

A.11. Impact of the Pre- and Main-Amplification Stages on the Rising Edge at PHELIX

In the PA and MA at PHELIX the beam can be amplified from the 20 mJ at the input up to 1 kJ [57]. At this energy, the intensity after compression is so high that it is locally of the order of the damage threshold of the second compressor grating. Thus, for short-pulse experiments, the peak energy is limited to around 200 J.

For the experimental campaign described in cha. 4, the PA and MA stages are not pumped, meaning that no amplification takes place. However, I will still estimate the amount of on-shot B-Integral here in order to give an estimate of the differences in the rising edge between the measurements and the on-shot contrast, which is hard to measure. The various transmissive optical elements that contribute to the B-Integral in the PA and MA are first two passes through 19 mm thick and 250 mm long Nd:Glass rods, two passes through 45 mm thick and 250 mm long Nd:Glass rods, in the PA and 20 passes through the ten 315 mm thick and 43 mm long Nd:Glass slabs under Brewster angle [57]. It is to be noted here that I neglected the B-Integral of beam splitters, lenses, windows, and waveplates due to their small length and only consider the long rods.

In order to estimate the B-integral the energy at the various elements must be estimated. Directly after the regenerative amplifier approximately half the energy of the beam is lost at the serrated aperture. Afterward, the energy can be estimated by assuming that each pass through an amplifier rod in the PA contributes with the same gain to a total gain in the PA of around 55 and for the MA of a gain of around 55 over a total of 20 equivalent passes through the slabs. The beam area is well characterized at each position and varies between 14 mm-15 mm in the 19 mm rod. In the 45 mm rod the beam diameter is approximately 38 mm and in the MA around 240 mm, for the largest available serrated aperture configuration (compare sec. 4.5). With these values and again a stretched pulse length of 1.5 ns together with a nonlinear refractive index of Nd:Glass of around $1.13 \cdot 10^{-13}$ esu$\approx 3.1 \cdot 10^{16}$ cm^2/W (APG-1 Phosphate Laser Glass by Schott) [135]

the impact of the B-integral on the rising edge is negligible and the calculated profiles do not significantly differ from the input pulse profile over the dynamic range available to the used numeric calculation. This is a good indication that measurements of the temporal-contrast curves that are commonly done off-shot, at laser facilities with low repetition rates and high-intensity laser systems like PHELIX, are comparable to the on-shot contrast.

Obviously, other effects like gain narrowing of the spectrum in the laser chain play a role in the temporal profile in the detector. However, during the experimental campaign at PHELIX, which is the main concern of this work, the bandwidth is limited by spectral clipping in the stretchers and the compressor.

A.12. Identification of the relevant surface interactions for the rising edge at PTAS

The PW-compressor consists of two gratings in a single-pass configuration, which leaves the beam spectrally dispersed after transmission. Accordingly, each optical element after the PW-compressor introduces a rising edge. However, most of them are negligible as demonstrated below.
The surfaces to consider are the second grating, several dielectric turning mirrors, and a glass parabola in the PTAS and a smaller copper parabola, also in the PTAS. Together, both parabolic mirrors form an off-axis telescope for beam demagnification. After this demagnification, the beam path consists of several turning mirrors and lens-based telescopes before arriving at the detector, which is discussed in sec. 4.7.

For spectral-phase effects all surfaces after the demagnification are negligible, which can be reasoned as follows: after the parabolic mirrors the beam is demagnified, which can be expressed in the analytical considerations by first adjusting the scaling of the spatial profile to $f(x/M)$, where M is the magnification, and then scaling the dispersion coefficient in eq. 2.7 to Ma_ω which results in

$$E_{\mathrm{SP,M}}(\omega) = \int f(\frac{x - Ma_\omega\omega}{M})P(x)dxE_0(\omega). \tag{A.25}$$

Repeating the calculations of the temporal profile yields similar results as eq. 2.18, with the effect of the magnification exclusively in the PSD

$$I_{\mathrm{SP,M}}(t) = I_0(t) + \frac{16\pi^2\epsilon_s}{a_\omega^2\lambda_0^2\Delta k}\left|\tilde{f}\Big(\frac{t}{a_\omega}\Big)\right|^2 \mathrm{PSD}\Big(\frac{t}{Ma_\omega}\Big). \tag{A.26}$$

When considering all investigated PSD in fig. A.4 and assuming that these shapes are representative of all considered elements, then it is clear that

$$\mathrm{PSD}\Big(\frac{t}{Ma_\omega}\Big) < \mathrm{PSD}\Big(\frac{t}{a_\omega}\Big), \tag{A.27}$$

when $0 < M < 1$. Under these assumptions, it is valid to conclude, that, for similar surfaces, the rising edge from spectral-phase effects introduced after the telescope is negligible.

This leaves the second grating of the PW-compressor, flat dielectric turning mirrors, and a parabola. I assume the dominating surface to be the second compressor grating since the considerations in app. A.2 suggest a systematically higher PSD for gratings than for the flat, dielectric turning mirrors or focusing element. An investigation of the validity of this approximation is currently ongoing for the copper parabolas, which are used as a standard configuration during user experiments. For now, I however assume that the

PSD of the parabolas is systematically smaller than that of the grating and I restrict the investigation of spectral-phase effects to this surface.

For spectral clipping, the dominating surfaces can be identified based on the optical element sizes and the beam size at the optical element. The limiting element is the second compressor grating.

A.13. Impact of Line Density Mismatch on the Temporal Contrast

The TW-Compressor at PHELIX features a grating with a line density different from the rest of the discussed dispersive elements in the PHELIX laser chain.
While all other components utilize gratings with a line density of 1740 l/mm, the TW-compressor employs a grating with a line density of 1480 l/mm.

The effect that this has is that the spectral phase can not be perfectly matched between the compressor and the stretcher, always leaving a residual spectral phase. The degrees of freedom that can be used for the matching are the angle of incidence α and the grating distance D. In a similar fashion to the removal of the residual phases caused by the (linear and nonlinear) refractive index of the Ti:Sa crystal in the regenerative amplifier (compare sec. A.8) we can find a solution to the grating alignment that minimizes the residual phase.

It is possible to analytically find the configuration where both the quadratic phase coefficient and the cubic phase coefficient are equal for the compressor and the stretcher. Since this analytical solution is tedious to find, I settled again on numerically solving this which results in $\alpha_{\mathrm{TW}} = 41.51°$ and $D_{\mathrm{TW}} = 4.79\,\mathrm{m}$. This differs from the parameters specified during the construction of the compressor. Repeating the calculation of the rising edge for clipping and the PSD with these ideal parameters rather than with the specified parameters does however yield almost identical results. Reasons to explain the discrepancy between design parameters and the calculated ideal parameters are that in the intended setup the compressor was under vacuum, which changes the index of refraction, and that for the calculation during the commissioning, additional effects like the accumulation of dispersion due to the propagation through air and diverse laser optics were considered. However, considering those effects as well would not decrease the phase mismatch but rather add to it. Since I am in this context only interested in the impact of the line density mismatch, I will neglect the other effect, which I have, during the considerations of the regenerative amplifier, already demonstrated to be negligible for the bandwidth at PHELIX (compare sec. A.8).

The spectral phase mismatch calculated from those assumptions is depicted in fig. A.11 (left) together with the resulting derivation from an FTL pulse (right). For the estimation of the FTL the bandwidth after the folded stretcher was used since it features the broadest spectrum and can thus be expected to be the most sensitive to spectral phase. However, the PtV of the spectral phase is with $<0.18\,\mathrm{rad}$ negligible, as evident in the small derivation of the temporal profile from the FTL.

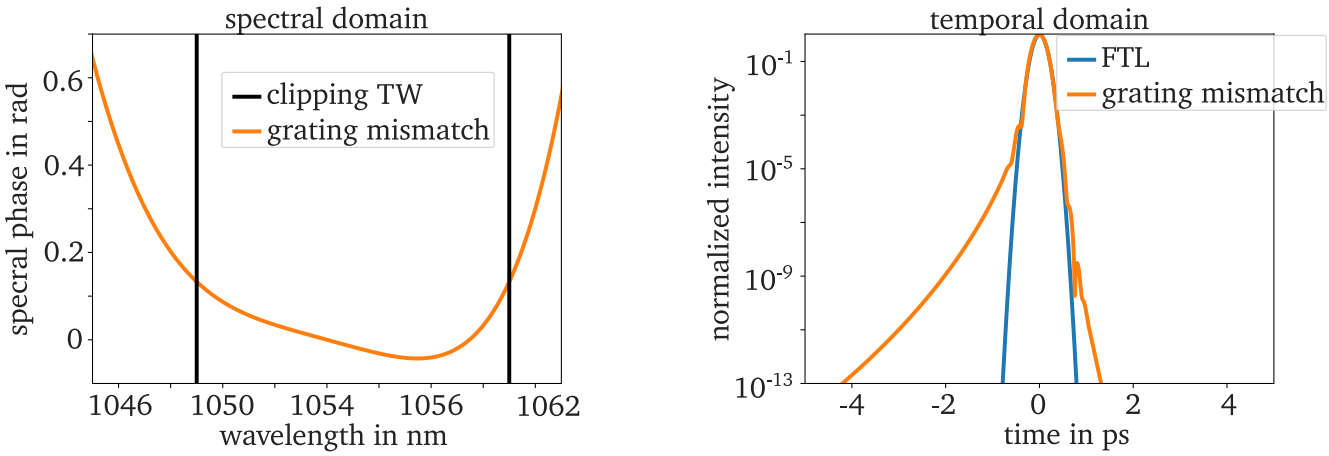

Figure A.11.: Left: residual spectral phase after an idealized stretcher and compressor with mismatching line density (1740 l/mm in the stretcher and 1480 l/mm in the compressor). Right: impact of the residual phase on a Fourier-transform limited pulse with a spectral width similar to the transmitted bandwidth through the folded stretcher design. The black lines indicate the wavelengths of spectral clipping in the TW-compressor. The peak-to-valley of the spectral phase in the transmitted area is below 0.18 rad.